

The interplay between the biochemical and biomechanical properties to the establishment of perineuronal nets

Luke Souter

The University of Leeds
Institute of Medical and Biological Engineering
Faculty of Engineering

Supervisors: Dr Jessica Kwok, Professor Richard Hall, Dr Ralf Richter

September, 2020

The candidate confirms that the work submitted is his own, except where work which has formed part of jointly-authored publications has been included. The contribution of the candidate and the other authors to this work has been explicitly indicated below. The candidate confirms that appropriate credit has been given within the thesis where reference has been made to the work of others.

The image presented in Figure 20 was produced by Emma Sewart, supervised by Jessica Kwok at the University of Cambridge.

Results for the ratio of $\Delta D / -\Delta f$ for films of CS in chapter 4 used to help validate the GAG sizing methodology were provided from the Master's thesis of Ashleigh Goodenough, supervised by Jessica Kwok at the University of Leeds (Goodenough, 2018).

Diocetadecyldimethylammonium (DODA) lipid analogue with a chelator tris-nitrilotriacetic acid (NTA) headgroup used in chapter 4 was kindly provided by Changjiang You and Jacob Piehler (Osnabrück University, Osnabrück, Germany) and were prepared as described by Beutel *et al* (2014).

This copy has been supplied on the understanding that it is copyright material and that no quotation from the thesis may be published without proper acknowledgement.

The right of Luke Souter to be identified as Author of this work has been asserted by him in accordance with the Copyright, Designs and Patents Act 1988.

Acknowledgements

I would firstly like to thank my supervisors Jessica Kwok, Ralf Richter and Richard Hall, as without your guidance, patience and kindness I would not be sat here at the end of writing this. Especially Jessica and Ralf, I cannot thank you both enough for the opportunity to work in your laboratories over the past few years, it has been a pleasure that I will remember fondly forever. This neatly brings me onto their incredible laboratory teams. I would like to thank from the Kwok lab: Stuart Dickens and Ashleigh Goodenough for being the best colleagues and friends I could have possibly asked for, always on hand to help when I needed it most; Lynda Djerbal for always making me smile; Sylvain Gigout for your peculiar sense of humour that was a joy to behold, please never change; Sian Irvine for your patience when I first joined the team and the training you provided. From the Richter lab I would like to give a special thank you to Fouzia Bano and Rickard Frost for all of the training you both gave me, I honestly could not have asked for two better, more patient teachers.

The next thank you is for everyone in the 5.55 office space for making it such a wonderful working environment. Although there was no natural light, it was still a bright place to work. Special mentions to Richard Dickson, Rafeal Aguiar, Piyanee Sriya, Thomas Richards and Mungo Elms for your humour and friendship, long may it last.

Without having such incredible friends to support me along the way who knows where I would be. Gareth York, I have spent far too much time with you, in too many universes to count, thank you for always making me laugh and being one of the best friends I could ask for. Equally Richard Thorning and Alex Mathews, you have both always been there helping and supporting me since our undergraduate days at Bristol, thank you for being genuinely awesome friends, even if we only get to see each other in person a couple a times a year. Also, a special thank you to Angelica Compatangelo for being so incredibly supportive during such a tricky time, you really have been amazing, not even a global pandemic could get in the way of us. I would also like to thank Kat Hutchinson, Laura Rice, Chris Partington, Alice Webb, Chris Bennigsen and Brad Balmer for all your help, support and friendship throughout my time in Leeds.

Last, but by no means least I would like to thank my family for always being there to support me: I bet you sure are glad that this is now finished.

Abstract

Perineuronal nets (PNNs) are an important pericellular matrix structure that form around the soma and dendrites of sub-populations of neurons in the mature central nervous system (CNS). They have been implicated in regulating synaptic plasticity, increasing synaptic stability, neuroprotection and memory formation. They are composed of hyaluronan (HA), chondroitin sulfate proteoglycans (CSPGs), Haplns and tenascin-R, that can assemble in many different potential configurations to form morphologically distinct PNNs. Currently there is a proposed model for the assembly of this extracellular matrix structure, but the detailed mechanism for the stabilisation of the morphologies of PNNs is not yet known. The aim of this thesis project is to characterise the biochemical heterogeneity of PNNs and understand how PNN molecules assemble to form a pericellular coat with distinct morphologies, while ascertaining the biomechanical contribution of each molecule to the pericellular coat.

Using Western blotting, regional variations in the molecular composition of PNN-associated molecules were observed that may present an opportunity to modulate PNNs region specifically in the future. Different splice variants and levels of glycosylation of CSPGs were profiled in different CNS regions. To analyse the assembly of PNNs in real-time and measure the biomechanical properties of the film, an *in vitro* methodology was established using quartz crystal microbalance with dissipation monitoring (QCM-D). The PNN film was modelled using a tethered film of HA, to which HA and proteoglycan link protein 1 (Hapln1) and aggrecan (Acan) were sequentially added. Hapln1 bound to HA films stably, while binding of Acan was reversible, though could be stabilised by sequentially adding Acan to Hapln1-presenting HA films. While the density of HA films influenced the interaction of Acan, increasing the density of pre-bound Hapln1 did not. Furthermore, Hapln1 addition caused a rigidification of HA films, while Acan addition caused a softening effect, highlighting the important role of Hapln1 in stabilising the PNN matrix and a potential mechanism for regulating the biomechanical properties of PNNs. As cells in the CNS can mechanosense, understanding these mechanisms may offer new therapeutic avenues for targeting neurological diseases correlated with changes to PNNs.

In addition, a new methodology for sizing surface-anchored GAG chains was established using QCM-D by utilising the relationship between the ratio of $\Delta D / -\Delta f$ and GAG size. This methodology highlights the effect of HA size on the biomechanical properties of the PNN film and presents a potential future methodology for the characterisation of PNN HA size. Mechanisms for biomechanically manipulating PNN films by increasing HA size and varying the density of Hapln1 and HA suggest PNNs may partially function via a biomechanical signalling mechanism in addition to already established mechanisms.

Table of Contents

Table of Contents	iv
Chapter 1: Introduction	1
1.1 Overview	1
1.2 Functional importance of PNNs	3
1.2.1 Synaptic plasticity.....	3
1.2.2 Modulating PNNs	4
1.2.3 A Sink for cation storage to allow increased neuronal activity to occur.....	5
1.2.4 PNN molecular components may directly regulate neuronal activity through signalling	6
1.2.5 Signalling molecules interact with PNNs to regulate activity	6
1.2.6 A barrier to the movement of post-synaptic receptors on the cells surface.....	7
1.2.7 Physical barrier.....	8
1.3 The importance of cellular mechanosensing in the nervous system	9
1.3.1 Defining mechanosensing	9
1.3.2 Hypothesised mechanisms of mechanosensing	10
1.3.3 Cells in the nervous system detect and respond to biomechanical changes of substrates.....	11
1.4 Molecular components of PNNs	13
1.4.1 HA	13
1.4.2 Haplns	14
1.4.3 CSPGs	14
1.4.4 Tn-R	17
1.4.5 Cellular contributions of molecular components to PNNs	17
1.4.6 Temporal expression and staining pattern of PNN components	18
1.5 Structural heterogeneity of PNNs	19
1.5.1 Heterogeneity in the PNN-associated components.....	19
1.5.2 Proposed structure of PNNs.....	21
1.5.3 Heterogeneity of PNN morphologies.....	22
1.6 Objectives of this thesis	24
Chapter 2: Methodology	26
2.1 Western blotting	26
2.1.1 Animals.....	26
2.1.2 Brain lysate preparation	26
2.1.3 Sodium dodecyl sulfate – polyacrylamide gel electrophoresis (SDS-PAGE)	26

2.1.4 Western blotting	27
2.1.5 Densitometry	28
2.1.6 Statistics	28
2.2 Quartz crystal microbalance with dissipation monitoring (QCM-D)	29
2.2.1 Quantitative explanation of QCM-D.....	29
2.2.2 Measurements using QCM-D.....	33
2.2.3 Preparation of liposomes.....	34
2.2.4 Passivation of tubes and chamber preparation	34
2.2.5 Lipid bilayer and streptavidin monolayer formation	35
2.2.6 Washing protocol.....	35
2.2.7 Data acquisition and analysis.....	35
Chapter 3: A systematic analysis of the molecular components of PNNs using Western blotting	36
3.1 Introduction	36
3.2 Methodology	39
3.2.1 SDS-PAGE and Western blotting.....	39
3.2.2 Acan samples.....	39
3.2.3 ChABC incubation	39
3.3 Results	40
3.3.1 Acan: multiple distinct molecular species of Acan are present in the CNS	40
3.3.2 Pcan: glycosylated Pcan was most prevalent in the cerebellar region.....	45
3.3.3 Bcan: species of Bcan are differentially distributed throughout the CNS	46
3.3.4 Vcan: no differences in Vcan abundance throughout the CNS	48
3.3.5 Ncan: glycosylated Ncan is most prevalent in the cortical region	49
3.3.6 Hapln1 is most abundant in the cortical region	50
3.3.7 Hapln4 distribution was different to the distribution of Hapln1	51
3.3.8 Tn-R: no differences in Tn-R abundance throughout the CNS	52
3.3.9 HA: Lack of smearing suggests HA is observed at discrete sizes throughout the CNS regions	53
3.3.10 Summary of Western blot results	57
3.4 Discussion.....	58
Chapter 4: QCM-D as a methodology to analyse molecular interactions and supramolecular self-organisation underpinning PNN formation... 64	
4.1 Introduction	64
4.1.1 Target PNN model and the main design principles	66
4.2 Methodology	69

4.2.1 Producing the supported lipid bilayer and streptavidin monolayer	69
4.2.2 Creating HA films	69
4.2.3 Manipulating Hapln1 density	72
4.2.4 Preparation of DODA-tris-NTA lipid bilayers for trapping polyhistidine-tagged Tn-R	72
4.2.5 Statistics	72
4.3 Results	73
4.3.1 Successful establishment of the HA model surface	73
4.3.2 Decreasing the density of HA films increased the binding of Acan and Hapln1..	77
4.3.3 Stabilisation of HA and Acan is achieved by the addition of Hapln1 irrespective of the order of incubation.....	82
4.3.4 The density of Hapln1 influenced Acan interaction with HA / Hapln1 films	84
4.3.5 Tn-R was not detected interacting with the HA / Hapln1 / Acan films	86
4.4 Discussion.....	91
Chapter 5: Sizing GAGs.....	95
5.1 Introduction	95
5.2 Methodology	100
5.2.1 HA samples	100
5.2.2 PAGE	101
5.2.3 QCM-D	102
5.3 Results	103
5.3.1 Measuring GAGs using PAGE	103
5.3.2 Quantifying GAG sizes using QCM-D	107
5.3.3 Validating QCM-D and PAGE CS sample estimates	116
5.4 Discussion.....	118
5.4.1 Sizing GAG chains using PAGE.....	118
5.4.2 QCM-D sizing method	119
5.4.3 Conclusion.....	121
Chapter 6: General discussion & future perspectives	122
6.1 Heterogeneity in the distribution of PNN components	123
6.2 Important factors in the assembly of PNNs	124
6.3 Potential mechanisms for biomechanical signalling	126
6.3.1 Mechanisms for altering the biomechanical properties of PNNs.....	127
6.3.2 Potential mechanisms for biomechanical signalling	129
6.4 The successful establishment of methodologies for analysing PNNs	130

Chapter 7: Conclusions.....	132
Chapter 8: References.....	133
Chapter 9: Appendices.....	158

List of figures and tables

Figures

Figure 1. Schematic representation of the PNN structure.....	2
Figure 2. A schematic representation of hypothesised mechanisms for how PNNs may exert functional change to neurological systems.....	5
Figure 3. Size comparison of PNN-associated molecules.....	20
Figure 4. A schematic representation of the macromolecularr structure of PNNs.....	21
Figure 5. Images taken from a recent paper suggesting that 2 distinct morphological PNN states are present in the CNS.....	22
Figure 6. Representative confocal microscopy images of PNNs taken in the cortical and cerebellar regions of the CNS	23
Figure 7. The total amount of Acan was higher in the cSC, in comparison with the brain regions.	41
Figure 8. Densitometry comparison of the different Acan species in each CNS region demonstrated the heterogeneity in the distribution of Acan species between the different CNS regions.....	42
Figure 9. Comparison of Acan species.....	45
Figure 10. Comparison of Pcan abundance between CNS regions.....	46
Figure 11. Comparison of Bcan abundance between CNS regions.....	47
Figure 12. Comparisons of specific Bcan species between the different regions of the CNS.....	48
Figure 13. Comparison of Vcan abundance between CNS regions.....	49
Figure 14. Comparison of Ncan abundance between CNS regions.....	50
Figure 15. Hapln1 is most abundant in cortical lysate, in comparison with the other CNS regions observed by Western blot.....	51
Figure 16. Comparison of Hapln4 abundancy between CNS regions.....	52
Figure 17. Comparison of Tn-R abundance between CNS regions.....	53
Figure 18. Comparison of HA amounts in CNS regions.....	55
Figure 19. Densitometry comparison of the different HA sizes demonstrates the heterogeneity of HA throughout the CNS.	56
Figure 20. Comparison of rat nasal cartilage HA with brain lysate HA indicated that lower molecular weight HA species are brain specific. CNS.	57
Figure 21. Schematic representations of the structure of cartilage Acan, alongside the possible structural variation observed in CNS Acan.	62

Figure 22. Schematic representation of how the orientation of HA is achieved on the sensor surface.	67
Figure 23. Relationship between HA50 surface density and Δf	70
Figure 24. Successful establishment of the supported lipid bilayer and a monolayer of streptavidin on the QCM-D sensor surface.	74
Figure 25. Both HapIn1 and Acan did not interact with the streptavidin monolayer measured using QCM-D.	75
Figure 26. Values of Δf and ΔD that demonstrated that Sparse HA50 and dense HA50 films are highly reproducible.	76
Figure 27. Ratio of $\Delta D / -\Delta f$ was equal for both sparse and dense HA50 films.	77
Figure 28. The density of HA50 films influenced Acan assembly.	79
Figure 29. The ratio of $\Delta D / -\Delta f$ for sparse and dense HA50 films with and without the addition of Acan.	79
Figure 30. The density of HA50 films influenced HapIn1 assembly.	81
Figure 31. The ratio of $\Delta D / -\Delta f$ for sparse and dense HA50 films with and without the addition of HapIn1.	81
Figure 32. Acan interacts unstably with sparse (cyan and orange) and dense (blue and red) HA films without the presence of HapIn1.	82
Figure 33. Acan interacts stably with sparse (cyan and orange) and dense (blue and red) HA / HapIn1 films.	83
Figure 34. The density of HapIn1 within sparse HA films influenced the ability of Acan to change the $\Delta D / -\Delta f$ ratio.	85
Figure 35. The density of HapIn1 within dense HA films did not influence the ability of Acan to change the $\Delta D / -\Delta f$ ratio.	86
Figure 36. Both sparse HA50 (cyan and orange lines) and dense HA50 (blue and red lines) films containing HapIn1 and Acan did not interact with Tn-R.	87
Figure 37. A schematic representation of the predicted interaction of Tn-R and Acan when the Tn-R is trapped to the sensor surface via a lipid bilayer containing tris-Ni ²⁺ -NTA groups.	88
Figure 38. Tn-R interacts with bovine articular cartilage Acan in a calcium-dependent manner.	90
Figure 39. The relationship between GAG chains and protein standards using PAGE.	105
Figure 40. The relationship between protein standard d_{mig} and $M_{w,protein}$ plot on a log-linear scale.	106
Figure 41. Molecular mass values for the CS samples estimated using PAGE.	107

Figure 42. The relationship between Δf and ΔD for a range of HA sizes measured using QCM-D.	108
Figure 43. Representative plots of the relationship between the ratio of $\Delta D / -\Delta f$ and $-\Delta f$ throughout the binding process.	110
Figure 44. Comparison of different methods for analysing the ratio of $\Delta D / -\Delta f$ for HA chains.	111
Figure 45. The ratio of $\Delta D / -\Delta f$ as a function of HA N_{ds}	115
Figure 46. Comparison of CS M_w estimates using PAGE, QCM-D and company estimates.	117
Figure 47. An example of how d_{mig} , d_{min} and d_{max} were measured is represented in the image below.	160

Tables

Table 1. Antibodies used for Western blot analysis.	28
Table 2. Molecules used in QCM-D experiments.	34
Table 3. A heat map summarising the relative abundance of PNN molecules using Western blot densitometry analysis.	58
Table 4. HA samples used in the PAGE and QCM-D analysis.	101
Table 5. The number of repeats of each HA size used in the QCM-D analysis.	103
Table 6. The p values measuring the differences between the ratio of $\Delta D / -\Delta f$ for different HA sizes.	112
Table 7. The values of $\Delta D / -\Delta f$ for CS chains used to validate the model.	116
Table 8. HA and CS migration distance values (normalised).	160
Table 9. $M_{w,protein}$ values for HA50 and CS samples.	160
Table 10. $M_{w,GAG}$ values for CS samples.	161
Table 11. Protein standard results.	162
Table 12. Values for measuring HA $\Delta D / -\Delta f$ using different methods.	163

Abbreviations

Acan: Aggrecan

AMPA: α -amino-3-hydroxy-5-methyl-4-isoxazolepropionic acid

ANOVA: Analysis of variance

BCA: bicinchoninic acid assay

Bcan: Brevican

BSA: Bovine serum albumin

Bral: Brain link protein

Crtl: Cartilage and proteoglycan link protein

ChABC: Chondroitinase ABC

CNS: Central nervous system

COC: cumulus cell-oocyte complex

CS: Chondroitin sulfate

CSPG: Chondroitin sulfate proteoglycan

cSC: Cervical spinal cord

DODA-tris-NTA: Dioctadecyldimethylammonium-tris-nitrilotriacetic acid

DOPC: 1,2-dioleoyl-sn-glycero-3-phosphocholine

DOPE-cap-biotin: 1,2-dioleoyl-sn-glycero-3-phosphoethanolamine-N-(cap biotinyl)

ECL: Enhanced chemiluminescence

ECM: Extracellular matrix

EDTA: Ethylenediaminetetraacetic acid

G1: Globular domain 1

G2: Globular domain 2

G3: Globular domain 3

GAG: Glycosaminoglycan

GPI: glycosylphosphatidylinositol

HA: Hyaluronan

Hapln: Hyaluronan and proteoglycan link protein

HAS: Hyaluronan synthase

HEPES: 4-(2-hydroxyethyl)-1-piperazineethanesulfonic acid

HMW: High molecular weight

HRP: Horseradish peroxidase

LDS: Lithium dodecyl sulfate

LMW: Low molecular weight

MMPs: matrix metalloproteinases

Ncan: Neurocan

Otx2: Orthodenticle Homeobox 2

PBS: Phosphate buffered saline

Pcan: Phosphacan

PES: Polyethersulfone

PNN(s): Perineuronal net(s)

PVDF: Polyvinylidene fluoride

QCM-D: Quartz crystal microbalance with dissipation monitoring

SDS-PAGE: sodium dodecyl sulfate-polyacrylamide gel electrophoresis

SEC-MALL: Size exclusion chromatography – Multi angle laser light scattering

Sema3a: Semaphorin 3a

SRF: serum response factor

SDS – PAGE: Sodium dodecyl sulfate - polyacrylamide gel electrophoresis

SPR: surface plasmon resonance

TBS: Tris buffered saline

TBS-T: Tris buffered saline with tween

TGS: Tris-glycine SDS

TN-R: Tenascin-R

Vcan: Versican

WFA: *Wisteria floribunda* agglutinin

Chapter 1: Introduction

1.1 Overview

Perineuronal nets (PNNs) were first described as a reticular structure on the surface of neurons in 1898 (Golgi, 1898). PNNs are found surrounding the soma and dendrites of subpopulations of neurons in the central nervous system (CNS) (Kwok *et al.*, 2011; Wang and Fawcett, 2012). Importantly, they form a condensed 'net-like' layer around the outside of neurons, therefore are considered an extracellular matrix (ECM) structure. Though the structure was first described over a century ago, how the structure spontaneously self-organises and the mechanisms by which PNNs exert changes to biological processes remain poorly understood. Although the mechanisms remain unclear, the importance of PNNs to biological processes is evident, as when enzymatically removed, clear changes at both the cellular and behavioural level have been observed that will be discussed in section 1.2 (Celio *et al.*, 1998; Kwok *et al.*, 2011; Wang and Fawcett, 2012; Sorg *et al.*, 2016).

PNNs have been observed in the CNS of several mammals including, mice, rats, Chilean fat-tailed mouse opossums, cows, hamsters, macaques, and humans (Kalb and Hockfield, 1988; Asher *et al.*, 1995; Carulli *et al.*, 2006; Deepa *et al.*, 2006; Brückner *et al.*, 2006; Galtrey *et al.*, 2008; Carulli *et al.*, 2010; Mueller *et al.*, 2016; Enwright *et al.*, 2016). There is also some evidence suggesting fish may also have PNNs (Genade and Lang, 2013). It may be that PNNs are a conserved pericellular structure that are common in the CNS of most animals. However, the PNN structure is specific to the CNS, as PNNs have not been observed in the peripheral nervous system.

The molecular components of PNNs aggregate spontaneously in an activity dependent manner (Dityatev *et al.*, 2007; Reimers *et al.*, 2007; McRae *et al.*, 2007). Briefly, PNNs are formed of hyaluronan (HA) that is synthesised on the cell surface by hyaluronan synthase (HAS) molecules. Chondroitin sulfate proteoglycans (CSPGs) then interact with HA via their N-terminal globular domain (G1) (Carulli *et al.*, 2006; Kwok *et al.*, 2010; Kwok *et al.*, 2011). The interaction of CSPGs with HA is strengthened through the interaction with Haplns (Binette *et al.*, 1994; Matsumoto *et al.*, 2003; Shi *et al.*, 2004). The trimeric structure of tenascin-R (Tn-R) has been hypothesised to cross-link the CSPGs via their C-terminal domain (Lundell *et al.*, 2004). A model for the structure of PNNs has been hypothesised demonstrating how the components may self-organise to form the supra-molecular PNN structure (Figure 1; Kwok *et al.*, 2011). The structure will be described in greater detail in section 1.5.

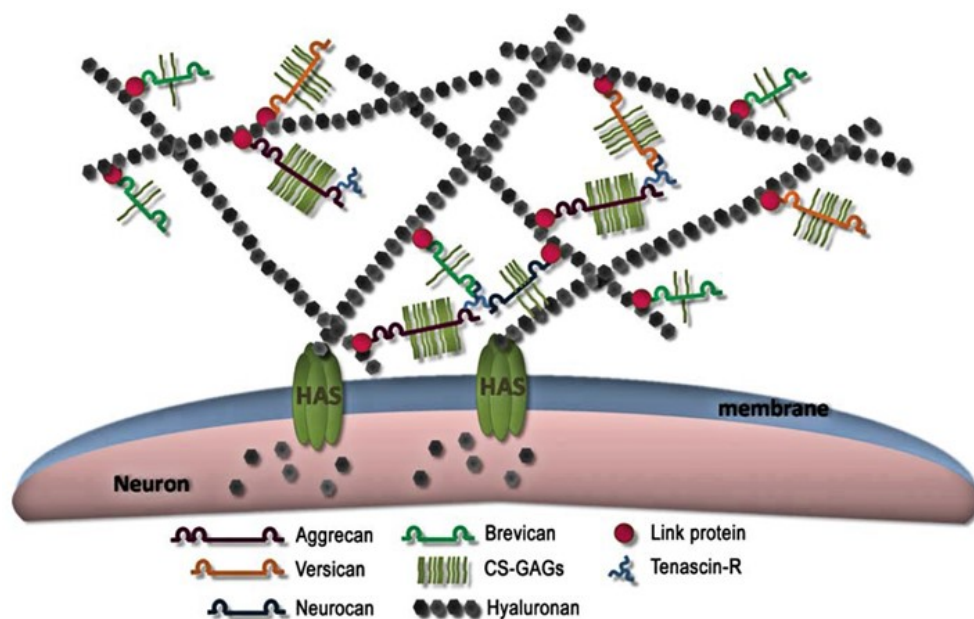


Figure 1. Schematic representation of the PNN structure.

It demonstrates HAS anchoring HA to the cell membrane. CSPGs (aggrecan, brevican, neurocan and brevican) then interact with HA via their N-terminus in the presence of link protein. The C-terminus of CSPGs are then crosslinked by tenascin-R. In this schematic the molecules are not drawn to scale. The figure is courtesy of: Kwok *et al* (2011).

Parvalbumin-expressing GABAergic interneurons, many of which express the fast reactivating voltage-gated potassium channel subtype Kv3.1b, are the most well characterised cell type found to be ensheathed by PNNs (Chang *et al.*, 2010; Kwok *et al.*, 2011; de Winter *et al.*, 2016). However, PNNs surrounding: pyramidal neurons in the hippocampus and parietal cortex; motor neurons in the spinal cord and neurons in the medial nucleus of the trapezoid body, have also been observed (Takahashi-Iwanaga *et al.*, 1998; Härtig *et al.*, 2001; Wegner *et al.*, 2003; Carstens *et al.*, 2016; Irvine and Kwok, 2018). Furthermore, PNNs have been observed throughout the CNS including the regions of the visual cortex, barrel cortex, substantia nigra, deep cerebellar nuclei, spinal cord and hippocampus (Pizzorusso, 2002; Carulli *et al.*, 2006; McRae *et al.*, 2007; Brückner *et al.*, 2008; Galtrey *et al.*, 2008). PNNs are found throughout the CNS surrounding multiple neuronal cell types. To date a systematic analysis investigating the exact populations of neurons PNNs surround in the CNS regions has not been undertaken, so it is plausible that PNNs may also surround other cell types that have yet to be characterised (this is addressed in objective 1 in section 1.6).

Although PNNs are often considered to be a singular structure, this may be an over-simplification as recent evidence has suggested that the structures may be more heterogeneous than first predicted (Brückner *et al.*, 2006;

Yamada and Jinno, 2017; Richter *et al.*, 2018). What remains unclear is how the different PNN phenotypes are established (this is also addressed in objective 1 in section 1.6). In this introduction the functional importance of PNNs will first be described, alongside a description of the biological concepts of synaptic plasticity. The reasoning for why a biomechanical signalling mechanism is being proposed for PNNs will then be provided through the evidence of cellular mechanosensing in the nervous system. A description of the PNN components will then be provided, followed by a section explaining how these components could potentially combine to produce structurally heterogeneous PNNs.

1.2 Functional importance of PNNs

PNNs have been implicated in numerous neurological diseases including epilepsy, schizophrenia and Alzheimer's disease (Morawski *et al.*, 2004; Pantazopoulos *et al.*, 2010; Markus Morawski *et al.*, 2012; McRae and Porter, 2012; Pantazopoulos *et al.*, 2015; Yang *et al.*, 2015; Rankin-Gee *et al.*, 2015; Enwright *et al.*, 2016). A role in memory formation and addiction has also been suggested (Hyllin *et al.*, 2013; Romberg *et al.*, 2013; Xue *et al.*, 2014; Slaker *et al.*, 2016; Banerjee *et al.*, 2017; Carulli *et al.*, 2020). Furthermore, a hypothesised mechanism for long term memory formation has been suggested, though there is currently no evidence to support this notion (Tsien, 2013). It is important to note that most evidence that has suggested a functional role in neurological diseases is correlational, with little direct evidence implicating PNN modulation with a causal role in disease progression. The functional importance of PNNs has largely been inferred by experimentally modulating PNNs and measuring changes to neurological behaviour.

1.2.1 Synaptic plasticity

Synaptic plasticity is the ability of synaptic connections to strengthen or weaken, meaning that synaptic connections have the ability to establish or withdraw over time and adapt to changes in the environment. This mechanism has been proposed to play a central role in the brain's ability to turn transient experiences into memories (Citri and Malenka, 2008). In this PhD thesis when referring to a reduction in synaptic plasticity it relates specifically to the limitation of plastic changes to synapses only. Therefore, reducing synaptic plasticity preserves existing connections and neuronal circuitry. It is also worth

highlighting that a synapse is made up of: a presynaptic axon terminal, the synaptic cleft, a post-synaptic terminal that is the dendrites or neuronal cell body. As PNNs surround the cell body and proximal dendrites of neurons in the CNS, they are ensheathing the post-synaptic terminal.

1.2.2 Modulating PNNs

Many studies looking to implicate PNNs in neurological functions have used the enzyme chondroitinase ABC (ChABC) to enzymatically remove PNNs from the CNS (Pizzorusso, 2002; Pizzorusso *et al.*, 2006; Massey *et al.*, 2006; Hrabětová *et al.*, 2009; Pyka *et al.*, 2011). ChABC digests chondroitin sulfate (CS), as well as HA in the experimental conditions used (Prabhakar *et al.*, 2005). It is important to note that preferential digestion of CS and HA can be achieved using ChABC by carefully manipulating the digestion conditions *in vitro*. As HA is an integral part of the PNN structure and has been implicated in tethering PNNs to the cell surfaces, the removal of HA enzymatically removes PNNs (Kwok *et al.*, 2010). Furthermore, the CS chains present within PNNs, that are attached to the CSPG core proteins will also be enzymatically cleaved using ChABC (Deepa *et al.*, 2006). Using ChABC in the CNS has resulted in a variety of behavioural phenotypes, including the restoration of juvenile levels of synaptic plasticity in the adult visual cortex (Pizzorusso, 2002; Pizzorusso *et al.*, 2006). In the spinal cord following a spinal cord injury the use of ChABC caused increased synaptic plasticity and higher levels of functional recovery to be observed (Massey *et al.*, 2006).

The fundamental drawback of using ChABC is it does not specifically remove PNNs, as it also digests CS and HA present throughout the ECM of the CNS. Therefore, methodologies that use ChABC struggle to separate the effects caused by the removal of PNNs, from the effects caused by the removal of CS and HA from the loose ECM. Experiments using ChABC have highlighted potential functional roles of PNNs that required further characterisation to specifically implicate PNNs.

Alternative methods for directly altering PNN structure have been devised to more specifically modulate PNNs. One method involved creating a *hapln1* knockout mouse model (Carulli *et al.*, 2010). By targeting *hapln1* this method was able to disrupt PNN assembly while limiting the changes to the loose ECM. The *hapln1*-knockout mice maintained juvenile levels of synaptic plasticity in the visual cortex and cuneate nucleus, providing strong evidence that PNNs are directly involved in regulating synaptic plasticity in the CNS.

Further evidence implicating PNNs in reducing synaptic plasticity strengthens this hypothesised function (Pizzorusso, 2002; Pizzorusso *et al.*, 2006; Massey *et al.*, 2006; Galtrey *et al.*, 2008; Carulli *et al.*, 2010). The work by Carulli *et al.* (2010) specifically implicated the role of the PNN structure in modulating neuronal function. However, the mechanism by which the removal of PNNs changed neuronal function remained unclear.

A number of mechanisms have been suggested for how PNNs may alter neuronal function (Figure 2; Wang and Fawcett, 2012). Each mechanism will be described in more detail in the remainder of this section below. The likelihood is that PNNs use a combination of mechanisms to alter neurological function, which may partially explain the varying disease pathologies that PNNs have been associated with.

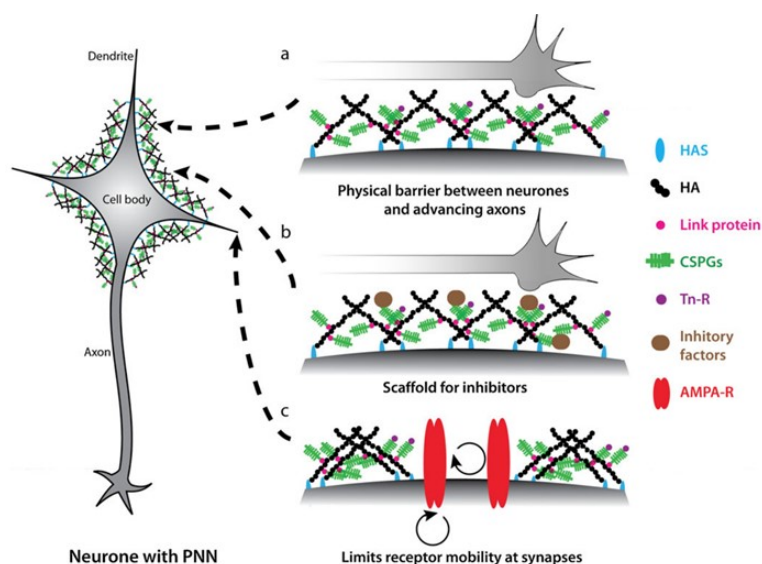


Figure 2. A schematic representation of hypothesised mechanisms for how PNNs may exert functional change to neurological systems.
The figure is courtesy of: (Wang and Fawcett, 2012).

1.2.3 A Sink for cation storage to allow increased neuronal activity to occur

PNNs are polyanionic in nature which may attract cations that enhance the excitability of fast-spiking neurons (Balmer, 2016). Fast-firing neurons are often surrounded by PNNs which has been observed both *in vivo* as well as *in vitro* (Härtig *et al.*, 1994; Härtig *et al.*, 1999; Morris and Henderson, 2000; Reimers *et al.*, 2007). It has been hypothesised that PNNs may provide insulation from excess potassium produced by the cell during periods of high activity (Brückner *et al.*, 1993). PNNs have been observed to surround fast spiking, parvalbumin positive, inhibitory GABAergic interneurons, therefore it may be possible that PNNs help maintain this fast-firing behaviour by

providing a favourable ECM environment for this activity to occur (Härtig *et al.*, 1992). Therefore, this mechanism proposes that the structural properties of the PNN create a favourable environment through the anionic nature of the biochemical components accumulating counterions (cations) within the pericellular coat.

1.2.4 PNN molecular components may directly regulate neuronal activity through signalling

CSPGs are an essential component of PNNs that have been observed to directly inhibit neurite outgrowth (Oohira *et al.*, 1991; Wang and Fawcett, 2012). The CSPG core proteins, absent of glycosaminoglycan (GAG) chains, were sufficient to inhibit neurite outgrowth (Oohira *et al.*, 1991). CS chains have also been observed to have an inhibitory effect on CNS neurons (Snow *et al.*, 1996; Niederöst *et al.*, 1999; Dyck and Karimi-Abdolrezaee, 2015). Therefore, the direct signalling of the PNN molecular components provides a potential biochemical mechanism for altering neuronal behaviour (Lee *et al.*, 2010; Fisher *et al.*, 2011; Wang and Fawcett, 2012; Harris *et al.*, 2013). The mechanism may require the presence of GAGs, as ChABC caused this signalling to be altered (Lee *et al.*, 2010; Harris *et al.*, 2013). The neuronal transmembrane leucocyte common antigen-related phosphatase receptor has also been implicated in interacting with CSPGs to negatively regulate axonal growth (Fisher *et al.*, 2011). What remains unknown is if the direct signalling observed when presenting these molecules to CNS cells alone, as opposed to presenting them as part of a supramolecular structure, changes or potentially impedes this direct signalling. To analyse this, it is important to understand how PNNs are assembled and how the molecular components are embedded within the structure (this is addressed in objective 2 in section 1.6).

1.2.5 Signalling molecules interact with PNNs to regulate activity

PNNs have been observed to sequester numerous guidance molecules, via their interaction with CS chains (Sugiyama *et al.*, 2008; Chang *et al.*, 2010; Kwok *et al.*, 2011; Miyata *et al.*, 2012; de Winter *et al.*, 2016). In particular, molecules linked with reducing, or limiting synaptic plasticity and axonal growth have been identified, including semaphorins and Orthodenticle Homeobox 2 (Otx2) (Pasterkamp and Kolodkin, 2003; Bouzioukh *et al.*, 2006; Beurdeley *et al.*, 2012; Dick *et al.*, 2013; de Winter *et al.*, 2016). Semaphorins

have been implicated in synaptic plasticity and stabilisation (Pasterkamp and Kolodkin, 2003; Bouzioukh *et al.*, 2006). CS-E has been observed to sequester semaphorin 3a (Sema3a) with high affinity, suggesting that regulating specific GAG sulfation patterns within the PNN may act as a mechanism for regulating guidance molecule sequestration (Dick *et al.*, 2013; Vo *et al.*, 2013; Djerbal *et al.*, 2019). Otx2 has been linked with reducing synaptic plasticity (Beurdeley *et al.*, 2012). Otx2 is sequestered through the binding of the RK peptide sequence of Otx2 to CS-GAGs within the PNN. Otx2 also interacts specifically with the di-sulfated CS-D and CS-E with high affinity, further supporting the role of GAG sulfation pattern regulation in facilitating PNN function (Beurdeley *et al.*, 2012). These two examples of sequestered signalling molecules demonstrate how PNNs could function through regulating the abundance of these molecules interacting with the PNN surface. It further demonstrates the need for a systematic analysis of the distribution of the PNN-associated molecules, as the biochemical composition of the film will affect the interactions of these sequestered molecules (this is addressed in objective 1 in section 1.6).

1.2.6 A barrier to the movement of post-synaptic receptors on the cells surface

PNNs may also function by limiting post-synaptic receptor movement on the cell surface. The observation that the lateral diffusion of α -amino-3-hydroxy-5-methyl-4-isoxazolepropionic acid (AMPA) receptors was limited by the presence of PNNs surrounding hippocampal neurons provided strong evidence for this mechanism (Frischknecht *et al.*, 2009). It is therefore plausible that PNNs may compartmentalise the neuronal surface limiting the movement of post-synaptic receptors. This compartmentalisation may act as a mechanism for stabilising synapse formation in the CNS. To date only AMPA receptors have been observed to be affected by this mechanism, so it is unknown if other post-synaptic membrane-bound proteins are affected in the same way. Other receptor types have yet to be analysed. Also, the exact mechanism for the reduction in lateral diffusion remains unclear, as it is not known whether AMPA receptors are being tethered to the PNN structure or are being physically blocked by the presence of the PNN structure on the cell surface. Through understanding the assembly and structural properties of PNNs it may provide an insight into the precise mechanism for this mechanism of compartmentalising post-synaptic receptors (this is addressed in objective 2 in section 1.6).

1.2.7 Physical barrier

PNNs may function through acting as a physical barrier, preventing new synaptic connections from forming. This hypothesis specifically highlights the presence of PNNs physically blocking the availability of the neuronal surface preventing new synapses from forming. It is currently unclear whether PNNs assemble around already formed synapses, or if PNNs compartmentalise the surface to facilitate the formation of certain synaptic types. This research gap highlights the importance in analysing the assembly and formation of PNNs (this is addressed in objective 2 in section 1.6).

As well as potentially blocking synapse formation, the physical barrier produced by PNNs may also provide a neuroprotective function. It has been demonstrated that neurons were less affected by the Tau-protein, a molecule associated with Alzheimer's disease, when they were surrounded by PNNs (Suttkus *et al.*, 2016). Furthermore, neurons ensheathed by PNNs have increased protection from β -amyloid protein, another toxic protein aggregate linked to Alzheimer's disease (Miyata *et al.*, 2007). Potentially the mechanism of protection provided by PNNs may be through physically blocking these molecules from reaching the cell surface. If the PNN structure is too dense for the molecules to pass through the PNN surface, then it may not be possible to diffuse through the pericellular structure and be internalised by the cell. Surfaces of HA have previously been demonstrated to exclude certain protein macromolecules (Ogston, 1966). It remains unknown if PNNs can influence the diffusion of molecules to the cell surface, however, by gaining an understanding of the biomechanical properties of PNNs will help in understanding if this mechanism is partially responsible for PNNs function.

It is also worth noting that the neuroprotective function may also be provided by the negatively charged PNN structure, that repels similarly charged molecules and traps oppositely charged molecules within the PNN. Support for this hypothesis is provided by the observation that PNNs provide neuroprotection against oxidative stress (Morawski *et al.*, 2004; Suttkus *et al.*, 2012; Cabungcal *et al.*, 2013; Suttkus *et al.*, 2014). Therefore, the physical PNN barrier on the surface of neurons may prevent molecules that are detrimental to neurons from being internalised through trapping them via their charge. Therefore, by understanding the biochemical composition of PNNs will allow for a greater understanding of how these mechanisms could be regulated.

1.3 The importance of cellular mechanosensing in the nervous system

Having identified the numerous potential mechanisms for how PNNs may function, what remains clear is the need to establish the precise structure of PNNs. PNNs are a large, aggregated pericellular structure that form on the surface of neurons in the CNS, whereby they are likely to fundamentally change the physical properties of the neuronal surface. One mechanism that has yet to be discussed is the possibility that PNNs could function via a biomechanical signalling mechanism. In this section biomechanical signalling within the nervous system will be discussed to provide the reasoning for proposing this potential mechanism of function for how PNNs partially exert their function in the CNS.

1.3.1 Defining mechanosensing

Mechanosensing requires the conversion of mechanical forces into intracellular biochemical signals (Franze *et al.*, 2013). When considering the role of mechanosensing in relation to PNNs there are two distinct types of mechanosensing to consider. First is mechanosensing by cells ensheathed by PNNs. In this case the conversion of a mechanical force is in reference to the cell being deformed by an external force such as fluid flow (Franze *et al.*, 2013). It is possible that the presence of a PNN ensheathing a neuron could provide a layer of protection to modulate mechanical deformation, thereby reducing the ability of the cell to detect changes to the biomechanical properties of its environment. The second type of mechanosensing is by the incoming cell that then interacts with the PNN surface. In this case the mechanical forces are generated from the incoming cell itself through actin myosin contractility along stress fibres or within the cell cortex (Sukharev and Sachs, 2012; Franze *et al.*, 2013). The actively generated forces are then converted into intracellular biochemical signals to actively measure the stiffness of its environment, modulating neuronal behaviour, which will be described further in section 1.3.3.

1.3.2 Hypothesised mechanisms of mechanosensing

1.3.2.1 Stress sensitive ion channels

Stress sensitive ion channels are fast-acting channels located within the cell membrane (Sukharev and Sachs, 2012; Franze *et al.*, 2013). One example of a stress-sensitive ion channel is the potassium-selective ion channel TREK1 that has been identified as being involved in setting the resting potential of neurons (Patel and Honore, 2002; Honoré, 2007; Sukharev and Sachs, 2012). Changes in tension in the cell membrane lead to a conformational change in the ion channel resulting in a fast and immediate influx of ions into the cell (Franze *et al.*, 2009; Chalfie, 2009; Hardie and Franze, 2012; Sukharev and Sachs, 2012). The resulting ion influx has been observed to influence axon pathfinding, cell movement and the retraction of the growth cone (Lee *et al.*, 1999; Gomez and Zheng, 2006; Franze *et al.*, 2009; Franze *et al.*, 2013). Tension in the cell membrane detected by stress sensitive ion channels has also been linked with the clustering of neurotransmitter vesicles at the presynaptic cleft and clustering membrane receptors (Orr *et al.*, 2006; Siechen *et al.*, 2009; Franze *et al.*, 2013).

1.3.2.2 Integrin mediated

Integrins are transmembrane proteins that cluster together to form macromolecular complexes called focal adhesions on the cell surface (Moore *et al.*, 2010; Roca-Cusachs *et al.*, 2012; Halder *et al.*, 2012; Franze *et al.*, 2013). Actin-myosin stress fibres can attach to these focal adhesions and exert tensile forces on the integrins that is exerted onto the ECM through the physical attachment. In response to this tensile force soft ECM surfaces would easily deform, therefore the integrins would maintain their conformational shape, while stiffer ECM surfaces would deform less, therefore the tension put on the integrins would increase which may lead to the exposing of cryptic binding sites that facilitate biomechanical signalling (Moore *et al.*, 2010; Roca-Cusachs *et al.*, 2012; Halder *et al.*, 2012; Franze *et al.*, 2013). It is important to note that integrins are not the only mechanosensitive molecules present within focal adhesions, as focal adhesions are complex structures made up of over 150 different types of proteins (Zaidel-Bar *et al.*, 2007; Oakes and Gardel, 2014). Both talin and vinculin molecules have also been observed to be mechanosensitive molecules present within focal adhesions (Del Rio *et al.*, 2009; Grashoff *et al.*, 2010; Kanchanawong *et al.*, 2010).

1.3.2.3 Transcriptional regulation

The previous two mechanisms are short-term, immediate mechanosensing mechanisms. It is important to note that there is also evidence for longer term mechanosensing that occurs through transcriptional regulation (Mammoto *et al.*, 2012; Franze *et al.*, 2013). This regulation may occur through the direct mechanosensing of the nucleus, which is directly connected to the cytoskeleton (Maniotis *et al.*, 1997; Wang *et al.*, 2009). This hypothesised mechanism suggests that as there is evidence that the nucleus is already under pre-tension, any deformations caused by the cell surface will directly transmit to the nucleus causing a change to nuclear shape, that results in a change in transcriptional regulation (Mazumder *et al.*, 2008; Mazumder and Shivashankar, 2010).

G-actin levels have also been implicated as they have been observed to change in response to stiffness of substrates which correspondingly regulate transcription factors such as serum response factor (SRF) (Miralles *et al.*, 2003; Franze *et al.*, 2013). SRF inactivation has been specifically linked to reduced neurite growth during development, ineffective neuronal migration and a decrease in dendritic length and number (Kalita *et al.*, 2012). Therefore, mechanosensing may affect neuronal cells over longer time-periods.

1.3.3 Cells in the nervous system detect and respond to biomechanical changes of substrates

As discussed in section 1.2 the properties of the PNN structure is likely to play an important function in various mechanisms of PNN function, including regulating synaptic plasticity, increasing synaptic stability and neuroprotection. It is important to note that there is currently no evidence that PNNs change the biomechanical properties of the neuronal surface, though it appears that the structure of PNNs are important to their function, as attenuated PNNs caused changes to neuronal plasticity (Carulli *et al.*, 2010). Therefore, the structural properties of PNNs appears to be functionally important. Cell bodies and growth cones in the nervous system actively pull on their surroundings to measure the stiffness of substrates (Bray, 1979; Harris *et al.*, 1980; Betz *et al.*, 2011; Koch *et al.*, 2012). A softer substrate causes less strain to the active cell (Schwarz and Gardel, 2012). Therefore, the cell bodies and growth cones of cells in the CNS have the ability to detect changes to the biomechanical properties of substrates. Growth cones, which have been measured by atomic force microscopy (AFM), appear to

structurally more sensitive to detecting changes to the mechanical properties of substrates (Betz *et al.*, 2011).

Various studies have demonstrated the ability of neuronal and glial cells to respond to changes in the mechanical properties of the ECM surface (Flanagan *et al.*, 2002; Georges *et al.*, 2006; Kostic *et al.*, 2007; Jiang *et al.*, 2008; Jiang *et al.*, 2010; Previtiera *et al.*, 2010; Stabenfeldt and Laplaca, 2011; Franze *et al.*, 2013; Moshayedi *et al.*, 2014). In reference to PNNs, this suggests that both glial cells and neurons could actively detect the PNN surface and potentially respond to it. Neurons have been observed to preferentially grow on softer, more compliant surfaces, displaying greater branching, increased neurite extension and longer axons (Flanagan *et al.*, 2002; Kostic *et al.*, 2007; Jiang *et al.*, 2008; Jiang *et al.*, 2010; Previtiera *et al.*, 2010; Stabenfeldt and Laplaca, 2011). Glial cells have been observed to increase in cell attachment area in response to stiffer surfaces (Georges *et al.*, 2006; Cullen *et al.*, 2007; Jiang *et al.*, 2008; Moshayedi *et al.*, 2010; Moshayedi *et al.*, 2014). The foreign body response by astrocytes and microglia has also been observed to be upregulated in response to stiffer surfaces (Moshayedi *et al.*, 2014). It remains unknown if PNNs are able to modulate astrocytes and microglia behaviour through a biomechanical signalling mechanism. This highlights the importance in determining the biomechanical properties of PNNs and how these properties may be modulated through cross-linking molecules, as currently these properties remain uncharacterised (this is addressed in objective 2 in section 1.6).

As well as actively detecting their physical environment, neuronal cells have also been observed to respond to dynamic mechanical stimuli in their environment (LaPlaca *et al.*, 2005; Cullen and LaPlaca, 2006; Franze *et al.*, 2013). Neurons have been observed to change dendritic length in response to dynamic mechanical cues (Jiang *et al.*, 2010). Additionally, changes to the cytoskeletal composition, morphological shape and survival rates have also been observed in response to dynamic cues (LaPlaca *et al.*, 2005; Cullen and LaPlaca, 2006; Franze *et al.*, 2013). With reference to PNNs, it is possible that the cells ensheathed by PNNs may have this active mechanosensing impeded by the presence of the PNN structure on the surface. Furthermore, the presence of PNNs ensheathing neurons may provide insulation and neuroprotection from these mechanical stimuli. Therefore, it is important to consider the structure of the PNN and the biomechanical properties of the macromolecular structure.

1.4 Molecular components of PNNs

To better understand the biomechanical properties of PNNs it is important to consider the various molecular components that combine to form the supramolecular PNN structure. A variety of PNN-associated molecular components are known with the potential to form highly heterogeneous biochemical compositions (Carulli *et al.*, 2006; Galtrey *et al.*, 2008; Foscarin *et al.*, 2017; Irvine and Kwok, 2018). The importance of CSPGs, HA and Hapln aggregation was highlighted by work in cartilage where aggrecan (Acan) was specifically studied (Hascall and Heinegård, 1974a; Hascall and Heinegård, 1974b; Heinegård and Hascall, 1974). Although PNNs are also composed of an aggregation of CSPGs, HA and Haplns, the ultrastructure of PNNs is different, as HA is tethered to the cell surface of neurons. Further work has since observed other CSPGs aggregating in these cartilage-like structures (Matsumoto *et al.*, 2003; Rauch *et al.*, 2004; Seyfried *et al.*, 2005). It is important to consider the molecules associated with PNNs. In this section HA, Haplns, CSPGs and Tn-R will be discussed in detail in reference to PNNs, as all of have been observed within the macromolecular structure.

1.4.1 HA

HA is a ubiquitous ECM and cell surface GAG that is composed of repeating disaccharide units of D-glucuronic acid and N-acetylglucosamine, bound through alternating β -1,4 and β -1,3 glycosidic bonds (Meyer, 1958; Rodriguez-Martinez *et al.*, 2016). HA is the only non sulfated GAG, making it a linear polymer with a molecular composition consistent across the polysaccharide chain. HA synthesis occurs on the cell surface, as opposed to the Golgi apparatus where other GAGs are synthesised (Prehm, 1984). HAS molecules, of which there are 3 isoforms: HAS1, HAS2 and HAS3 synthesise HA and extrude it into the pericellular space (Spicer and McDonald, 1998; Tien and Spicer, 2005; Törrönen *et al.*, 2014). The different HAS isoforms produce HA at different rates and of varying molecular weight (Itano *et al.*, 1999). Both neurons and astrocytes express HAS, therefore possess the potential to synthesise HA that is contributed to the PNN surface (Asher and Bignami, 1991; Marret *et al.*, 1994; Miyata *et al.*, 2005; Giamanco *et al.*, 2010; Cargill *et al.*, 2012; Bugiani *et al.*, 2013). It is important to note that only HA provided by neurons to the PNN structure is likely to be surface-tethered, as HA provided by glial cells is unlikely to come into contact with the neuronal surface where it could be captured by CD44 receptors. The relative amounts

of HA contributed by each cell type to the production of PNNs remains unknown. Furthermore, the size of the HA molecules within PNNs is not known either (this is addressed in objectives 1 and 3 in section 1.6).

1.4.2 Haplns

Haplns are a family of glycoproteins that were first characterised in cartilage through the identification of cartilage and proteoglycan link protein (Crtl1) / Hapln1 (Hardingham, 1979). Later brain link protein (Bral1) / Hapln2 and Bral2 / Hapln4 were identified (Hirakawa *et al.*, 2000; Spicer *et al.*, 2003). Hapln1 contains 2 link modules and an Ig-like loop that function to stabilise the HA / CSPG complex (Hardingham, 1979; Nieduszynski *et al.*, 1980; Binette *et al.*, 1994; Morgelin *et al.*, 1994; Watanabe *et al.*, 1997; Matsumoto *et al.*, 2003; Spicer *et al.*, 2003; Bekku *et al.*, 2003; Rauch *et al.*, 2004; Shi *et al.*, 2004). Both Hapln1 and Hapln4 have been observed to co-localise with PNNs in the CNS (Asher *et al.*, 1995; Carulli *et al.*, 2006; Deepa *et al.*, 2006; Galtrey *et al.*, 2008; Carulli *et al.*, 2010; Kwok *et al.*, 2010; Bekku *et al.*, 2012; Edamatsu *et al.*, 2018). Hapln4 has been observed to be specifically upregulated in the cerebellum and brainstem (Bekku *et al.*, 2012; Edamatsu *et al.*, 2018). Interestingly, the removal of Hapln1 was enough to cause the attenuation of PNNs in the brain and was correlated with an increase in synaptic plasticity (Carulli *et al.*, 2010; Romberg *et al.*, 2013). Furthermore, Hapln1 has also been observed to preferentially interact with the versican (Vcan) G1 domain in comparison with the Acan G1 domain (Shi *et al.*, 2004). Little is known about the combinatorial rules of interactions for how each of the Haplns interacts with each CSPG to stabilise a ternary complex with HA. Therefore, it is plausible that the distribution of Haplns may regulate the CSPGs that are incorporated into the assembly of PNNs. Currently, the distribution of Haplns throughout the CNS is not known, therefore a systematic analysis, as done in chapter 3, would provide insights into how the Haplns may be involved in the structural regulation of PNNs.

1.4.3 CSPGs

CSPGs are large molecules comprised of a core protein and a number of covalently linked GAGs. Specifically, phosphacan (Pcan), as well as the lectican family of CSPGs, that includes Acan, brevican (Bcan), Vcan and neurocan (Ncan) have been found to interact with PNNs and known to be important in the formation of the ECM (Ruoslahti, 1996; Carulli *et al.*, 2006;

Deepa *et al.*, 2006; Galtrey *et al.*, 2008; Aspberg, 2012). The core protein of lecticans are relatively conserved, as they all contain an N-terminal globular domain (G1) and a C-terminal globular domain (G3) (Sandy *et al.*, 1990; Yamaguchi, 2000). Of note Pcan does not contain a G3 domain. The G1 domain contains an immunoglobulin repeat and 2 link modules and is known to interact with HA and Haplns (Watanabe *et al.*, 1997; Yamaguchi, 2000; Matsumoto *et al.*, 2003; Kwok *et al.*, 2011). The G3 domain contains a C-type lectin domain that is flanked by 2 epidermal growth factor-like repeats and a complement regulatory protein-like domain (Doege *et al.*, 1987; Zimmermann and Ruoslahti, 1989; Rauch *et al.*, 1992; Yamada *et al.*, 1994; Yamaguchi, 2000; Kwok *et al.*, 2011; Aspberg, 2012). With reference to PNNs the G3 domain has been observed to interact with Tn-R in a calcium-dependent manner (Aspberg, 1995; Aspberg *et al.*, 1997). It is however worth noting that fibulin-1, fibulin-2, tenascin-C and fibrillin-1 have also been observed to interact with the G3 domain of lecticans (Rauch *et al.*, 1997; Aspberg *et al.*, 1999; Olin *et al.*, 2001; Isogai *et al.*, 2002; Day *et al.*, 2004; Aspberg, 2012). Between the G1 and G3 domain is a central region of different lengths depending on the molecule, which is the region where GAGs are attached to the core protein covalently via a tetrasaccharide linker.

1.4.3.1 Acan

In the CNS, Acan has been observed to primarily be produced by neurons (Matthews *et al.*, 2002; Carulli *et al.*, 2006; Giamanco and Matthews, 2012). It is the most well characterised CSPG known to co-localise with PNNs throughout the CNS (Carulli *et al.*, 2006; Deepa *et al.*, 2006; Galtrey *et al.*, 2008; Irvine and Kwok, 2018). A conditional CNS *Acan* knockout mouse model has also been produced that demonstrated that the loss of *Acan in vivo* caused the ablation of PNN structures in the brain (Rowlands *et al.*, 2018). Acan is the most well characterised lectican due to it being present in cartilage tissue where it was first described (Hascall and Sajdera, 1970; Hascall, 1988). Acan is the only lectican that contains a G2 domain that possess 2 link modules (Kwok *et al.*, 2011; Aspberg, 2012). The central domain of Acan is made up of approximately 1161 amino acid residues and has previously been characterised as being the most glycosylated lectican, containing between 80 – 120 GAGs (Yamaguchi, 2000; Kiani *et al.*, 2002). Acan in cartilage tissue has been specifically measured using AFM, therefore of all the CSPGs its size has been the well characterised (Ng *et al.*, 2003). However, it is important to

note that it not known if cartilage Acan is representative of Acan found in the brain (this is addressed in objective 1 in section 1.6).

1.4.3.2 Bcan

Bcan was first cloned in 1994 and has been observed to have the shortest central domain of the lecticans, containing approximately 300 amino acid residues (Yamada *et al.*, 1994; Yamaguchi, 2000). Approximately 3 GAG chains are thought to interact with the central domain of Bcan (Yamaguchi, 2000). Bcan is a lectican that is specific to the CNS and is known to co-localise with PNNs (Yamaguchi, 2000; Carulli *et al.*, 2006; Deepa *et al.*, 2006; Galtrey *et al.*, 2008). In the adult brain a significant proportion of Bcan has previously been observed to exist without any GAG side-chains attached (Yamada *et al.*, 1994; Yamaguchi, 1996). Furthermore, there is a splice variant of Bcan that is glycosylphosphatidylinositol (GPI)-anchored to the cell surface, containing a cleaved central domain with a short signal sequence (Seidenbecher *et al.*, 1995; Yamaguchi, 2000).

1.4.3.3 Vcan

Vcan exists in the CNS in at least 4 isoforms that have previously been characterised (Zimmermann and Ruoslahti, 1989; Dours-Zimmermann and Zimmermann, 1994; Zako *et al.*, 1995; Ito *et al.*, 1995). The central domain of each Vcan isoform differ in size, with one isoform lacking the entire central domain (Yamaguchi, 2000). The length of the entire fully-formed central domain creates the largest lectican species, though due to its numerous spliced forms it is considered to be the lectican most varied in size (Ito *et al.*, 1995; Zako *et al.*, 1995; Yamaguchi, 2000). Unglycosylated full-length Vcan is ~ 360 kDa (Ito *et al.*, 1995; Zako *et al.*, 1995). Throughout the CNS Vcan is known to associate with PNNs (Carulli *et al.*, 2006; Deepa *et al.*, 2006; Galtrey *et al.*, 2008).

1.4.3.4 Ncan

Ncan is a lectican specific to the CNS (Rauch *et al.*, 1992; Yamaguchi, 2000). Ncan has been found to co-localise with PNNs throughout the CNS (Carulli *et al.*, 2006; Deepa *et al.*, 2006; Galtrey *et al.*, 2008). Multiple splice variants of Ncan exist, though full length the core protein is ~ 245 kDa in an adult rodent brain, with ~ 3 CS GAG chains interacting with the central domain (Rauch *et*

al., 1991). Ncan is expressed by both neurons and astrocytes, though astrocytes have been observed to express Ncan more abundantly in culture (Oohira *et al.*, 1994).

1.4.3.5 Pcan

Pcan is a soluble splice variant of the receptor-type protein tyrosine phosphatase transmembrane protein (Maurel *et al.*, 1994). Although it is not a lectican, Pcan is a CSPG that shares some similarities to the lectican family, containing an N-terminal (G1), and a central domain, though lacking a G3 domain (Maurel *et al.*, 1994). However, the RPTP form of Pcan has a C-type lectin domain. Pcan has also been found to co-localise with PNNs throughout the CNS (Carulli *et al.*, 2006; Deepa *et al.*, 2006; Galtrey *et al.*, 2008). Tn-R has also been observed to interact with Pcan, with this interaction being calcium-dependent (Xiao *et al.*, 1997).

1.4.4 Tn-R

Tn-R is a glycoprotein predominantly expressed in the CNS where 2 isoforms have been observed (Schachner *et al.*, 1994; Aspberg, 1995; Faissner, 1997; Woodworth *et al.*, 2002; Lundell *et al.*, 2004; Morawski *et al.*, 2014). Tn-R is known to interact with the G3 domain of lecticans and Pcan in a calcium-dependent manner (Aspberg, 1995; Aspberg *et al.*, 1997). The lecticans interact with Tn-R with different affinities, as Bcan has been observed to interact with the highest affinity of the lecticans (Aspberg *et al.*, 1997; Hagihara *et al.*, 1999). Tn-R has been hypothesised as an integral part of PNNs, with a proposed role in the cross-linking of the PNN structures due to Tn-R forming dimeric and trimeric structures (Aspberg, 1995; Chiquet-Ehrismann and Tucker, 2011; Morawski *et al.*, 2014).

1.4.5 Cellular contributions of molecular components to PNNs

To gain an understanding of how these PNN-associated molecular components self-organise to assemble the supramolecular PNN structure it is important to consider where the components are contributed from. Components contributed by cells ensheathed by PNNs will be added to the PNN surface differently to components contributed by the ECM where the components will interact with the surface of the PNN structure first. To highlight this, only HA provided by the cells ensheathed by PNNs can be

surface bound to the cell, therefore will be incorporated differently to the PNN surface in comparison with HA contributed from the ECM by other cells. Using a combination of *in situ* hybridisation and immunohistochemistry to analyse the contributions of PNN components provided by neurons and glial cells in the rat cerebellum found: neurons contributed Acan, Ncan, Tn-R and low levels of Bcan; astrocytes contributed Bcan at much higher levels compared with neurons; oligodendrocytes contributed Vcan, Bcan and expressed Tn-R at higher levels compared with neurons; oligodendrocyte precursor cells and synantocytes contributed Vcan, Pcan and contributed Tn-R at higher levels compared with neurons (Carulli *et al.*, 2006). Additionally, Ncan has also been observed to be contributed by astrocytes during development, but is contributed only by neurons in the adult rat cerebellum (Carulli *et al.*, 2007).

To further analyse how the contributions of components affects PNN assembly neurons were cultured *in vitro* to observe PNN formation in the absence of glial cells (Miyata *et al.*, 2005; Giamanco and Matthews, 2012). Miyata *et al* (2005) observed neurons cultured *in vitro* produced PNNs that contained Ncan, HA and Pcan. In this particular analysis no other PNN components were investigated. Giamanco & Matthews (2012) observed that Acan was transcriptionally upregulated in the absence of glial cells, while PNNs produced in the absence of glia did not contain Bcan, Hapln1 or Tn-R. Additionally, glial cells have been observed to express most PNN components when analysed by reverse transcription polymerase chain reaction, where they were specifically found to not express Acan or HAS3, which supports the *in situ* hybridisation analysis (Carulli *et al.*, 2006; Giamanco and Matthews, 2012). Therefore, it is possible for PNNs to be assembled by neurons *in vitro* in the absence of glial cells, however the biochemical composition of these structures are different, supporting the hypothesis that PNN components are contributed by both neurons and glial cells.

1.4.6 Temporal expression and staining pattern of PNN components

It is important to consider when the PNN components are expressed when considering how they assemble and self-organise to form the supramolecular structure on the neuronal cell surface. PNNs, are first detected at P7 in the rat CNS, which correlates with the expression of Acan and Hapln1 at low levels (Carulli *et al.*, 2007; Galtrey *et al.*, 2008). This observation suggests that Hapln1 and Acan, may be important in triggering the assembly of PNNs. Although PNNs are first observed around P7 in the rat cerebellum and spinal cord, in the visual cortex of mice PNNs are not observed until later, around

P14 (Carulli *et al.*, 2010). This implies that there may be temporal differences in the expression of PNN components in different CNS regions. It is important to note that analysis of gene expression does not consider the potential for the components to be post-transcriptionally regulated.

1.5 Structural heterogeneity of PNNs

1.5.1 Heterogeneity in the PNN-associated components

Although a variety of molecular components have been identified it remains unclear how these molecules precisely interact during the formation of PNNs (this is addressed in objective 2 in section 1.6). PNN-associated molecules have been observed to be differentially distributed throughout the CNS regions, however this has not yet been correlated with changes to PNN structure (Carulli *et al.*, 2006; Galtrey *et al.*, 2008; Bekku *et al.*, 2012). Furthermore, heterogeneity in the biochemical composition of PNNs has been previously observed (McRae *et al.*, 2007; Irvine and Kwok, 2018; Ueno *et al.*, 2018; Miyata *et al.*, 2018).

HA, Haplns and CSPGs are known to be essential to the formation of PNNs (Deepa *et al.*, 2006; Carulli *et al.*, 2010; Kwok *et al.*, 2010). It is important to note the potential molecular diversity in these essential PNN components that are present in the CNS. HA can be synthesised at different sizes by three isoforms of HAS (HAS1, 2 and 3) (Itano *et al.*, 1999). There are also five CSPGs (Acan, Bcan, Vcan, Ncan and Pcan) known to be associated with the PNN structure, as well as three Haplns (Hapln1, Hapln2 and Hapln4) (Miyata *et al.*, 2005; Carulli *et al.*, 2006; Deepa *et al.*, 2006; Carulli *et al.*, 2007; Galtrey *et al.*, 2008; Zimmermann and Dours-Zimmermann, 2008; Kwok *et al.*, 2011; Wang and Fawcett, 2012; Giamanco and Matthews, 2012). The variety of sizes and varying degree of glycosylation observed in the different molecular components of PNNs is demonstrated in Figure 3. This highlights how the relative contribution of each individual molecular component could change the physical properties of the surfaces in a unique way. Specifically, the sizes of the different CSPGs range from approximately 100 – 375 nm, therefore the relative abundance of each CSPG within PNNs are likely to change the physical properties of the film. Furthermore, the different levels of glycosylation observed on the different CSPGs will also contribute to changes to the structure of PNNs. Although the presence of the molecules within PNNs have been observed, the relative abundance of PNN-associated components

in different CNS regions remains unclear (this is addressed in objective 1 in section 1.6).

Each specific CSPG molecule also has the potential to be highly heterogeneous in structure due to alternative splicing of the core protein that could occur during synthesis, or as a product of enzymatic cleavage by matrix metalloproteinases (MMPs) (Yamaguchi, 2000; Kiani *et al.*, 2002; Morawski *et al.*, 2012). Additional heterogeneity in CSPG structure could be produced through varying the degree of glycosylation of the core protein. It is unknown whether lecticans in different regions display varying glycosylation patterns (this is addressed in objective 1 in section 1.6). Furthermore, it is important to note that yet further heterogeneity could be produced through varying the sulfation pattern of the GAG chains (Foscarin *et al.*, 2017).

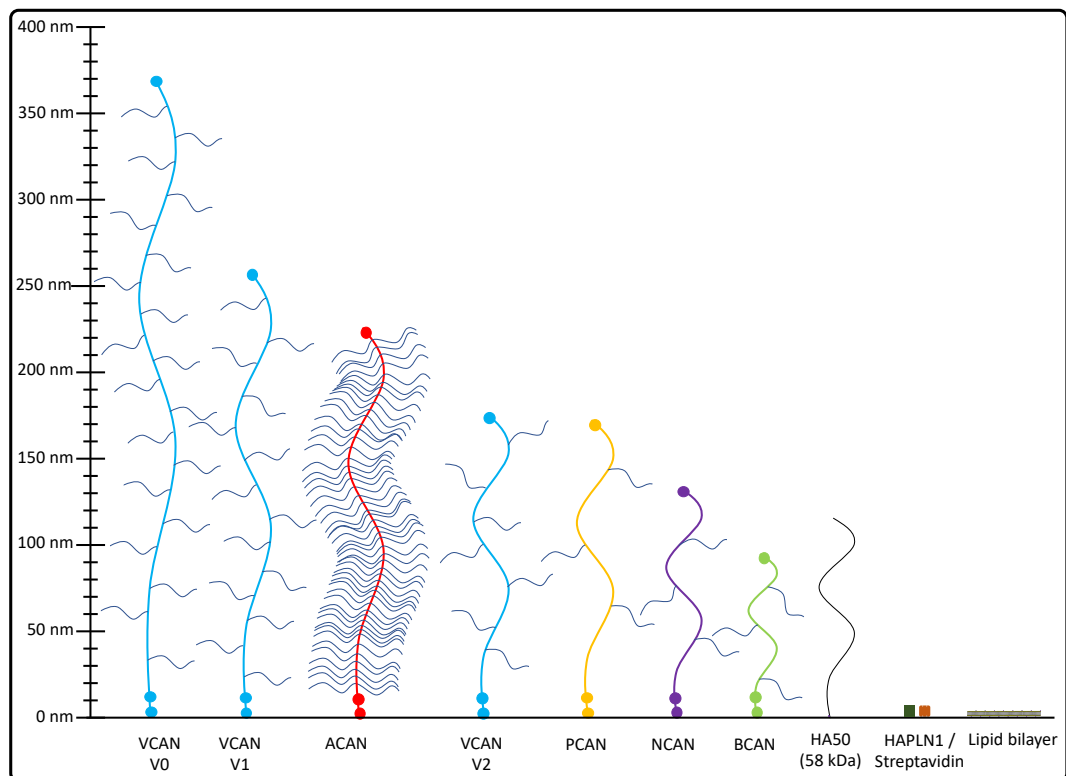


Figure 3. Size comparison of PNN-associated molecules.

This figure was produced using the core protein and GAG chain amounts summarised in the review by Bandtlow and Zimmermann (2000). To determine the nm size the CSPGs were compared with the size of the Acan core protein determined by Ng *et al* (2003). Therefore, the sizes of the other CSPGs are an approximate estimate extrapolated from the ratio of core protein molecular weight with Acan.

1.5.2 Proposed structure of PNNs

A macromolecular structure of PNNs was proposed by (Kwok *et al.*, 2011). This model proposed that Acan interacts with HA within the HA films that are tethered to the cell surface by HAS molecules (Figure 4). On interaction with surface bound HA films Acan has previously been observed to increase the surface compliance of HA films, highlighting the ability of CSPGs to influence the biomechanical properties of HA films (Attili and Richter, 2013). It has not yet been established if other CSPGs have a similar effect, though theoretically there is no reason why the interaction would not be similar. The interaction of HA and CSPGs is then stabilised by Hapln1, as has previously been observed using surface plasmon resonance (SPR) (Shi *et al.*, 2004). Furthermore, the proposed model of the macromolecular structure of PNNs suggests Tn-R crosslinks CSPGs via their G3 domain (Aspberg, 1995; Deepa *et al.*, 2006; Galtrey *et al.*, 2008; Suttkus *et al.*, 2014; Morawski *et al.*, 2014). What remains unclear is how these molecules self-organise and assemble into the proposed macromolecular structure (this is addressed in objective 2 in section 1.6).

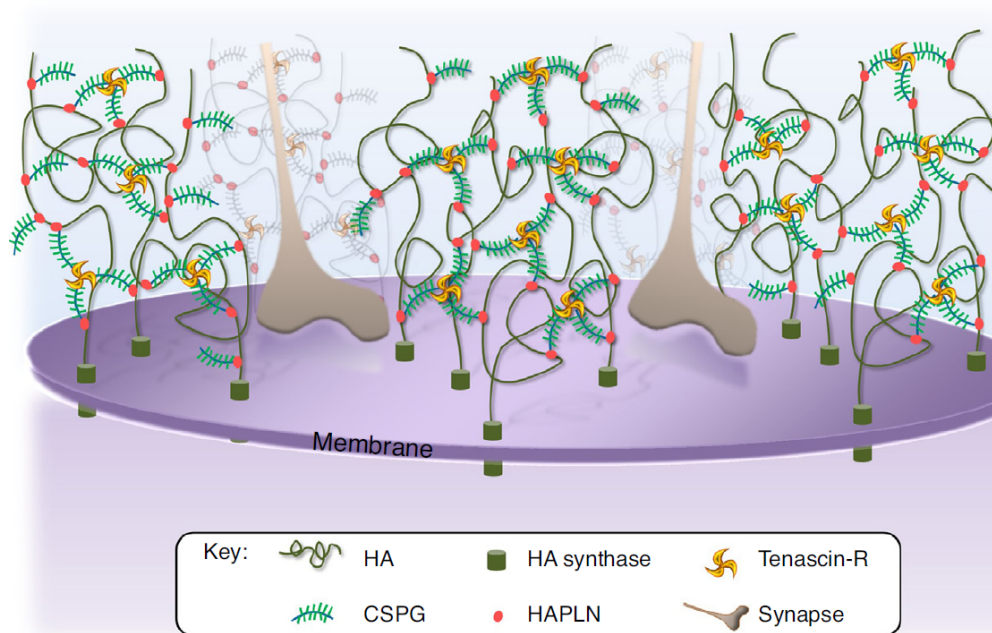


Figure 4. A schematic representation of the macromolecular structure of PNNs. The figure is courtesy of: (Richter *et al.*, 2018).

1.5.3 Heterogeneity of PNN morphologies

PNNs have been observed in many CNS regions, with a couple of studies that have focussed on analysing the distribution of PNNs throughout the CNS (Seeger *et al.*, 1994; Bertolotto *et al.*, 1996). Numerous sub-populations of neurons were observed to be ensheathed by PNNs, with both studies highlighting the differences in appearance of PNNs surrounding specific neuronal populations (Seeger *et al.*, 1994; Bertolotto *et al.*, 1996). A variety of PNN structures have been observed throughout the CNS (Arnst *et al.*, 2016; Ueno *et al.*, 2017b; Dzyubenko *et al.*, 2018; Sigal *et al.*, 2019). Specifically, two distinct PNN morphologies have been observed that have been suggested to be associated with different maturation states: a reticular PNN structure observed in the adult CNS; a punctate structure observed with greater frequency in the younger CNS, implying an immature PNN state (Figure 5) (Ueno *et al.*, 2017a; Ueno *et al.*, 2017b; Richter *et al.*, 2018). If the hypothesis that the two morphological states being associated with different maturation states is correct, then it proposes a further question of what causes the phase transition from the punctate to the reticular state. This currently remains unknown (this is addressed in objective 2 in section 1.6).

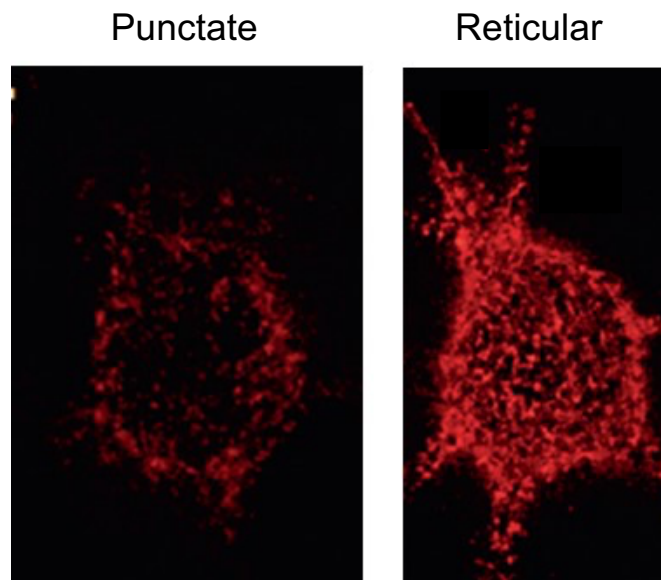


Figure 5. Images taken from a recent paper suggesting that 2 distinct morphological PNN states are present in the CNS.

Punctate was defined as patchy stain surrounding neurons, while reticular is defined as the identifiable net-like structure. Images are taken from (Ueno *et al.*, 2017a).

When comparing studies that have utilised histochemistry and imaging techniques to analyse PNNs, there appears to be morphologically distinct PNNs observed in different CNS regions (Brückner *et al.*, 1996; Carulli *et al.*, 2006; Deepa *et al.*, 2006; Gert Brückner *et al.*, 2006; Carulli *et al.*, 2007; Galtrey and Fawcett, 2007; Ueno *et al.*, 2017b; Yamada and Jinno, 2017). Specifically, PNNs in the cortical and hippocampal regions look morphologically distinct to PNNs observed in the cerebellum and spinal cord (Figure 6). Cortical and hippocampal PNNs form around the soma and proximal dendrites of neurons and appear to produce a thinner surface layer. In comparison cerebellar and spinal cord PNNs form only around the soma and appear to have a thicker morphology. The difference in the size of soma implies that the neuronal sub-types that the PNNs are surrounding in these regions is likely to be different. What remains unknown is if the morphologically distinct PNNs are caused by changes to the biochemical composition of the surface (this is addressed in objective 1 in section 1.6). Furthermore, it remains unclear if the different morphologies are integral to PNN function.

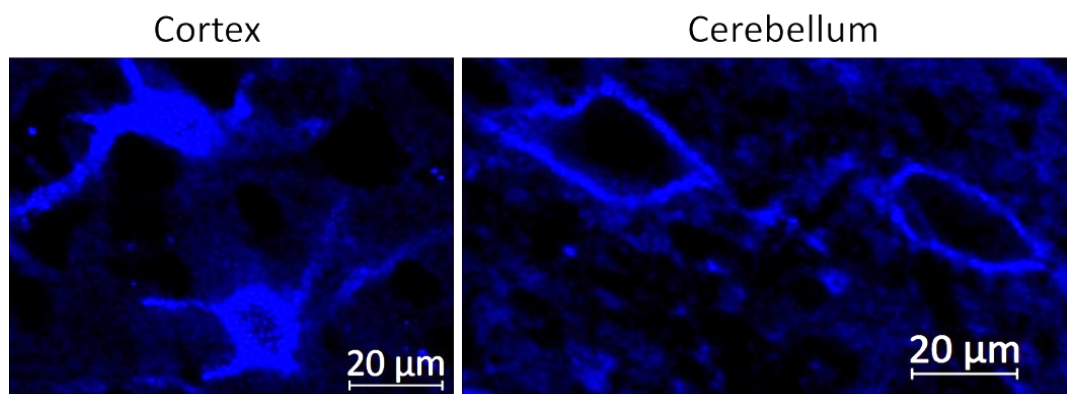


Figure 6. Representative confocal microscopy images of PNNs taken in the cortical and cerebellar regions of the CNS

The marker *Wisteria floribunda* agglutinin (WFA) was used to stain PNNs using the protocol described by Souter and Kwok (2020). Cortical PNNs display observable staining on the soma and dendrites of neurons. Cerebellar PNNs only display observable staining around the soma. The net-like structure observed in cortical image may not be present in the cerebellar image due to the size of the soma of the neurons being different.

1.6 Objectives of this thesis

Throughout the introduction numerous knowledge gaps have been highlighted that represent the objectives of this thesis. Section 1.4 defined the biochemical components often observed in PNNs, highlighting the numerous splice variants and enzymatically cleaved forms of each molecule. Section 1.5 then highlighted the heterogeneity of PNN biochemical components and identified that a systematic analysis that interrogated this heterogeneity has not yet been done. By defining the biochemical heterogeneity of PNN components in specific CNS regions may present an opportunity to modulate PNNs region specifically in the future. Therefore, this became the first objective of this thesis.

Section 1.3 explained the importance of biomechanical signalling in the CNS and highlighted that to date an analysis of how PNNs change the biomechanical properties of the neurons they surround has not been done. Furthermore, section 1.5 defined different PNN phenotypes that have been observed throughout the CNS and presented a knowledge gap in the understanding of how the PNN components interact and self-organise into these supramolecular PNN structures. As PNNs play an important role in synaptic plasticity in the CNS, it is important to understand the mechanisms by which PNNs exert their function. Cells in the CNS have been observed to mechanosense and alter their behaviour depending on stiffness of surfaces, therefore the formation of PNNs and the resulting changes to the biomechanical properties of the surface may modulate cell behaviour. Understanding these mechanisms may offer new therapeutic avenues for targeting neurological diseases linked with PNNs. Therefore, objective 2 aimed to investigate the interactions involved in establishing PNNs by establishing a methodology for measuring PNN formation using QCM-D that allowed for both biochemical and biomechanical measurements of the surfaces simultaneously.

In section 1.4 the importance of GAGs, specifically HA and CS chains attached to CSPGS were explained. The importance of surface-bound HA in the establishment of PNNs is further discussed in section 1.5. Although current methodologies for sizing GAGs exist, that are discussed extensively in section 5.1, currently there is not a methodology for measuring the size of surface-bound GAGs. As there is a growing number of therapeutic products that are incorporating GAGs that requires stringent quality control of GAGs that includes the sizing of GAG chains, a methodology that can size GAGs efficiently and cheaply would be useful for both industrial and academic

applications. Therefore objective 3 aimed to establish a methodology for sizing surface-bound GAGs using QCM-D. A secondary aim was to also expand on current methodologies using polyacrylamide gel electrophoresis (PAGE) by increasing the range of size markers available.

Therefore, the explicit objectives of this thesis are:

1. To conduct a systematic analysis of the molecular components of PNNs using Western blotting.
 - a. Investigate the distribution of each component in distinct anatomical areas in the CNS. The specific regions included were the cortical, hippocampal, cerebellar and cervical spinal cord regions.
 - b. Determine the heterogeneity and relative abundance of splice variants of the various PNN components.
 - c. Determine if there is biochemical heterogeneity of PNN components present in distinct CNS regions.

2. To investigate the molecular interactions and supramolecular self-organisation underpinning PNN formation using QCM-D.
 - a. Investigate the molecular interactions that underpin the supramolecular self-organisation and assembly of PNNs.
 - b. Establish a methodology for investigating the assembly of PNNs and measuring the biomechanical properties of PNNs.

3. To establish a methodology for measuring the length of GAGs.
 - a. Expand on current methodologies for sizing GAGs using PAGE by defining the ratio of GAG migration rate with protein migration rate to expand the range of size markers available.
 - b. Establish a methodology for measuring the size of surface-bound GAGs using QCM-D.

Chapter 2: Methodology

2.1 Western blotting

2.1.1 Animals

Adult, female Sprague-Dawley rats (260 – 290 g) from Charles River were used in this study. All animals were housed in standard housing conditions with a 12 hour light / dark cycle with food *ad libitum*. Where possible animals were housed in groups of 2 – 4 per cage. The work was performed under the regulations of the Animals Scientific Procedures Act 1986 and covered by the Home Office project license (number: 70/8085) and PIL for Luke Souter (number: IAF9AE2C3).

2.1.2 Brain lysate preparation

Three adult, female Sprague-Dawley rats were sacrificed using a CO₂ chamber and the cortex, hippocampus, cerebellum and cervical spinal cord (cSC) regions were dissected and isolated. Each of the rat dissections was done separately, creating 12 samples in total ($n = 3$ for each CNS region). Once dissected the tissue was immediately submerged in 1 mL cold cOmplete™ Lysis-M, ethylenediaminetetraacetic acid (EDTA) - free buffer (Roche: 04719964001) within a homogeniser that was submerged in ice. Samples were homogenised on ice for 1 min then transferred to a 1.5 mL Eppendorf tube. They were then centrifuged at 13,000 rpm for 5 min at 4 °C. The supernatant was collected and a Pierce™ bicinchoninic acid assay (BCA) assay (Thermo Scientific: 23225) was performed. The BCA results were analysed using a plate reader (FLUOstar Omega) to determine protein concentration. Each sample was then diluted to 5 mg/mL with phosphate buffered saline (PBS) pH 7.4, aliquoted and stored at -80 °C until required.

2.1.3 Sodium dodecyl sulfate – polyacrylamide gel electrophoresis (SDS-PAGE)

One aliquot of each sample was thawed and 30 µg of total protein was mixed with loading buffer. The loading buffer consisted of 2.5% (v/v) 2-mercaptoethanol and Laemmli buffer (69.45 mM Tris-HCl, pH 6.8, 11.1% [v/v] glycerol, 1.1% lithium dodecyl sulfate (LDS), 0.005% bromophenol blue). As all samples were previously diluted to the same concentration the ratio of sample to loading buffer was equal in each lane. All samples were then heated

at 90 °C for 5 min using a dri-block™ (Techne). The denatured samples were loaded into a pre-cast 15 well, 1 mm thick, 4 – 15% Tris-glycine gel (Biorad: 456-8086) and ran using Tris-glycine SDS (TGS) running buffer (Bio Rad: 161-0772; 25 mM Tris, 192 mM glycine, 0.1% w/v SDS, pH 8.3). Initially, the samples were run for 15 minutes at 80 V to allow for efficient stacking to occur, then the voltage was increased to 100 V for 1 hour 45 min. The first 2 lanes of each gel contained protein ladders: lane one contained 10 µL Hi-mark™ pre-stained high molecular weight (HMW) protein standard (Invitrogen), the second lane contained 10 µL of precision plus protein™ all blue protein standards (Biorad). Two ladders were chosen instead of one due to the large range of sizes of molecules being analysed. Using the two ladders together allowed for a larger range of sizes to be analysed on the same gel. Triplicates of each sample were measured on different days for reproducibility of the results.

2.1.4 Western blotting

After protein separation using SDS-PAGE the samples were electro-transferred onto a Polyvinylidene fluoride (PVDF) membrane (0.4 µL pore size) in transfer buffer (25 mM Tris-HCL, 192 mM glycine, 10% methanol) overnight (\leq 16 hours) at 50 V at 4 °C in Biorad transfer tanks. These transfer conditions required careful optimisation to ensure that efficient transfer of the HMW material occurred, without affecting the lower molecular weight molecules. By transferring in the cold room, it ensured the gel did not overheat throughout the long transfer time.

All of the following wash steps were performed at room temperature. The membranes were briefly rinsed with Tris buffered saline with tween (TBS-T: 20 mM Tris base, 130 mM NaCl₂, 0.1% tween, pH 7.4), then blocked in 5 % (w/v) milk (Biorad) for 1 hour, before incubating with primary antibodies (Table 1) for 2 hours in TBS-T containing 5% milk. The membranes were briefly rinsed 3 times with TBS-T then washed 3 times with TBS-T 10 min per wash. They were then incubated with secondary antibodies (Table 1) for 1 hour, then a further 3 brief rinses with TBS-T, followed by 2 times washes with TBS-T. Finally, 2 washes 5 min per wash in Tris buffered saline (TBS) were done before treating with Pierce™ enhanced chemiluminescence (ECL) western blotting substrate (Thermo Scientific: 32106) then documented using a Fujifilm chemiluminescent imager.

The membranes were stripped with 0.1 M glycine pH 2.5 for 15 min at room temperature, then 45 min at 37 °C. The membranes were then briefly rinsed 5 times with TBS-T before repeating the steps above probing for actin.

Table 1. Antibodies used for Western blot analysis.

Antibody	Species Origin	Dilution	Working Conc. (µg/mL)	Company (Product number)
Primary Antibodies				
Anti-Acan	Rabbit	1 : 1,200	0.42	Abcam (ab1031)
Anti-Bcan	Sheep	1 : 1,200	0.83	R&D (AF009)
Anti-Ncan	Mouse	1 : 500	0.74	DSHB ^c (1F6)
Anti-Vcan	Mouse	1 : 500	0.34	DSHB ^c (12C5)
Anti-Pcan	Mouse	1 : 500	0.33	DSHB ^c (3F8)
Anti-Hapln4	Mouse	1 : 1,200	0.83	R&D (AF4085)
Anti-Hapln1	Goat	1 : 1,200	0.83	R&D (AF2608)
Anti-Tn-R	Goat	1 : 1,200	0.83	R&D (AF3865)
HABP ^a	-	1 : 1,200	0.20	Amsbio (HKD-BC41)
Anti-actin	Mouse	1 : 10,000	0.20	Abcam (ab6276)
Secondary Antibodies				
Anti-mouse HRP ^b	Horse	1 : 20,000	0.05	Vector labs (PI-2000)
Anti-rabbit HRP ^b	Goat	1 : 20,000	0.05	Vector labs (PI-1000)
Anti-goat HRP ^b	Horse	1 : 20,000	0.05	Vector labs (PI-9500)

a) HA binding protein (HABP)

b) Horseradish peroxidase (HRP)

c) Developmental studies hybridoma bank (DSHB)

2.1.5 Densitometry

The results from each lane in each gel were normalised by dividing the intensity of the PNN-associated molecule by the intensity of actin. This creates a percentage that is used as the arbitrary unit (A.U.) measurement throughout this thesis. Densitometry was performed using FIJI ImageJ imaging software (NIH), drawing boxes around each of the bands in the lanes. A box was then drawn in the same lane where no bands were present. The mean intensity in the un-banded box, was then subtracted from the banded box to standardise for the gel background. The same process was then done for the actin results in the same lanes. By dividing the densitometry result for the molecules by the actin result taken from the same lane the data is normalised and accounted for any discrepancies in the amount of sample loaded into each lane.

2.1.6 Statistics

Each sample was run in triplicate, therefore the mean and standard deviation could be taken. A linear regression analysis was performed using a one-way

analysis of variance (ANOVA) to compare the different CNS regions for each PNN-associated molecule, followed by a *post hoc* Tukey test. Similarly, the same statistical setup was used to compare different size bands where multiple bands were present. Results were classed as statistically significant at $p \leq 0.05$. As the affinities of each antibody to its target is different, it was not possible to statistically compare results where different antibodies were used.

2.2 Quartz crystal microbalance with dissipation monitoring (QCM-D)

QCM-D is an acoustic measuring technique that works in liquid and can be used to examine soft surfaces (Reviakine, Johannsmann and Richter, 2011). The benefit of the technique is it allows for changes in surface organisation at the interface to be analysed in real-time *in vitro*. The technique can measure the areal mass density and the mechanical properties of the surface bound layer. The areal mass density includes the adsorption of molecules as well as hydrodynamically coupled solvent. The following section aims to describe how the measurements ascertained by QCM-D can be used quantitatively to define the properties of the surface. To do this the detailed explanations provided by Reviakine, Johannsmann and Richter (2011) and Tellechea *et al* (2009) will be summarised below.

2.2.1 Quantitative explanation of QCM-D

QCM-D functions by oscillating a piezo-electric crystal at its resonance frequency f_n defined as (Reviakine, Johannsmann and Richter, 2011):

$$f_n = nc/2d \quad (1)$$

Where n is the overtone order (odd), c is the speed of sound in quartz and d is the crystal thickness. By switching the external voltage on and off intermittently the piezoelectric produces a voltage during these decaying mechanical oscillations. Therefore, both the frequency, and the rate of decay are measured, yielding two parameters per overtone: the resonance frequency f_n and the dissipation D_n (Reviakine, Johannsmann and Richter, 2011). As there is a linear relationship between resonance frequency and changes in the resonator mass it is possible to use QCM-D as a microbalance

(Sauerbrey, 1959). The relationship can be defined as (Reviakine, Johannsmann and Richter, 2011):

$$\Delta f_n = -\frac{n}{C} m_{\text{film}} = -\frac{n}{C} \rho_{\text{film}} h_{\text{film}} \quad (2)$$

Where m_{film} is the areal mass density of the film, ρ_{film} is the density of the adsorbed film, h_{film} is the thickness of the adsorbed film and C is the mass sensitivity constant (dependent solely on the material properties of the quartz crystal and the fundamental resonance frequency f_F). The relationship between the resonance frequency / bandwidth, the liquid's viscosity and liquid's density can be used to measure the viscosity of the material surface as it can be defined by (Reviakine, Johannsmann and Richter, 2011):

$$\Delta f_n = -\Delta \Gamma_n = -\frac{f_n}{2} \Delta D_n = -\frac{1}{C} \sqrt{\frac{n \rho_{\text{liq}} \eta_{\text{liq}}}{2 \omega_F}} \quad (3)$$

Where Γ_n is the quantity gamma, ρ_{liq} is the liquids density, η_{liq} is the liquids viscosity and ω_F is the angular fundamental resonance frequency. ω_F can be defined in terms of f_F by (Reviakine, Johannsmann and Richter, 2011):

$$\omega_F = 2\pi f_F \quad (4)$$

Equation 3 describes a decrease in frequency and increase in dissipation as both being proportional to the square root of the product of liquid viscosity and liquid density (Reviakine, Johannsmann and Richter, 2011). The measurements are sensitive to the bulk liquid, hence it is imperative to make additional measurements in the liquid alone in order to define the contribution of the material surface. D_n is the inverse of the quality factor (Q factor) which is a dimensionless parameter that describes the damping of the oscillation at resonance. This is achieved by relating the amount of energy stored to the amount of energy lost. Therefore, D_n is defined as the energy dissipated per oscillation, divided by the total energy stored in the system.

Equations 1 – 4 above introduce how Δf and ΔD are related to the areal mass density and the material properties of the surface, specifically viscosity. It is therefore possible to derive the density of material being deposited on the surface, the surface thickness and the biomechanical properties of the film under certain conditions. One of the key assumptions when quantitatively analysing QCM-D data is that the surface is laterally homogeneous, meaning there is an even spread of each molecule across the material surface.

Depending on the properties of the film being formed on the sensor surface varying methodologies for analysing the data quantitatively can be used. An important distinction is defining the difference between a soft and a sufficiently

rigid film by using the statements (Reviakine, Johannsmann and Richter, 2011):

$$\Delta\Gamma_n \ll -f_n \quad (5)$$

Or

$$\Delta D_n / (-\Delta f_n / n) \ll 4 \times 10^{-7} \text{Hz}^{-1} \quad (6)$$

Where $4 \times 10^{-7} \text{Hz}^{-1}$ is the value for the resonance frequency of a 5 MHz crystal (derived from Equation 1), used for the experiments throughout this thesis. All HA films formed throughout this thesis were classified as soft films (Equation 6; see appendix 1). These equations derive from the physics of the sensing methodology. The oscillation of a rigid film couples fully to the oscillation of the sensor, and therefore its dissipation would be expected to be zero. Soft films will produce a finite dissipation as they will not couple. A surface is required to be sufficiently rigid for the Sauerbrey equation to be used to ascertain the areal mass density of the surface. As the surface-bound films produced throughout this thesis are soft, the Sauerbrey equation could not be used. However, as all surfaces produced throughout this thesis had a measure of $\Delta D > 0$, the surfaces are thick and soft enough for the viscoelastic properties of the film to be measured (Reviakine, Johannsmann and Richter, 2011). The viscoelastic properties are represented by (Reviakine, Johannsmann and Richter, 2011):

$$G = G' + iG'' \quad (7)$$

Where G is the complex shear modulus, G' is the storage modulus (otherwise known as the spring constant), i is the imaginary unit (the square root of -1) and G'' is the loss modulus. The loss modulus can be described as (Reviakine, Johannsmann and Richter, 2011):

$$G'' = \omega\eta \quad (8)$$

Where $\omega = 2\pi f$ is the angular frequency of deformation. In Equation 8 viscosity η relates the applied force to the rate of deformation, therefore can be thought of as a friction coefficient (Reviakine, Johannsmann and Richter, 2011). In order to be measured the thickness of the films being produced on the sensor surface have to be thinner than the wavelength of the shear-acoustic wave propagating throughout the surface. Therefore, there is a maximum thickness for which QCM-D measurements can be accurately measured. To determine this maximum penetration depth of the shear wave in liquid δ can be determined by (Reviakine, Johannsmann and Richter, 2011):

$$\delta = (2\eta_{liq} / (2\pi n f_F \rho_{liq}))^{0.5} \quad (9)$$

For water at 5 MHz ($n = 1$), $\delta \sim 250\text{nm}$, therefore any surfaces larger than this size would require different methodologies for assessing their material properties. For surfaces thinner than this maximum thickness the relationship between frequency, bandwidth, areal mass density of the film and its viscoelastic properties can be defined by (Reviakine, Johannsmann and Richter, 2011):

$$\Delta f_n \approx -\frac{n}{C} m_{\text{film}} \left(1 - n\omega_F \rho_{liq} \eta_{liq} \frac{G_f''}{\rho_{\text{film}}(G_{\text{film}}'^2 + G_{\text{film}}''^2)} \right) = -\frac{n}{C} m_{\text{film}} \left(1 - n\omega_F \rho_{liq} \eta_{liq} \frac{J'_{\text{film}}}{\rho_{\text{film}}} \right) \quad (10)$$

$$\Delta D_n \approx \frac{n}{C} m_{\text{film}} n\omega_F \rho_{liq} \eta_{liq} \frac{G_f'}{\rho_{\text{film}}(G_{\text{film}}'^2 + G_{\text{film}}''^2)} = \frac{n}{C} m_{\text{film}} n\omega_F \rho_{liq} \eta_{liq} \frac{J'_{\text{film}}}{\rho_{\text{film}}} \quad (11)$$

Where m_{film} can be described by (Reviakine, Johannsmann and Richter, 2011):

$$m_{\text{film}} = \rho_{\text{film}} h_{\text{film}} \quad (12)$$

The frequency dependent compliance of the film J can be described by (Reviakine, Johannsmann and Richter, 2011):

$$J = J' - iJ'' = G^{-1} \quad (13)$$

Where J' is the elastic and J'' is viscous component of compliance, respectively. The value of ρ_{film} in soft matter can be roughly approximated to be 1 g/cm^3 for biopolymer films solvated by water (Reviakine, Johannsmann and Richter, 2011). Equations 10 and 11 can be re-written when ($n = 1$), $\delta \sim 250\text{nm}$ as the dispersion in $\Delta f_n/n$ will be small, therefore it is possible to calculate J' from (Reviakine, Johannsmann and Richter, 2011):

$$\frac{\Delta D_n}{\Delta f_n} = -\frac{\rho_{liq}}{\rho_{\text{film}}} n\omega_F \eta_{liq} J'_{\text{film}} \quad (14)$$

To summarise the section above, it is possible to use Δf and ΔD to measure the material properties of the film by comparing the relationship between them to determine the elastic compliance. For simplicity, throughout the thesis Equation 14 has been re-written as $\Delta D / -\Delta f$. The benefit of Equation 14 is it is a very simple relationship that can be readily extracted from QCM-D data to provide a simple, relative measure of film softness. This is in contrast to other, potentially more accurate analytical methods which require some form of nonlinear regression analysis, referred to as viscoelastic modelling. More compliant, soft films will have a higher $\Delta D / -\Delta f$, while a less compliant, rigid film will have a low $\Delta D / -\Delta f$.

The areal mass density measured by Δf includes both the mass of the molecule adsorbing onto the surface, as well as the mass of the solvent. Therefore, in order to define the density of molecules adsorbing onto the surface the contribution to mass by the solvent needs to be defined. This can be done by using an additional optical technique for measuring the mass of the molecules adsorbing onto the surface, such as spectroscopic ellipsometry. This has previously been done for the HA molecule HA50, therefore the density of HA50 on the surface can be defined. However, it has not yet been done for Acan or HapIn1 therefore it is not possible to measure the density of these molecules using this technique, but instead the results compare the relative changes in Δf to define the relative abundance of each molecule.

Although it is possible to fit the data to viscoelastic model, due to the large number of parameters required it is difficult to gain meaningful data without the requirement of further measurements being made with different measuring techniques to ascertain the film properties required.

2.2.2 Measurements using QCM-D

All measurements were performed *in situ* under continuous sample flow with sub-second time resolution at room temperature (23 °C) with a Q-Sense E4 system with 4 independent standard flow modules (Biolin Scientific AB). Flow speeds of 10 to 20 $\mu\text{L}/\text{min}$ were kept constant using a syringe pump (World precision instruments) with 20 mL syringes (Terumo).

Measurements of shifts in frequency (Δf) and shifts in dissipation (ΔD) were taken at the fundamental frequency ($n = 1$), and six overtones ($n = 3, 5, 7, 9, 11$ and 13), which correspond to resonance frequencies ($f_n \approx 15, 25, 35, 45, 55$ and 65 respectively). For chapter 4 the 5th overtone ($n = 5$) was used to present Δf and ΔD . Any other overtone would have provided comparable results. For chapter 5 the 3rd overtone was used, to facilitate comparison with previously published data which were collected by collaborators using the 3rd overtone.

Running buffer (10 mM 4-(2-hydroxyethyl)-1-piperazineethanesulfonic acid (HEPES), 150 mM NaCl_2 , 5 mM CaCl_2 , pH 7.4) was used in all experiments unless specified otherwise and used within 2 weeks. Before use the running buffer was filtered using 0.22 μm Polyethersulfone (PES) membrane syringe filters (Merck: SLGPO33RS) and de-gassed. All of the molecules used throughout the QCM-D measurements are provided in Table 2.

Table 2. Molecules used in QCM-D experiments

Molecule	Molecular Weight (kDa)	Company (Product number)
Lipids		
DOPC ^a	-	Avanti (850375P)
DOPE-cap-biotin ^b	-	Avanti (870273P)
DODA-tris-NTA ^c	-	-
Protein		
Streptavidin	55	Sigma (S4762)
Hapln1	45	R&D (2608-HP)
Tenascin-R	147	R&D (3865-TR)
Proteoglycan		
Acan (bovine articular cartilage)	~ 2,500	Sigma (A1960)
Acan (pig laryngeal)	~ 2,500	-
Biotinylated HA		
HA_dp15	3.2	-
HA50	58 ± 3	Hyalose (HYA-B50-200)
HA250	280 ± 14	Hyalose (HYA-B250-200)
HA500	530 ± 27	Hyalose (HYA- B500-200)
HA1000	837 ± 42	Hyalose (HYA-B1000-200)

a) 1,2-dioleoyl-sn-glycero-3-phosphocholine (DOPC).

b) 1,2-dioleoyl-sn-glycero-3-phosphoethanolamine-N-(cap biotiny) (DOPE-cap-biotin).

c) Dioctadecyldimethylammonium-tris-nitrilotriacetic acid

2.2.3 Preparation of liposomes

Liposomes were prepared using the protocol established by Richter and Brisson (2003). Briefly, lipids were dissolved in chloroform, then mixed in desired amounts to achieve the ratio of lipids required (see appendix 2). A stream of nitrogen gas was used to dry the lipids in order to form a thin film that is beneficial for maximising the extraction of organic solvent. Further drying was achieved using a vacuum desiccator for 2 hours. The lipids were then re-suspended to a concentration of 2 mg/mL by vortexing with HEPES buffer. Small unilaminar vesicles were achieved through 5 freeze-thaw cycles using a combination of liquid nitrogen and warm water, followed by sonication using a tip-sonicator (Fisher Scientific) operated in pulse mode at 30% duty cycle for 30 min at 4 °C. To remove any metal debris from sonication, the lipid samples were centrifuged at 4 °C for 15 min (16,000 g), then transferred to a fresh 1.5 mL tube and stored at 4 °C for up to 6 months.

2.2.4 Passivation of tubes and chamber preparation

The chamber walls and tubing were first passivated using 600 µL of 10 mg/mL bovine serum albumin (BSA) (Sigma: A1933) per flow chamber at 50 µL/min flow speed. At an increased flow rate of 100 µL/min for 20 minutes, 2 mL of ultrapure water (resistance 18.2 MΩ • cm at 25 °C; Barnstead Nanopure

Diamond, Thermo Scientific) was flowed through each chamber to remove any excess BSA. After the passivation step the chambers were dried by flowing air through the chambers at 200 $\mu\text{L}/\text{min}$ for 5 minutes, then each chamber was dried further manually with nitrogen gas before placing the experimental sensor into the chamber.

Silicon sensors (Biolin Scientific: QSX303) were used for all QCM-D measurements. Before use the sensors were cleaned by briefly rinsing them with ultrapure water, 100% ethanol, ultrapure water then drying with nitrogen gas. The sensors were placed in a UV/ozone chamber ProCleaner™ plus chamber (Bioforce nanosciences) for at least 30 minutes then immediately placed into the QCM-D chambers.

2.2.5 Lipid bilayer and streptavidin monolayer formation

Both the liposomes, followed by streptavidin were injected in HEPES buffer at a flow speed of 20 $\mu\text{L}/\text{min}$. Liposomes were injected for 15 min, followed by a wash step that involved injecting HEPES for 10 min at 20 $\mu\text{L}/\text{min}$. Then streptavidin was injected for 15 min followed by a further 10 min wash step with HEPES.

2.2.6 Washing protocol

The wash protocol was done after each experiment on the QCM-D sensors, tubes and chamber, allowing the same sensors and equipment to be re-used. The flow rate was increased to 200 $\mu\text{L}/\text{min}$, then ultrapure water was injected for 5 minutes, followed by 2% SDS for 10 minutes, then 5 minutes ultrapure water and 10 minutes 100% ethanol. A final 5 min ultrapure water injection was performed before clearing the tubes and chamber for 5 minutes with air. The sensors and chambers were then dried with nitrogen gas before storing at room temperature for reuse.

2.2.7 Data acquisition and analysis

All QCM-D results were collected using QSoft (Biolin) and were analysed using a combination of QTools (Biolin) and Origin. Using QTools values of Δf and ΔD could be recorded, while Origin was used to create the graphs, including the $\Delta D / -\Delta f$ plots. All experiments were run in at least duplicate. The average result, plus or minus the standard deviation are recorded throughout this thesis when discussing Δf and ΔD .

Chapter 3: A systematic analysis of the molecular components of PNNs using Western blotting

3.1 Introduction

To establish the interplay between the biochemical and biomechanical properties of PNNs ultrastructure, it is essential to first characterise the biochemical components of mature PNNs. The structure of PNNs are known to include a variety of molecular components that have the potential to establish highly heterogeneous biochemical compositions (Carulli *et al.*, 2006; Galtrey *et al.*, 2008; Foscarin *et al.*, 2017; Irvine and Kwok, 2018). However, the information remains scattered. A systemic characterisation and understanding of their heterogeneity will provide an important foundation for determining the surface properties of PNN neurones.

The essential components of PNNs have been described in detail in chapter 1 and will be briefly summarised here. HA, CSPGs, and Haplns have been observed to be essential to the formation of PNNs (Deepa *et al.*, 2006; Carulli *et al.*, 2010; Kwok *et al.*, 2010). Considering there are three isoforms of HAS (HAS1, 2 and 3), five common CSPGs (Acan, Vcan, Bcan, Ncan and Pcan) and three Haplns (Hapln1/Crtl1, Hapln2/Bral1 and Hapln4/Bral2) that have been associated with PNNs the molecular diversity of the molecules alone could potentially establish a variety of distinct PNN structures (Miyata *et al.*, 2005; Carulli *et al.*, 2006; Deepa *et al.*, 2006; Carulli *et al.*, 2007; Galtrey *et al.*, 2008; Zimmermann and Dours-Zimmermann, 2008; Kwok *et al.*, 2011; Wang and Fawcett, 2012; Giamanco and Matthews, 2012). Tn-R has been established as an essential PNN molecule that has a proposed cross-linking role through the binding of CSPG G3 domains (Aspberg, 1995; Deepa *et al.*, 2006; Galtrey *et al.*, 2008; Suttikus *et al.*, 2014; Morawski *et al.*, 2014). Furthermore, other molecules are also known to interact with the PNN surface, including Otx2 and Sema3a (Beurdeley *et al.*, 2012; Dick *et al.*, 2013; Carulli *et al.*, 2013; de Winter *et al.*, 2016; Djerbal *et al.*, 2019). Recently, Sema3a has been observed to cross-link GAG surfaces, therefore has also been implicated in the cross-linking of the PNN surface (Djerbal *et al.*, 2019).

Many of the PNN-associated molecules show yet more molecular diversity. Each CSPG molecule in particular can be highly heterogenous in structure, due to alternative splicing of the core protein. This could occur during the synthesis of the molecule, or as a product of enzymatic cleavage by MMPs (Yamaguchi, 2000; Kiani *et al.*, 2002; M Morawski *et al.*, 2012). Additional heterogeneity of each CSPG can then be produced through the degree of

glycosylation of CS chains associated with the core protein. Although beyond the scope of this chapter, it is worth noting that further heterogeneity can be produced through differing the sulfation pattern of GAG chains, as these have been observed to be differentially regulated within PNNs as a function of age (Kitagawa *et al.*, 1997; Foscarin *et al.*, 2017). Therefore, a variety of molecular structures for each individual CSPG is possible yet has not been systematically analysed in the CNS.

Two multimeric variants of Tn-R have been observed in the CNS at different molecular weights (Woodworth *et al.*, 2002; Morawski *et al.*, 2014). The mechanism of Tn-R cross-linking of CSPG molecules has been proposed through the clustering of Tn-R molecules into dimeric and trimeric structures, therefore the degree of Tn-R clustering offers further potential heterogeneity (Yamaguchi, 2000). Each HAS molecule synthesises different lengths of HA, therefore further heterogeneity of PNN structure could be regulated through the size of the HA chains (Itano *et al.*, 1999). Thus, one would predict that a variety of PNN morphologies would be observed through the production of PNNs using different combinations of the PNN-associated molecules.

Numerous PNN structures have been observed using a combination of histochemical and imaging techniques (Arnst *et al.*, 2016; Ueno *et al.*, 2017b; Dzyubenko *et al.*, 2018; Sigal *et al.*, 2019). Specifically, two distinct morphological surface states have been observed that have been attributed to different maturation states: a punctate structure observed with greater frequency in the younger CNS, suggesting an immature PNN state; a reticular PNN structure observed in the adult CNS resembling the more commonly reported structure (Ueno *et al.*, 2017b; Richter *et al.*, 2018). It is unknown what changes occur to PNNs to cause the phase transition from the granular to the reticular state.

The key proposal of this chapter is that some of the structural heterogeneity of PNNs is at least partially caused by biochemically distinct compositions of PNN-associated molecules. Heterogeneity in biochemical composition has been previously observed (McRae *et al.*, 2007; Irvine and Kwok, 2018; Ueno *et al.*, 2018; Miyata *et al.*, 2018). Differences in the distribution of PNN-associated molecular components has also been observed throughout the CNS, however this has so far not been correlated specifically with changes to the structure of PNNs (Carulli *et al.*, 2006; Galtrey *et al.*, 2008; Bekku *et al.*, 2012). An established PNN marker is the lectin *Wisteria floribunda* agglutinin (WFA) that preferentially interacts with the GalNAc sugar moiety, a key component in CS chains (Kurokawa *et al.*, 1976; Härtig *et al.*, 1992; Seeger

et al., 1994). Recently, many independent observations have been made that WFA-negative PNNs exist, implying that there are biochemically distinct populations of PNNs (McRae *et al.*, 2007; Ueno *et al.*, 2017b; Yamada and Jinno, 2017; Irvine and Kwok, 2018; Ueno *et al.*, 2018; Miyata *et al.*, 2018).

The previous research referenced above has focussed on the use of histochemical and imaging techniques to analyse the biochemical composition of PNNs. Although useful for understanding the molecular distribution of PNN-associated molecules, a key limitation of the technique is its inability to distinguish between splice variants, molecular clusters, or differentially glycosylated molecules of the same species. Therefore, PNNs could have the same imaging profile yet have structurally distinct compositions. The aim of this chapter was to use Western blotting to profile these potential differences. As Western blotting differentiates molecules by molecular weight, splice variants and clustered molecules would migrate through the gel at different migration rates, so would therefore be distinguishable via this method. Furthermore, the degree of glycosylation would also be distinguishable, as the addition of GAG chains would also affect the migration rate of the molecules. To date, limited evidence using Western blotting has compared the relative abundance of each PNN-associated molecule within CNS regions. Deepa *et al.* (2006) have previously isolated and analysed PNN-specific material from whole brain samples using Western blotting, however a regional analysis was not conducted.

Four CNS regions were compared in this chapter to reflect the morphologically distinct PNN structures found throughout the CNS. As well as granular and reticular morphologies that have been observed to reflect PNN maturity, other morphologically distinct populations have been observed. Specifically, PNNs in the cortex, hippocampus, cerebellum and spinal cord have been particularly well characterised using histochemistry and fluorescent microscopy techniques (Brückner *et al.*, 1996; Carulli *et al.*, 2006; Deepa *et al.*, 2006; Gert Brückner *et al.*, 2006; Carulli *et al.*, 2007; Galtrey and Fawcett, 2007; Ueno *et al.*, 2017b; Yamada and Jinno, 2017). When comparing images of PNNs analysed in the spinal cord and cerebellum they have distinct morphological features in contrast to images analysed in the cortex and hippocampus, as discussed in section 1.5.3. Cerebellar and spinal cord PNNs only form around the soma of neurons and appear to form a thicker surface layer, in comparison to cortical and hippocampal PNNs that form around the soma and proximal dendrites and appear to have a thinner morphology. It has not yet been

established what biochemical differences in PNNs in these regions may cause these distinct morphological phenotypes.

Differences in the distribution of PNN-associated molecular components have been observed independently via researchers focussing specifically on one of the molecular component or one distinct CNS region (Carulli *et al.*, 2006; Galtrey *et al.*, 2008; Bekku *et al.*, 2012). It is difficult however to directly compare this research through the composition of a meta-analysis due to variations in the rodent models and the age of the animals used. Currently no systematic analysis investigating the distribution of the PNN-associated molecules throughout the CNS, alongside the distribution of their potential splice variants has been performed. The aim of this chapter was to conduct this analysis to highlight insights into the potential molecular heterogeneity that may be present in PNNs in different CNS regions that may partially reflect the different morphological phenotypes.

3.2 Methodology

3.2.1 SDS-PAGE and Western blotting

A comprehensive description of the methodologies for the brain lysate preparation, SDS-PAGE and Western blotting can be found in section 2.1. Section 2.1 also contains a list of antibodies used.

3.2.2 Acan samples

Bovine articular cartilage Acan (Sigma: A1960) was dissolved in PBS buffer to 1 mg/mL. Acan isolated from pig laryngeal cartilage in general lacks a G3 domain and was kindly provided by John Sheehan (University of North Carolina, USA). Both bovine articular cartilage and pig laryngeal cartilage were used as a comparison to aid the characterisation of CNS Acan isolated from CNS tissue lysate.

3.2.3 ChABC incubation

60 µg of protein from cervical spinal cord (cSC) samples, and 10 µg of bovine articular cartilage ACAN and glycosylated Acan without a G3 domain were incubated O/N at 37°C with 1 U/mL ChABC in TBS (20 mM Tris base, 130 mM NaCl₂, pH 8.0) that also contained 0.05 M sodium acetate to activate the enzyme ChABC. The next day 10 µg sample per lane was then loaded into a 4-15% tris-glycine gel.

3.3 Results

Specifically, the PNN-associated molecules that were targeted in this analysis included, HA, HapIn1 and HapIn4, as they have previously been observed to be crucial in PNN formation (Deepa *et al.*, 2006; Carulli *et al.*, 2007; Zimmermann and Dours-Zimmermann, 2008; Carulli *et al.*, 2010; Kwok *et al.*, 2010; Kwok *et al.*, 2011; Wang and Fawcett, 2012; Giamanco and Matthews, 2012). HapIn2 was not included because an effective antibody to detect the molecule in Western blots is currently lacking. HapIn3 was not analysed as it is not expressed in the CNS (Ogawa *et al.*, 2004). The lecticans (Acan, Bcan, Ncan, Vcan) and the CSPG Pcan were also targeted as they are known to be prominent binding partners of HA and have been observed to contribute to the PNN structure (Ruoslahti, 1996; Yamaguchi, 2000; Bandtlow and Zimmermann, 2000; Rauch *et al.*, 2004; Carulli *et al.*, 2006; Deepa *et al.*, 2006; Galtrey *et al.*, 2008; Zimmermann and Dours-Zimmermann, 2008; Kwok *et al.*, 2011; Wang and Fawcett, 2012; Giamanco and Matthews, 2012). Tn-R was targeted as it has been previously characterised as associating with PNNs and has been implicated in a cross-linking role in the stabilisation and formation of PNNs (Aspberg, 1995; Lundell *et al.*, 2004; Morawski *et al.*, 2014).

3.3.1 Acan: multiple distinct molecular species of Acan are present in the CNS

Acan is the most prominent and well characterised member of the lecticans, co-localising widely with the PNN binding lectin WFA to such a degree that Acan has been suggested as being a marker for PNNs in the ventral spinal cord (Ueno *et al.*, 2017b; Irvine and Kwok, 2018). The size of Acan can be affected by the enzymatic cleavage by MMPs, as well as by the number of GAG chains attached to the core protein (Kiani *et al.*, 2002; M Morawski *et al.*, 2012). The aim was to determine the relative abundance of these Acan species in the CNS regions of the cortex, hippocampus cerebellum and cSC.

When comparing the total amount of Acan in each region, there was significantly higher levels of Acan present in the cSC in comparison with the cortical and cerebellar regions ($p \leq 0.005$ and $p \leq 0.05$ respectively), with it trending towards significance in the hippocampus ($p = 0.091$; Figure 7). Between the cortical, cerebellar and hippocampal regions there were no significant differences observed. However, the relative abundance of the spliced variants of Acan were unique in each CNS regions, as multiple bands

of different molecular weights were present in each lane. Therefore, three specific molecular weight ranges were defined to analyse the distribution of Acan species further. Acan species ≥ 250 kDa reflected relatively full-length Acan with varying degrees of glycosylation, as the molecular weight of Acan core protein is ~ 250 kDa (Kiani *et al.*, 2002). The differing degree of glycosylation of the Acan core protein is responsible for the smearing effect observed at this size range, which will be discussed in section 3.3.1.1. Furthermore, section 3.3.1.1 will address the possibility that there is an Acan fraction that is too large to enter the gel. Acan species between 100 – 250 kDa reflected both the less glycosylated and enzymatically cleaved forms of the core protein as bands were present in this size region as opposed to a smear. An Acan species at ~ 45 kDa suggested an unglycosylated, highly truncated core protein of Acan. Previously, Mort *et al* (2016) observed Acan species between these size ranges when Acan was cleaved by MMPs in osteoarthritic cartilage.

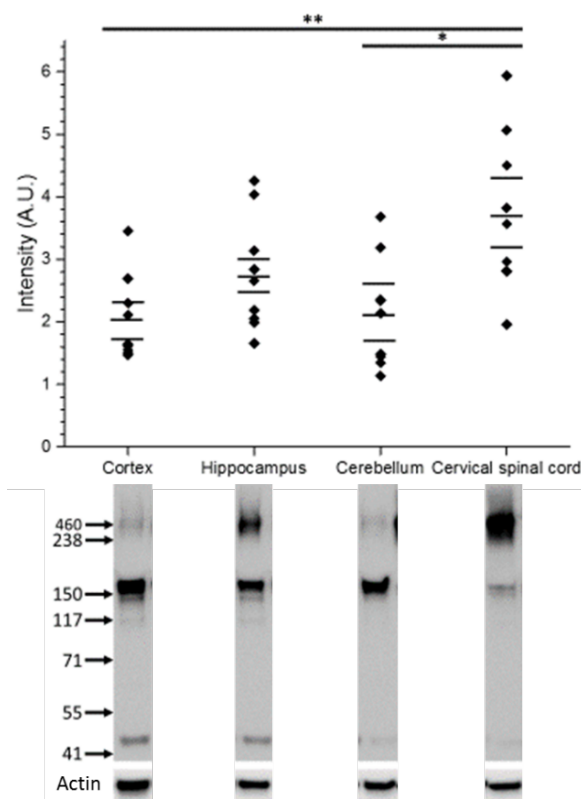


Figure 7. The total amount of Acan was higher in the cSC, in comparison with the brain regions.

Densitometry results alongside a representative Western blot image for Acan in each CNS region. Actin was used as a control for the amount of protein loaded and used to standardise the densitometry results. The lines within the graph represent the mean and standard deviation ($n = 3$). Each sample was ran in triplicate. The lines above the graph represent statistical significance: $p \leq 0.05$ (*), $p \leq 0.005$ (**).

There were significantly higher levels of Acan species ≥ 250 kDa in the cSC in comparison with the other 3 regions (Figure 8A). This implies that less post-translational modification of Acan species occurs in the cSC in comparison to the brain regions. This is further supported when comparing Acan species between 100 – 250 kDa, as although not statistically significant there was a trend suggesting less Acan species were present at this size range in comparison with the cortical, hippocampal and cerebellar regions (Figure 8B). For the Acan species at ~ 45 kDa there were no significant differences found between any of the CNS regions, however this may reflect the comparatively small amounts of these Acan species present in the tissue lysate in contrast to the other size ranges. Although not significant, there was a trend suggesting a larger amount of Acan species at ~ 45 kDa were present in the cortical and hippocampal regions in comparison with the cerebellar and cSC regions (Figure 8C).

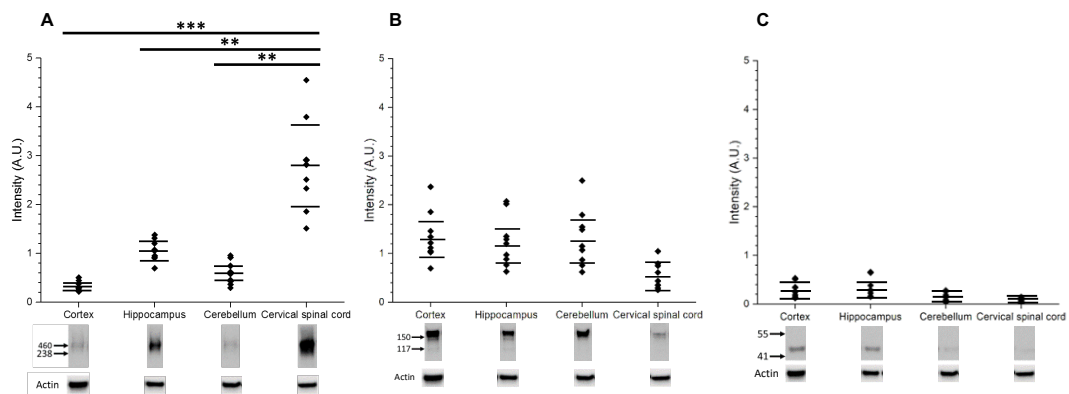


Figure 8. Densitometry comparison of the different Acan species in each CNS region demonstrated the heterogeneity in the distribution of Acan species between the different CNS regions.

Densitometry results alongside a representative Western blot image for Acan in each CNS region. All graphs are presented using the same scale to aid comparisons between the different Acan species. **A** Acan ≥ 250 kDa comparison. **B** Acan 100 – 250 kDa comparison. **C** ~ 45 kDa Acan comparison. For all results Actin was used as a control for amount of protein loaded and used to standardise the densitometry results. The lines within the graph represent the mean and standard deviation (n = 3). Each sample was ran in triplicate. The lines above the graph represent statistical significance: p ≤ 0.005 (**), p ≤ 0.0005 (***)

To further analyse the Acan distribution, Acan species within each specific CNS region were also compared. This was achieved by comparing the values presented in Figure 8A, B and C for each specific CNS region, which is why the 3 plots are presented on the same scale.

Within the cortical region there was significantly more Acan species between 100 – 250 kDa in comparison to Acan species at ~ 45 kDa and ≥ 250 kDa ($p \leq 0.05$ and $p \leq 0.05$ respectively). There was no trend observed between Acan species at ~ 45 kDa and ≥ 250 kDa. Therefore, the less glycosylated, enzymatically cleaved Acan species was most abundant in the cortical region.

A similar distribution was observed in Acan species in the cerebellum, a less glycosylated, enzymatically cleaved Acan species was also found to be the most abundant. There was significantly more Acan species between 100 – 250 kDa compared with Acan species at ~ 45 kDa ($p \leq 0.05$). Although not significant, there was trend towards more Acan species being present in comparison to Acan species ≥ 250 kDa ($p = 0.093$), yet there was no trend observed between Acan species at ~ 45 kDa and ≥ 250 kDa.

Within the hippocampus, there were significantly less Acan species at ~ 45 kDa Acan in comparison with Acan species between 100 – 250 kDa ($p \leq 0.05$). There was also a trend, though not significant of less Acan species at ~ 45 kDa in comparison with Acan species ≥ 250 kDa ($p = 0.099$). There was no statistical difference found between Acan species between 100 – 250 kDa and Acan species ≥ 250 kDa ($p = 0.775$). Therefore, in the hippocampal region there was relatively similar levels of Acan species that were full length to species that were enzymatically cleaved, though fewer highly truncated Acan species were observed.

Within the cSC there was significantly more Acan species ≥ 250 kDa in comparison to Acan species between ~ 45 kDa and 100 – 250 kDa ($p \leq 0.005$ and $p \leq 0.005$ respectively). No trend was observed between Acan species between ~ 45 kDa and 100 – 250 kDa. Therefore, in the cSC region full-length, glycosylated Acan species were the most abundant.

3.3.1.1 Acan in the CNS is less glycosylated than Acan found in cartilage

As Acan species in the cSC were observed to be the most glycosylated, Acan species in this region were further investigated to observe the degree of glycosylation observed when compared with Acan outside the CNS. Bovine articular cartilage and Acan from pig larynx were used for comparison. They were selected as Acan species in cartilage are known to be highly glycosylated and pig laryngeal Acan is highly glycosylated though in general lacks a G3 domain (Kiani *et al.*, 2002). To determine the degree of glycosylation a less glycosylated control was prepared for each sample by

incubating the samples with ChABC to enzymatically cleave the CS sidechains (Figure 9).

Acan species were not observed in the untreated samples of bovine articular cartilage and the pig larynx, while a smear of 200 – 500 kDa was observed in cSC sample. After ChABC treatment, a smear of 250 – 500 kDa was observed in the bovine articular cartilage sample and a smear of 200 – 500 kDa was observed in the pig laryngeal sample, suggesting that the native untreated samples were too large to migrate into the 4-12% polyacrylamide gel. The smearing also indicated that only a partial digestion of the CS sidechains was achieved for these samples. This suggested that untreated Acan species found in bovine articular cartilage and the pig laryngeal Acan were too large to migrate into the 4-12% polyacrylamide gel and this was caused by the degree of glycosylation of the core protein. In contrast the majority of untreated cSC Acan species was able to penetrate into the gel, suggesting that the Acan species are comparatively less glycosylated in the cSC. When the cSC Acan species were treated with ChABC the smear migrated further down the gel to ~200 kDa, implying that the core proteins were partially glycosylated. Similar to bovine articular cartilage and pig laryngeal Acan, an overnight ChABC treatment did not seem to be sufficient in digesting all CS chains and therefore did not reduce the samples to single neat bands.

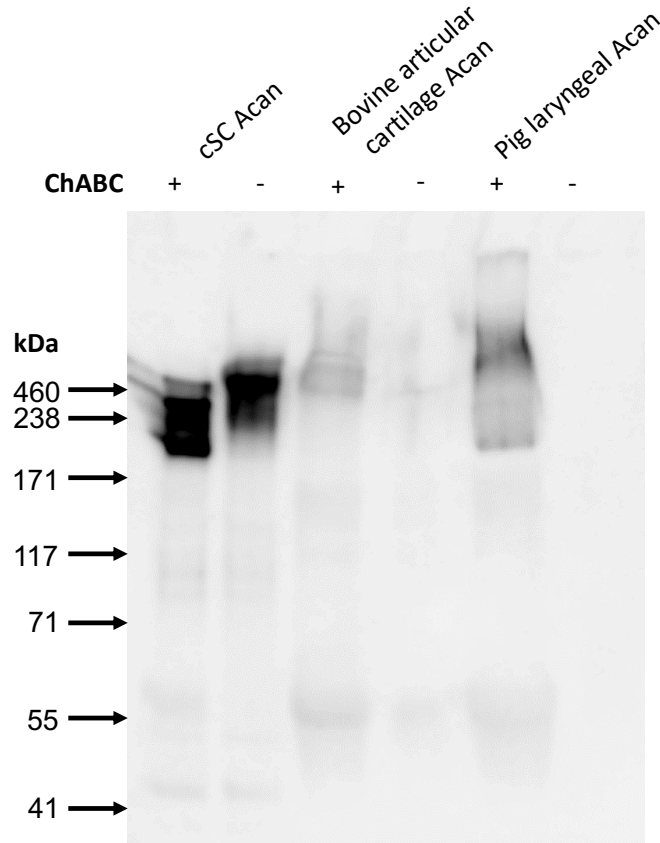


Figure 9. Comparison of Acan species.

Acan from cSC tissue lysate (rat SD2) was compared with bovine articular cartilage and pig laryngeal Acan that was either ChABC (+) or untreated (-).

3.3.2 Pcan: glycosylated Pcan was most prevalent in the cerebellar region

Pcan has been observed in PNNs and is able to interact with Tn-R in a calcium-dependent manner (Xiao *et al.*, 1997; Carulli *et al.*, 2006; Deepa *et al.*, 2006; Galtrey *et al.*, 2008). The core protein can be alternatively spliced, therefore core proteins of multiple molecular weights can be produced. The aim was to characterise the relative abundance of these Pcan species in the four CNS regions.

Pcan is significantly more prevalent in the cerebellum in comparison with the cSC ($p \leq 0.0005$), cortex ($p \leq 0.0005$) and hippocampus ($p \leq 0.05$; Figure 10). There was also significantly more Pcan present in the hippocampus in comparison with the cSC ($p \leq 0.005$). Comparatively, there was less Pcan present in the cSC in contrast to the other CNS regions. In all regions smearing was present above 460 kDa, which is larger than the size of the unglycosylated ~ 173 kDa core protein (Maurel *et al.*, 1994). The smearing is therefore likely to be a consequence of the variation in the degree of

glycosylation of the Pcan species. It is worth noting the absence of Pcan at lower molecular weights, suggesting no enzymatic cleavage has occurred to the core protein and that Pcan species remain glycosylated throughout the CNS.

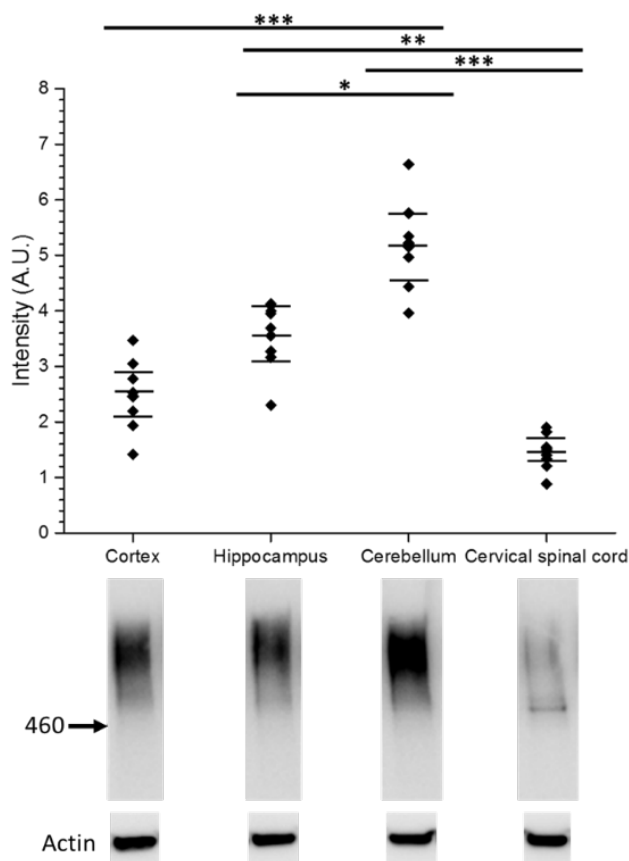


Figure 10. Comparison of Pcan abundance between CNS regions.

Densitometry results alongside a representative Western blot image for Pcan in each CNS region. Actin was used as a control for the amount of protein loaded and used to standardise the densitometry results. The lines within the graph represent the mean and standard deviation ($n = 3$). Each sample was ran in triplicate. The lines above the graph represent statistical significance: $p \leq 0.05$ (*), $p \leq 0.005$ (**), $p \leq 0.0005$ (***)

3.3.3 Bcan: species of Bcan are differentially distributed throughout the CNS

Bcan is a nervous-system specific lectican that is known to co-localise with PNNs in the CNS (Yamaguchi, 2000; Carulli *et al.*, 2006; Deepa *et al.*, 2006; Galtrey *et al.*, 2008). It has the shortest core protein central domain of the lecticans measuring ~ 145 kDa, therefore is also proposed to have the least CS chains attached to it, with a significant portion of Bcan existing without any CS chains (Yamada *et al.*, 1994; Yamaguchi, 1996; Yamaguchi, 2000). Bcan is known to be alternatively spliced, as there is a GPI – anchored form of Bcan

that is the only known example of a membrane-bound lectican (Seidenbecher *et al.*, 1995). The aim was to characterise the relative abundance of these Bcan species in the four CNS regions.

Although there were no statistical differences in Bcan amounts between any of the CNS regions there were differences in the Bcan species observed (Figure 11). In the cortex and hippocampus there was a trend of increased Bcan species between 145 kDa and 460 kDa in comparison with the cerebellum and cSC (Figure 12A). Smearing was not observed in the cerebellum and cSC, with only a band observed at ~145 kDa that corresponds with the molecular weight of the unglycosylated full-length Bcan (Yamada *et al.*, 1994). In contrast smearing was observed in the cortical and hippocampal regions, suggesting Bcan in these regions were more glycosylated. In the cSC there was a trend observed of an increased level of a ~ 50 kDa Bcan species that was present in lower amounts in the other CNS regions (Figure 12B). Interestingly, this specific size has previously been characterised as a product of enzymatic cleavage by MMPs (Matthews *et al.*, 2000). It is also worth noting that an 80 kDa splice variant of Bcan that has previously been observed in the CNS was not observed at detectable levels in these CNS regions (Yamada *et al.*, 1994).

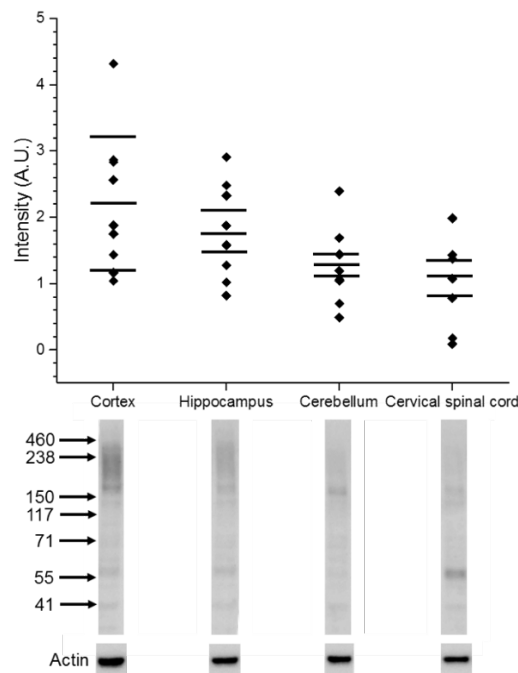


Figure 11. Comparison of Bcan abundance between CNS regions.

Densitometry results alongside a representative Western blot image for Bcan in each CNS region. Actin was used as a control for the amount of protein loaded and used to standardise the densitometry results. The lines within the graph represent the mean and standard deviation ($n = 3$). Each sample was ran in triplicate.

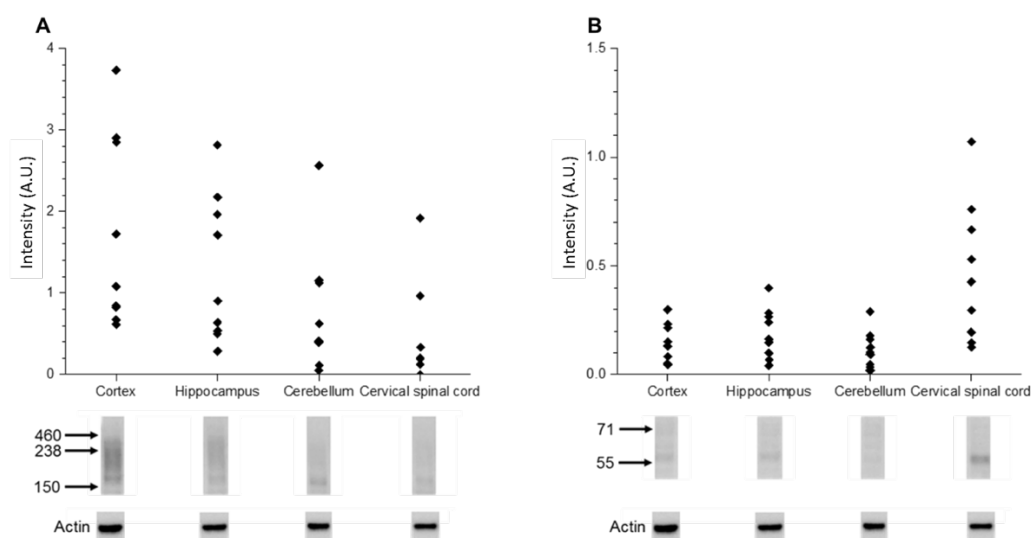


Figure 12. Comparisons of specific Bcan species between the different regions of the CNS.

Densitometry results alongside a representative Western blot image for Bcan in each CNS region. **A** Bcan species between 145 kDa and 460 kDa were compared. **B** Bcan fragment size ~50 kDa were compared.

3.3.4 Vcan: no differences in Vcan abundance throughout the CNS

Vcan is a lectican that is known to associate with PNN structures in the CNS (Carulli *et al.*, 2006; Deepa *et al.*, 2006; Galtrey *et al.*, 2008). The unglycosylated full-length core protein is ~ 360 kDa, however it is known to have many splice variants therefore there is a diversity of potential Vcan species (Ito *et al.*, 1995; Zako *et al.*, 1995; Yamaguchi, 2000). The aim was to characterise the relative abundance of these Vcan species in the four CNS regions.

Bands of Vcan species were observed at ~ 360 kDa, ~ 200 kDa, ~ 160 kDa and ~ 40 kDa, which suggests a diverse range of core protein sizes in each CNS region (Figure 13). When compared to previous studies these sizes are comparable to the 2 isoforms (V0 and V1) that are found >350 kDa and the isoform V2 that is found ~ 200 kDa (Foulcer *et al.*, 2015). The band at ~ 40 kDa may be the cleaved N-terminal fragment of V1 (Sandy *et al.*, 2001; McCulloch *et al.*, 2009). There was no trend observed in the total abundance of Vcan present in each CNS region, as all displayed similar Vcan levels. Smearing was not observed in any of the CNS regions, indicating that Vcan may be relatively unglycosylated in these regions.

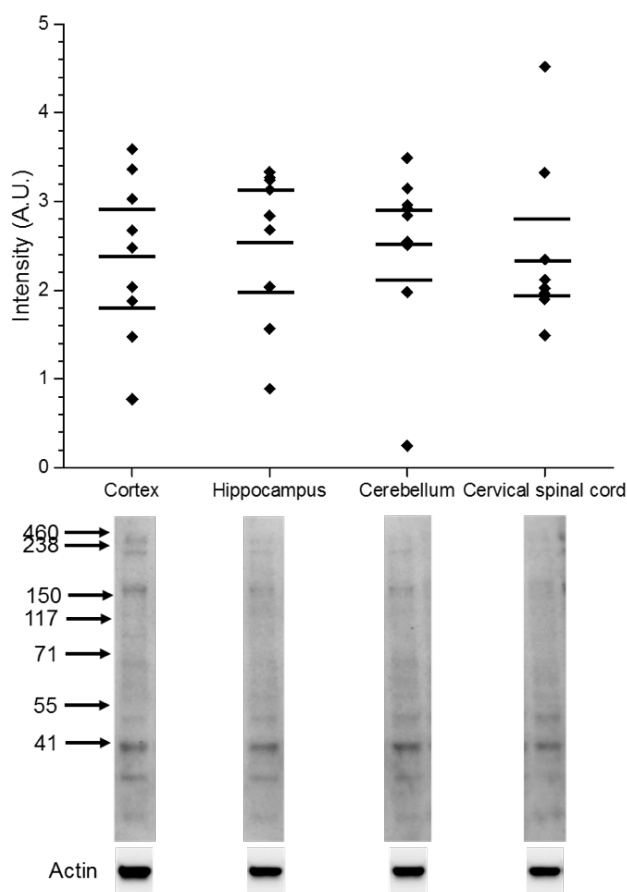


Figure 13. Comparison of Vcan abundance between CNS regions.

Densitometry results alongside a representative Western blot image for Vcan in each CNS region. Actin was used as a control for the amount of protein loaded and used to standardise the densitometry results. The lines within the graph represent the mean and standard deviation ($n = 3$). Each sample was ran in triplicate.

3.3.5 Ncan: glycosylated Ncan is most prevalent in the cortical region

Ncan is also a nervous-system specific lectican that is known to co-localise with PNNs in the CNS (Rauch *et al.*, 1992; Yamaguchi, 2000; Carulli *et al.*, 2006; Deepa *et al.*, 2006; Galtrey *et al.*, 2008). Full-length unglycosylated Ncan in the adult rat brain has a core protein ~ 245 kDa and has been observed to average 3 CS chains per core protein making the glycosylated Ncan species ~ 300 kDa in total size (Rauch *et al.*, 1991). Ncan also has splice variants of approximately ~ 150 kDa and ~ 180 kDa that have previously been characterised (Rauch *et al.*, 1991). The aim was to characterise the relative abundance of Ncan species in the four CNS regions.

Ncan species were observed as a smear between 150 – 300 kDa (Figure 14), suggesting a combination of glycosylated full-length and truncated Ncan were present. The size of the smear also suggests that Ncan in these regions may have more than 3 CS chains, making them more glycosylated than has

previously been reported (Rauch *et al.*, 1991). Ncan was most prevalent in the cortical region, in comparison with hippocampal, cerebellar and cSC regions ($p \leq 0.005$). There was no trend observed between the other regions, as they all had similar levels of Ncan present. A band at ~ 100 kDa in the cerebellar and cSC regions was observed that was not detected in the cortex and hippocampus, suggesting a particularly unglycosylated enzymatically cleaved species of the Ncan core protein was present in these regions.

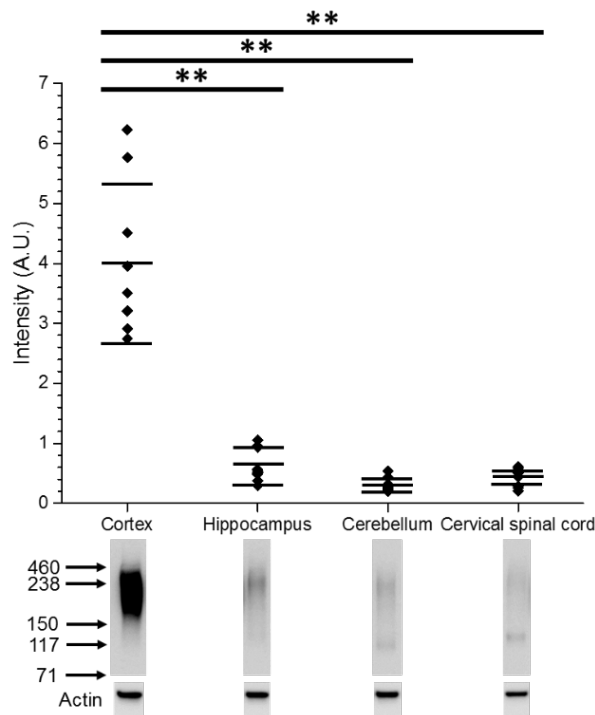


Figure 14. Comparison of Ncan abundance between CNS regions.

Densitometry results alongside a representative Western blot image for Ncan in each CNS region. Actin was used as a control for the amount of protein loaded and used to standardise the densitometry results. The lines within the graph represent the mean and standard deviation ($n = 3$). Each sample was ran in triplicate. The lines above the graph represent statistical significance: $p \leq 0.005$ (**).

3.3.6 Hapln1 is most abundant in the cortical region

Hapln1 is a 45 kDa protein that has been observed to co-localise with PNN markers in the CNS and is an essential component of the PNN structure (Carulli *et al.*, 2006; Deepa *et al.*, 2006; Galtrey *et al.*, 2008; Carulli *et al.*, 2010; Kwok *et al.*, 2010). The removal of Hapln1 was enough to cause the attenuation of PNN structures in the brain (Carulli *et al.*, 2010; Romberg *et al.*, 2013). The aim was to characterise the abundance of Hapln1 in the four CNS regions.

Only one band at 45 kDa was observed in all CNS regions (Figure 15). There was significantly more Hapln1 present in the cortical region in comparison with the hippocampal, cerebellar and cSC regions ($p \leq 0.0005$, $p \leq 0.0005$, $p \leq 0.005$, respectively). A trend suggested that Hapln1 was least abundant in the hippocampal region, though this trend was only significant when compared with the cSC ($p \leq 0.005$) and cortical regions.

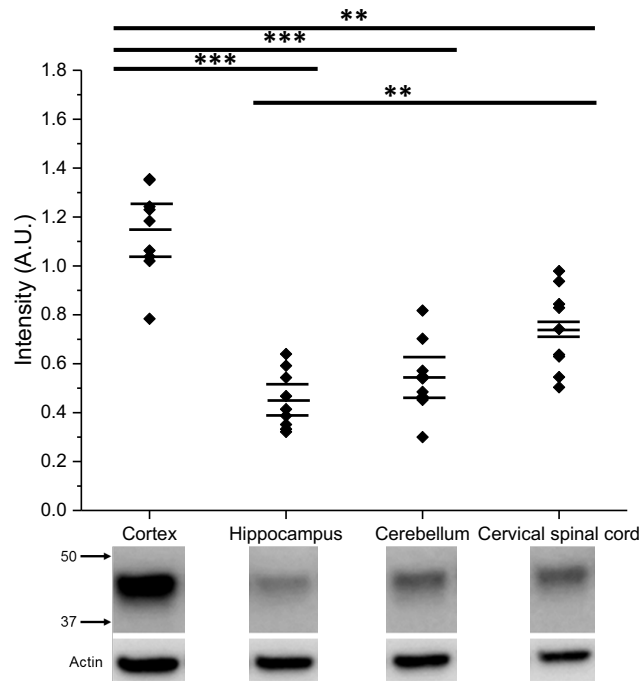


Figure 15. Hapln1 is most abundant in cortical lysate, in comparison with the other CNS regions observed by Western blot.

Densitometry results alongside a representative Western blot image for Hapln1 in each CNS region. Actin was used as a control for the amount of protein loaded and used to standardise the densitometry results. The lines within the graph represent the mean and standard deviation ($n = 3$). Each sample was ran in triplicate. The lines above the graph represent statistical significance: $p \leq 0.05$ (*), $p \leq 0.005$ (**), $p \leq 0.0005$ (***).

3.3.7 Hapln4 distribution was different to the distribution of Hapln1

Hapln4 is also a 45 kDa protein that has been established as an important PNN molecule, especially in the formation and function of PNNs in cerebellum and brainstem (Bekku *et al.*, 2012; Edamatsu *et al.*, 2018). The aim was to characterise the abundance of Hapln4 in the four CNS regions.

Only one band at 45 kDa was observed in all CNS regions, with all regions observed to contain approximately equal amounts of Hapln4 (Figure 16). As the staining was not strong, it is difficult to assess if any differences in the relative abundance of Hapln4 is present between the regions. However, when

the distribution pattern of Hapln4 was compared with the distribution pattern of Hapln1, it was clear that they are distinctively different, as Hapln4 is not significantly upregulated in any one of the CNS regions analysed.

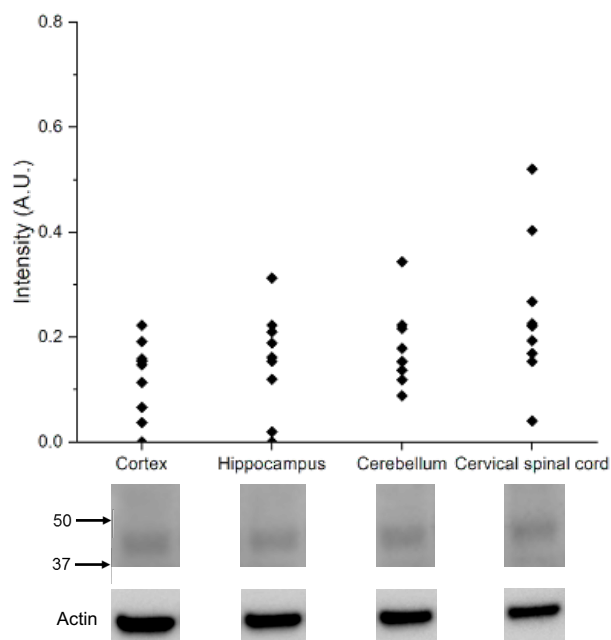


Figure 16. Comparison of Hapln4 abundance between CNS regions.

Densitometry results alongside a representative Western blot image for Hapln4 in each CNS region. Actin was used as a control for the amount of protein loaded and used to standardise the densitometry results. The lines within the graph represent the mean and standard deviation ($n = 3$). Each sample was ran in triplicate.

3.3.8 Tn-R: no differences in Tn-R abundance throughout the CNS

Tn-R is specific to the CNS where it has been observed to associate with PNNs through the cross-linking of CSPGs (Aspberg, 1995; Lundell *et al.*, 2004; Morawski *et al.*, 2014). Two isoforms have been characterised at 160 kDa and 180 kDa, however Tn-R molecules can interact with each other to form dimeric and trimeric Tn-R structures (Chiquet-Ehrismann and Tucker, 2011; Morawski *et al.*, 2014). The aim was to characterise the abundance of Tn-R in the four CNS regions.

Multiple bands of Tn-R were observed in all CNS regions ranging from ~ 160 kDa to molecular weights much greater than (\gg) 460 kDa with the total abundance of Tn-R found to be similar in all regions (Figure 17). Four distinct size ranges were observed in all CNS regions that reflect the different aggregates of Tn-R that were formed: monomeric Tn-R between 160 – 180 kDa, dimeric Tn-R between 320 – 360 kDa, trimeric Tn-R between 480 – 540

kDa and large aggregates of Tn-R \gg 460 kDa. This was slightly unexpected as the samples were ran in reducing conditions, therefore the aggregates would have been expected to disassociate into their monomeric Tn-R subunits of either 160 or 180 kDa, as has been observed previously (Aspberg, 1995; Aspberg *et al.*, 1997). The results reported here were similar to observations by Woodworth *et al* (2002) where dimeric and trimeric aggregates were found after heat treating tissue lysate and using SDS-PAGE gel. Potentially, in this experiment the percentage of 2-mercaptoethanol (2.5% v/v) was not sufficient to efficiently dissociate the aggregates. This may also explain why a band \gg 460 kDa is observed, as it may resemble an aggregated Tn-R species that is forming a complex with CSPGs, though this is only a suggestion.

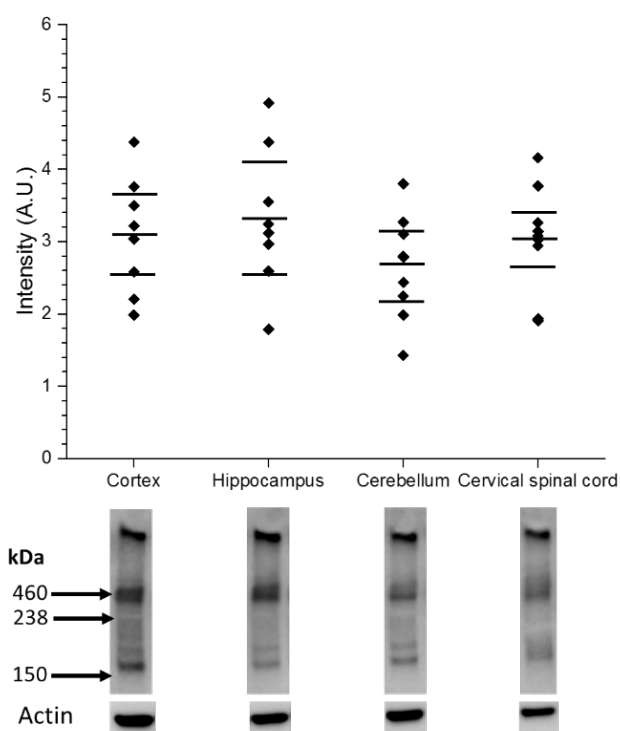


Figure 17. Comparison of Tn-R abundance between CNS regions.

Densitometry results alongside a representative Western blot image for Tn-R in each CNS region. Actin was used as a control for the amount of protein loaded and used to standardise the densitometry results. The lines within the graph represent the mean and standard deviation ($n = 3$). Each sample was ran in triplicate.

3.3.9 HA: Lack of smearing suggests HA is observed at discrete sizes throughout the CNS regions

HA is a non-sulfated GAG that is essential for the formation of PNNs. HA molecular weight ($M_{w,GAG}$) has the potential to be highly heterogeneous, as HA chains synthesised by HAS enzymes have been characterised between 100 kDa to 2 MDA (Itano *et al.*, 1999). Furthermore, both hyaluronidases and

chondroitinases can enzymatically cleave HA chains to vary the size distribution further (Stern, 2004; Stern and Jedrzejewski, 2006). Therefore, the expectation was that large smears would be present in each of the 4 CNS regions, reflecting the heterogeneity $M_{w,GAG}$.

It is important to note that in this analysis HA chains were being compared with the molecular weight of protein standards ($M_{w,protein}$). As the migration rate between GAG chains and proteins would not be expected to be equal $M_{w,GAG}$ could not be identified without first characterising the relationship between $M_{w,protein}$ and $M_{w,GAG}$ migration rates. In chapter 5 this relationship is quantitatively described at a ratio of 1 kDa ($M_{w,GAG}$): 1.7 ± 0.1 kDa ($M_{w,protein}$). For this reason the results will be reported using $M_{w,protein}$ and $M_{w,GAG}$ values for clarity.

In all CNS regions smearing was not observed, as 4 distinct HA bands were observed at: $M_{w,protein} \sim 65$ kDa, ~ 120 kDa, ~ 500 kDa and $\gg 460$ kDa (Figure 18). The relative abundance of total HA was significantly higher in the cSC region in comparison with cortical ($p \leq 0.005$), hippocampal ($p \leq 0.05$) and cerebellar ($p \leq 0.005$) regions. When the distinct HA size bands were compared, the cSC region had significantly more HA at $M_{w,protein} \sim 500$ kDa and $M_{w,protein} \gg 460$ kDa in comparison with the cortical, hippocampal and cerebellar regions (Figure 19). Furthermore, for $M_{w,protein} \gg 460$ kDa HA it was least abundant in the cerebellar region that was significantly different when compared with the hippocampal and cSC regions (Figure 19A). For $M_{w,protein} \sim 120$ kDa HA there was a trend suggesting HA was least abundant in the cortical region, though this trend was only significant when compared with the cSC region (Figure 19C). No differences were found between the CNS regions for $M_{w,protein} \sim 65$ kDa HA.

The lack of smearing was unexpected as it implies that HA within the CNS is produced at specific sizes. For $M_{w,protein} \gg 460$ kDa it is possible that there is a large range of potential HA chains within the band that cannot be discriminated due to insufficient power in separation of high molecular weight species using 4-20% polyacrylamide gel. Therefore, it is not the gel system that cannot resolve the bands, but the percentage of the gel used which limited separation due to insufficiently large pore sizes. To discriminate these larger HA bands in future work the use of agarose gels may be more appropriate. Similar phenomenon of defined HA sizes has also been observed previously with our project student (Figure 20). Separation of GAGs isolated from rat brain and nasal cartilage showed that HA bands were present specifically in brain samples. HA bands of ~ 65 kDa and ~ 120 kDa were observed in brain,

while these are absent in the nasal cartilage. The lack of bands or a smear in nasal cartilage sample is likely due to the retention of large HA species stuck in the well. Therefore, the presence of specific HA bands may be a feature specific to the CNS. In addition, the appearance of bands suggests that the HA may still be associating with HA binding molecules. To test this hypothesis in future work the experiment could be ran again with the samples first being pre-treated with proteases to remove proteins from the sample. Furthermore, ChABC treatment had no effect on the HA band sizes of the brain lysate samples. The absence of HA between under 400 kDa in the nasal cartilage samples suggested that the HA was too large to migrate into the polyacrylamide gel. It is important to note that the results may also be caused by non-specific binding of the HA marker HABP, as the bands at ~ 65 kDa and ~ 120 kDa were not removed by ChABC treatment, which suggested that they were not HA fragments. Further experiments will be required to confirm the identity of HA in the CNS (Clark *et al.*, 2011; Yuan *et al.*, 2015).

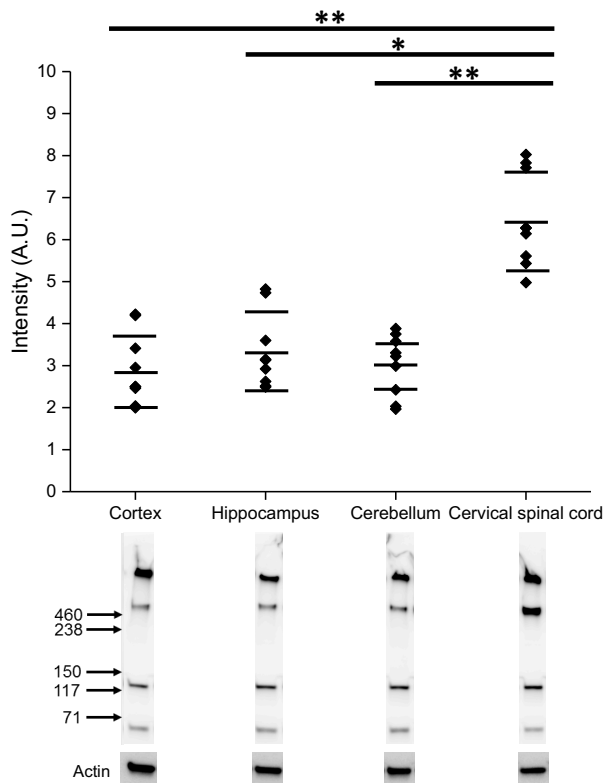


Figure 18. Comparison of HA amounts in CNS regions.

Densitometry results alongside a representative Western blot image for HA in each CNS region. Actin was ran as a control for amount of protein loaded, and used to standardise the densitometry results. The lines within the graph represent the mean and standard deviation (n =3). Each sample was ran in triplicate. The lines above the graph represent statistical significance: $p \leq 0.05$ (*), $p \leq 0.005$ (**).

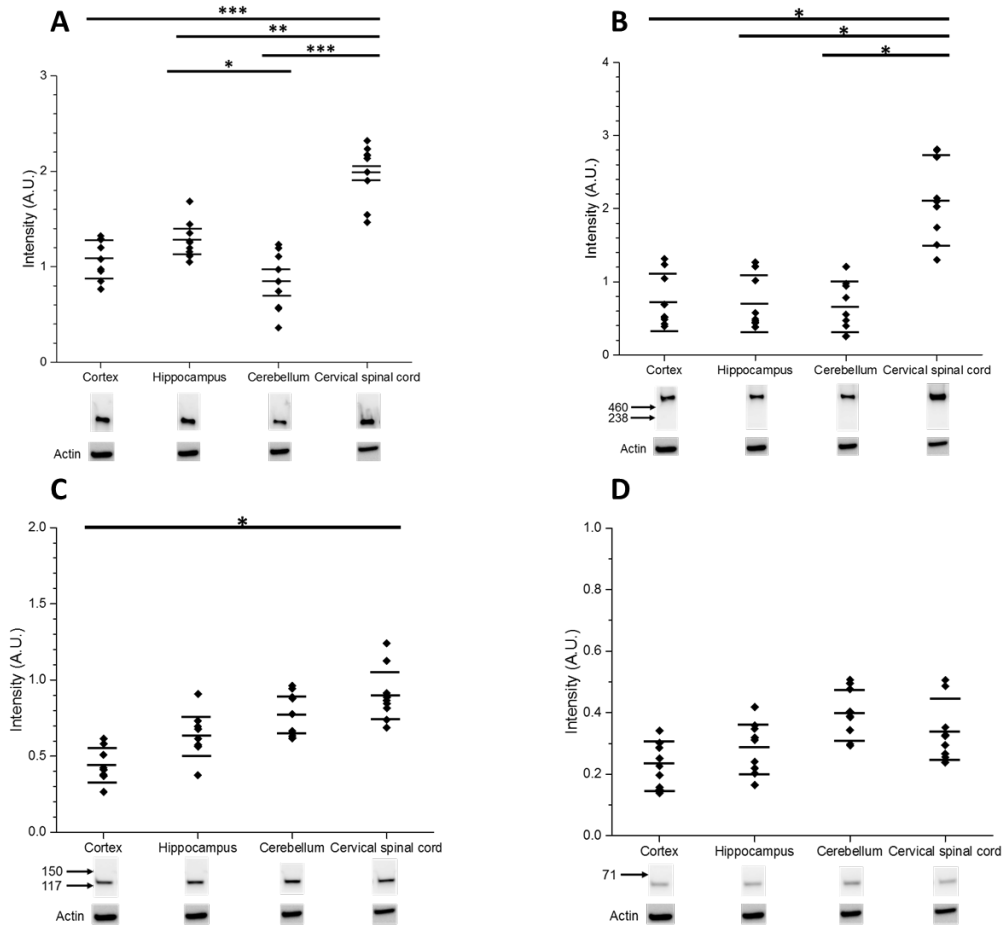


Figure 19. Densitometry comparison of the different HA sizes demonstrates the heterogeneity of HA throughout the CNS.

Densitometry results alongside a representative Western blot image for HA in each CNS region. **A** HA >> 460 kDa at the top of the gel. **B** HA band ~ 500 kDa **C** HA band ~ 120 kDa. **D** HA band ~ 65 kDa. For all results Actin was run as a control for amount of protein loaded and used to standardise the densitometry results. The lines within the graph represent the mean and Standard deviation (n=3). Each sample was ran in triplicate. The lines above the graph represent statistical significance: $p \leq 0.05$ (*), $p \leq 0.005$ (**), $p \leq 0.0005$ (***)

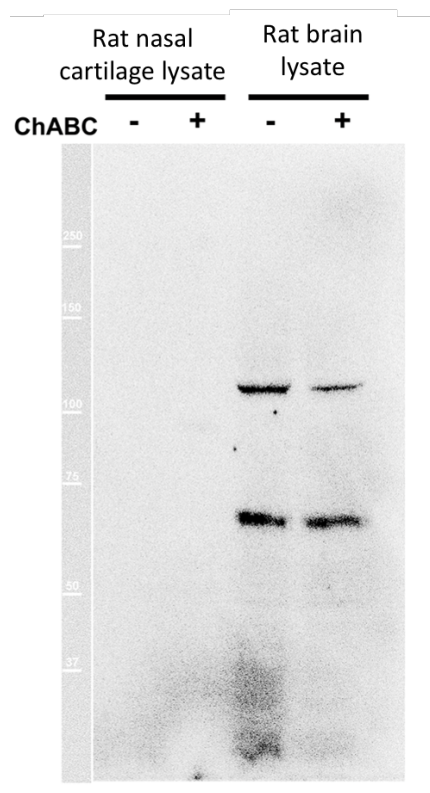


Figure 20. Comparison of rat nasal cartilage HA with brain lysate HA indicated that lower molecular weight HA species are brain specific. CNS.

Western blot image of rat nasal cartilage and brain lysate that has been incubated (40 mU overnight) with (+) and without (-) ChABC. Only HA species below 400 kDa were interrogated in this analysis using HABP as the probe for HA. No difference in band sizes were observed between rat brain lysate samples that were incubated with and without ChABC. Rat nasal cartilage lysate was absent of HA bands below 400 kDa. This image is courtesy of Emma Sewart supervised by Jessica Kwok at the University of Cambridge.

3.3.10 Summary of Western blot results

The results of the Western blot analysis were summarised into a single table to allow for an easier comparison of the distribution molecules present in each CNS region (Table 3). Although direct comparisons between the PNN-associated molecules was not possible due to the differing binding affinities of the antibodies used, the relative abundance of each molecule throughout the different CNS regions could be compared.

In the cSC region the relative abundance of ≥ 250 kDa Acan, and Hapln1 and was higher. The relative abundance of Pcan, 100 – 250 kDa Acan and Hapln1 was higher in the cerebellar region. In the hippocampus species of Acan ≥ 250 kDa and between 100 – 250 kDa were comparatively more abundant, alongside an increased abundance of Pcan. The cortical region a comparatively increased abundance of Acan species between 100 – 250 kDa, Pcan, Bcan, Ncan and Hapln1. In all regions the relative abundance of Tn-R,

Vcan, Hapln4 and Acan species between ~ 45 kDa was similar in all CNS regions.

Table 3. A heat map summarising the relative abundance of PNN molecules using Western blot densitometry analysis.

All molecules were graded as either: low intensity (blue), medium intensity (orange) or strong intensity (red) by comparing the relative abundance of each molecule within each CNS region.

Molecule (kDa)	Cortex	Hippocampus	Cerebellum	cSC
CSPGs				
Acan (≥ 250)	Blue	Orange	Blue	Red
Acan (100 – 250)	Red	Red	Red	Blue
Acan (~ 45)	Blue	Blue	Blue	Blue
Pcan	Orange	Orange	Red	Blue
Bcan	Orange	Blue	Blue	Blue
Vcan	Blue	Blue	Blue	Blue
Ncan	Red	Blue	Blue	Blue
Proteins				
Hapln1	Red	Blue	Orange	Orange
Hapln4	Blue	Blue	Blue	Blue
Tn-R	Red	Red	Red	Red
HA				
HA (~ 65)	Blue	Blue	Blue	Blue
HA (~ 120)	Orange	Orange	Orange	Orange
HA (~ 500)	Orange	Orange	Blue	Red
HA ($\gg 460$)	Orange	Orange	Blue	Red

3.4 Discussion

Heterogeneity in the distribution of PNN-associated molecules analysed was observed when comparing the cortical, hippocampal, cerebellar and cSC regions. Furthermore, it is important to note that all molecules were observed in all CNS regions. When comparing the relative abundance of the PNN-associated molecules between the CNS regions there was a unique abundance of molecules in each region. There was no simple trend of relative molecular abundance to describe the relationship between the 2 PNN morphologies described in section 1.5.3 when comparing the cortical and hippocampal regions with the cerebellar and cSC regions. Therefore, the distinct PNN morphologies cannot be distinguished by the molecules in this chapter alone, suggesting further molecules are involved such as Sema3a and Otx2 that are both known to interact with PNNs (Beurdeley *et al.*, 2012; Dick *et al.*, 2013; Djerbal *et al.*, 2019). Alternatively, another explanation for

the results observed may be that the biochemical differences only become apparent at the level of PNN-specific lysates, and not at the level of whole tissue lysates owing to confounding contributions of the loose ECM.

The high abundance of less or un-glycosylated CSPG species observed in all CNS regions provided a possible explanation for why histochemistry and imaging techniques detect PNNs that stain positively for Acan yet negatively for WFA (McRae *et al.*, 2007; Irvine and Kwok, 2018; Ueno *et al.*, 2018; Miyata *et al.*, 2018). The varying degree of glycosylated CSPG species observed in this analysis implied that the degree of CSPG glycosylation may be regulated on the PNN surface. The sulfation pattern of CS within PNNs is known to be under temporal regulation, therefore there is precedent for GAG chain regulation influencing PNN function (Miyata and Kitagawa, 2015; Foscarin *et al.*, 2017; Miyata *et al.*, 2018). Furthermore, the interaction of PNN-associated molecules including Sema3a is influenced by the degree of glycosylation and can influence the structure of the PNN surface (Djeral *et al.*, 2019). The degree of glycosylation also has been shown to change the structural conformation of CSPGs, as a reduction in Acan glycosylation caused a reduction in the molecules persistence length (Ng *et al.*, 2003). Determining the relationship between degree of CSPG glycosylation and the distinct PNN morphologies presents a potential mechanism for influencing the biomechanical properties of PNNs, specifically the thickness of the PNN surface.

Pcan is known to have a smaller molecular weight in comparison with Acan due to it being less glycosylated and having a smaller core protein size (Yamaguchi, 2000). Therefore, the observation that Acan and Pcan glycosylated CSPG species were found at similar molecular weights at > 460 kDa suggested that Acan is less glycosylated than in other previously characterised regions such as cartilage (Morgelin *et al.*, 1994; Kiani *et al.*, 2002; Matthews *et al.*, 2002; Roughley and Mort, 2014; Mort *et al.*, 2016). This was then supported by the comparison with cartilage tissue that suggested Acan was more glycosylated in comparison with the CNS (Figure 9). The distinct Acan species observed in the CNS is quite dramatically different in size in comparison with other tissues and has not previously been reported. The smaller size of Acan in the CNS suggests it may function, at least in part, via a different mechanism other than resisting compressive forces. This unique result will require further interrogation to understand the mechanistic role of these Acan species.

The degree of glycosylation could be affected not only by the number of GAG chains associated with the PNN surface, but also the size of the individual GAG chains. When modelling other tissues it has been observed that increasing the size of GAG chains increased the hydrodynamic radii of the CSPGs, which increased their ability to resist stress (Grande-Allen *et al.*, 2004). Although the size of GAG chains has not been specifically interrogated in cartilage, a reduction in overall GAG composition was associated with reduced quality of the joint (Mort *et al.*, 2016). There is also specific evidence that the CSPG Acan caused a swelling of tethered HA surfaces (Attili and Richter, 2013). Therefore, by reducing the abundance of GAG chains associated with CSPGs, either through reduced size or the amount of GAG chains, presents a potential mechanism for altering the thickness of PNN surfaces. It would also affect the phase separation behaviour quite substantially, with films made from less voluminous molecules being easier to phase separate than films made from bulky molecules.

The ~ 45 kDa ACAN species was relatively more abundant in the hippocampal and cortical regions, in comparison with the cerebellar and cSC regions which suggested that more ACAN degradation is occurring within these regions. This may indicate more aggrecanases being present in the cortical and hippocampal regions. Interestingly, the difference in the relative abundance of the ~ 45 kDa ACAN species was the only correlation that was observed between the distinct PNN morphologies (cortical and hippocampal PNNs versus cerebellar and cSC PNNs). Acan is known to be a prominent PNN-associating molecule, therefore the regulation of Acan abundance within PNNs by MMPs may be partially responsible for the distinct morphologies observed.

The variation in molecular abundance may also be a reflection in the variation of different cell types. The molecular contributions to PNNs by different cell types has previously been observed (Carulli *et al.*, 2006; Giamanco and Matthews, 2012). The results suggest that the ratio of neurons to glial cells, as well as the ratio of different glial cells, will likely change the molecular makeup of the loose ECM, as the different cell types synthesise different molecules (Carulli *et al.*, 2006).

The high relative abundance of Hapln1 in the cortical region may reflect the involvement of the molecule in other processes besides its role as an essential component of PNNs. Hapln1 plays an important role in the ECM for producing cortical folding in the neocortex, therefore the increased abundance of Hapln1 in this region may reflect this (Long *et al.*, 2018). This may go some way to

also providing an explanation for why an increase in the relative abundance of Hapln4 is not observed in the cortical region. This highlights the difficulty in extrapolating too much when considering the effect of the relative molecular abundance on PNN structures alone. However, the higher abundance of Hapln1 may as a result make the forming PNNs easier in this region, as without Hapln1 PNNs lose their structure (Carulli *et al.*, 2010).

Previous work has established the presence of Hapln4 as a component found in PNNs in both the cerebellum and cortex (Edamatsu *et al.*, 2018; Sucha *et al.*, 2020). Interestingly when Hapln4 is not present it does not prevent PNN formation, but does change the molecular composition of other ECM components (Sucha *et al.*, 2020). However, it is important to note that the Hapln proteins appear to preferentially bind specific CSPGs with higher affinity, therefore the distribution of these proteins throughout the CNS may alter the composition of CSPGs in the region (Shi *et al.*, 2004). Yet, although Hapln1 preferentially interacts with Vcan an increase in Hapln1 in the cortical region was not correlated with an increase in Vcan. An interesting future perspective would be to observe the relative proportion of Hapln1 molecules that are found interacting with Vcan, as opposed to other CSPGs, as it would indicate a mechanism for how the composition of CSPGs found interacting with the PNN surface could be regulated.

One of the limitations of the Western blot technique is it is difficult to discriminate between the structure of molecules if they contain similar molecular weight. Therefore, the CSPG species that form the smears have the potential to be heterogenous in molecular structure (Figure 21A, B and C). As degree of glycosylation is affected by both the amount of GAG chains, as well as the size of each individual GAG chain Western blot analysis alone cannot distinguish between these distinct structures. Previously, heterogeneity in GAG chain sizes attached to CSPGs has been observed, however to date a systematic analysis of GAG chains attached to CSPGs has not been conducted (Rauch *et al.*, 1991; Yamaguchi, 2000; Avram *et al.*, 2014). To determine if further heterogeneity in CSPG species are present, techniques such as AFM could be used to image individual CSPG molecules in the future, as was previously done when analysing Acan in cartilage tissue (Ng *et al.*, 2003).

The original intention of this analysis was to interrogate the PNN-associated molecules within each CNS region using a technique that specifically extracted the molecular components that form the PNN structure (Deepa *et al.*, 2006; Kwok *et al.*, 2014). Deepa *et al.* (2006) examined PNN components

taken from whole brain lysates. However, when adapted for analysing specific brain regions the reduced amount of starting material reduced the sensitivity of the analysis making analysis difficult. In the future this could be achieved by increasing the animal samples used in the analysis to increase the amount of starting material. The analysis in this chapter was developed and optimised to efficiently transfer glycosylated CSPGs, therefore providing a robust methodology for analysing glycosylated CSPGs using Western blotting. Importantly, it provides an overview of the relative distribution of the PNN-associated molecules in four CNS regions previously characterised as being PNN rich.

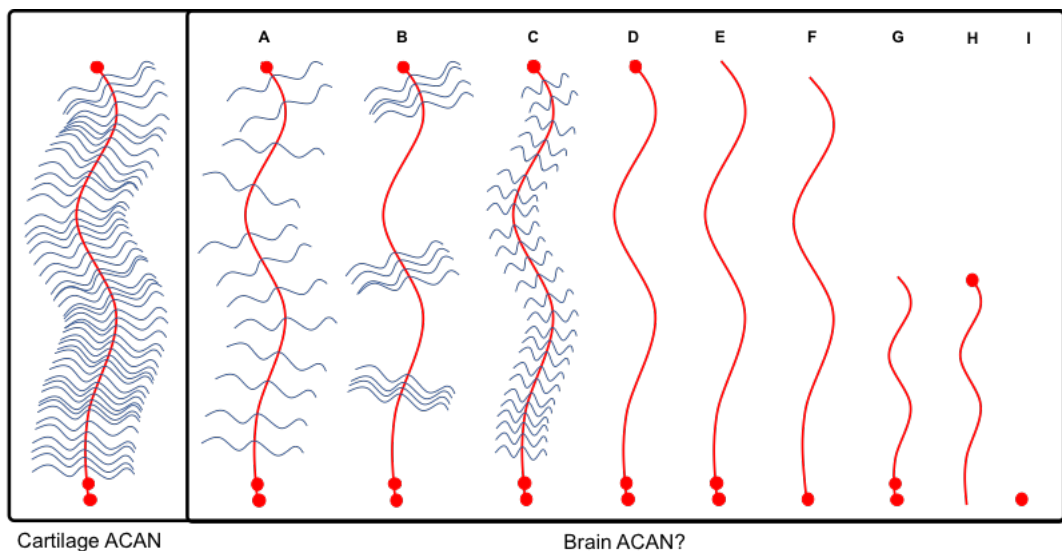


Figure 21. Schematic representations of the structure of cartilage Acan, alongside the possible structural variation observed in CNS Acan.

Specifically, **A**, **B** and **C** would be of the same molecular weight yet present 3 entirely different Acan structures that cannot be discriminated between using the Western blotting methodology. **D** full length non-glycosylated Acan chain. **E** Acan without the G3 domain **F** Acan without the G1 domain. **G** A cleaved variant of Acan containing the G1 and G2 domain. **H** A cleaved variant of Acan containing the G3 domain. One cleavage event could create both G and H variants. **I** A cleaved Acan variant that could represent either the G1 or G3 domain.

In conclusion, this chapter highlights the heterogeneous distribution of PNN-associated molecules in the CNS, providing unique insights into the molecular make-up of the PNN surfaces. Ncan and Hapln1 were found to be most abundant in the cortical region, while Pcan was found to be most abundant in the cerebellar region. Both Acan and Bcan were found to have multiple variants that were differentially distributed throughout the four CNS region analysed. The distribution of the molecules suggests how the differences in the different PNN morphologies may be biochemically produced, as well as

providing insights into the availability of molecules in different regions of the CNS that may allow for the maintenance, as well as dynamic regulation of PNN surfaces. Future work focussing on how the molecular heterogeneity manifests in functional changes to the CNS will likely provide key insights into the mechanisms behind how the surfaces regulate CNS activity.

Chapter 4: QCM-D as a methodology to analyse molecular interactions and supramolecular self-organisation underpinning PNN formation

4.1 Introduction

Although there is a proposed model for the assembly of PNNs, the detailed mechanism for the stabilisation of the morphologies of PNNs is not yet known (Yamaguchi, 2000; Kwok *et al.*, 2011; Richter *et al.*, 2018). Furthermore, although the PNNs form a large pericellular layer on the surface of neurons they surround, the biomechanical changes to the surface have yet to be described.

The observation that punctate and reticular PNNs are distinct morphologies that reflect the maturation state of PNNs suggests that the formation of the PNN surface is gradual and can be influenced by molecules present in the extracellular space (Richter *et al.*, 2018). Punctate PNNs are observed in the developing CNS, while reticular PNNs are more commonly observed in the developed CNS (Ueno *et al.*, 2017b; Richter *et al.*, 2018). How the transition occurs between these two morphological phenotypes is currently unclear. The application of perspectives from soft matter physics may offer the best current hypotheses for how this transition may occur. Firstly, self-organisation refers to the emergence of an overall order in space as a result of the collective interactions of individual components (Wedlich-Söldner and Betz, 2018). The individual components form supramolecular structures that aim to limit the overall free energy in the system. The lowest energy state is favoured. In terms of a system involving polymers of HA attached at one end to a surface two of the most important physical parameters are the mean surface density of HA and the surface tension at phase boundaries (Richter *et al.*, 2018). Therefore, the process of supramolecular self-organisation can drive phase transitions in structures as new molecules are added to the system. One demonstration of this is the phase transition of HA surfaces caused by a smaller variant of tumour necrosis factor-stimulated gene-6 (TSG-6) referred to as Link_TSG6 that is dependent on the mean surface density of HA attached to the surface (Richter *et al.*, 2018). At high surface densities of HA reticular structures formed, while at low densities punctate structures formed (Baranova *et al.*, 2011; Richter *et al.*, 2018). Link_TSG-6 was responsible for the phase transition but it was dependent on other physical parameters of the system. One of the aims of this chapter was to understand the factors driving self-organisation in PNN formation by altering the density of molecular

components, as well as the sequential order of presentation of PNN-associated molecules.

PNNs are a large pericellular structure that fundamentally changes the biochemical composition of the cell surface that they surround (Carulli *et al.*, 2006; Deepa *et al.*, 2006; Galtrey *et al.*, 2008). They are also likely to change the biomechanical properties of the cell surface as well. What is currently unclear is what these biomechanical changes are. Cells in the CNS have the ability to sense changes to biomechanical properties of surfaces, with these interactions causing changes to cell behaviour (Flanagan *et al.*, 2002; Georges *et al.*, 2006; Jiang *et al.*, 2008; Moshayedi *et al.*, 2010; Koch *et al.*, 2012; Franze *et al.*, 2013; Moshayedi *et al.*, 2014; Bollmann *et al.*, 2015; Koser *et al.*, 2016; Moeendarbary *et al.*, 2017). Therefore, it is plausible that PNNs may partially function via a biomechanical signalling mechanism. This highlights the importance of characterising the biomechanical properties of PNNs to help define how these properties differ from the properties of the cellular membrane, as well as the loose ECM.

As the previous chapter demonstrated, PNNs have the potential to be composed of a large variety of PNN-associated molecules. The heterogeneity in the molecular composition of PNNs highlights why a well-defined *in-vitro* model is necessary to investigate which parameters are responsible for the supramolecular self-organisation of PNNs. One such parameter that can be carefully controlled in a well-defined *in vitro* system is the mean surface density of HA, which is difficult to define *in vivo*. It is currently unknown if the surface density of HA has an effect on the formation of PNNs. Furthermore, the density of other PNN associated molecules, including Haplns and CSPGs is not well understood in PNN structures, yet its effect can be investigated using an *in vitro* system. Therefore, by carefully controlling the molecular parameters during the formation of PNNs, it is possible to investigate self-organisation, while simultaneously measuring the biomechanical properties of the film.

To analyse the supramolecular self-organisation of PNNs the aim was to design a methodology to recreate PNNs in a carefully controlled, cell-free, *in vitro* system and measure the surfaces using QCM-D. QCM-D is an acoustic measuring technique that is described in detail in chapter 2. Briefly, the technique can measure changes in frequency (Δf) to determine areal mass density (which includes hydrodynamically trapped solvent) and changes in dissipation (ΔD) to determine the mechanical properties of the surface bound layer. By combining these two measures the ratio $\Delta D / -\Delta f$ can be determined,

which for ultrathin films (in the range of a few nm) is strictly proportional to elastic compliance. For thicker films although the proportionality is lost, the ratio of $\Delta D / -\Delta f$ ratio remains a useful measure to quantify film softness (Du and Johannsmann, 2004; Reviakine *et al.*, 2011; Eisele *et al.*, 2012).

Through the use of QCM-D, the molecular interactions of PNN-associated molecules can be observed, while simultaneously gaining information about the biomechanical properties of the surface. Furthermore, a model system has previously been developed for producing HA brushes, *i.e.* films of HA molecules that are surface-bound at one end, using QCM-D (Richter *et al.*, 2007; Baranova *et al.*, 2011; Thakar *et al.*, 2014). Briefly, by creating a monolayer of streptavidin on the sensor surface, HA biotinylated at the reducing end can then be immobilised with the reducing end attached to the surface (Richter *et al.*, 2007; Baranova *et al.*, 2011; Thakar *et al.*, 2014). This is beneficial for modelling PNN surfaces as HA is synthesised by HAS enzymes on the cell surface that are extruded into the pericellular space (Spicer and McDonald, 1998; Itano *et al.*, 1999; Tien and Spicer, 2005). HA is a vital component of PNNs and is hypothesised to remain bound to the HAS enzymes on the cell surface during the formation of PNNs. Therefore, the establishment of a methodology for the production of *in vitro* HA films using QCM-D aimed to recreate the hypothesised mode of HA attachment to HAS molecules that is predicted to attach HA molecules via the reducing end (Weigel, 2015).

Previously, the interaction of Acan with HA films has been measured using a combination of QCM-D, spectroscopic ellipsometry, AFM and reflection interference contrast microscopy (Attili and Richter, 2013). Interestingly, they found that Acan caused an increase in HA film compliance, highlighting the potential of PNN-associated molecules to influence the biomechanical properties of PNNs. Within this particular study QCM-D was used as a method that provided information on both the assembly of films, as well as providing a biomechanical measurement of the film, which was then further rigorously characterised using the other methodologies (Attili and Richter, 2013). The aim of this chapter was to build on this work to present PNN-associated molecules to the HA films sequentially.

4.1.1 Target PNN model and the main design principles

To establish a model for analysing the assembly of PNNs it is important to highlight the specific aspects of PNN supramolecular organisation that the

model is being optimised for. Firstly, the model aimed to recreate the presentation of HA as it would be on the cell surface while attached to HAS at the reducing end (Weigel, 2015). The methodology for the creation of HA brushes required the formation of a streptavidin monolayer, that in turn is attached to the QCM-D sensor surface via a supported lipid bilayer (Figure 22). The production of stable lipid bilayers that form on QCM-D sensor surfaces has previously been described (Keller and Kasemo, 1998; Richter *et al.*, 2006). It is important to note that the streptavidin in the monolayer is not likely to be mobile in 2D, as at very high streptavidin density it is known to undergo 2D crystallisation (Ilya and Brisson, 2001).

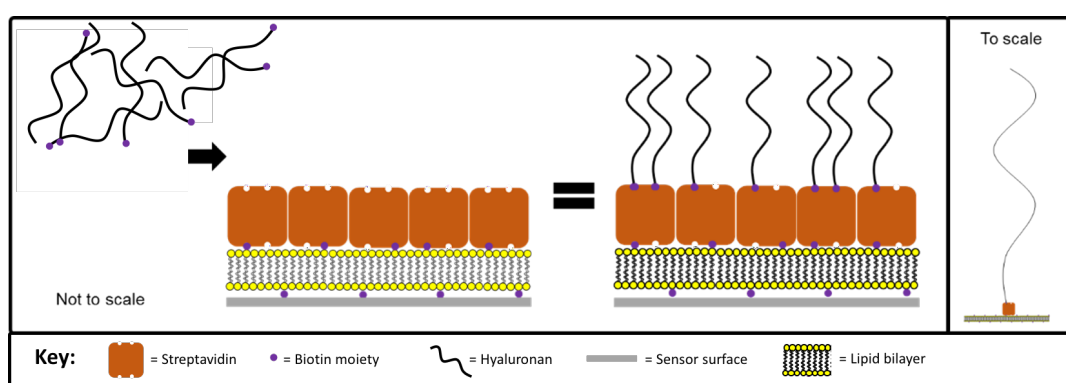


Figure 22. Schematic representation of how the orientation of HA is achieved on the sensor surface.

The stably bound biotinylated lipid bilayer and streptavidin surface anchor HA50 biotinylated at the reducing end.

By producing a monolayer of streptavidin that is standardised for all experiments it established a reproducible baseline for Δf and ΔD measurements. This made comparisons between HA films of varying densities simpler, as non-specific binding of the PNN-associated molecules is standardised to the interaction with the streptavidin monolayer alone. HA density could then be controlled by altering the HA incubation time.

Secondly, the model aimed to establish if the surface density of HA impacts the supramolecular assembly of the surfaces. In order to examine this, the molecular weight of HA used to establish the PNN model surface is an important consideration. The size of HA has an influence on the types of films that are formed, with increased HA size associated with creating less dense, more compliant HA films, as described in detail in chapter 5. Currently, the molecular weight of HA in PNNs is unknown, with chapter 3 highlighting HA molecules of varying length present within the CNS. Although an estimate of the size of HA is important for the accurate recreation of PNN surfaces, in

determining the molecular interactions with other PNN-associated molecules, as well as the formation of supramolecular structures the size of HA is less integral to the experiment.

The surface density of HA is known to impact HA films, as it has the potential to change the conformational shape of each HA molecule (Richter *et al.*, 2018). As each HA molecule is negatively charged, the chains repel each other, therefore at higher surface densities this causes the HA chains to become more stretched, in an attempt to increase the distance between the HA molecules (Richter *et al.*, 2018). Furthermore, high surface density HA surfaces may also sterically hinder the ability of PNN-associated molecules to interact with HA chains. If the spaces between the HA molecules are too small then molecules may only be able to interact with HA on the top of the HA films, as opposed to interacting within the films. To determine if HA density had an impact on the formation of PNNs the aim was to produce both high density and low density HA films. Specifically, the aim was to interrogate the effect of steric hindrance as a potential mechanism that could affect PNN formation.

Thirdly, the model aimed to establish how the supramolecular structure self-organised to stably assemble PNNs. Therefore, to investigate this process it was important to select appropriate PNN components for analysis. As mentioned previously, Acan is found in the majority of PNNs, therefore it was selected as the CSPG to model PNN surface formation (Carulli *et al.*, 2006; Deepa *et al.*, 2006; Galtrey *et al.*, 2008; Kwok *et al.*, 2010). Hapln1 was selected as it has also been established as an essential component in PNN formation (Carulli *et al.*, 2006; Deepa *et al.*, 2006; Galtrey *et al.*, 2008; Kwok *et al.*, 2010). The interesting distribution in the CNS observed in chapter 3 also suggested that the relative density of Hapln1 is regulated in different CNS regions, making it an interesting candidate for further analysis. The interaction of Acan with HA films has previously been observed using QCM-D, however this study did not investigate the role of Hapln1 (Attili and Richter, 2013). It is currently unknown whether the order of incubation is important to the formation of PNN surfaces. By differing the order of presentation of Acan and Hapln1 the aim was to establish if Hapln1 could stabilise these supramolecular assemblies either while pre-bound to HA, or with Acan pre-bound to HA.

It is important to highlight the challenges in attempting to establish an *in vitro* model of PNNs. Previous work has highlighted that one CSPG, one link protein and HAS that synthesised HA and extruded it into the pericellular space were the essential molecules required to produce a PNN surface (Kwok *et al.*, 2010). Kwok *et al.* (2010) specifically used Hapln1 and Acan as the link

protein and CSPG, respectively, to recreate the cellular *in vitro* model. Hapln1 has previously been observed to be essential to PNN formation (Carulli *et al.*, 2010). Acan has been suggested as an integral PNN component that is found surrounding the majority of PNNs in the CNS (Carulli *et al.*, 2006; Deepa *et al.*, 2006; Galtrey *et al.*, 2008; Ueno *et al.*, 2017b; Irvine and Kwok, 2018). Therefore, Acan and Hapln1 were selected as the molecules used to establish the *in vitro* PNN model. The aim of this chapter was to establish a new technique for modelling the formation of PNNs by presenting Hapln1 and Acan to the HA films sequentially.

4.2 Methodology

The QCM-D methodology is described in detail in chapter 2. In chapter 2 a quantitative description of QCM-D is provided, followed by a section describing how the measurements were taken using QCM-D. Chapter 2 also describes the passivation of tubes and chamber preparation, as well as the preparation of liposomes used to form the lipid bilayers. The methodology for forming the lipid bilayers and streptavidin monolayer are also provided in chapter 2. Values of Δf and ΔD are presented at the end of the incubation period. The values of Δf and ΔD were averaged over a 1 min period to account for any outliers.

4.2.1 Producing the supported lipid bilayer and streptavidin monolayer

The directional orientation of HA films was achieved by using HA biotinylated at the reducing end and the same methodology described by Richter *et al.* (2007). Briefly, liposomes made of a combination of DOPC and DOPE-cap-biotin in a ratio of 95 : 5 respectively were incubated over the sensor surface for 15 min at a flow speed of 20 $\mu\text{L}/\text{min}$ at a concentration of 50 $\mu\text{g}/\text{mL}$. Streptavidin was then injected for 15 min at a flow speed of 20 $\mu\text{L}/\text{min}$ at a concentration of 20 $\mu\text{g}/\text{mL}$.

4.2.2 Creating HA films

It is important to note that areal mass density measured by Δf includes both the mass of the molecule adsorbing onto the surface, as well as the mass of the solvent. Therefore, an additional optical technique is required to separate the contribution to mass by the solvent to allow the density of HA to be defined. This has previously been measured for HA50, therefore it was possible to

define the surface density of HA molecules on the sensor surface using measurements of Δf (Figure 23; Baranova *et al.*, 2011).

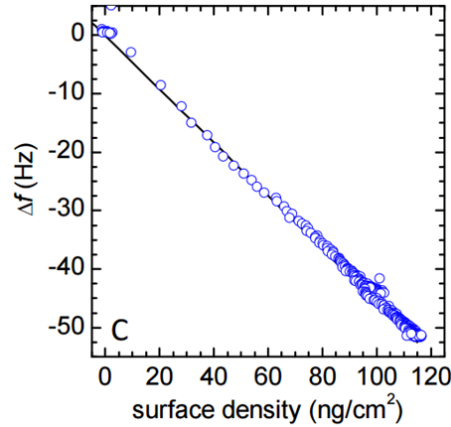


Figure 23. Relationship between HA50 surface density and Δf .

This was achieved by simultaneously measuring HA surfaces using QCM-D and spectroscopic ellipsometry (Baranova *et al.*, 2011).

CSPGs are very large molecules, with measurements of Acan contour length (L_c) $\sim 257 \pm 87$ nm for highly glycosylated Acan species (Ng *et al.*, 2003). Ng *et al.* (2003) also measured GAG L_c between 27 – 48 nm for GAGs attached to the core protein of Acan, allowing for the approximate width of Acan to be extrapolated from these measurements. The 52 – 96 nm range of Acan width is the largest possible width, as it assumes GAG chains at full extension, which is unlikely to be the case as the end-to-end length of GAG chain were measured between 19 and 40 nm, suggesting the width of Acan is more likely to be between 38 – 80 nm (Ng *et al.*, 2003). Therefore, for Acan to insert itself between HA chains the approximate spacing of HA was required to be 38 – 80 nm apart.

4.2.2.1 Defining sparse HA50 films

Assuming the width of Acan to be ~ 60 nm, the change in value of Δf required to achieve a surface where the HA50 molecules are spaced approximately 60 nm apart could be calculated using the following equations:

$$rms = \sqrt{A} \tag{15}$$

$$A = \frac{M_w}{m \times N_A} \tag{16}$$

Where rms is root mean square (distance between each HA50 molecule), A is the area covered by each HA50 molecule, M_w is the molecular weight of HA50, m is the areal mass density of HA50 and N_A is Avogadro's constant. To calculate the change in Δf for spacing HA50 ($M_w = 58,000$ Da) 60 nm apart: $rms = 6 \times 10^{-8}$ m, therefore using Equation 15, A (3.6×10^{-15} m²) could be calculated. The areal mass density m of HA50 could then be calculated using Equation 16 to produce the value $m = 2.68 \times 10^{-5}$ g/m². To determine the Δf value from Figure 23, the value was converted to 2.68 ng/cm². The range of Δf values was therefore considered to be ~ -1 Hz.

As this value is a very small shift in Δf for practical reasons the value $\Delta f = -5$ Hz as the value for sparse HA50 surfaces as a compromise between keeping the surface density as small as possible while still being able to detect the formation of HA50 films. -5 Hz shift corresponds to the value 10 ng/cm², therefore the value $m = 1.0 \times 10^{-5}$ g/m². Using Equations 15 and 16, this sparse HA50 films have an $rms = 31.0$ nm. To summarise, in the sparse HA50 condition HA50 molecules were spaced approximately 31.0 nm apart from each other on average.

Using the worm-like chain model it was possible to approximate the radius of gyration of the HA50 chains as being 13 nm, which was extrapolated from the work previously published by Takahashi *et al* (2003). This can then be used to approximate the transition between 2 morphological HA surface types that has previously been described by Richter *et al* (2018). When HA50 chains are spaced close together (less than 13 nm) a combination of electrostatic repulsions and volume exclusion, caused by the close packing of HA molecules, will cause the HA50 chains to swell and produce a brush-like morphology. In contrast, when the HA50 chains are spaced far apart from each other (more than 13 nm) the HA50 chains are not able to interact with each other, therefore a mushroom-like morphology is more likely. Therefore, the HA50 surface morphology is likely to be in the mushroom-like state as the HA50 chains are spaced 31 nm apart.

4.2.2.2 Defining dense HA50 films

In contrast, high density HA films were defined at $\Delta f \sim -36$ Hz, which corresponded to surface density of ~ 80 ng/cm². Therefore, $m = 8.0 \times 10^{-5}$ g/m², which gave an rms value of 11.0 nm when Equations 15 and 16 were used. So, in the dense HA50 condition HA50 molecules were spaced approximately 11 nm apart from each other on average. Using the worm-like

chain model to approximate the radius of gyration of HA50 to 13 nm, it indicated that the dense HA50 surfaces would be in the brush-like morphology.

4.2.3 Manipulating HapIn1 density

Two densities of HapIn1 were established to analyse how the density of HapIn1 effects the supramolecular self-organisation of the PNN surfaces. Dense HapIn1 was established as 50 min incubation of 5 $\mu\text{g}/\text{mL}$. This value was chosen as it was at this point that the binding interaction became less efficient, suggesting it was nearing equilibrium. The second condition was referred to as sparse HapIn1 and was established by incubating HapIn1 for 10 min at 5 $\mu\text{g}/\text{mL}$. This was chosen as it caused a detectable shift in Δf on dense HA films while being far smaller than the dense HapIn1 condition.

4.2.4 Preparation of DODA-tris-NTA lipid bilayers for trapping polyhistidine-tagged Tn-R

A dioctadecyldimethylammonium (DODA) lipid analogue with a chelator tris-nitrilotriacetic acid (NTA) headgroup was kindly provided by Changjiang You and Jacob Piehler (Osnabrück University, Osnabrück, Germany) and was prepared as described by Beutel *et al* (2014). The tris-NTA headgroup comprised of three nitrilotriacetic acid moieties and was used to trap polyhistidine-tagged molecules to the sensor surface after Ni^{2+} ions were chelated to the tris-NTA headgroup. For the Ni^{2+} chelation to occur 10 mM NiCl_2 was added to the HEPES buffer during liposome incubation. The liposomes were prepared using the methodology describe in section 2.2.3. To prepare the supported bilayers liposomes made of a combination of DOPC and DODA-tris-NTA in a molar ratio of 99.5 : 0.5 were incubated over the sensor surface in HEPES buffer containing 10 mM NiCl_2 for 15 min at a flow speed of 20 $\mu\text{L}/\text{min}$ and a concentration 50 $\mu\text{g}/\text{mL}$.

4.2.5 Statistics

When two values were compared, an independent sample T-test was performed to ascertain if the values were significantly different. In all cases the assumptions were met, as there were no significant outliers, the samples were normally distributed, and the variances of the dependent variable were similar in each group. When comparing the difference caused by the addition

of a molecule to the same HA film, such as the change in the ratio of $\Delta D / -\Delta f$ before and after Acan incubation, a repeated measures T-test was used to test for significance. When comparing multiple groups with each other, a general linear model was used, followed by a post hoc Tukey test. For all statistical tests, significance was established as $p \leq 0.05$.

4.3 Results

4.3.1 Successful establishment of the HA model surface

The first aim was to successfully recreate the supported lipid bilayer and streptavidin model surface that would provide the foundation for analysing the formation of PNN supramolecular self-organisation. When liposomes were incubated over the sensor surface, the characteristic two-phase behaviour was observed using Δf and ΔD measurements as previously described by Richter *et al* (2007) (Figure 24). The first phase involved a decrease in Δf and an increase in ΔD , indicating that the vesicles were absorbing onto the sensor surface and remaining intact (Richter *et al.*, 2006). In the second phase an increase in Δf and a decrease in ΔD could be observed, before both Δf and ΔD measurements stabilised ($\Delta f = -24 \pm 0.4$ Hz; $\Delta D = 0.02 \pm 0.02 \times 10^{-6}$; $n = 12$), representative of the vesicles rupturing at high vesicular coverage and rupturing to form a good quality supported lipid bilayer (Richter *et al.*, 2006; Richter *et al.*, 2007). Taken together it implied that the formation of a stable lipid bilayer on the QCM-D sensor was successfully established and formed as expected.

Streptavidin was then presented to the surface where it bound stably to the free biotin moieties (Figure 24). The interaction of streptavidin with the lipid bilayer caused shifts in Δf and ΔD ($\Delta f = -28 \pm 0.3$ Hz; $\Delta D = 0.31 \pm 0.04 \times 10^{-6}$; $n = 12$) that agreed with previously published results, therefore the interaction behaved as expected (Larsson *et al.*, 2003; Richter *et al.*, 2007; Dubacheva *et al.*, 2017). Both Δf and ΔD values stabilise before the end of the incubation period, suggesting all of the available streptavidin binding sites are occupied. Furthermore, the small increase in ΔD alongside the larger decrease in Δf implied that the symmetric streptavidin molecules are densely packed on the surface (Larsson *et al.*, 2003).

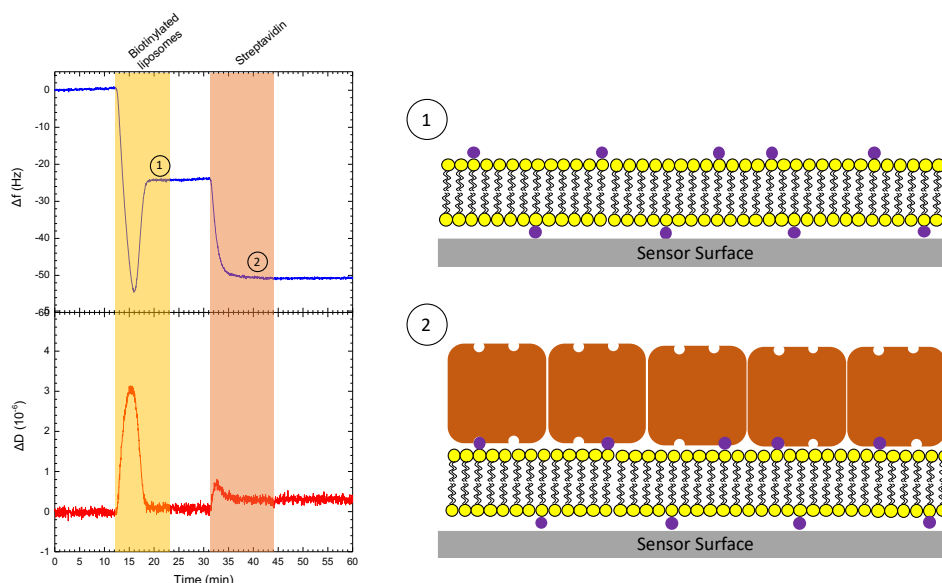


Figure 24. Successful establishment of the supported lipid bilayer and a monolayer of streptavidin on the QCM-D sensor surface.

The 5th overtone was used to present shifts in frequency (Δf ; top row) and dissipation (ΔD ; bottom row). Biotinylated liposomes were incubated at 50 $\mu\text{g/mL}$, while streptavidin was incubated at 20 $\mu\text{g/mL}$. The flow rate was kept constant at 20 $\mu\text{L/min}$. The coloured regions establish the incubation period for the biotinylated liposomes (yellow) and streptavidin (beige). HEPES buffer was flowed over the surface for the other time periods. The QCM-D responses were consistent with the formation of good quality supported lipid bilayers and a monolayer of streptavidin respectively (Richter *et al.*, 2007). To the right of the graphs are schematic representations of the predicted surface formed on the sensor surface at point 1, and 2.

Throughout all the experiments the formation of the lipid bilayer and the streptavidin monolayer was standardised, therefore both parameters were fixed. Equally, it is worth noting that other parameters that were fixed throughout the experiments included the temperature of the chamber, the flow rate and the buffer used. An advantage of this experimental setup was the streptavidin monolayer did not interact strongly with either HapIn1 or Acan (Figure 25). Therefore, any interaction with the surface observed on incubating these molecules was due to the presence of the HA film.

It is worth noting that unlike HA50 where a combinatorial approach using an optical technique and QCM-D has previously been analysed, for both HapIn1 and Acan this has not been done. Therefore, although it is possible to measure the density of HA50 within the assembling film, it is not possible to measure the density of Acan or HapIn1 molecules that attached to the HA films. Instead, the relative changes in Δf and ΔD were used to analyse the relative abundance of these molecules.

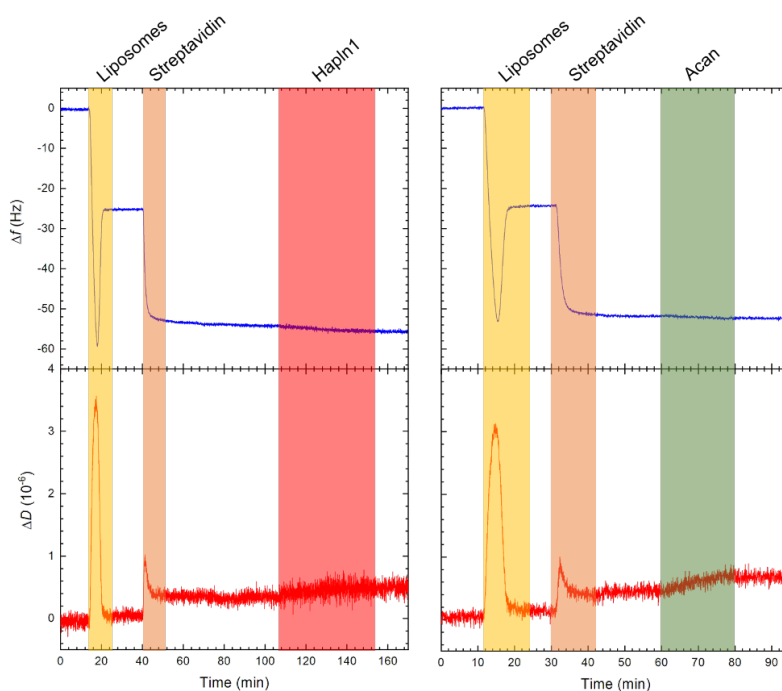


Figure 25. Both HapIn1 and Acan did not interact with the streptavidin monolayer measured using QCM-D.

Both HapIn1 (5 $\mu\text{g/mL}$) and Acan (100 $\mu\text{g/mL}$) were incubated at a flow rate of 10 $\mu\text{L/min}$. For Acan, the flow rate was increased to 20 $\mu\text{L/min}$ for the duration of the incubation period after the dashed line.

Having successfully recreated the lipid bilayer and streptavidin surfaces, the next step was to consistently produce sparse and dense HA50 films. Sparse HA50 films could consistently be reproduced, with values of $\Delta f = -6 \pm 1$ Hz and $\Delta D = 2.3 \pm 0.4 \times 10^{-6}$ (Figure 26). The aim was to produce sparse HA50 films with a shift in Δf of approximately -5 Hz to space HA50 molecules approximately 31.0 nm apart ($rms = 31.0$ nm), therefore the results demonstrated that this was successfully achieved. For dense HA50 surfaces HA50 was incubated for 50 min, producing shifts in Δf of -36 ± 2 Hz and ΔD $14.2 \pm 0.6 \times 10^{-6}$, with the HA50 molecules being spaced approximately 11.0 nm apart ($rms = 11.0$ nm) (Figure 26). These results demonstrated that the creation of sparse and dense HA50 films were highly reproducible. The rms values relate to the approximate distance between each HA50 anchor-point to the streptavidin monolayer.

The next step was to determine the ratio of $\Delta D / -\Delta f$ for dense and sparse surface bound HA50 films to approximate the measure of elastic compliance of the films (Figure 27). The ratio of $\Delta D / -\Delta f$ were $0.39 \pm 0.01 \times 10^{-6}/\text{Hz}$ for dense HA surfaces and $0.40 \pm 0.03 \times 10^{-6}/\text{Hz}$ for sparse HA surfaces. Therefore, the change in density between sparse and dense HA50 films did

not have any implication on the ratio of $\Delta D / -\Delta f$ as the results were not significantly different.

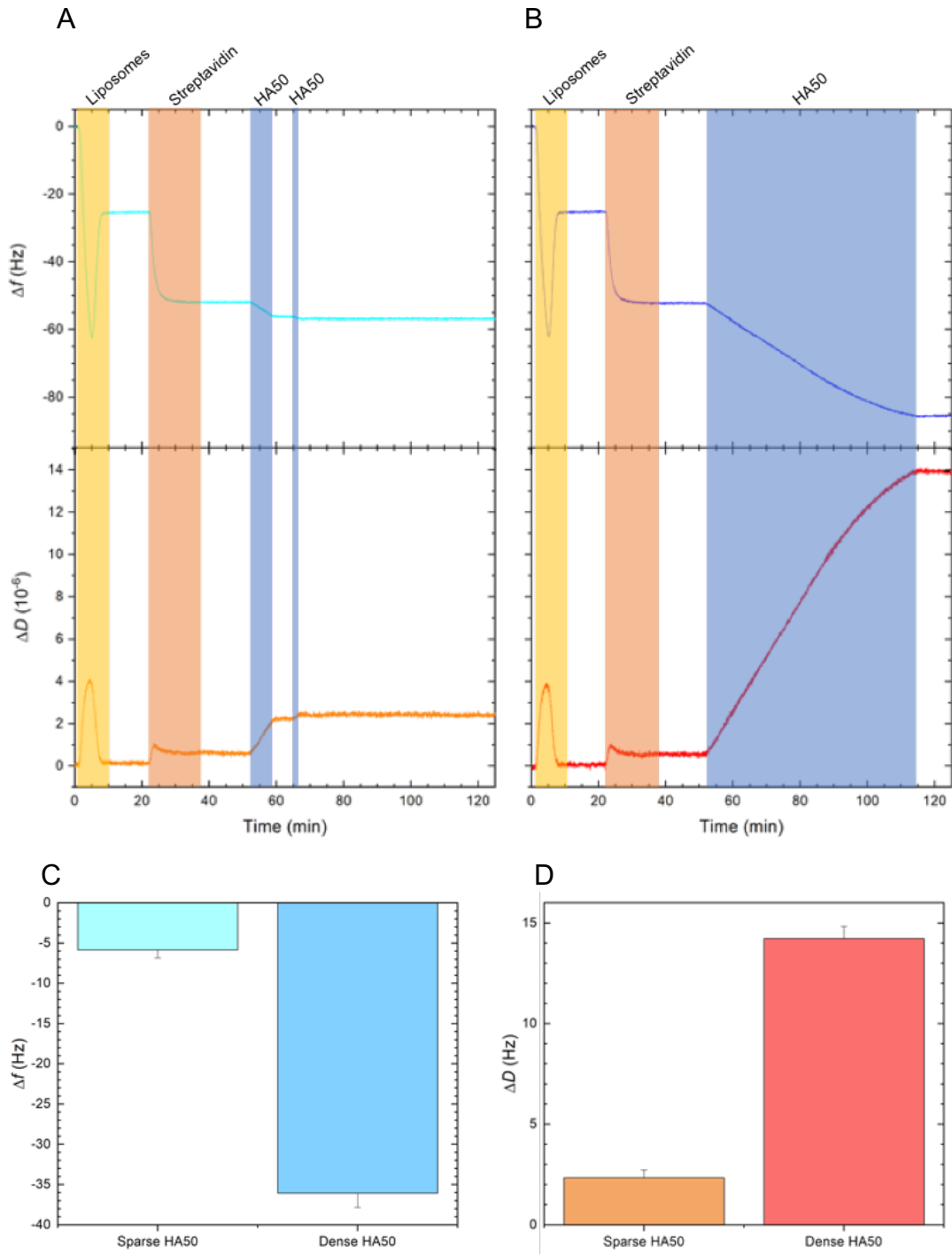


Figure 26. Values of Δf and ΔD that demonstrated that Sparse HA50 and dense HA50 films are highly reproducible.

Biotinylated HA50 (1 $\mu\text{g/mL}$) was incubated over a streptavidin monolayer at a flow rate of 10 $\mu\text{L/min}$. **A** Representative Δf and ΔD QCM-D plots for sparse (cyan and orange lines) HA films. **B** Representative Δf and ΔD QCM-D plots for dense (blue and red lines) HA films. The plots include the formation of the lipid bilayer (yellow region) and the streptavidin monolayer (beige region). The blue regions indicate the incubation of HA50 **C+D** Sparse HA50 (n = 11 ; cyan and orange) and dense HA50 (n = 21 ; blue and red) are presented with the error bars indicating the standard deviation.

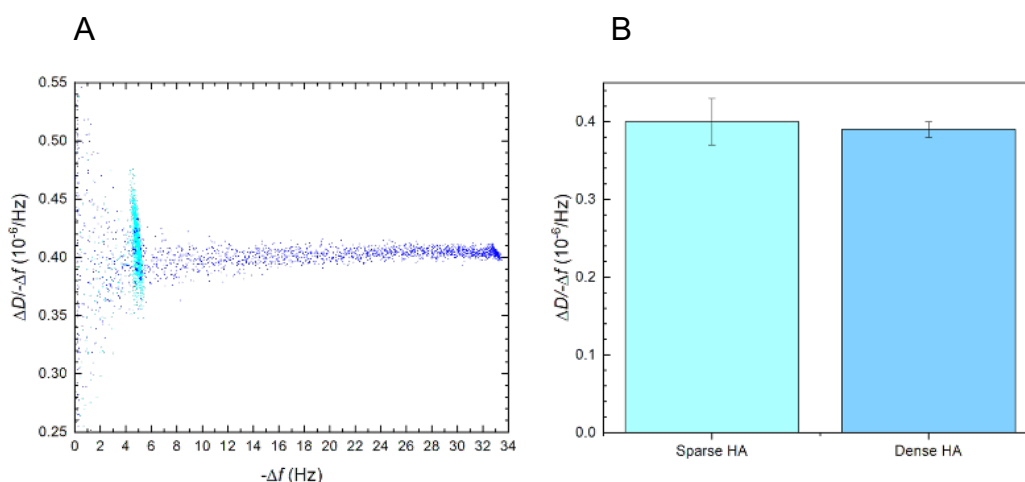


Figure 27. Ratio of $\Delta D / -\Delta f$ was equal for both sparse and dense HA50 films.

A Representative plots of $\Delta D / -\Delta f$ during the formation of sparse (cyan) and dense (blue) HA50 films. Formation of HA50 films was measured through the increase in $-\Delta f$. The variability of results between $-\Delta f$ values of 0 to 3 Hz is larger due to the tendencies for outliers affecting the measurements of the $\Delta D / -\Delta f$ ratio, as small changes in both Δf and ΔD in this range have a large effect on the ratio, that stabilised around 4 Hz. **B** Values of $\Delta D / -\Delta f$ measured at the end of incubation for sparse HA50 ($n = 11$; cyan) and dense HA50 ($n = 21$; blue) films.

4.3.2 Decreasing the density of HA films increased the binding of Acan and HapIn1

4.3.2.1 Unstable interaction of Acan to HA films

When Acan was introduced to sparse and dense HA films significantly larger shifts in Δf and ΔD were observed on interaction with sparse HA films in comparison to dense HA films (Figure 28). The results described here indicate that Acan can interact with HA films irrespective of HA surface densities, although binding is apparently reduced for denser HA films. The negative Δf ($\Delta f = -1.8 \pm 0.4$ Hz and positive ΔD ($\Delta D = 2.3 \pm 0.4 \times 10^{-6}$) values indicated that Acan was able to interact with the sparse HA films. The positive ΔD ($\Delta D = 1.6 \pm 0.2 \times 10^{-6}$) value on interaction with dense HA films indicated that Acan interacted with the surface, however this interaction was undetectable using Δf ($\Delta f = 0.7 \pm 1.2$ Hz). Of note, the slight positive Δf value could have been caused by either a re-organisation of the HA film, suggesting a phase transition, or more likely it is an artefact of the very small values of Δf detected. As expected, the results indicated that Acan interacted more strongly with sparse HA50 films, in contrast to dense HA films. The sparse HA50 films were produced specifically to space HA50 molecules approximately 11.0 nm apart to aid the penetration of Acan to interact within the film, by reducing steric hinderance. The results suggested that the larger interaction detected on

sparse HA50 films in comparison with dense HA films where HA molecules were packed closer together (approximately 11 nm apart), may be due to Acan interacting within the HA film.

After the Acan incubation period during the wash step an increase in Δf (2 ± 0.01 Hz) and a decrease in ΔD ($-1 \pm 0.01 \times 10^{-6}$) values could be observed on sparse HA films (Figure 28A). A decrease in ΔD ($-1.25 \pm 0.25 \times 10^{-6}$) was also observed on dense HA films. This implied that Acan was dissociating from the HA films over time and was therefore not stably bound. To ensure that the changes in Δf and ΔD were caused by Acan dissociation, Acan was then re-introduced to the same HA films, where on re-incubation the original decrease in Δf and increase in ΔD values were restored (Figure 28A). Therefore, Acan alone is not stably bound to HA films.

The shifts in Δf observed on Acan addition are small on both sparse and dense HA50 films in comparison with Δf shifts on streptavidin and HA addition. Considering the large size of Acan, this result at first appears surprising. Values of Δf are also affected by other parameters, including hydrodynamically trapped solvent, the thickness of the film, the mechanical properties of the bound molecules and the mechanical properties of the resulting film. To further determine how the surfaces change in response to Acan incubation the ratio of $\Delta D / -\Delta f$ was analysed.

The addition of Acan significantly increased the ratio of $\Delta D / -\Delta f$ for both dense ($p \leq 0.0005$) and sparse ($p \leq 0.0005$) HA surfaces when compared with HA surfaces alone (Figure 29). These results indicated that the surfaces were becoming more compliant. The $\Delta D / -\Delta f$ ratio was significantly larger on sparse HA surfaces ($0.70 \pm 0.06 \times 10^{-6}/\text{Hz}$) in comparison with dense HA surfaces ($0.46 \pm 0.01 \times 10^{-6}/\text{Hz}$) (Figure 29). Therefore, the addition of Acan caused sparse HA films to become significantly more compliant than dense HA films.

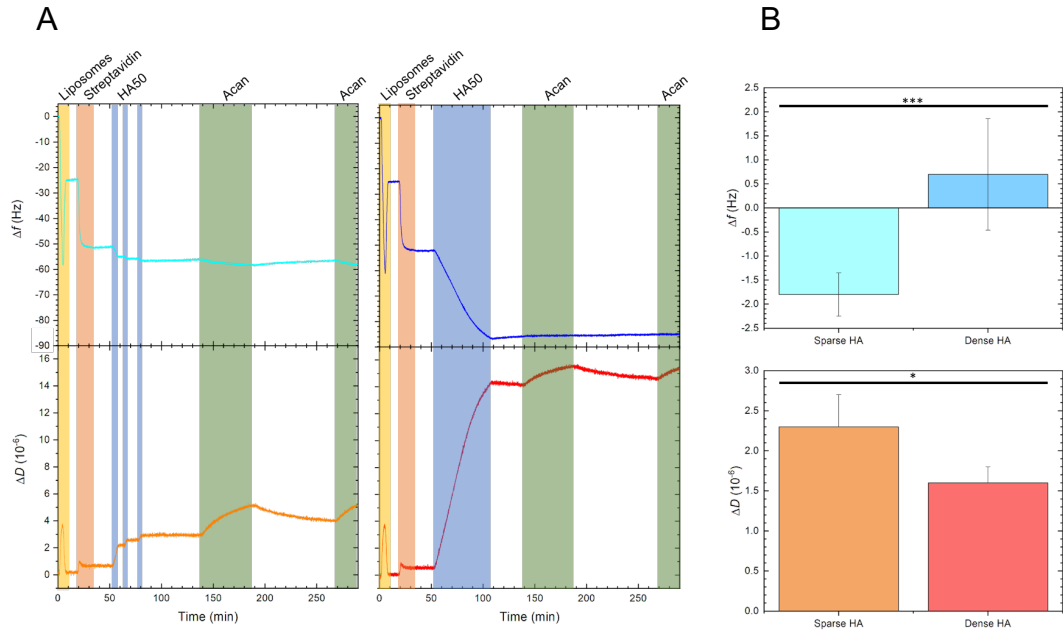


Figure 28. The density of HA50 films influenced Acan assembly.

A Representative Δf and ΔD QCM-D plots for sparse (cyan and orange lines) and dense (blue and red lines) HA films. The plots include the formation of the lipid bilayer (yellow region) and the streptavidin monolayer (beige region). The blue regions indicate the incubation of HA50 (1 $\mu\text{g}/\text{mL}$), with the green regions indicating the incubation of Acan (100 $\mu\text{g}/\text{mL}$). **B** Changes in Δf and ΔD when Acan is introduced to sparse (cyan and orange; $n = 5$) and dense (blue and red; $n = 10$) HA50 films. The values represent the changes in Δf and ΔD between the start and the end of Acan incubation (the difference between the start and end of the green region). Both Δf ($p \leq 0.0005$) and ΔD ($p = 0.018$) values were significantly different. The mean and standard deviations are presented. The lines above the graph represent statistical significance: $p \leq 0.05$ (*), $p \leq 0.0005$ (***)

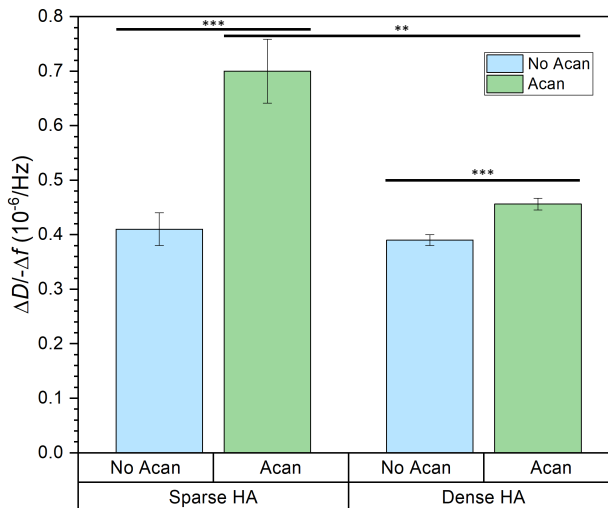


Figure 29. The ratio of $\Delta D / -\Delta f$ for sparse and dense HA50 films with and without the addition of Acan.

Sparse HA50 films without Acan had a $\Delta D / -\Delta f$ ratio of $0.40 \pm 0.03 \times 10^{-6}/\text{Hz}$ ($n = 11$) and a $\Delta D / -\Delta f$ ratio of $0.70 \pm 0.06 \times 10^{-6}/\text{Hz}$ ($n = 5$) with the addition of Acan. Dense HA50 films without Acan had a $\Delta D / -\Delta f$ ratio of $0.39 \pm 0.01 \times 10^{-6}/\text{Hz}$ ($n = 21$) and a $\Delta D / -\Delta f$ ratio of $0.46 \pm 0.01 \times 10^{-6}/\text{Hz}$ ($n = 10$) with the addition of Acan. The mean and standard deviation are presented. The lines above the graph represents statistical significance: $p \leq 0.005$ (**), $p \leq 0.0005$ (***)

4.3.2.2 Stable interaction of Hapln1 with HA films

Hapln1 was observed to readily interact stably with both dense and sparse HA50 films (Figure 30A). Hapln1 interaction with HA50 was stable, as no change in Δf or ΔD was observed after the Hapln1 incubation during the wash step. A larger shift in Δf was observed on Hapln1 interaction with sparse HA50 films in comparison with dense HA50 films ($p \leq 0.05$) (Figure 30B). The larger negative shifts in Δf observed on sparse HA50 films ($\Delta f = -42 \pm 6$ Hz) in comparison with dense HA50 films ($\Delta f = -29 \pm 10$ Hz) suggested that more Hapln1 was able to interact with the surface. However, it is difficult to conclude with certainty that more Hapln1 is interacting with sparse HA50 films, as other factors also contribute to shifts in Δf including solute binding, trapped solvent and changes to the mechanical properties of the film. Until QCM-D is paired with another technique such as spectroscopic ellipsometry to gain a measurement of the change in density and thickness of the film on Hapln1 incubation the difference in shifts in Δf observed on dense and sparse HA50 films indicate that HA density is causing a change to the assembly of films that requires further analysis. For this reason, to further determine how the surfaces change in response to Hapln1 incubation the ratio of $\Delta D / -\Delta f$ was analysed. There was no difference in ΔD values measured on interaction with dense ($\Delta D = 5.1 \pm 1.0 \times 10^{-6}$) and sparse ($\Delta D = 5.0 \pm 0.4 \times 10^{-6}$) HA films.

The ratio of $\Delta D / -\Delta f$ for sparse HA / Hapln1 films ($0.15 \pm 0.01 \times 10^{-6}/\text{Hz}$) was significantly lower than the ratio of dense HA / Hapln1 films ($0.29 \pm 0.02 \times 10^{-6}/\text{Hz}$) (Figure 31). For both dense and sparse HA films the addition of Hapln1 caused a decrease in the $\Delta D / -\Delta f$ ratio, indicating that Hapln1 caused HA films to become less compliant (more rigid).

Although the size of Hapln1 is not known, it is assumed to be a globular protein so its size could be roughly estimated using its spherical volume to be approximately 3 – 5 nm in diameter (Erickson, 2009). In contrast, the size of HA50 is approximately 116 nm, therefore it is theoretically possible for approximately 29 Hapln1 molecules to interact with a single HA50 molecule. In both the sparse and dense HA50 conditions Hapln1 does not reach saturation, therefore there are still available Hapln1 binding sites after incubation. Although it cannot be concluded with certainty until additional measurements of the change in density of the surface are measured, the results indicated that it is likely that multiple Hapln1 molecules are interacting with each HA50 molecule, as reducing the density of HA50 in the sparse HA condition did not result in Hapln1 reaching saturation during the incubation period.

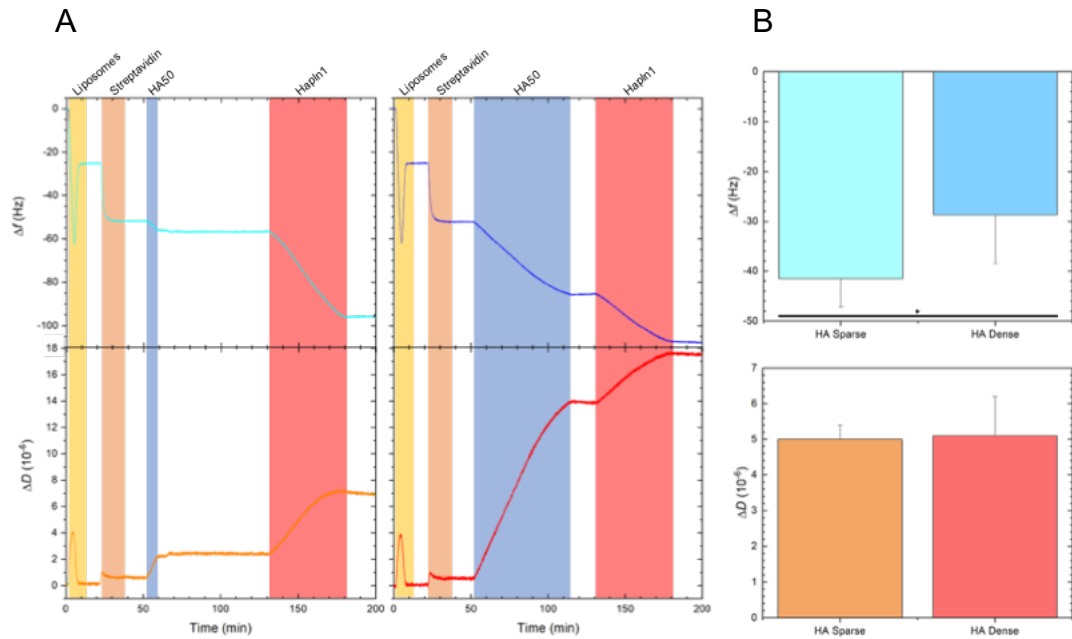


Figure 30. The density of HA50 films influenced HapIn1 assembly.

A Representative Δf and ΔD QCM-D plots for sparse (cyan and orange lines) and dense (blue and red lines) HA films. The plots include the formation of the lipid bilayer (yellow region) and the streptavidin monolayer (beige region). The blue regions indicate the incubation of HA50 (1 $\mu\text{g}/\text{mL}$), with the red regions indicating the incubation of HapIn1 (5 $\mu\text{g}/\text{mL}$). **B** Changes in Δf and ΔD when HapIn1 is introduced to sparse (cyan and orange; $n = 4$) and dense (blue and red; $n = 6$) HA50 films. The values represent the changes in Δf and ΔD between the start and the end of HapIn1 incubation (the difference between the start and end of the red region). The mean and standard deviation are presented. The line below the graph represents statistical significance: $p \leq 0.05$ (*).

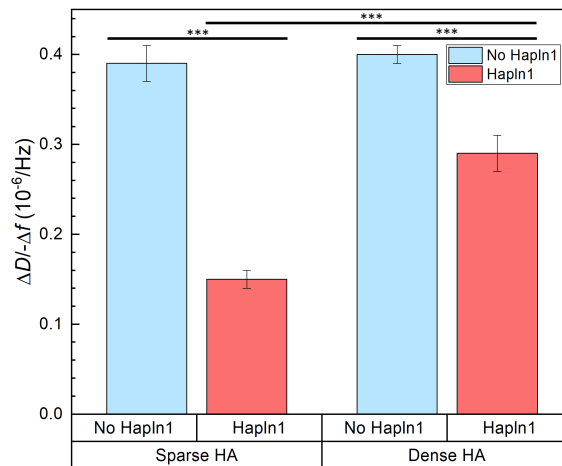


Figure 31. The ratio of $\Delta D / -\Delta f$ for sparse and dense HA50 films with and without the addition of HapIn1.

Sparse HA50 films without HapIn1 had a $\Delta D / -\Delta f$ ratio of $0.40 \pm 0.03 \times 10^{-6}/\text{Hz}$ ($n = 11$) and a $\Delta D / -\Delta f$ ratio of $0.15 \pm 0.01 \times 10^{-6}/\text{Hz}$ ($n = 4$) with the addition of HapIn1. Dense HA50 films without HapIn1 had a $\Delta D / -\Delta f$ ratio of $0.39 \pm 0.01 \times 10^{-6}/\text{Hz}$ ($n = 21$) and a $\Delta D / -\Delta f$ ratio of $0.29 \pm 0.02 \times 10^{-6}/\text{Hz}$ ($n = 6$) with the addition of HapIn1. The mean and standard deviation are presented. The lines above the graph represents statistical significance: $p \leq 0.0005$ (***)

4.3.3 Stabilisation of HA and Acan is achieved by the addition of Hapln1 irrespective of the order of incubation

Having established the interaction of Hapln1 and Acan individually on HA films, the next step was to understand how the three molecules interact together to form macromolecular HA / Hapln1 / Acan films. The order of incubation of Hapln1 and Acan was investigated to determine if the presence of one of the molecules affects the interaction of the other molecule with the HA50 films. If Hapln1 is then immediately presented to the surface following Acan incubation a large decrease in Δf and a large increase in ΔD can be observed (Figure 32D). Therefore, Hapln1 was able to interact with the HA / Acan surfaces. After HAPLN1 addition, during the wash step Δf values did not increase and values of ΔD did not decrease (Figure 32E). This implied that following Hapln1 incubation Acan bound stably to the HA films.

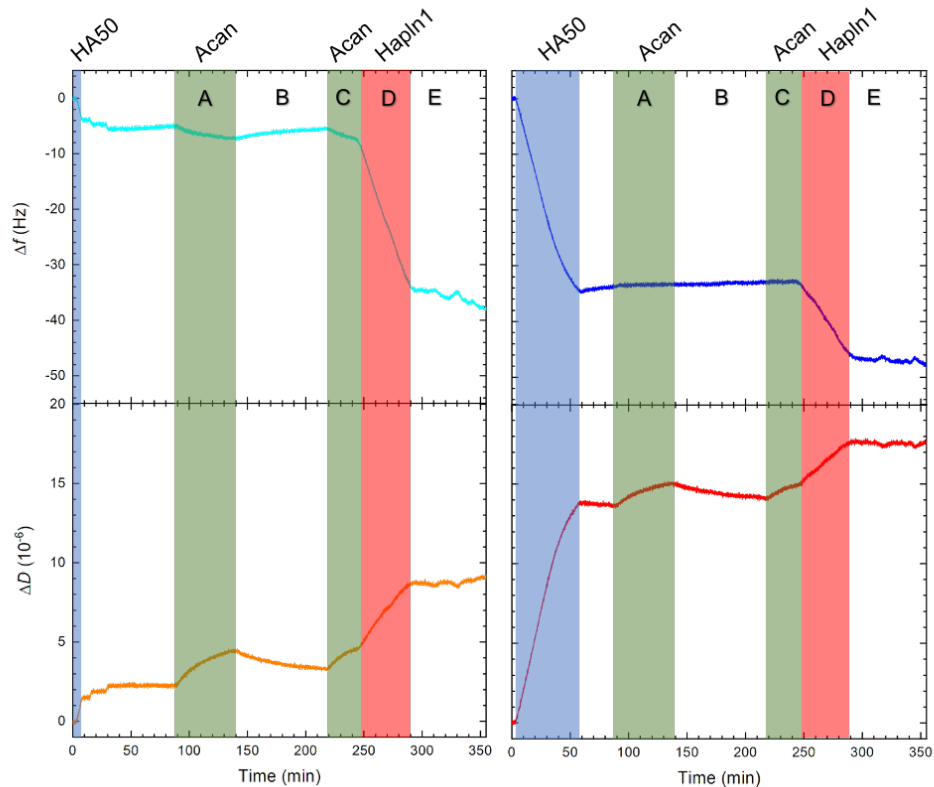


Figure 32. Acan interacts unstably with sparse (cyan and orange) and dense (blue and red) HA films without the presence of Hapln1.

Representative Δf and ΔD QCM-D plots for sparse ($n = 2$) and dense ($n = 2$) HA films. **A** The incubation period for Acan ($100 \mu\text{g/mL}$): $\Delta f = -2 \pm 0 \text{ Hz}$, $\Delta D = 2 \pm 0 \times 10^{-6}$ for sparse HA films and $\Delta f = -0.5 \pm 0.5 \text{ Hz}$, $\Delta D = 1.5 \pm 0 \times 10^{-6}$ for dense HA films. **B** Wash step following Acan incubation. **C** Re-incubation period of Acan ($100 \mu\text{g/mL}$): $\Delta f = -2 \pm 0 \text{ Hz}$, $\Delta D = 1 \pm 0 \times 10^{-6}$ for sparse HA films and ($\Delta f = 0.5 \pm 0.5 \text{ Hz}$, $\Delta D = -1.25 \pm 0.25 \times 10^{-6}$ for dense HA films. **D** The incubation period for Hapln1 ($5 \mu\text{g/mL}$): $\Delta f = -37 \pm 6 \text{ Hz}$, $\Delta D = 5.25 \pm 0.75 \times 10^{-6}$ for sparse HA films and $\Delta f = -18 \pm 1 \text{ Hz}$, $\Delta D = 3.25 \pm 0.25 \times 10^{-6}$ for dense HA films. **E** The wash step following Hapln1 incubation. The coloured areas represent the incubation period for HA (blue), Acan (green) and Hapln1 (red).

The sequential order of incubation was then switched so Hapln1 was presented to HA films first, followed by Acan incubation (Figure 33). Following Acan incubation to HA / Hapln1 films Acan Δf and ΔD values remained stable (Figure 33D). Therefore, Hapln1 was able to stabilise the interaction of Acan to HA films, irrespective of the order of incubation. The binding of Hapln1 to HA films did not interfere with its ability to stabilise Acan.

During the wash step following Hapln1 incubation over dense and sparse HA films there was no change in Δf or ΔD (Figure 33B). Therefore, the interaction of Hapln1 with HA films is stable, without the presence of Acan.

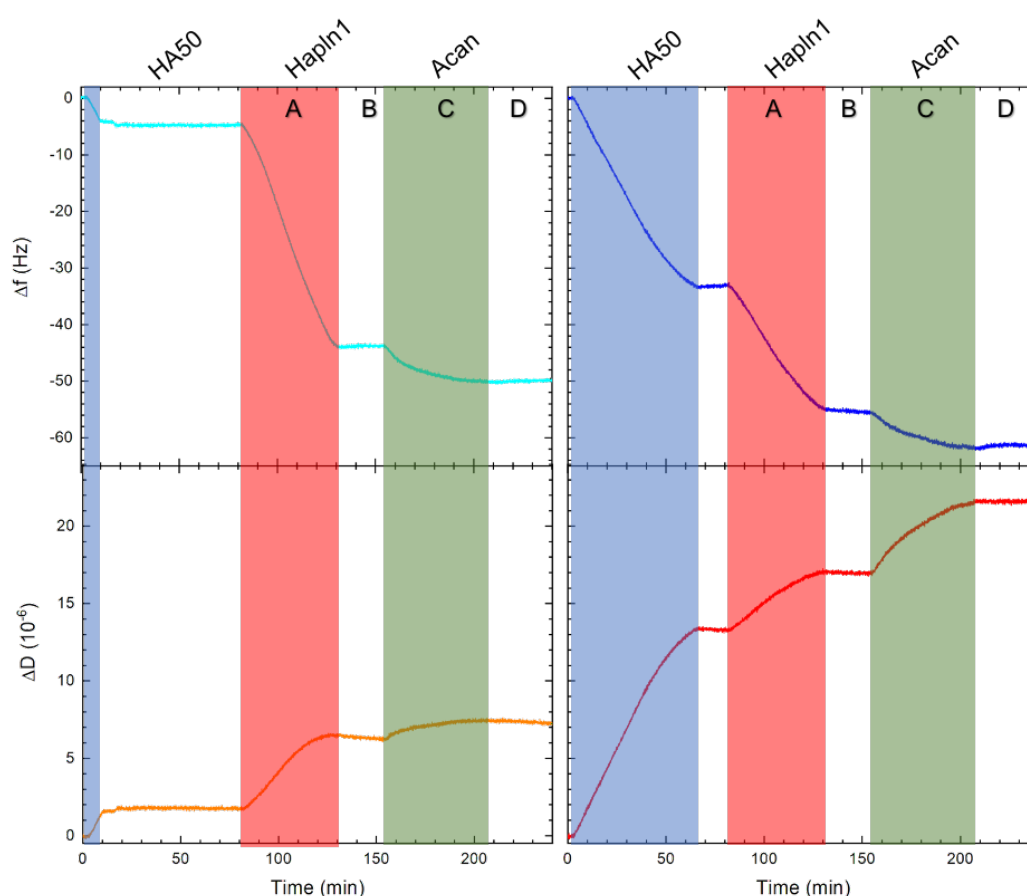


Figure 33. Acan interacts stably with sparse (cyan and orange) and dense (blue and red) HA / Hapln1 films.

Representative Δf and ΔD QCM-D plots for sparse ($n = 4$) and dense ($n = 6$) HA films. **A** The incubation period for Hapln1 ($5 \mu\text{g/mL}$): $\Delta f = -42 \pm 6 \text{ Hz}$, $\Delta D = 5 \pm 0.4 \times 10^{-6}$ for sparse HA films and $\Delta f = -29 \pm 10 \text{ Hz}$, $\Delta D = 5.1 \pm 1.1 \times 10^{-6}$ for dense HA films. **B** Wash step following Hapln1 incubation. **C** The incubation period for Acan ($100 \mu\text{g/mL}$): $\Delta f = -6.5 \pm 2.5 \text{ Hz}$, $\Delta D = 1.6 \pm 0.9 \times 10^{-6}$ for sparse HA films and $\Delta f = -7 \pm 3 \text{ Hz}$, $\Delta D = 4.5 \pm 0.3 \times 10^{-6}$ for dense HA films. **D** The wash step following Acan incubation. The coloured areas represent the incubation period for HA (blue), Hapln1 (red) and Acan (green).

4.3.4 The density of HapIn1 influenced Acan interaction with HA / HapIn1 films

To further understand how HapIn1 influenced the interaction of Acan with HA films, HA / HapIn1 films of different HapIn1 density were created to observe how Acan interacted with them. When comparing the interaction of Acan on sparse HA films with either no HapIn1, sparse amounts of HapIn1 or dense amounts of HapIn1 it is clear that the interactions are not equal (Figure 34). The change in Δf and ΔD on Acan incubation were not significantly different for sparse HA films ($\Delta f = -1.8 \pm 0.4$ Hz, $\Delta D = 2.3 \pm 0.4 \times 10^{-6}$) alone and sparse HA / sparse HapIn1 films ($\Delta f = -2.5 \pm 0.7$ Hz, $\Delta D = 3.5 \pm 0 \times 10^{-6}$) however, the change in the ratio of $\Delta D / -\Delta f$ was. Interestingly, in the sparse HA / dense HapIn1 condition a significantly larger decrease in Δf ($\Delta f = -6.5 \pm 2.5$ Hz) was measured in comparison to the other conditions, however this correlated with a significantly smaller shift in ΔD ($\Delta D = 1.6 \pm 0.9 \times 10^{-6}$). Therefore, the ratio of $\Delta D / -\Delta f$ was significantly smaller in the sparse HA / dense HapIn1 condition. Therefore, on sparse HA films Acan was less able to influence the mechanical properties as the density of HapIn1 increased. Sparse HA surfaces with less HapIn1 become more compliant on Acan incubation.

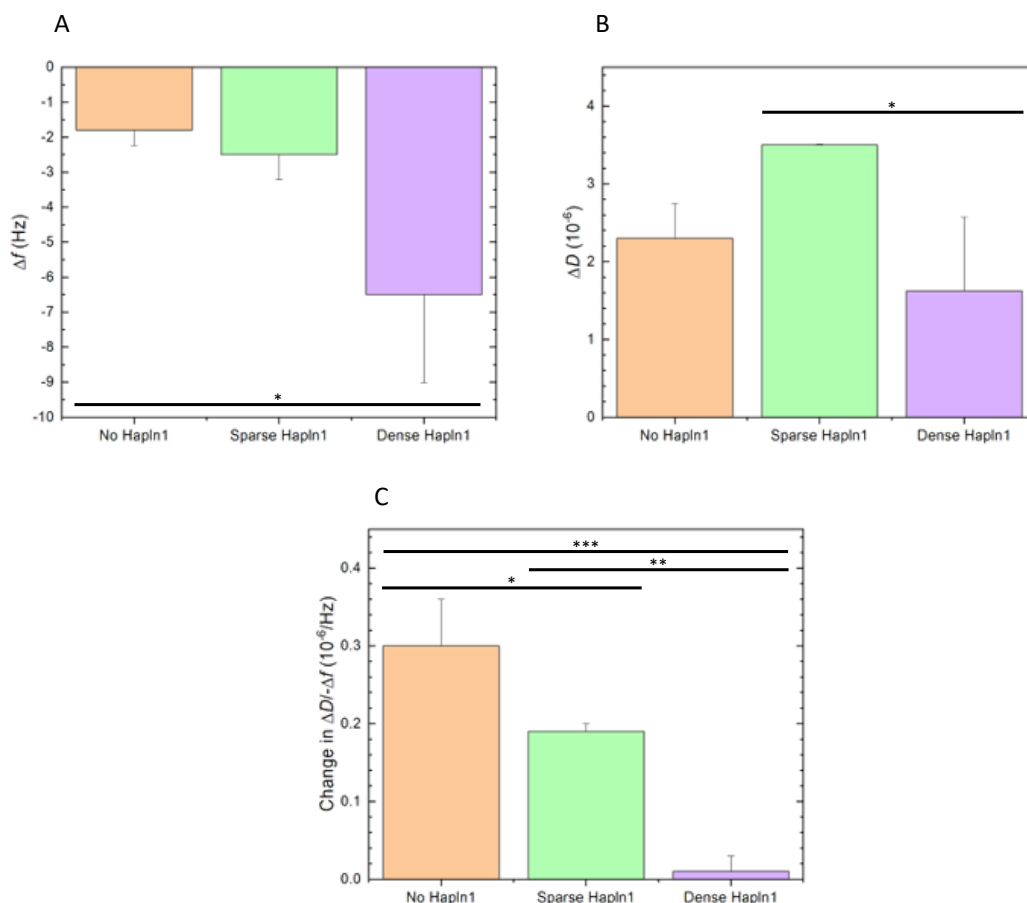


Figure 34. The density of Hapln1 within sparse HA films influenced the ability of Acan to change the $\Delta D / -\Delta f$ ratio.

Sparse HA films with either no Hapln1 (n = 5, beige), sparse amounts of Hapln1 (n = 2, green) or dense amounts of Hapln1 (n = 4, purple) were compared. **A** The change in Δf values on Acan incubation. **B** The change in ΔD values on Acan incubation. **C** The change in the $\Delta D / -\Delta f$ ratio on Acan incubation. The lines above the graph (below in A) represents statistical significance: $p \leq 0.05$ (*), $p \leq 0.005$ (**), and $p \leq 0.0005$ (***)

When Acan was incubated over dense HA films with no Hapln1 ($\Delta f = 0.7 \pm 1.2$ Hz, $\Delta D = 1.6 \pm 0.2 \times 10^{-6}$) and sparse amounts of Hapln1 ($\Delta f = 0.6 \pm 0.5$ Hz, $\Delta D = 1.8 \pm 0.3 \times 10^{-6}$), the change in values of Δf and ΔD were not significant (Figure 35A, B). The change in Δf and ΔD was significantly larger in the dense HA / dense Hapln1 condition ($\Delta f = -7 \pm 3$ Hz, $\Delta D = 4.5 \pm 0.3 \times 10^{-6}$) in comparison to the other conditions. Interestingly, in contrast to sparse HA surfaces, the change in the ratio $\Delta D / -\Delta f$ was unaffected by the density of Hapln1 (Figure 35C). Therefore, regardless of the density of Hapln1 present in the HA film, Acan influenced the mechanical properties of the films similarly, causing them to become slightly more compliant. It is important to note that although the surfaces become more compliant, the increase in the ratio of $\Delta D / -\Delta f$ is small.

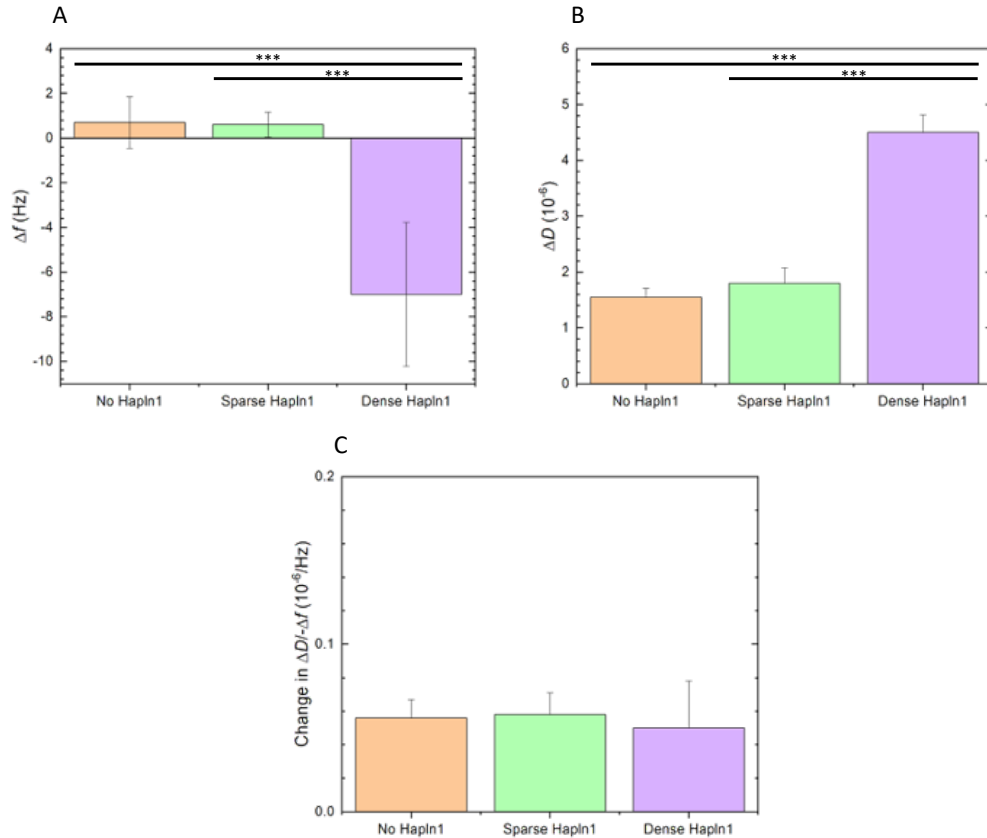


Figure 35. The density of Hapln1 within dense HA films did not influence the ability of Acan to change the $\Delta D / -\Delta f$ ratio.

Dense HA films with either no Hapln1 ($n = 10$, beige), sparse amounts of Hapln1 ($n = 5$, green) or dense amounts of Hapln1 ($n = 6$, purple) were compared. **A** The change in Δf values on Acan incubation. **B** The change in ΔD values on Acan incubation. **C** The change in the $\Delta D / -\Delta f$ ratio on Acan incubation. The lines above the graph represents statistical significance: $p \leq 0.0005$ (***)

4.3.5 Tn-R was not detected interacting with the HA / Hapln1 / Acan films

Having established stable HA50 / Hapln1 / Acan films the aim was to analyse how Tn-R, another PNN-associating molecule that has been linked with cross-linking Acan via the G3 domain, interacted with the films. Tn-R was not detected interacting with either the sparse HA50 or dense HA50 films that contained dense amounts of Hapln1 and Acan (Figure 36). This was an unexpected result as the assumption would be that Tn-R would be able to interact with the Acan present within the films. The result may indicate that the interaction of Tn-R with Acan cannot be detected due to the interaction taking place too far away from the sensor surface to be detected by shifts in Δf or ΔD . However, as Tn-R is hypothesised to cross-link CSPGs the expectation would have been that the interaction would have been detected by a decrease in $\Delta D / -\Delta f$ (Aspberg, 1995; Chiquet-Ehrismann and Tucker, 2011; Morawski *et al.*, 2014). Another possibility is that Tn-R is unable to interact with Acan

within the films due to the conformation of the film preventing the interactions from taking place. If the G3 domains of Acan are not present on the surface of the film, then the interaction with Tn-R may not be possible due to steric hinderance. Due to the size of Acan being distinctively larger than the HA50 and Hapln1 molecules it is unlikely that all the G3 domains would be concealed within the film. One further possibility is that the bovine articular cartilage Acan present within the films may not contain G3 domains. As the percentage of G3 positive Acan molecules in the bovine articular cartilage was unknown this was considered to be the most likely explanation for the lack of Tn-R interactions observed.

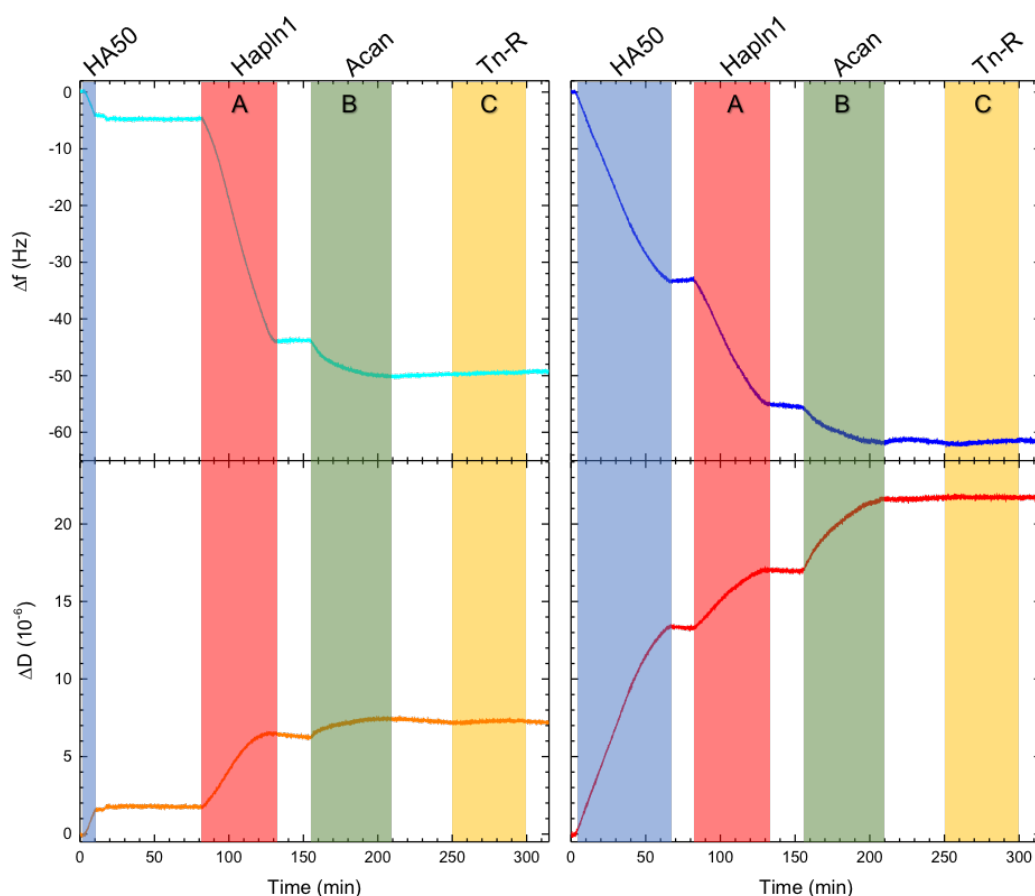


Figure 36. Both sparse HA50 (cyan and orange lines) and dense HA50 (blue and red lines) films containing Hapln1 and Acan did not interact with Tn-R. Representative Δf and ΔD QCM-D plots for sparse ($n = 2$) and dense ($n = 2$) HA films. **A** The incubation period for Hapln1 ($5 \mu\text{g/mL}$). **B** The incubation period for Acan ($100 \mu\text{g/mL}$). **C** The incubation period for Tn-R ($20 \mu\text{g/mL}$) where no detectable changes in ΔD or Δf were observed. The coloured areas represent the incubation period for HA (blue), Hapln1 (red), Acan (green) and Tn-R (yellow).

To further understand why Tn-R was not detected interacting with the films the interaction assay and surface functionalisation with the QCM-D chamber was changed and used to investigate whether the interaction of Tn-R and Acan could be detected using QCM-D. This was achieved by using a lipid bilayer that contained tris-Ni²⁺-NTA groups that could anchor Tn-R molecules via their C-terminal polyhistidine-tag, which would be expected to lead to a favourable protein orientation on the surface (Figure 37). This meant that a stable surface of Tn-R could be produced that allowed Acan samples to be injected over it. As the interaction would occur closer to the sensor surface it was more likely to be detected by shifts in Δf and ΔD . This setup was possible as both the bovine articular cartilage Acan and pig laryngeal Acan samples used do not contain polyhistidine-tags. The reason for using pig laryngeal cartilage was due to it being mostly void of G3 domains. As the interaction of Tn-R with Acan is known to be calcium-dependent via the G3 domains of Acan the expectation was that Tn-R would be unable to interact with the pig laryngeal Acan and would only interact in conditions that contained calcium ions (Aspberg, 1995; Aspberg *et al.*, 1997).

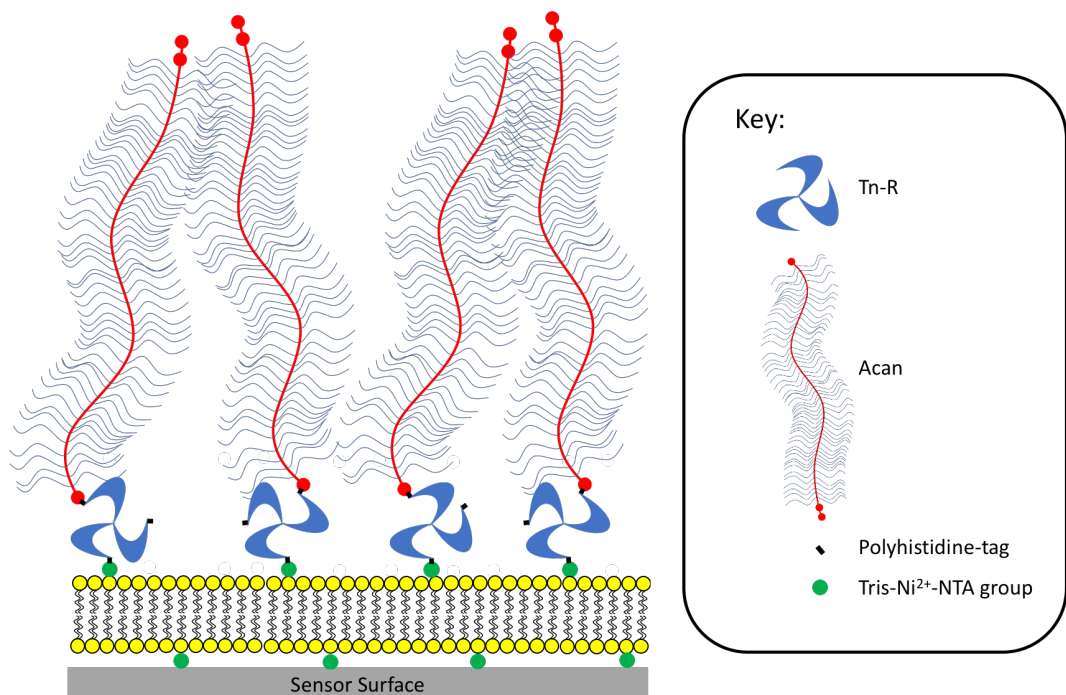


Figure 37. A schematic representation of the predicted interaction of Tn-R and Acan when the Tn-R is trapped to the sensor surface via a lipid bilayer containing tris-Ni²⁺-NTA groups.

Tn-R stably interacted with the DODA-tris-Ni²⁺-NTA lipid bilayer (Figure 38A). Unexpectedly, the interaction of Tn-R with the tris-Ni²⁺-NTA groups was

negatively affected by the presence of EGTA, as following Tn-R incubation shifts in Δf and ΔD were $\Delta f = -4.5 \pm 0.5$ Hz, $\Delta D = 1.5 \pm 0.3 \times 10^{-6}$ (n = 3) in the no calcium ion conditions and $\Delta f = -19 \pm 4.6$ Hz, $\Delta D = 3.7 \pm 0.9 \times 10^{-6}$ (n = 5) in conditions containing calcium ions. Although the interaction of the Tn-R polyhistidine-tag with the tris-Ni²⁺-NTA group is not calcium ion dependent, the presence of EGTA may have chelated Ni²⁺ ions that are involved in the process, resulting in the differences observed. To observe whether the two Acan samples interacted with the lipid bilayer controls were ran by injecting Acan into the chamber without the presence of Tn-R. Both bovine articular cartilage ($\Delta f = -1.5 \pm 0.5$ Hz, $\Delta D = 0.8 \pm 0.01 \times 10^{-6}$; n = 2) and pig laryngeal Acan ($\Delta f = -1.5$ Hz, $\Delta D = 2 \times 10^{-6}$; n = 1) interacted with the lipid bilayer, though the responses were small, suggesting that the interactions were minor. To account for these non-specific interactions these values were subtracted from the Δf and ΔD values when assessing the interaction of the Acan samples with Tn-R.

Both bovine articular cartilage and pig laryngeal Acan were not detected interacting with Tn-R in conditions without calcium ions, as no shifts in Δf or ΔD were observed (Figure 38). When bovine articular cartilage Acan was presented to Tn-R that was pre-bound to the lipid bilayer an interaction was detected that was more than the non-specific interactions of Acan with the lipid bilayer ($\Delta f = -1 \pm 0.5$ Hz, $\Delta D = 2.9 \pm 0.15 \times 10^{-6}$; n = 3). In contrast, when pig laryngeal cartilage was presented to the same surfaces the interactions were minor, as the shifts in Δf and ΔD were very similar to the shifts observed when presented to the lipid bilayer alone. Therefore, these results indicated that the interaction of Tn-R and Acan can be detected using QCM-D, with the interactions behaving as expected, as it required the presence of Acan G3 domains and calcium ions (Aspberg, 1995; Aspberg *et al.*, 1997).

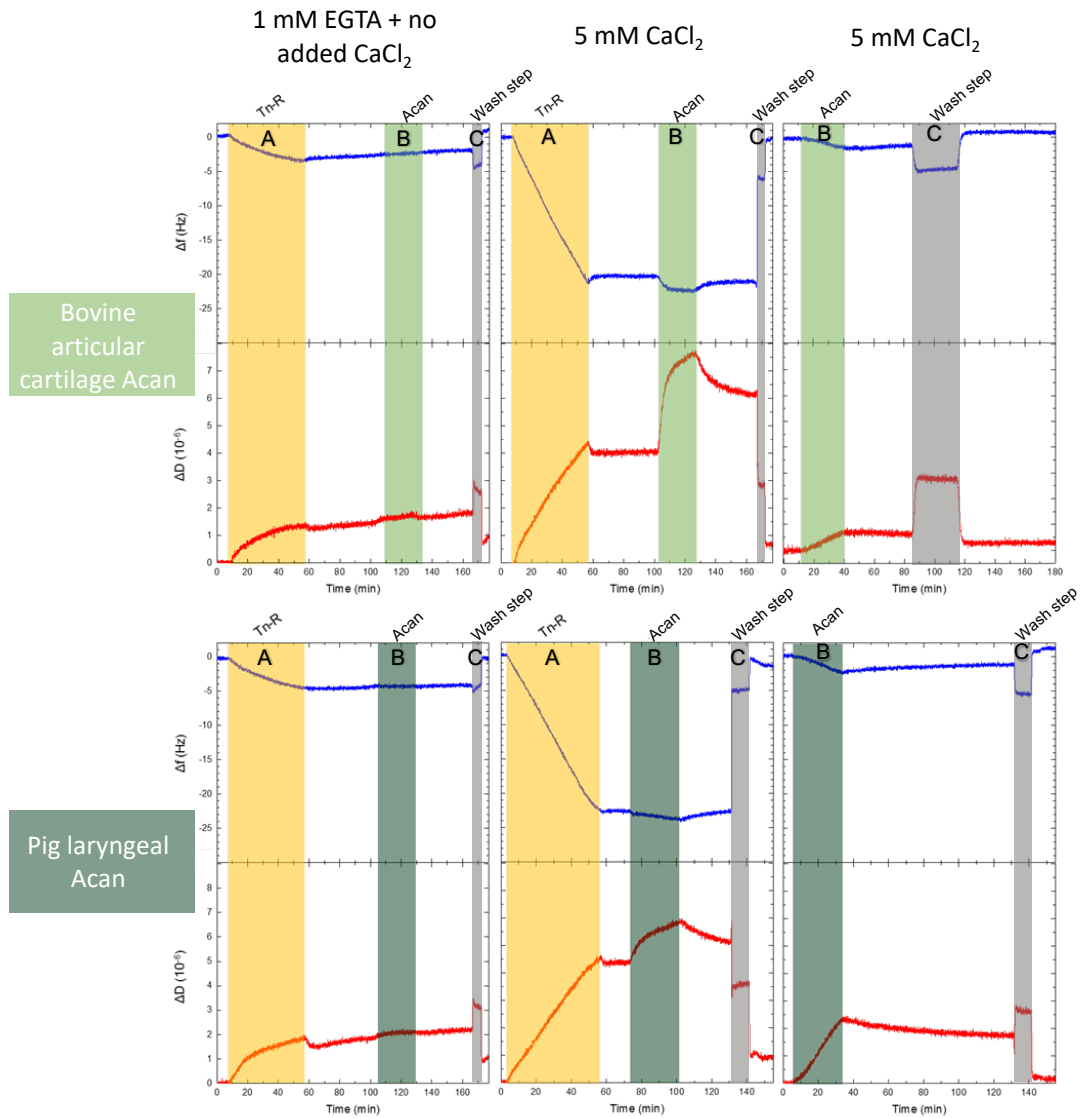


Figure 38. Tn-R interacts with bovine articular cartilage Acan in a calcium-dependent manner.

Representative Δf and ΔD QCM-D plots for the interaction of bovine articular cartilage (light green ; 100 $\mu\text{g/mL}$). and pig laryngeal cartilage (dark green; 100 $\mu\text{g/mL}$) with Tn-R (yellow ; 20 $\mu\text{g/mL}$). The top row represents bovine articular cartilage, while the bottom row represents pig laryngeal Acan. The plots in the leftmost column represent experiments conducted without calcium ions due to the addition of 1mM EGTA (a calcium ion chelator) to the HEPES buffer. Both the middle and rightmost columns represent experiments conducted in HEPES buffer with the addition of 5 mM CaCl_2 . The wash step (grey) involved injecting 500 mM imidazole into the chamber. In all experiments following the wash step both Δf and ΔD returned to the baseline. **A** The incubation period for Tn-R. **B** The incubation period for Acan. **C** The incubation period for 500 mM imidazole. The shifts in Δf and ΔD detected when moving from imidazole to HEPES buffer do not represent surface events but are due to changes in the solution viscosity and density upon imidazole addition which are also sensed by QCM-D.

4.4 Discussion

Through the successful establishment of a model surface for analysing the supramolecular self-organisation of PNN components, the importance of HA density has been highlighted. The binding of both Acan and Hapln1 were both affected by manipulating the density of HA50 films. Furthermore, the density of Hapln1 also influenced Acan interaction with HA / Hapln1 films, indicating that density of PNN components may be an important and integral factor in PNN assembly. The stabilisation of HA and Acan is achieved by the addition of Hapln1 irrespective of the order of incubation, emphasising the importance of Hapln1 in stabilising the supramolecular PNN surface.

The interaction of Acan with HA films required Hapln1 to stabilise the interaction. Acan interaction with HA films alone is unstable. This supported previous work that measured the interaction of HA, Hapln1 and the G1 domain of Acan using SPR (Shi *et al.*, 2004). Shi *et al* (2004) used pre-incubated Acan and Hapln1 and incubated them over HA surfaces together. Furthermore, Acan has previously been observed to interact with HA films reversibly (Attili and Richter, 2013).

The results in this chapter suggested that Acan and Hapln1 do not need to form a complex prior to being introduced to HA films to form HA / Hapln1 / Acan complexes. Therefore, the sequential order of incubation of Hapln1 and Acan was unimportant for the formation of stable macromolecular complexes. In the formation of PNNs, Hapln1 has previously been highlighted as an essential component to the stable interaction of CSPGs with HA, as when Hapln1 is not present PNN surfaces are more diffuse and unstable (Carulli *et al.*, 2010; Kwok *et al.*, 2010). Mechanistically, this may partially be explained through the reversible binding of CSPGs to surface-bound HA without the presence of link protein.

Hapln1 was able to interact with Acan when already bound to HA. The Acan binding site on Hapln1 was unimpeded by the interaction of Hapln1 with HA. Equally, Acan was able to form a stable complex with Hapln1 even when previously bound to HA. Although the crystal structure of Hapln1 is not known, it implied that the HA and Acan binding sites on the Hapln1 molecules must be spaced far enough away to not sterically impede each other.

The interaction of Hapln1 with HA films was stable without the presence of Acan being required. This could present a potential mechanism for the restricted formation of PNNs on cell surfaces. HA is ubiquitously present in the pericellular space of most cells and within the CNS CSPGs are abundant

and integral to the ECM, yet not all cells in the CNS produce PNNs (Deepa *et al.*, 2006; Rodriguez-Martinez *et al.*, 2016). Potentially, Hapln1 may be required to stably interact with surface-bound HA, whereby the stabilised interaction would result in an accumulation of Hapln1 over time. As HA / Hapln1 films are able to stably interact with Acan, they would aggregate Acan over time. This may partially explain why the formation of PNNs was reduced without the presence of Hapln1 to stabilise the PNN structure.

Dense HA films resulted in a reduction in the molecular interactions on Acan and Hapln1 incubation in comparison with sparse HA films. Therefore, a reduction in HA density resulted in an increase in surface-bound molecules. As the sparse HA films were specifically designed to space the HA molecules at a distance similar to the thickness of Acan molecules, this result implied that the reduced interaction with dense HA films is a result of steric hindrance. With the HA molecules spaced close together both Acan and Hapln1 appear to be unable to penetrate into the surface. On sparse HA films more binding sites were accessible which resulted in the greater interaction observed in this condition. This result suggests the importance of HA density within the pericellular space during the formation of PNNs. Currently, it is unknown how densely packed the HA molecules are within the pericellular space during the formation of PNNs. Potentially, further research could be done to predict this density by assessing the density of HAS molecules present within the cell surface using histochemical and imaging techniques.

The introduction of Acan to both sparse and dense HA films caused an increase in $\Delta D / -\Delta f$ that is likely to be a consequence of two-dimensional confinement (Attili and Richter, 2013). The increase in $\Delta D / -\Delta f$ suggested that there is a swelling of the HA films that caused the softening effect measured. This swelling of the HA film and stretching of the HA chains is likely caused by a combination of volume exclusion by the presence of the additional Acan molecules and electrostatic repulsion caused by the negatively charged GAG chains (Attili and Richter, 2013). On sparse HA films caused the ratio $\Delta D / -\Delta f$ to increase, while this increase was small on dense HA films. On sparse HA films it suggested that Acan was able to interact between the HA molecules, as was previously observed on larger HA molecules where the interaction of Acan greatly increased the value of ΔD (Attili and Richter, 2013). Therefore, the surfaces become more compliant as a result of the combination of HA and Acan forming a homogenous film. In contrast, the limited increase in the $\Delta D / -\Delta f$ ratio measured on dense HA films

suggested that the surface being formed was different. Potentially, Acan was only able to interact with the top of the dense HA50 surface. As the ratio of $\Delta D / -\Delta f$ is a measurement of the bulk surface, potentially the Acan may not interact in large enough densities to form a homogenous film on the surface of HA50 to effect the mechanical properties of the bulk film (Reviakine *et al.*, 2011). Future work investigating the topological properties of the surfaces formed by AFM may provide a greater indication of whether this explanation is correct.

The interaction of HapIn1 with HA films alone was influenced by the density of the HA film. HapIn1 caused a reduction in the ratio $\Delta D / -\Delta f$ which implied that HapIn1 is able to rigidify the surface, making it less compliant. This effect was more pronounced on sparse HA films, likely as a consequence of the increased HapIn1 interactions. This presents a potential mechanism for influencing the biomechanical properties of HA films through varying the degree of HapIn1 interaction.

Furthermore, the density of HapIn1 also influenced the molecular binding of Acan. On sparse HA films, the presence of dense amounts of HapIn1 caused a reduction in the ability of Acan to affect the $\Delta D / -\Delta f$ ratio. This may suggest that a high density of HapIn1 is able to collapse the HA films. This would present a scenario similar to the dense HA50 films, as Acan could then only interact with the top of the sparse HA surface. Without being able to incorporate into the HA surface Acan would be unable to influence the mechanical properties of the bulk HA surface. As HapIn1 density is reduced, the HA becomes less collapsed, thereby allowing Acan to become more incorporated into the HA surface between the HA molecules, where it could then affect the bulk properties of the surface more significantly. Therefore, this presents a potential mechanism for influencing the mechanical properties of PNNs through the regulation of HapIn1 density.

The observation that Tn-R was not detected interacting with HA films that contained Acan suggested that there may not be enough Acan G3 domains available within the film to interact with. Furthermore, the interaction of Tn-R with Acan could be detected using QCM-D when Acan was presented to surface-anchored Tn-R. The interaction behaved as expected, supporting previous results that Tn-R interacts with Acan via the G3 domain in a calcium dependent manner (Aspberg, 1995; Aspberg *et al.*, 1997). This result also provided evidence that the Acan sample used to create the *in vitro* PNN model surfaces does contain G3 domains. However, as the experiment used pre-bound Tn-R that would only interact with G3 containing Acan variants, what

remains unknown is the percentage of Acan variants within the bovine articular cartilage Acan that are G3 positive. As the shifts in both Δf and ΔD were relatively small, it may indicate that the percentage of G3 positive Acan molecules is also small. This may explain why the interaction of Tn-R with Acan was not detectable.

Through the demonstration of stable HA / Hapln1 / Acan films being formed within the QCM-D chambers, these results provided a proof of principle that it is possible to establish an *in vitro* PNN model surface using QCM-D that can measure both biochemical and biomechanical properties of the surface in real-time. As PNNs have been observed to be potentially therapeutically relevant to a variety of neurological diseases, it highlights the importance of producing a method to interrogate PNN surfaces in an *in vitro* system that has the ability to be commercially scaled (Morawski *et al.*, 2004; Pantazopoulos *et al.*, 2010; McRae and Porter, 2012; Yang *et al.*, 2015; Rankin-Gee *et al.*, 2015; Enwright *et al.*, 2016). To develop this model further, a measurement for the range of sizes of HA present within PNNs is required. Furthermore, developing this method through the purification of other PNN molecules, such as the other CSPGs and Haplns found in PNNs will allow for the recreation of more accurate PNN surfaces.

In conclusion, a new technique for modelling the formation of PNNs has been established. This new method provides an extremely useful platform for the study and analysis of various PNN molecules to its formation. The technique has provided unique insights into the formation of PNNs, as irrespective of the order of incubation Hapln1 and Acan were able to form stable, PNN-like, macromolecular structures with surface-bound HA. Through altering the density of surface-bound HA, as well as the density of Hapln1 the mechanical properties of the films can be altered. Therefore, this indicates two potential mechanisms for altering the biomechanical properties of PNNs.

Chapter 5: Sizing GAGs

5.1 Introduction

This chapter focuses on the production of a methodology to measure the size of GAG chains using QCM-D. Although the methodology could eventually be used to measure the size of any disordered polysaccharide chain, the methodology has been produced and optimised for measuring the size of HA chains. The use of this method for measuring other GAG chains will be considered in the discussion section, with the introduction specifically focussing on the importance of HA size. As well as being the molecule that optimised the methodology, it is also essential for the formation PNNs (Kwok *et al.*, 2010). Unlike other GAGs, HA is not sulfated and has no known post-translational modifications, Therefore the size of the HA chains and where they are expressed are likely to contribute a major part of their function.

HA function and biosynthesis by HAS is described in detail in section 1.4.1, therefore this chapter will focus specifically on the size of HA and the methodologies that can measure the size of the polymer chains. HA is known to have different biological functions depending on size (Jiang *et al.*, 2007; Cyphert *et al.*, 2015; Tavianatou *et al.*, 2019). HA chain length appears to influence cell apoptosis, proliferation and mobility in vertebrates (West and Kumar, 1989; Day and Prestwich, 2002; Ghatak *et al.*, 2002; Noble, 2002; Stern, 2003; Jing *et al.*, 2006). The importance of HA size is suggested by the presence of 3 isozymes of HAS (HAS1, HAS2 and HAS3) that synthesise differing lengths of HA chains (Itano *et al.*, 1999). HAS1 and HAS2 synthesise longer HA chains (200 kDa to 2 MDa) in comparison with HAS3 that synthesises shorter HA chain lengths (100 kDa to 1 MDa) (Itano *et al.*, 1999). The range of sizes synthesised by HAS1 and HAS2 also differed, as HAS2 consistently produced the largest HA chains, with HAS1 synthesising a wider range of HA sizes (Itano *et al.*, 1999). The HAS enzymes also show differential expression patterns throughout embryogenesis, with HAS1 being preferentially expressed during early stages of development, HAS3 in late stages of development and HAS2 expression occurring throughout development, overlapping with the expression of both HAS1 and HAS3 (Tien and Spicer, 2005). Within the mature CNS it has been observed that HAS1 mRNA is absent in the adult cerebellum (Carulli *et al.*, 2006), though present in other regions suggesting that the pattern of HAS expression may differ in different CNS regions.

In addition to control of HA size being regulated by its synthesis, the breakdown of HA by hyaluronidases present a second method for regulating HA size. Hyaluronidases function by specifically hydrolysing the β -1,4 linkage of the HA molecule (Stern, 2004; Stern and Jedrzejas, 2006). The expression pattern of different hyaluronidases differ throughout the mammalian body (Triggs-Raine *et al.*, 1999). Hyaluronidases are known to be important in regulating the concentrations of HA, as deficiencies in hyaluronidases are associated with certain disorders including mucopolysaccharidosis IX, where increased levels of HA are observed (Natowicz *et al.*, 1996; Triggs-Raine *et al.*, 1999). It is also worth noting that reactive oxygen species produced during the inflammatory response have the ability to breakdown HA chains (Šoltés *et al.*, 2006). Smaller HA chain sizes are associated with the inflammatory response, though alone do not appear to be enough to trigger inflammation in the skin (Muto *et al.*, 2014). What is currently unknown is if hyaluronidases are used to regulate the size of HA chains tethered to the surface of cells.

HA size is also an important consideration when determining its function in forming supramolecular assemblies with proteins. HA size could alter the ability for these structures to form, as well as potentially alter the biomolecular properties of the supramolecular assemblies. When discussing supramolecular assemblies throughout this thesis it has been in reference to the assembly of PNNs. However, it is important to note HA is important in the production of other supramolecular assemblies. One example is in the formation of cartilage, where HA is responsible for producing the soft, hydrated ECM supramolecular composition that helps protect joints from compressive forces, while also lubricating the joint (Balazs *et al.*, 1967). In young, healthy cartilage, the majority of HA sizes were over 2.5 MDa, however, age-related decreases in HA size were observed over time, which correlated with decrease in the joint quality (Temple-Wong *et al.*, 2016). Another example of a supramolecular assembly where HA is essential is the assembly of the cumulus cell-oocyte complex (COC) matrix (Cherr *et al.*, 1990). Like PNNs, the COC matrix requires cross-linking to stabilise the structure, as when cross-linking proteins were enzymatically degraded the structure was unstable (Cherr *et al.*, 1990). Research on the COC matrix has identified heavy chains as direct cross-linkers of HA (Zhuo *et al.*, 2001), as well as indirect cross-linkers including a tertiary complex involving pentraxin 3 (PTX3), TNF-stimulated gene-6 (TSG-6) and inter- α -inhibitor (I α I) (Salustri *et al.*, 2004; Scarchilli *et al.*, 2007; Baranova *et al.*, 2013; Baranova *et al.*, 2014). TSG-6 induced cross-linking of HA has also been suggested as being

important to the inflammatory response (Baranova *et al.*, 2011). The ability for HA to cross-link is likely to be dependent on the size of the HA chains.

HA size is also important for recognition of cell surface receptors, such as CD44, where the mechanism of superselectivity has been proposed (English *et al.*, 1998; Lesley *et al.*, 2000; Wolny *et al.*, 2010; Dubacheva *et al.*, 2015). The mechanism of superselectivity proposed by Dubacheva *et al.* (2015) directly implicates HA size as an important factor in this mechanism as increased HA size facilitated increased binding to more CD44 receptors, strengthening the interaction on artificial membranes (Wolny *et al.*, 2010).

It is important to note that there is a growing number of therapeutic products that are incorporating HA, therefore there is a requirement for the stringent quality control of HA that will include sizing of the HA chains, that would benefit from methodologies that can size HA efficiently and cheaply (Goa and Benfield, 1994). Protocols that aim to do this may eventually be useful to industrial applications, as well as to academia.

Defining the relative size ranges of HA chains is important, as currently there is no agreed nomenclature for defining the different HA size ranges. A consequence of this is the differential categorisation of HA chains into HMW and low molecular weight (LMW). Depending on the article LMW HA can be categorised from being a few disaccharides to being 700 kDa (Cyphert *et al.*, 2015). Although there is agreement that HA chains of over 1 MDa are considered HMW (Cyphert *et al.*, 2015), there is still debate on where the lower boundary of HMW HA should be. For this reason, throughout this chapter instead of using the HMW and LMW nomenclature, the sizes of the HA chain ranges will instead be directly stated.

Methodologies for measuring the size of GAGs, as well as other polysaccharide chains are limited due to the disordered nature of the molecules. Unlike proteins that are more stable and can have their structure resolved using imaging techniques this is not possible with polysaccharides, as they do not form secondary or tertiary structures with themselves. The techniques for assessing GAG chain size often require a large amount of time to undertake and require a large volume of sample. Techniques that have been used in the past and will be discussed further in the following paragraphs include: AFM, polyacrylamide gel electrophoresis (PAGE), size exclusion chromatography - multi-angle laser light scattering (SEC-MALLS) and more recently solid-state nanopore sensors.

The benefit of using AFM to image GAGs by electrochemically trapping GAGs to a mica surface to prevent the movement of the chains is that through imaging multiple chains the heterogeneity of each GAG sample can be directly observed. Imaging the GAG chains and measuring the chains from the images generates a precise measure of GAG chain size, as demonstrated by the use of the technique to measure the size of CS chains attached to the core protein of Acan (Ng *et al.*, 2003). The major drawback to this technique is the time taken to produce these measurements. Firstly, optimising an AFM methodology to create HA surfaces that are sparse enough to image, while dense enough to allow for multiple HA chains to be imaged at any one time is not a trivial task. The deposition of molecules is also potentially problematic for accurately measuring chain size, as if the HA chains coil, or form larger complexes with itself, it makes measuring chain length difficult or impossible. Furthermore, purifying the HA chains to a degree that allows for optimal imaging that avoids impurities in the starting sample is also not a simple task. Then optimising the AFM settings to image the HA chains and imaging enough HA chains to determine an average HA size for the population of HA molecules makes it prohibitively time consuming to perform on heterogeneous material. The major benefit of this technique is if the time was taken to perform the analysis a very precise measure of the size and heterogeneity of the HA chains would be produced. Also, as a validation technique to check the size of a known HA sample AFM is a useful technique.

SEC-MALLS has been used successfully to quantify the size of HA chains (Hokputsa *et al.*, 2003). It provides quantitative data and is often used by companies to validate the size of synthesised HA, where the aim is to produce HA with a small range of sizes. The limitation of this technique is in its sensitivity, especially when sizing smaller HA fragments (Hokputsa *et al.*, 2003). Also, from a technical aspect the experiments require long run times and slow column flow rates meaning the use of this technique as a high-throughput method is limited by practical constraints.

A recent development is the use of solid-state nanopore sensors to quantitatively assess HA size using small amounts of material (Rivas *et al.*, 2018). For HA larger than 1 MDa it performs well, however for HA below 500 kDa it is less accurate (Rivas *et al.*, 2018). The current lack of accessibility of nanopore technology to laboratories is also another constraint on the use of the methodology currently. This method shows great promise as a quantitative method for measuring HA in solution, so may be a complimentary method for

assessing HA chains alongside a methodology for measuring HA chains that are tethered to surfaces.

PAGE has been used previously as a method for measuring HA chain length between 5 - 500 kDa (Bhilocha *et al.*, 2011; Cowman *et al.*, 2011). Furthermore, in chapter 3 PAGE was used to observe distinct differences in HA chain length in the CNS in comparison to other tissues such as cartilage. One benefit of the method is they are cheap and quick to conduct. Furthermore, the samples do not require purifying if the method is used alongside Western blotting with a HA probe, making it a useful technique when determining size composition from cell or tissue lysate with minimal sample preparation, as demonstrated in chapter 3. Equally, using purified HA samples PAGE can also be conducted using Alcian blue to stain the polysaccharide chains (Lin *et al.*, 1997). Using PAGE, it is possible to assess the broad heterogeneity of HA sizes in the sample, by measuring the length of the sample smear on the gel. It is also possible to size HA using a HA ladder of known sizes to standardise the results against (Lee and Cowman, 1994; DeAngelis *et al.*, 1998). Protein standards have not been used previously to characterise HA size because the negative charge imparted on proteins is provided by the binding of SDS to the protein chain, while HA chains are naturally negatively charged and do not associate with SDS. This results in HA migrating through the gel at different rates to the protein ladders, therefore the migration distance cannot be directly compared. This affect will be further compounded by the difference in hydrodynamic radius between protein, HA and other GAGs. To date, no study has compared the different migrate rates of protein and HA within the same gel and aimed to quantify this relationship. One of the aims of this chapter is to measure this relationship to provide a method for qualitatively assessing HA size using protein standards.

Although PAGE offers a qualitative assessment of GAG size, as has previously been demonstrated when analysing heparin, a linear sulfated polysaccharide (Volpi *et al.*, 2012), the technique struggles to separate large HA chains due to the difficulty in creating polyacrylamide gels that have large enough pore sizes for the molecules to migrate. Furthermore, due to the smearing of heterogeneous GAG samples it makes it difficult to quantitatively compare average sizes from different samples. Therefore, a more thorough technique that produces a quantitative assessment would be more beneficial.

With this in mind the aim was to develop a protocol for analysing unknown GAG sizes using QCM-D. The quantitative analysis of QCM-D measurements is discussed in detail in chapter 2 and will be briefly summarised here. QCM-

D is an acoustic measuring technique that can measure changes in frequency (Δf) to determine areal mass density and changes in dissipation (ΔD) to determine the mechanical properties of the surface bound layer. Using QCM-D, a methodology for analysing the terminal functionalisation of GAGs has previously been established (Richter *et al.*, 2007; Thakar *et al.*, 2014). In this chapter, the aim was to build on this work by using the technique to measure the ratio of $\Delta D / -\Delta f$ for HA chains of known sizes, producing a standard curve to describe this relationship. The ratio $\Delta D / -\Delta f$ is described in detail in chapter 2. It has previously been shown to be a valuable measurement for molecular characterisation, specifically of shape and size (Tsortos *et al.*, 2008; Papadakis *et al.*, 2010). Previously, the viscoelastic model has been used to analyse QCM-D responses and has been used successfully to quantify the mechanical properties of surfaces of disordered proteins (Eisele *et al.*, 2012). However, in order to fit the data to the viscoelastic model complimentary measurements using AFM and spectroscopic ellipsometry were required to ascertain meaningful results (Reviakine *et al.*, 2011; Eisele *et al.*, 2012). Richter *et al.* (2007) were able to model film thickness of very soft HA films, but only when the film was constrained using reflection interference contrast microscopy. In an attempt to circumvent this requirement for extra measuring techniques, the aim was to establish a technique for measuring GAG chain length using only the ratio of $\Delta D / -\Delta f$. For ultrathin films (in the range of a few nm) this quantity is strictly proportional to elastic compliance. For thicker films, the proportionality is lost but the $\Delta D / -\Delta f$ ratio remains a useful measure to quantify film softness (Du and Johannsmann, 2004; Reviakine *et al.*, 2011; Eisele *et al.*, 2012).

To summarise, the aims of this chapter are to first quantify the relationship of PAGE migration between protein and GAG samples to provide a method for qualitatively assessing GAG size using protein standards to establish a larger range of markers for use in GAG analysis using PAGE. The second aim is to establish a methodology for sizing GAG chains using the ratio of $\Delta D / -\Delta f$ measured by QCM-D.

5.2 Methodology

5.2.1 HA samples

A range of 5 differently sized HA samples biotinylated at the reducing end were used for both the PAGE and QCM-D analysis (Table 4). These were

HA_dp15, the source and material is described in detail by Dubacheva *et al*, (2017); HA50 (Hyalose: SelectHA-B50), HA250 (Hyalose: SelectHA-B250), HA500 (Hyalose: SelectHA-B500) and HA1000 (Hyalose: SelectHA-B1000). The M_w of the HA samples were provided by the company (Hyalose) using SEC-MALLS.

Samples of CS-A from sturgeon notochord (Seikagaku: 400658-1A), CS-B/DS from porcine intestinal mucosa (Sigma: CAS54328-33-5), CS-C from shark cartilage (Amsbio: 400675-1A), CS-D from shark cartilage (Amsbio: 400676-1A) and CS-E from squid cartilage (Seikagaku: 400678-1A) were biotinylated at the reducing end by Goodenough (2018) and used in both the PAGE and QCM-D analysis.

5.2.2 PAGE

Using a 4-12% bis-tris glycine gel in denatured reducing conditions 3 μ g of each CS sample was prepared at a 1:1 ratio with gel loading buffer (1 \times 20% glycerol, orange G1%, 80 mM tris and ran using the XCell SureLock™ (Novex, Invitrogen) system using 1 \times MOPS SDS running buffer (Novex, Invitrogen). The HA samples were prepared at the concentrations and molarity displayed in Table 4. After running the gel for 1 hour at constant 200 V the gel was then stained with 0.5% Alcian blue 8GX (Sigma: A5268) mixed with 2% acetic acid to allow for the polysaccharide chains to become visible, and de-stained with 40% methanol, 8% acetic acid solution. As the Hi-Mark™ pre-stained HMW protein standard (Invitrogen) and precision plus protein™ all blue protein standards (Biorad) used were already pre-stained they were visible without requiring a further protein stain.

Table 4. HA samples used in the PAGE and QCM-D analysis.

Mean \pm standard deviation (sd) were recorded.

Biotinylated HA	HA M_w^a mean \pm sd (kDa)	$N_{ds}^b \pm$ sd	Concentration ^c (μ g/mL)	Molarity ^c (M)
HA_dp15	3.2 ^d	7.5 ^d	1	2.67×10^{-7}
HA50	58 \pm 3	116 \pm 6	1	1.72×10^{-8}
HA250	280 \pm 14	560 \pm 28	5	1.78×10^{-8}
HA500	530 \pm 27	1060 \pm 54	10	1.89×10^{-8}
HA1000	837 \pm 42	1674 \pm 84	20	2.39×10^{-8}

a) M_w is the molecular weight.

b) N_{ds} is the number of disaccharides.

c) Working concentration and molarity used for both PAGE and QCM-D experiments.

d) Pure oligosaccharide with effectively no size variation.

5.2.2.1 Quantitative analysis

To determine the migration distance (d_{mig}) the distance between the top and bottom of the gel was measured d_{total} . The d_{mig} of each GAG sample was measured through quantitative analysis of the greyscale pixel intensity along each lane (see Appendix 3). The pixel intensity was measured by drawing a straight line spanning d_{total} and measuring the intensity across the line. In photographs of the gel, a light colour (high pixel intensity) represents the background and a darkening (lower pixel intensity) the presence of sample. The position in the lane with the smallest pixel intensity, representing the location where most sample has accumulated, was defined as d_{mig} . Values of d_{max} and d_{min} were quantified by identifying the points in the lane below and above d_{mig} , respectively, where the pixel intensities measured half the value between the background intensity and the minimal intensity. d_{max} and d_{min} are measures of the spread in migration. For each lane, 3 lines were drawn and the mean value was measured. All d_{mig} , d_{max} and d_{min} values were then divided by d_{total} for normalisation, such that all values range between 0.00 and 1.00. All data shown represent normalised values.

To determine the relationship between d_{mig} (as well as d_{max} and d_{min}) and $M_{w,protein}$ the values of the protein standards were combined (see Appendix 4) and a plot was produced. A line of best fit was then interpolated and used to determine the values of $M_{w,protein}$ for each GAG sample. The relationship between $M_{w,protein}$ to $M_{w,GAG}$ was defined by the result measured for HA50. The relationship provided a ratio that was used to convert the effective $M_{w,protein}$ values for CS samples to $M_{w,GAG}$ values.

5.2.3 QCM-D

The same QCM-D protocol as described in chapter 4 was used to conduct the measurements, with the same flow rate and buffers used. The only difference in the analysis is the third overtone ($n = 3$) was used here to facilitate comparison with other, previously published data (Thakar *et al.*, 2014). The molarity and concentration of HA presented to the sensor surface is displayed in Table 4. HA samples used in the PAGE and QCM-D analysis.. The number of repeats for each HA sample is displayed in Table 5. HA500 was measured in duplicate only due to limited sample availability. For each sample Δf and ΔD were measured and $\Delta D / -\Delta f$ was calculated.

Table 5. The number of repeats of each HA size used in the QCM-D analysis.

Biotinylated HA	Number of repeats
HA_dp15	7
HA50	4
HA250	3
HA500	2
HA1000	3

5.2.3.1 Modelling and statistics

For each sample, the mean $\Delta D / -\Delta f \pm$ standard deviation was used to model the data to generate the standard curves. The quality of the fit of each standard curve was measured using R^2 . The Difference between sample $\Delta D / -\Delta f$ was compared using a one-way ANOVA with a post-hoc Tukey test, with statistical significance defined as $p \leq 0.05$.

5.3 Results

The HA samples were synthesised *in vitro* to a defined molecular weight (M_w) with a narrow size distribution using a synchronised, stoichiometrically controlled polymerisation process involving *Pasteurella multocida* HAS by the company Hyalose (Jing and DeAngelis, 2004). These HA samples were used to establish trends for measuring GAG chain $M_{w,GAG}$ using PAGE and QCM-D. In the PAGE experiments $M_{w,GAG}$ were compared with protein standards of a defined $M_{w,protein}$.

CS samples of a larger range of chain sizes were used to validate the standard curves, as they have previously been analysed using PAGE and QCM-D by Goodenough (2018). Through the use of CS samples with a larger size distribution the samples could also be used to test the robustness of the methodologies for measuring heterogeneous GAG samples. Ideally, HA samples would have been used to validate the PAGE and QCM-D methodologies, however due to sample availability this was not possible.

5.3.1 Measuring GAGs using PAGE

The aim was to establish the relationship between migration rates of GAG and protein samples using PAGE by comparing the migration distance (d_{mig}) of HA

samples of known $M_{w,GAG}$ (GAG samples) with the d_{mig} of protein standards of known $M_{w,protein}$ using PAGE.

5.3.1.1 Qualitative PAGE results

The HA samples formed much tighter bands, in comparison to the CS samples which formed smears (Figure 39). This suggested that the HA samples have a smaller range of sizes in comparison to the CS samples, as expected. For HA250, HA500 and HA1000 d_{mig} was small, therefore it is possible that the range of sizes may be larger than what is observed qualitatively, as the HA chains have migrated less to facilitate separation. Furthermore, the value of d_{mig} for HA250, HA500 and HA1000 samples was smaller than the d_{mig} for the largest protein standard making it difficult to define $M_{w,protein}$ for these samples. HA_dp15 was not observed in the gel, however as it is only 3.2 kDa it is likely that it migrated through the entire gel, as the 10 kDa protein marker was observed at the bottom of the gel.

HA50 d_{mig} was the only HA measurement used for comparison with protein standard d_{mig} , as it was the only sample that migrated within range of d_{mig} protein standard measurements. HA50 (58 kDa) had a value according to the protein standards of $M_{w,protein} \sim 100 \pm 20$ kDa when the PAGE results were qualitatively assessed. In contrast, the CS samples all produced smears, indicating that the samples contained a large range of CS chain sizes. Comparatively, CS-A migrated furthest through the gel, followed by CS-B, CS-D and CS-C, with CS-E having migrated the least. However, to gain a more precise measurement of $M_{w,protein}$ for HA50 and the CS samples, the results were compared using a quantitative analysis. This was performed by defining d_{mig} (location where most sample has accumulated), d_{min} and d_{max} (measures of the spread in migration above and below d_{mig} , respectively) as described in the methodology section for each GAG sample, and comparing these values with a plot comparing the d_{mig} and $M_{w,protein}$ values of the 2 protein standard ladders.

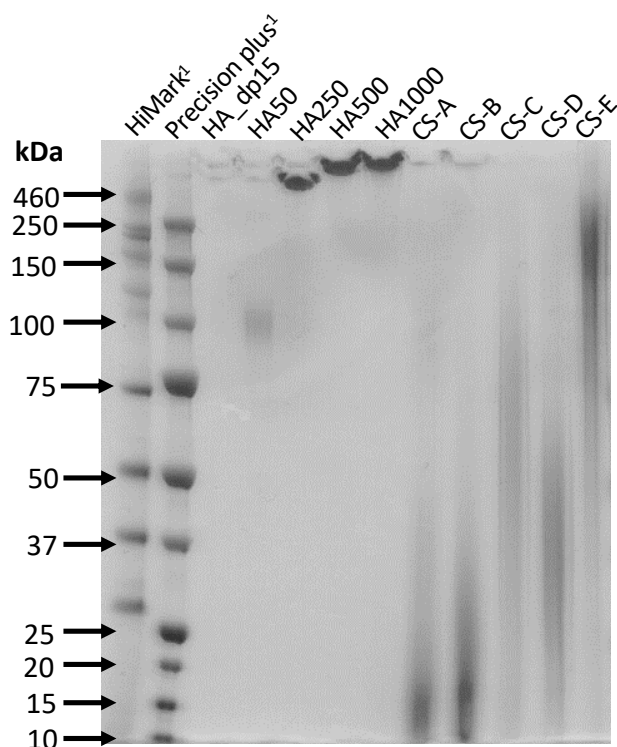


Figure 39. The relationship between GAG chains and protein standards using PAGE.

Using Alcian blue both HA and CS chains can be observed. HA samples formed bands, suggesting a small range of HA sizes. Due to the distinct bands, it is possible to compare HA samples with the protein standards to determine the difference in migration rates. The CS chains formed smears, indicating that the samples are composed of a large range of GAG chain sizes.

1) Protein ladders: Lane 1 is HiMark™ (Invitrogen) with molecular weights of 460, 268, 238, 171, 117, 71, 55, 41 and 31 kDa; Lane 2 is Precision plus protein™ (Biorad) with molecular weights of 250, 150, 100, 75, 50, 37, 25, 20, 15 and 10 kDa.

5.3.1.2 Relationship between protein standard d_{mig} and $M_{w,protein}$

Using a non-gradient, linear gel the expectation would be the value of protein standard d_{mig} would decrease exponentially with increasing $M_{w,protein}$, therefore a log-linear scale was used to plot the datapoints (Figure 40) (Winston, 1989). The gradient gel used in this chapter caused the trend to deviate from a strict exponential dependence, though the monotonous relationship between increasing $M_{w,protein}$ and decreasing d_{mig} was maintained. A line of best fit was drawn to describe the relationship and was used to convert HA and CS d_{mig} to $M_{w,protein}$.

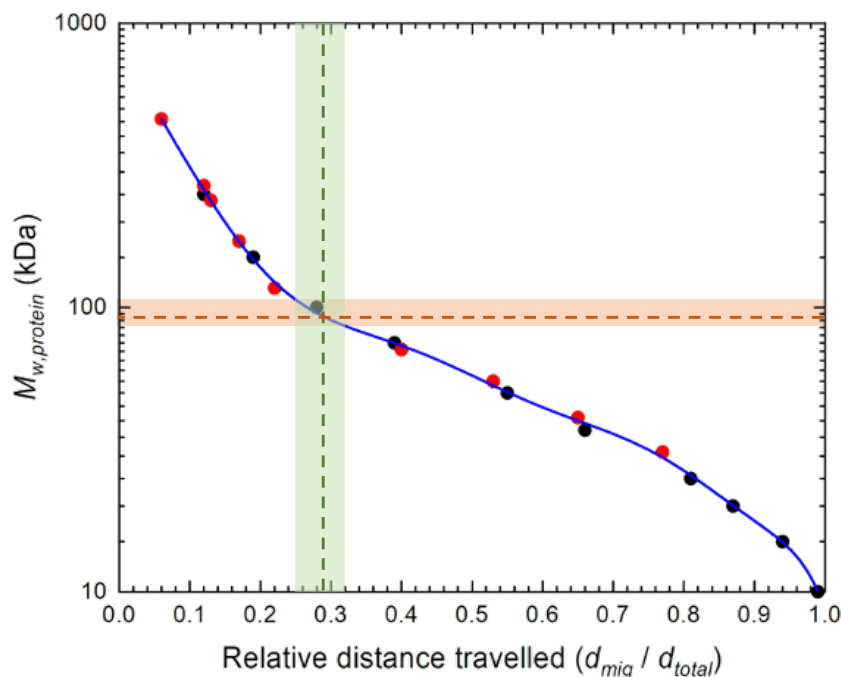


Figure 40. The relationship between protein standard d_{mig} and $M_{w,protein}$ plot on a log-linear scale.

A line of best fit was manually drawn (blue line) to estimate $M_{w,protein}$ for HA50 and CS samples. The dashed green line represents the HA50 d_{mig} measurement, with the dashed orange line representing the predicted $M_{w,protein}$. The coloured green area either side of the dashed lines represent d_{min} and d_{max} values. The orange area represents the corresponding M_w range. Precision plus protein™ (black dots) and HiMark™ (red dots) protein standards were used. The symbol size corresponds to the estimated error on the individual datapoints.

5.3.1.3 Establishing ratio between $M_{w,protein}$ and $M_{w,GAG}$

GAG samples, unlike the protein standards, formed smears, therefore measurements of d_{mig} as well as d_{min} and d_{max} were used to measure the range of GAG chain sizes present in the sample. Values of d_{mig} , d_{max} and d_{min} for HA50 were converted to $M_{w,protein}$ using the trendline in Figure 40 to 93 kDa, 86 kDa and 110 kDa, respectively. These values were then compared with the company estimates for $M_{w,GAG}$ (58 ± 3 kDa) to produce a ratio of 1 kDa ($M_{w,GAG}$): 1.7 \pm 0.1 kDa ($M_{w,protein}$). Thus, HA50 runs at the same rate as a protein of 1.7 times its molecular mass.

5.3.1.4 Estimating CS sample $M_{w,GAG}$ using PAGE

To estimate $M_{w,GAG}$ for CS samples a key assumption was made that that all GAG chains would run at an approximately equal rate, therefore the HA50 1 kDa ($M_{w,GAG}$): 1.7 kDa ($M_{w,protein}$) ratio was applied to convert CS $M_{w,protein}$ to $M_{w,GAG}$ (Figure 41). The results of the quantitative analysis support the qualitative assessment. For CS-C and CS-E, the median result used to

compare relative $M_{w,GAG}$ needed to be used cautiously, as the minimum in the intensity profile was rather shallow, making it difficult to locate the peak position with good resolution.

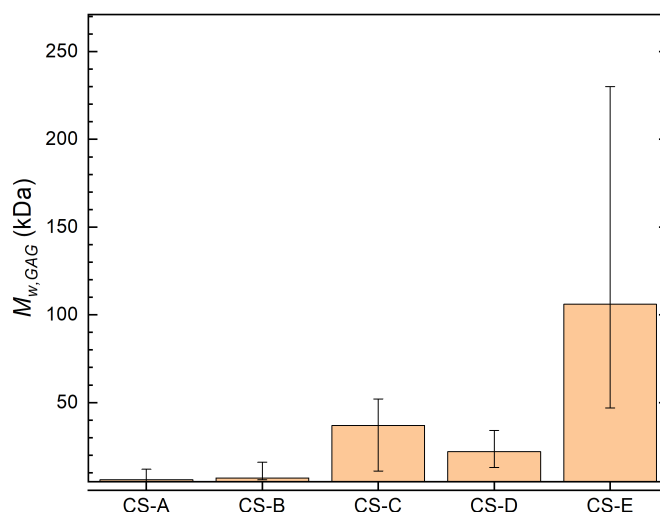


Figure 41. Molecular mass values for the CS samples estimated using PAGE. Orange bars represent median values or $M_{w,GAG}$ (derived from d_{mig}) and error bars reflect the spreads as derived from d_{min} and d_{max} . The y axis began at 5.9 kDa (10 / 1.7 kDa) to reflect the limit of detection and ended at 271 kDa (460 / 1.7 kDa) to reflect the accessible data range.

5.3.2 Quantifying GAG sizes using QCM-D

The aim was to establish the relationship between the ratio of $\Delta D / -\Delta f$ and $M_{w,GAG}$ of known HA samples (GAG samples) using QCM-D. The methodology was established by building on the methodology first described by Richter *et al* (2007) where a model system for creating reproducible surface-attached HA was described. This involved using a combination of a biotinylated lipid bilayer, a surface monolayer of streptavidin and HA biotinylated at the reducing end. This methodology is discussed in detail in chapter 4.

5.3.2.1 The relationship between HA size and independent Δf and ΔD measurements

Starting from the presentation of biotinylated-HA to the streptavidin monolayer the values of Δf and ΔD were measured throughout the incubation process. The minimum Δf and maximum ΔD measurements reflect where the incubation has stopped and were used throughout the QCM-D analysis, unless specified otherwise. There was no clear trend in the dependence

between the final Δf values and $M_{w,GAG}$, with HA50 showing the largest decrease in Δf (-46.5 ± 2 Hz), and HA500 showing the least (-5 ± 1.5 Hz) (Figure 42A, bottom). HA1000 (-6 ± 2 Hz), HA250 (-12 ± 0.5 Hz) and HA_dp15 (-14 ± 1 Hz) were in-between these two extremes. Equally, the relationship between the final ΔD values and $M_{w,GAG}$ was also not monotonous, as HA50 ($16.8 \pm 0.6 \times 10^{-6}$) showed the largest change and HA_dp15 the least ($1.7 \pm 0.1 \times 10^{-6}$), then HA1000 ($6.0 \pm 1.2 \times 10^{-6}$), HA500 ($6.5 \pm 0.0 \times 10^{-6}$) and HA250 ($10.7 \pm 0.4 \times 10^{-6}$). To summarise, there is no simple trend between changing Δf or ΔD and HA size. This is emphasised when the relationship between HA $M_{w,GAG}$ and ΔD (Figure 42B top) or Δf (Figure 42B bottom) are plot together. This was what motivated the use of the $\Delta D / -\Delta f$ ratio for measuring $M_{w,GAG}$ of HA chains.

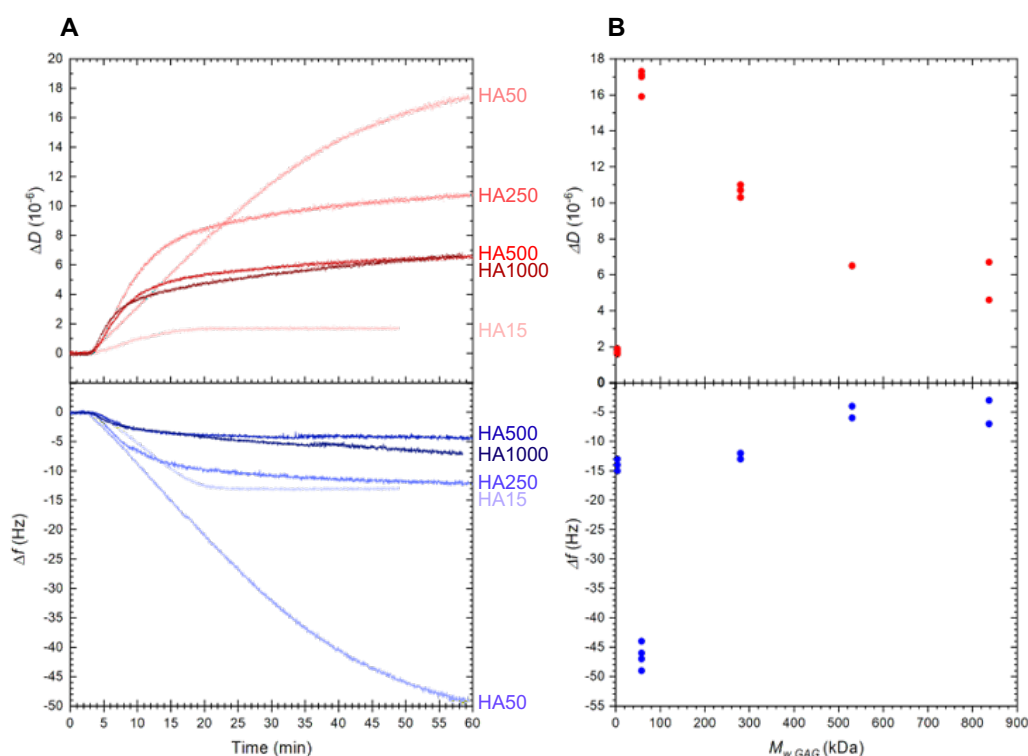


Figure 42. The relationship between Δf and ΔD for a range of HA sizes measured using QCM-D.

A Representative QCM-D responses for the formation of HA brushes for a range of HA sizes. The start of incubation was at 4 min and the complete incubation process is displayed. The rinsing step is not shown for ease of analysis; note that minimal changes occurred upon rinsing. **B** The relationship between M_w and final changes in Δf (bottom) and ΔD (top). Each datapoint reflects an independent experiment ($n = 7, 4, 3, 2$ and 3 for HA_dp15, HA50, HA250, HA500 and HA1000, respectively).

The lack of monotonous dependency between Δf and $M_{w,GAG}$ is due to Δf including the mass of the solvent, as well as the mass of adsorbed HA.

Furthermore, the surface coverage of HA films has previously been observed to change with increasing $M_{w,GAG}$. With surface coverage known to effect the value Δf values (Richter *et al.*, 2007; Reviakine *et al.*, 2011). At lower $M_{w,GAG}$ the density of bound GAG chains is likely to be limited by the number of available binding sites. At this size the maximal number of GAG chains per unit area would remain constant, however the mass per unit area would increase with increasing GAG size (Thakar *et al.*, 2014). In contrast, for larger GAG chains the forming GAG film impedes the binding of further GAG chains through steric hinderance, therefore causing a gradual reduction in the maximal number of GAG chains per unit area which could cause a reduction in the mass per unit area (Richter *et al.*, 2007). Furthermore, other parameters including the effect of film softness, as well as the impact on HA concentration and incubation time on the coverage reached could also influence Δf . Therefore, without an independent measure of surface coverage to compare the relative surface coverage at different $M_{w,GAG}$, it makes using Δf alone insufficient (Baranova *et al.*, 2011).

5.3.2.2 *The relationship between HA size and the ratio of $\Delta D / -\Delta f$*

The ratio of $\Delta D / -\Delta f$ is dependent on the shape and $M_{w,GAG}$ of the GAG chains (Tsontos, Papadakis and Gizeli, 2008; Tellechea *et al.*, 2009). For globular objects the ratio of $\Delta D / -\Delta f$ has been observed to reduce as a function of increased surface coverage due to the effect of hydrodynamically coupled water (Johannsmann *et al.*, 2009). However, GAGs are not globular. Tsontos *et al* (2008) observed the ratio of $\Delta D / -\Delta f$ to be independent of surface coverage when they measured deoxyribonucleic acid (DNA) polysaccharides, a none globular molecule. As $-\Delta f$ is a measure of the density of the adsorbed surface-bound molecules it was used to analyse how the measurement of the $\Delta D / -\Delta f$ ratio changed as a function of HA surface coverage. Therefore, the expectation was the ratio of $\Delta D / -\Delta f$ would either decrease or remain unchanged as a function of $-\Delta f$.

There is a clear trend observed between increased HA size and an increase in the $\Delta D / -\Delta f$ ratio (Figure 43). Interestingly, there was no clear trend observed between increased surface coverage and the ratio of $\Delta D / -\Delta f$. To analyse this further the ratio of $\Delta D / -\Delta f$ was measured by 3 different methodologies. The first method aimed to measure the HA films at low surface coverage towards the start of the incubation process, therefore the ratio of $\Delta D / -\Delta f$ was measured between $-\Delta f$ values of 4 and 5 Hz. The range between $-\Delta f$ values of 0 to 3 Hz could not be used due to the tendencies for

outliers affecting the measurements of the $\Delta D / -\Delta f$ ratio, as small changes in both Δf and ΔD in this range have a large effect on the ratio, that stabilised around 4 Hz. The second methodology aimed to measure the HA films at high surface coverage, towards the end of the incubation process, therefore the ratio of $\Delta D / -\Delta f$ was measured for values of $-\Delta f$ within 1 Hz of the final equilibrium measurement. The third methodology averaged all measurements of the $\Delta D / -\Delta f$ ratio throughout the binding process, excluding values between $-\Delta f$ values of 0 to 3 Hz range.

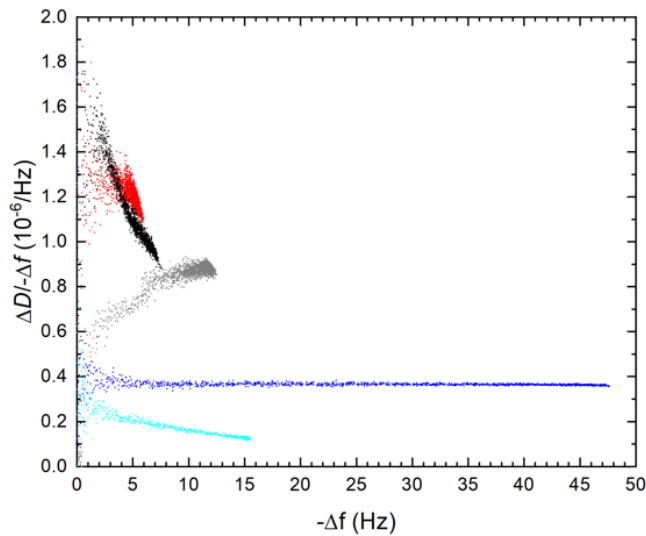


Figure 43. Representative plots of the relationship between the ratio of $\Delta D / -\Delta f$ and $-\Delta f$ throughout the binding process.

Each colour represents an individual experiment using one of the HA samples: HA_dp15 (cyan), HA50 (blue), HA250 (grey), HA500 (red), HA1000 (black). All datapoints recorded throughout the binding process are included to create the scatter plots for each sample.

The three methodologies all produced the same trend, as the ratio of $\Delta D / -\Delta f$ increased as a function of increased $M_{w,GAG}$ (Figure 44). However, there were differences in the values of $\Delta D / -\Delta f$ measured for HA_dp15 and HA250 samples, as at low surface coverage the values differed significantly from the other two methodologies. To emphasise the different effect of surface coverage on the ratio of $\Delta D / -\Delta f$ for different HA sizes, the differences between the 4 to 5 Hz and the final equilibrium measurements (low and high surface coverage respectively) were compared (Figure 44B). For HA50 ($0.00 \pm 0.02 \times 10^{-6}/\text{Hz}$) and HA500 ($0.01 \pm 0.01 \times 10^{-6}/\text{Hz}$) there was little change as a function of surface coverage. As surface coverage increased there was a small decrease in the $\Delta D / -\Delta f$ ratio for both HA_dp15 ($-0.06 \pm 0.01 \times 10^{-6}/\text{Hz}$) and HA1000 ($-0.09 \pm 0.02 \times 10^{-6}/\text{Hz}$). The increase in the ratio of

$\Delta D / -\Delta f$ as a function of surface coverage for HA250 ($0.15 \pm 0.02 \times 10^{-6}/\text{Hz}$) was a surprising observation, as the ratio of $\Delta D / -\Delta f$ increasing as a function of surface coverage has rarely been reported, though has been observed previously (Tellechea *et al.*, 2009). Perhaps the configuration of the HA chains on the surface form a particular coiled effect that produces an increase in $\Delta D / -\Delta f$, however this would require further measurements to understand this relationship further.

The results from the maximal coverage measurements and the average measurements were in agreement, with no significant differences found between the measurements for any of the HA samples. Therefore, either methodologies could have been used for the following quantitative analysis, without impacting the trend produced in any major way. The methodology taken forward was the average $\Delta D / -\Delta f$, as this standardised the differences in the $\Delta D / -\Delta f$ ratio observed with changing surface coverage.

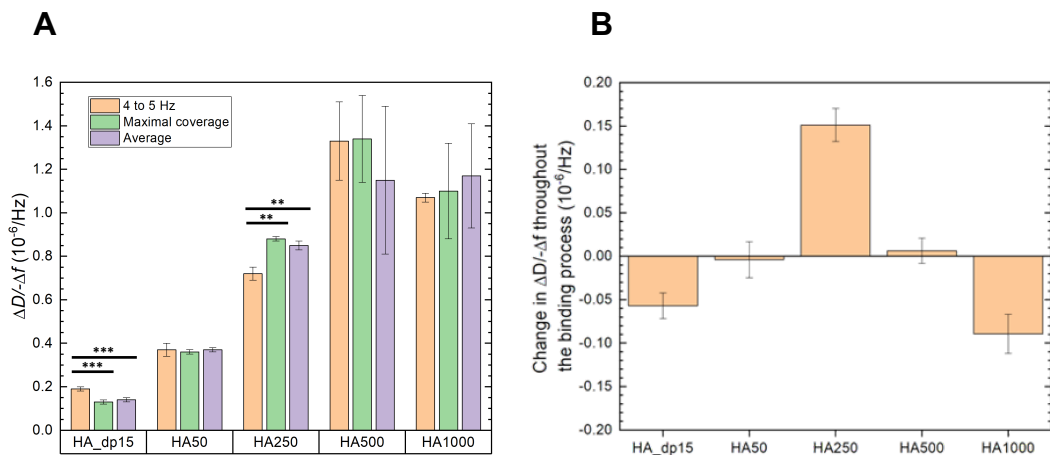


Figure 44. Comparison of different methods for analysing the ratio of $\Delta D / -\Delta f$ for HA chains.

A Comparison of mean values of the ratio of $\Delta D / -\Delta f$ for HA chains. The error bars represent the standard deviation ($n = 3$). The lines above the graph represent statistical significance: $p \leq 0.005$ (**), $p \leq 0.0005$ (***). **B** The change in the $\Delta D / -\Delta f$ value throughout the binding process. The maximal coverage $\Delta D / -\Delta f$ ratio value was compared with the $\Delta D / -\Delta f$ value at the start of the binding process. A positive result reflects an increase in $\Delta D / -\Delta f$ ratio throughout the binding process. The error bars represent the standard deviation. The data is provided in Appendix 5.

5.3.2.3 The relationship between HA size and the ratio of $\Delta D / -\Delta f$

The average $\Delta D / -\Delta f$ ratios between the different HA samples were all significantly different from each other, with the exception of the difference between the HA500 and HA1000 (Table 6). HA_dp15 ($0.14 \pm 0.01 \times 10^{-6}/\text{Hz}$) measured the lowest ratio, followed by HA50 ($0.37 \pm 0.01 \times 10^{-6}/\text{Hz}$) then

HA250 ($0.85 \pm 0.02 \times 10^{-6}/\text{Hz}$). For HA500 ($1.33 \pm 0.18 \times 10^{-6}/\text{Hz}$) and HA1000 ($1.17 \pm 0.23 \times 10^{-6}/\text{Hz}$) the values of $\Delta D / -\Delta f$ were not significantly different from each other (Figure 44: purple bars).

Table 6. The p values measuring the differences between the ratio of $\Delta D / -\Delta f$ for different HA sizes.

	HA_dp15	HA50	HA250	HA500	HA1000
HA_dp15					
HA50	0.022				
HA250	0	0			
HA500	0	0	0.001		
HA1000	0	0	0.013	0.451	

It is important to note the sensitivity for the ratio of $\Delta D / -\Delta f$ is determined by the ability of the shear-acoustic wave to propagate throughout the HA film ($\delta \sim 250$ nm; described in detail in chapter 2). Therefore, if the HA films formed are over 250 nm, the methodology won't be able to measure the $\Delta D / -\Delta f$ ratio as effectively. Previous work has measured the persistence length (L_p) of HA to be ~ 4 nm, therefore HA chains over 4 nm are likely to coil (Bano *et al.*, 2016). The contour length (L_c) is a measure of the maximum size of a polymer chain at full extension. For HA_dp15 ($L_c \sim 7.5$ nm) and HA50 ($L_c \sim 145$ nm) $L_c < 250$ nm therefore even at maximum extension the surfaces would be under this maximum.

For HA250 ($L_c \sim 700$ nm), HA500 ($L_c \sim 1300$ nm) and HA1000 ($L_c \sim 2092.5$ nm) $L_c > 250$ nm the polymer chains are likely to be coiled, making the respective size of the HA films far smaller than L_c . Previously, the film thickness of HA50 and HA1000 were found to be 140 ± 10 nm and 530 ± 20 nm respectively using colloidal probe reflection interference contrast microscopy (Richter *et al.*, 2007). Without a complimentary method to measure film thickness HA250 and HA500 film thickness is currently unknown. If HA1000 is thicker than the sensitivity of the shear acoustic wave, it may partially explain why the ratio of $\Delta D / -\Delta f$ did not differ significantly from HA500.

5.3.2.4 Quantitative description of the trend between $\Delta D / -\Delta f$ and $M_{w,GAG}$

As there was a clear trend observed between HA size and $\Delta D / -\Delta f$, the aim was quantitatively describe this relationship, to establish a standard curve that can be used to size unknown GAG chains using the $\Delta D / -\Delta f$ ratio. Thakar *et*

al (2014) have previously reported QCM-D data for films of size-defined HA and HS oligosaccharides. In their experiments, the GAG chains were immobilised in the same way as reported here (i.e. via biotin moieties at the reducing end to streptavidin monolayers). These data are complementary as they cover a GAG size range not explored in the present study. The ΔD versus Δf plots reported by Thakar *et al* (2014) showed a linear relationship to a good approximation. Thus, the ratio of $\Delta D / -\Delta f$ could readily be extracted as the slope in these graphs and the results are presented in Figure 45.

Thakar *et al* (2014) previously reported identical values of the $\Delta D / -\Delta f$ ratio for HA_dp8 and HS_dp8 GAGs. These molecules had the same length, yet different molecular masses, which suggested that the $\Delta D / -\Delta f$ ratio is dependent on the contour length (number of disaccharides). Therefore the number of disaccharides was used for as the unit of size in this analysis. $M_{w,GAG}$ of $N_{ds} = 1$ is 400 Da to a good approximation, therefore this conversion was used to convert company estimations of HA $M_{w,GAG}$ to N_{ds} using the ratio 1 kDa ($M_{w,GAG}$) : $N_{ds} = 2.5$.

There was a clear trend for all GAG sizes that the ratio of $\Delta D / -\Delta f$ increased as function of N_{ds} (Figure 45). However, the increase in the ratio of $\Delta D / -\Delta f$ as a function of N_{ds} was different at 2 distinct size ranges. Between $N_{ds} = 3$ and $N_{ds} = 7.5$ the increase in $\Delta D / -\Delta f$ as a function of N_{ds} was sharper than the increase between $N_{ds} = 7.5$ and $N_{ds} = 2092.5$. Therefore, 2 functions were required to describe the relationship between N_{ds} and $\Delta D / -\Delta f$, as no fit could be found that reproduced all the data well. Equally, neither of the two identified functions adequately reproduced all the data well, as is emphasised in Figure 45C.

To describe the trend between $N_{ds} = 3$ and $N_{ds} = 7.5$ non-linear regression analysis with the equation $\Delta D / -\Delta f = A - B \times C^{N_{ds}}$ was used to model the data ($R^2 = 0.9800$), with $A = (0.1746 \pm 0.0219) \times 10^{-6} / \text{Hz}$, $B = (0.3758 \pm 0.0620) \times 10^{-6} / \text{Hz}$ and $C = 0.7102 \pm 0.0695$ for the adjustable parameters (Figure 45B). This equation reproduced the data well with a small number of adjustable parameters. This equation can be rewritten as a function of N_{ds} as:

$$N_{ds} = \ln \left(\left(\frac{\Delta D}{-\Delta f} - 0.1746 \frac{10^{-6}}{\text{Hz}} \right) \div -0.3758 \frac{10^{-6}}{\text{Hz}} \right) \div \ln(0.7102) \quad (17)$$

Non-linear regression analysis also modelled the trend between $N_{ds} = 7.5$ and $N_{ds} = 2092.5$ most appropriately ($R^2 = 0.9996$) and could be described by the

equation $\Delta D / -\Delta f = A - B \times C^{N_{ds}}$ with $A = 1.1169 \pm 0.0288 \times 10^{-6} / \text{Hz}$, $B = 0.9897 \pm 0.0266 \times 10^{-6} / \text{Hz}$ and $C = 0.9976 \pm 0.0013$ for the adjustable parameters (Figure 45A). This equation reproduced the data well with a small number of adjustable parameters. This equation was also rewritten as a function of N_{ds} as:

$$N_{ds} = \ln \left(\left(\frac{\Delta D}{-\Delta f} - 1.1169 \frac{10^{-6}}{\text{Hz}} \right) \div -0.9897 \frac{10^{-6}}{\text{Hz}} \right) \div \ln(0.9976) \quad (18)$$

By using Equations 17 & 18 estimates of GAG chain size can be made if the ratio of $\Delta D / -\Delta f$ is known. However, between $N_{ds} = 7.5$ and $N_{ds} = 145$ the 2 models differ, which is emphasised in Figure 45C. Without further datapoints to plot within this 'region of uncertainty' it is unclear which relationship describes the relationship most appropriately. An explanation for the 2 different trends that result in this 'region of uncertainty' may be explained in terms of the persistence length (L_p) and contour length (L_c) of HA.

Previously, L_p of HA has been measured to be ~ 4 nm which converts to $N_{ds} \sim 4$ (Bano *et al.*, 2016). It is a measure of polymer chain structural rigidity that is commonly defined in 3 regimes in context of L_c as: rigid ($L_p \gg L_c$), semi-flexible ($L_p \approx L_c$) and flexible ($L_p \ll L_c$) (Manning, 1986; Grosberg and Khokhlov, 1994; Nelson, 2004). Therefore, between $N_{ds} = 3$ and $N_{ds} = 7.5$ the HA chains are in the semi-flexible regime while between $N_{ds} = 7.5$ and $N_{ds} = 2092.5$ the HA chains are in the flexible regime. The region of uncertainty is likely caused by the transition from the semi-flexible (flexible rod) regime to the flexible (random coil) regime. Future work is planned to produce HA standards in this size range to further resolve this region and define the transition point more accurately. Specifically, HA chain sizes of 20 disaccharides (10 kDa) and 60 disaccharides (30 kDa) are currently in the process of being designed for this purpose.

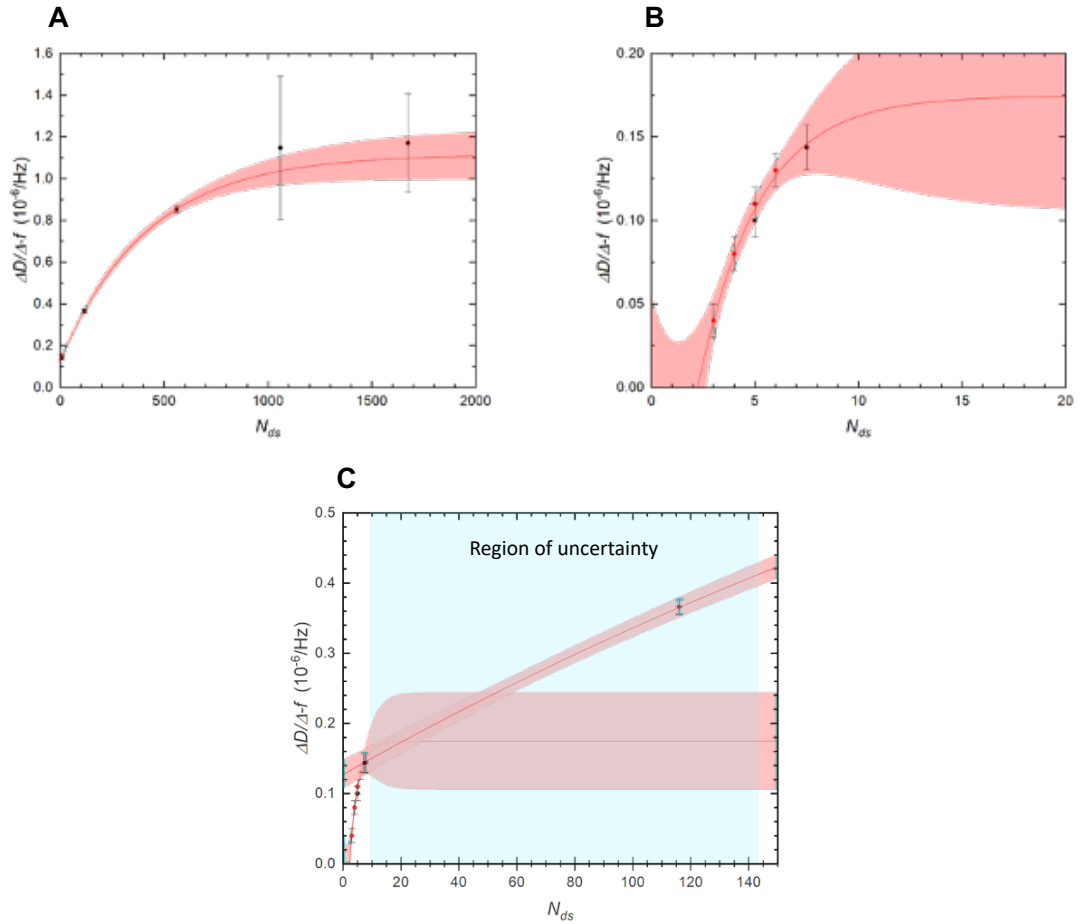


Figure 45. The ratio of $\Delta D / -\Delta f$ as a function of HA N_{ds} .

A The relationship between the N_{ds} and the ratio of $\Delta D / -\Delta f$ for HA chains between $N_{ds} = 7.5$ (3 kDa) and $N_{ds} = 2092.5$ (837 kDa). The standard curve ($R^2 = 0.9996$) is defined by $\Delta D / -\Delta f = A - B \times C^{N_{ds}}$. **B** The relationship between the N_{ds} and the ratio of $\Delta D / -\Delta f$ for HA and HS chains between $N_{ds} = 3$ and $N_{ds} = 7.5$. The standard curve ($R^2 = 0.9800$) is defined by $\Delta D / -\Delta f = A - B \times C^{N_{ds}}$. See main text for results of the best-fit values. **C** The two standard curves superimposed onto the same graph. The differences between the 2 trends are emphasised in this plot. The region in blue, defined as the region of uncertainty is the size range for which GAGs currently cannot be sized due to discrepancies between the models. For all graphs the red line represents the standard curve, with the black symbols (HA) and red symbols (HS) representing experimental data (mean \pm S.D.). The red bands on either side of the standard curve represent the 95% confidence intervals.

5.3.2.5 Interpolating the ratios of $\Delta D / -\Delta f$ to estimate the size of CS GAG chains.

So far samples of known N_{ds} have been used to establish the trend between N_{ds} and the ratio of $\Delta D / -\Delta f$. To validate the model the same CS samples used in the PAGE analysis were compared using QCM-D measurements. Goodenough (2018) had previously reported the ratio of $\Delta D / -\Delta f$ for films of CS using the same protocol as reported in this chapter. The values of the $\Delta D / -\Delta f$ ratio were interpolated using Equations 3 and converted from N_{ds} to

$M_{w,GAG}$ (Table 7). As $\Delta D / -\Delta f > 0.18 \times 10^{-6}/\text{Hz}$ Equation 2 could not be used. When the interpolated results were compared, CS-A and CS-B had the lowest $M_{w,GAG}$, then CS-D, CS-C and CS-E. Of note, all of the results were measured in the region of uncertainty.

Table 7. The values of $\Delta D / -\Delta f$ for CS chains used to validate the model.

N_{ds} , as well as molecular weight were interpolated using Equation 3.

CS	$\Delta D / -\Delta f$ ($10^{-6}/\text{Hz}$)	N_{ds}	Molecular weight [$N_{ds} \times 0.45 \pm 0.05^a$] (kDa)
CS-A	0.22	41	$\sim 18 \pm 2$
CS-B	0.23	46	$\sim 21 \pm 2$
CS-C	0.32	90	$\sim 41 \pm 5$
CS-D	0.29	75	$\sim 34 \pm 4$
CS-E	0.37	117	$\sim 53 \pm 6$

a) Molecular weight of CS was converted from disaccharides to kDa by assuming that the molecular weight of HA and CS are similar. An HA disaccharide (including a sodium counterion) is 400 Da to a good approximation. However, the value for CS is likely to be higher and dependent on the degree of sulfation. For this reason, 0.45 ± 0.05 was chosen to account for this uncertainty.

5.3.3 Validating QCM-D and PAGE CS sample estimates

So far values of CS $M_{w,GAG}$ have been measured using PAGE and QCM-D. To validate the methods, the results were compared with the estimated $M_{w,GAG}$ provided by the company datasheets (Figure 46).

Both PAGE and QCM-D results measured the CS samples in the same order of size. The ordering was in agreement with the ordering using the company datasheet estimates. The company estimate of CS-B and CS-D do not contain any error margins, therefore although the company estimates predict them to be of the same $M_{w,GAG}$ it is not unexpected that the actual values would be different.

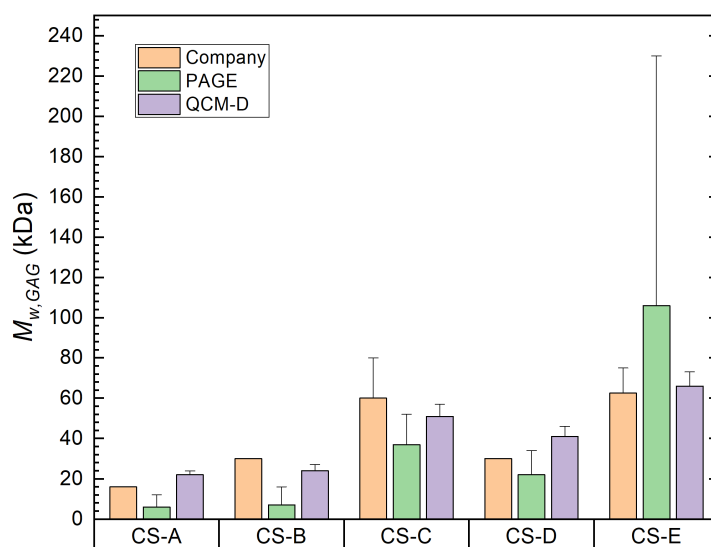
For CS-A, CS-B, CS-C and CS-D, PAGE $M_{w,GAG}$ values were smaller than the company estimates. Furthermore, comparatively the values of $M_{w,GAG}$ using PAGE were smaller than the values measured using QCM-D (excluding CS-E). This may reflect an underestimation of $M_{w,GAG}$ using PAGE. This underestimation may be accounted for by the assumption that HA and CS migrate at equal rates being invalid. The underestimation of CS $M_{w,GAG}$ may reflect the faster migration rate of CS, caused by the presence of the negatively charged sulfate group, when compared with HA. This would lead to a larger d_{mig} that would consequently produce a smaller $M_{w,GAG}$ value.

When the QCM-D values of $M_{w,GAG}$ were compared with the company values, CS-C, CS-D and CS-E fell within the company range. CS-B and CS-A were

close to the predicted sizes provided by the company (though lacking margin of error information by the company).

In comparison with PAGE, QCM-D was able to more accurately replicate the results predicted by the company estimates. The results of the CS measurements by QCM-D reported here are partially validated by the comparison with the company $M_{w,GAG}$, suggesting that the QCM-D technique is robust enough to measure samples with a large range of GAG chain sizes.

A



B

CS	Company M_w (kDa)	PAGE M_w Median [lower – upper estimates] kDa	QCM-D M_w (kDa ± sd)
CS-A	16	6 [5 – 12]	~ 18 ± 2
CS-B	30	7 [6 – 16]	~ 21 ± 2
CS-C	60 ± 20	37 [11 – 52]	~ 41 ± 5
CS-D	30	22 [13 – 34]	~ 34 ± 4
CS-E	62.5 ± 12.5	106 [47 – 230]	~ 53 ± 6

Figure 46. Comparison of CS M_w estimates using PAGE, QCM-D and company estimates.

A Comparison of the relative values of CS chain size using PAGE (green), QCM-D (lilac) and estimates provided by the company (beige). The error bars reflect the standard deviation. **B** The table of results presented graphically above.

5.4 Discussion

HA of known sizes have been used to successfully establish two new methodologies for measuring GAG chains using PAGE and QCM-D methodologies. A ratio describing the different migration rates of HA and protein standards using PAGE was established that will enable the sizing of unknown GAG chains by comparing them with protein standards. The second methodology established a relationship between HA size and $\Delta D / -\Delta f$ that was defined using 2 individual standard curves: one to define GAG chains between 3 and 7.5 disaccharides, the second to define GAG chains between 7.5 and 2092.5 disaccharides.

5.4.1 Sizing GAG chains using PAGE

By comparing the migration distance (d_{mig}) of the HA50 (58 kDa) sample with the d_{mig} of the protein standards, the HA sample migrated at a slower rate, which could be defined by the ratio 1 kDa (protein) : 1.7 kDa (GAG). As the proteins are in an unfolded, disordered state, the migration rate is largely dictated by the attachment of sodium dodecyl sulfate (SDS) which is highly negatively charged, to an extent that it far outweighs the charge imparted by the protein. Although HA is a linear polysaccharide chain, therefore should be conformationally similar in shape to the disordered protein, HA does not interact with SDS. As an approximation, the results here suggest that the HA chains are less negatively charged than SDS-bound protein at a ratio of 1 : 1.7. It has currently not been established if the migration rate scales with charge for GAGs, therefore an assumption is being made that the relationship scales similarly to that of proteins. Previously, the sizing of HA using PAGE has been established by comparing HA samples with specific HA ladders (Select-HA™ LoLadder and Select-HA™ HiLadder) (Cowman *et al.*, 2011; Bhilocha *et al.*, 2011). Between them, the HA ladders have a range between 30 and 1510 kDa. However, there is only 1 HA standard below 100 kDa (30 kDa), making the sizing of GAGs smaller than 100 kDa difficult using the current HA standards available. By defining the ratio of GAG migration rate with protein migration rate the range of size markers available for sizing GAGs at lower molecular weights has been expanded.

As HA250, HA500 and HA1000 migrated less than the largest M_w protein standard they could not be measured using this method. For this reason the current upper limit on GAG sizes that can be estimated using this specific 4 – 12% bis-Tris gel using PAGE is 271 kDa (460 kDa protein standard divided

by 1.7). Thus, larger pore sized gels and larger protein standards would be required to increase d_{mig} for larger GAG chains and expand the size range.

The large range of CS $M_{w,GAG}$ reflected the large range of GAG chain sizes in the samples that could be observed by the presence of the smear in the CS lanes. In contrast, HA samples were synthesised *in vitro* with a stoichiometrically controlled polymerization process using *Pasteurella multocida* HAS specifically to have small size variability (Jing and DeAngelis, 2004). The quantitative analysis of the PAGE gel was able to reflect these differences and suggest a method for quantitatively assessing the differences in the range of $M_{w,GAG}$ between samples using PAGE.

In conclusion, the ratio between migration rates of protein and HA were defined for the first time using PAGE. This method could be used to expand the range of standards that can be used to size GAG chains, especially at lower molecular weights. The PAGE measurements were also able to comparatively analyse CS samples in order of size, with the results reflecting the large range of GAG chain sizes in each sample.

5.4.2 QCM-D sizing method

The ratio of $\Delta D / -\Delta f$ increased as GAG size increased (Figure 43 and Figure 45). This relationship was also previously observed for GAG oligosaccharides, and DNA molecules (Tsortos, Papadakis and Gizeli, 2008; Papadakis *et al.*, 2010; Thakar *et al.*, 2014). The trend of increased values of $\Delta D / -\Delta f$ with increased size was true from GAG measurements of a few disaccharides, to GAG lengths larger than 500 kDa. The large size range for which this trend was observed suggests the technique is robust enough to measure samples with a large range of GAG sizes. The technique may also be applicable to measure other GAG types as the methodology was able to estimate CS samples mean $M_{w,GAG}$ within the company estimates. This is particularly interesting considering Equation 18 was produced exclusively with HA samples yet was able to predict the size of CS chains.

Previously, the results measured by Thakar *et al* (2014) suggested a function could be ascertained to describe the relationship between the ratio of $\Delta D / -\Delta f$ and $M_{w,GAG}$ of HA and HS oligosaccharides. When HA_dp15 was added to the same dataset the trend was not well described by a linear relationship ($R^2=0.91$), with Equation 17 describing the relationship more accurately. This is likely a reflection on the transition beginning to occur between the different size regimes of HA chains, as it is interesting that the datapoint added to the

previous oligosaccharide data was the largest GAG chain size in the dataset. With the addition of further datapoints using HA chain sizes in the 'region of uncertainty', the description of the 2 trends will be further refined.

The trend between $M_{w,GAG}$ and the ratio of $\Delta D / -\Delta f$ was successfully defined and used to develop a measuring technique to size $M_{w,GAG}$. The advantage of using the $\Delta D / -\Delta f$ ratio here is that it can be readily extracted from QCM-D data to provide a simple, relative measure of film softness without the requirement for further measuring techniques. Therefore, although methods exist for measuring film softness more accurately using a form of nonlinear regression analysis (also referred to as 'viscoelastic modelling') $\Delta D / -\Delta f$ was selected as it did not require any further measurements to model the data (Reviakine *et al.*, 2011; Eisele *et al.*, 2012).

Previously, the ratio of $\Delta D / -\Delta f$ has been measured for other polymer chains, though no attempt was made to measure the polymer chains using the ratio. As the ratio is affected by the shape of the polymer chains the methodology described in this chapter is unlikely to be a good predictor of the M_w for other polymer chains with different biomechanical properties. To emphasise this point when comparing the ratio of $\Delta D / -\Delta f$ for similar sized polymer chains of HA and double stranded DNA, the results were not equal ($0.4 \cdot 10^{-6}/\text{Hz}$ and $0.2 \cdot 10^{-6}/\text{Hz}$ respectively for a ~ 58 nm polymer chain) (Papadakis *et al.*, 2010). This result is not unexpected, as DNA polymer chains have a larger persistence length (50 – 80 nm for DNA) than HA (~ 4 nm) reflecting their more rigid polymer structure (Levicky *et al.*, 1998; Lu *et al.*, 2002; Bano *et al.*, 2016). Therefore, the use of the technique described in this chapter is only likely to be applicable to polymers with a similar persistence length. However, as the ratio of $\Delta D / -\Delta f$ also increased with the size of DNA polymers it makes it possible to conduct a similar analysis as described in this chapter to produce a separate trend for DNA polymers that could predict DNA chain size based off $\Delta D / -\Delta f$ measurements.

This protocol benefits from the ability to measure GAG M_w in real-time, while creating functional surfaces that can then be used in further experimental protocols. Therefore, the process could act as a validation step to check the molecules for intra-sample variability and reproducibility, before further testing the surfaces afterwards. This is especially useful when considering the methodology used in chapter 4 where the reproducibility of HA films is vital to the experimental protocol.

Previous work has used QCM-D as a detection method for determining whether DNA is present in complex samples that have not been purified where

the DNA was in low amounts (Papadakis *et al.*, 2017). It is plausible that the protocol described in this chapter could also be adapted for use as a detection system for determining the presence of GAGs in complex samples, providing that the oxime ligation of the biotin moiety does not occur on other biomolecules. Therefore, not only could the presence of GAG samples be determined, but an average size could then be interpolated from the data to provide extra insight into the GAG population present in the sample.

5.4.3 Conclusion

There is a growing need both scientifically and commercially for accurate methodologies for measuring $M_{w,GAG}$. This chapter has established 2 new methodologies for measuring $M_{w,GAG}$ using PAGE and QCM-D techniques. The former expands on previous PAGE methodologies by defining the relationship between HA and protein standard migration rates, thus expanding the range of standards that can be used to measure HA chains to include protein standards. The latter successfully established a relationship between $M_{w,GAG}$ and the ratio of $\Delta D / -\Delta f$ of HA films. These were used to establish 2 functions that measured $M_{w,GAG}$ between different size ranges. The method was then validated by correctly estimating the $M_{w,GAG}$ of heterogenous CS size samples by comparing them with company estimates.

Chapter 6: General discussion & future perspectives

This thesis has identified molecular heterogeneity in the distribution of PNN components throughout the CNS that could have significant implications for the organisation of PNNs. Furthermore, this thesis has established a methodology for measuring the size of HA, an essential component of PNNs, that can be combined with a further methodology for analysing the molecular interactions that underpin the formation of the supramolecular PNN structure *in vitro*.

PNNs are macromolecular pericellular structures that surround sub-populations of neurons in the CNS (Kwok *et al.*, 2011; Wang and Fawcett, 2012). Various molecular components have been identified as important in the formation of PNNs, with other molecules identified as associating with the PNN structure (Carulli *et al.*, 2006; Deepa *et al.*, 2006; Galtrey *et al.*, 2008). Together this already presents the potential for producing highly heterogeneous PNN structures. CSPGs particularly from the lectican family (Acan, Ncan, Vcan and Bcan) and Pcan have been well documented as important to PNN formation, and all have numerous splice variants, multimeric variants caused by proteolytic cleavage and can be glycosylated to varying degrees, presenting a variety of possible molecular components that could be present in PNNs (Ruoslahti, 1996; Yamaguchi, 2000; Bandtlow and Zimmermann, 2000; Rauch *et al.*, 2004; Carulli *et al.*, 2006; Deepa *et al.*, 2006; Galtrey *et al.*, 2008; Zimmermann and Dours-Zimmermann, 2008; Kwok *et al.*, 2011; Wang and Fawcett, 2012; Giamanco and Matthews, 2012). This heterogeneity is likely to be highly relevant to the function of PNNs, as numerous studies have singled out individual molecules within the PNNs for further investigation (John *et al.*, 2006; Giamanco *et al.*, 2010; Bekku *et al.*, 2012; Favuzzi *et al.*, 2017). However, to date there has been limited investigation of how the biochemical composition of PNNs affect the macromolecular structure itself. The assembly of the macromolecular structure of PNNs on cell surfaces is likely to change the biochemical and biomechanical properties of the cell surface that could then be detected via mechanosensing by the surrounding cells. Therefore, the aim of the project was to investigate the potential biochemical heterogeneity of PNN components, including their splice variants, then investigate how the PNN-associated molecules interacted to self-organise into the macromolecular PNN structure.

6.1 Heterogeneity in the distribution of PNN components

This project has highlighted the heterogeneity in distribution of PNN-associated molecular components observed throughout the CNS. Specifically, the characterisation of a large array molecular species of individual CSPGs, demonstrated that the structure of PNNs could be even more heterogenous than was previously thought. Not only are there 5 distinct CSPGs known to be associated with PNNs, but there are a number of CSPG sub-types that may also be present. How the distinct CSPG sub-types are regulated is currently unknown. It is also unknown if these sub-types are correlated with certain neuropathology's, however it may provide a new insight into the regulation and formation of PNNs. One mechanism for the regulation of these CSPG splice-variants is through post-transcriptional modulation of the CSPG molecules. A second possible mechanism for regulating the CSPG sub-types could be through the regulation of enzymes that cleave the core proteins. For example, the Acan core protein is known to be cleaved by a number of enzymes called aggrecanases (Yamaguchi, 2000; Kiani *et al.*, 2002; Morawski *et al.*, 2012). Future work looking into the potential role of these 2 mechanisms may provide further insight into the distribution of these PNN-associated molecules within the CNS.

Furthermore, the observation that CSPGs are also differentially glycosylated provides further potential for heterogenous components. The regulation of glycosylation may occur during the synthesis of the molecules, or through enzymatic degradation post-translationally by chondroitinases (Yamaguchi, 2000; Kiani *et al.*, 2002; Morawski *et al.*, 2012). Future work aimed at understanding the mechanisms responsible for the production of the splice variants may offer unique insights into how to potentially biochemically manipulate PNN composition.

The varied distribution of PNN molecular components suggested that PNNs in different CNS regions may be biochemically distinct. Unfortunately, it was not possible to investigate the specific molecules found within PNNs using the method described by Kwok *et al* (2014), due to methodological constraints on sensitivity. Therefore, by increasing the amount of starting tissue to increase the sensitivity of the assay, future work may focus on demonstrating if all of the molecular heterogeneity observed in this project is found within the structures of PNNs. Furthermore, it would be interesting to compare whether the biochemical composition of the whole CNS lysate (ECM + PNN) mirrors the biochemical composition of the PNN material alone, or if there are significant differences between them.

The lack of correlation between the two morphological phenotypes observed in the cortical and hippocampal regions, in comparison with the cerebellar and cSC regions suggest that the regulation of these morphological phenotypes may not be due to the presence of varied biochemical components. When combined with the observations from chapter 4 demonstrating how the density of PNN components can influence the assembly of PNNs it implies that the relative density of the components is likely to be an important factor that may be responsible producing these phenotypes. This is further supported by the size of HA, as well as the spacing of HA molecules on the surface having an influence on the assembly of PNNs and the biomechanical properties of the films produced. Therefore, the heterogeneity in components is likely to be an important factor in the structural properties of PNNs, however alone it is not enough to explain the presence of the morphologically distinct PNN phenotypes described in section 1.5.3.

6.2 Important factors in the assembly of PNNs

This project has provided unique insights into the processes underpinning the self-organisation of PNN components into the supramolecular PNN structure. Both Hapln1 and Acan were found to be able to interact with HA films. This is in agreement with previous observations measuring the relationship of Hapln1 and Acan with HA (Shi *et al.*, 2004; Attili and Richter, 2013). Although the films produced were biomechanically distinct, both Acan and Hapln1 were able to interact independently with HA films of varying HA density. Hapln1 was able to interact stably without the presence of Acan, though Acan required the presence of Hapln1 to interact stably with HA surfaces.

The importance of Haplns in the stabilisation of the macromolecular structure implied that it may be the essential molecular trigger for PNN formation to occur. This mechanism is reliant on the presence of CSPGs in the pericellular space that are close in proximity to the surface bound HA on the cellular surface. The results from chapter 3 suggest that within the ECM in the CNS, many CSPGs are present, supporting this mechanistic hypothesis. This mechanism is not reliant on Hapln1 being presented in a particular order, as the results from chapter 4 highlighted that Hapln1 was able to stably interact with HA and Acan, irrespective of the order of incubation. Therefore, the introduction of Hapln1 would provide two important functions to PNN assembly. First, it would bind CSPGs already present within the HA films stably to the forming PNN surface. Secondly, any future CSPGs that interact

with the forming PNN will then be stably bound to the surface, allowing for an accumulation of CSPGs to occur over time. This gradual aggregation hypothesis suggests that this accumulation would then lead to the stable assembly of the PNN structure. Experiments aimed at testing this hypothesis in cell cultures by varying the availability of Acan and Hapln1 are required in the future. This hypothesis also provides a potential mechanism for temporally regulating the formation of PNNs by varying the amount of Hapln1 present within the PNN surface. Future work aimed at observing if the other Haplns (Hapln2 and Hapln4) and CSPGs (Bcan, Ncan, Vcan and Pcan) interact similarly with HA surfaces would provide greater insights into how the stable formation of PNNs is assembled. Future work could also analyse whether the upregulation of PNNs is correlated with the upregulation of Haplns.

A unique insight provided by chapter 4 was the observation that the density of surface-bound HA films affected the interaction of both Hapln1 and Acan. It particularly highlighted the potential for steric hinderance playing an important factor in the ability for Acan to interact with the surface. For Acan to be incorporated into HA films HA molecules were required to be spaced far enough apart to allow Acan to interact within the HA film. If HA films were too dense then the interaction of Acan was hindered, observed by the reduced effect on the ratio of $\Delta D / -\Delta f$. Interestingly, when combined with the observations in chapter 3 that a number of the CSPG molecules in the CNS are present in a cleaved, truncated form, it remains unknown if the cleaved CSPGs variants would be more likely to be incorporated into the PNN structure. Future work analysing how the different splice variants are affected by HA density would provide unique insights into how PNNs assemble.

Two PNN-associating molecules Sema3a and Tn-R have previously been identified as being mechanistically linked to a role in cross-linking the PNN structure (Aspberg, 1995; Lundell *et al.*, 2004; Morawski *et al.*, 2014; Djerbal *et al.*, 2019). The density of CS-E units may be of particular importance, as Sema3a is known to specifically cross-link GAG chains (Dick *et al.*, 2013; Vo *et al.*, 2013; Djerbal *et al.*, 2019). CS-E units have previously been analysed within PNNs and were found to make up approximately 2.1% of the total GAG composition (Deepa *et al.*, 2006). The density of CSPGs and the respective distribution of their G3 domains is likely to be of importance for Tn-R cross-linking. Both these mechanisms imply that the abundance of CSPGs (particularly their G3 domain) and the degree of CSPG glycosylation could influence the ability of Sema3a and Tn-R to cross-link PNNs. Furthermore, the relative abundance of Sema3a and Tn-R may also influence the degree of

cross-linking. In this project, the abundance of Tn-R was observed to remain relatively consistent throughout the different CNS regions investigated (cortex, hippocampus, cerebellum and cSC), though interestingly the relative proportions of CSPGs were differentially distributed. Specifically, in chapter 3 it was observed that a large proportion of CSPG species existed in a truncated form, implying that many CSPG splice variants would be present without a G3 domain. Furthermore, the distribution of glycosylated CSPGs species were also differentially distributed, suggesting that the relative proportions of GAGs within PNNs may also be regulated. This suggested that a combination of post-transcriptional and post-translational modification during CSPG synthesis, as well enzymatic cleavage are responsible for these variants. In this project the relative abundance of G3 domains and CS-E were not specifically, therefore although this research highlights potential future research perspectives, it cannot be concluded that these mechanisms have been observed in this project. Though the observation in chapter 4 that Tn-R was unable to interact with HA / Hapln1 / Acan films suggested that the abundance of Acan G3 domains may be responsible for the lack of Tn-R interacting with the films. Though again, this result was not conclusive. Future work analysing the abundance of G3 domains and CS-E present within PNNs may provide a mechanistic insight into how PNNs may be biomechanically regulated through cross-linking by Tn-R and Sema3a.

Future work is also required to further validate the structural properties of the PNN surfaces formed. The use of combinatorial techniques such as pairing QCM-D measurements with an optical measurement of density such as spectroscopic ellipsometry would allow for more a rigorous understanding of the density of molecules present within the forming films. Further methodologies could also be used to understand the topographical nature of the surface, such as the use of AFM. This would provide key information on how the supramolecular structures are assembling.

6.3 Potential mechanisms for biomechanical signalling

Biomechanical signalling mechanisms have been well documented in the CNS (Flanagan *et al.*, 2002; Georges *et al.*, 2006; Jiang *et al.*, 2008; Moshayedi *et al.*, 2010; Koch *et al.*, 2012; Franze *et al.*, 2013; Moshayedi *et al.*, 2014; Bollmann *et al.*, 2015; Koser *et al.*, 2016; Moeendarbary *et al.*, 2017). Therefore, cells within the CNS have the ability to identify changes to the biomechanical properties of surfaces. What remains currently unknown is

what the biomechanical properties of the PNN surfaces are and what factors are important in defining the biomechanical properties of the surface.

6.3.1 Mechanisms for altering the biomechanical properties of PNNs

By altering the size of HA alone, the biomechanical properties of films are affected, as observed in chapter 5. Increased HA size correlated with softer films, suggesting a potential mechanism for regulating the compliance of PNNs via HAS synthesis of HA on the cell surface. In chapter 3 a wide variation of HA sizes in the CNS was observed, therefore it is possible that these varying sizes partially act to change the biomechanical properties of PNNs. It is important to note that the observations in chapter 3 were not PNN-specific, therefore this project indicated that HA size may be important to the structure of PNNs but is not conclusive. Manipulating HA size also contributes to other biological processes including the function of cell surface receptors, such as CD44, where the mechanism of superselectivity has been proposed (English *et al.*, 1998; Lesley *et al.*, 2000; Wolny *et al.*, 2010; Dubacheva *et al.*, 2015). Therefore, to further understand the role of varying HA size within PNNs it is important to establish the range of HA sizes found within PNNs. One potential study could involve a combinatorial approach using the method of isolating components described by Kwok *et al* (2014) with the QCM-D measuring method described in chapter 5. Through understanding the size of HA in PNNs it would allow the initial compliance of the HA film that provides the foundation for PNN assembly to be better characterised. Furthermore, it would be interesting to observe if differing HA sizes are correlated with morphologically distinct PNN structures. Therefore, this project highlights the potential for HA size to be an important factor in manipulating the biomechanical properties of PNNs.

Interestingly, it was also observed that altering the density of HA on the surface of PNNs contributed to changes to the properties of PNNs. In chapter 5 the effect of HA density on the compliance of HA films was different for different sized HA chains. Although it was not possible to define a simple relationship, it indicated that the biomechanical properties of HA films are formed by a combination of both density and size of HA molecules on the cell surface. Therefore, the knowledge of both parameters is important to understanding the surface properties of the film. This provides a further reason for the need to determine the size of HA found within PNN structures.

Furthermore, altering the density of HA films also influenced the supramolecular assembly of PNN-associated molecules with the HA films. The observation in chapter 4 that Acan interaction had a larger influence on the biomechanical properties of sparse HA films in comparison with dense HA films indicated steric hindrance may be an important factor to consider during PNN formation. Previous work has also observed that the interaction of Acan with HA films caused the surfaces to become more compliant (Attili and Richter, 2013). Interestingly, when the idea of steric hindrance is applied to the results observed in chapter 3, where a variety of smaller CSPG splice variants were identified it suggests that a combination of both the size of the CSPG molecules as well as the density of HA surfaces is likely to influence the assembly of the supramolecular PNN structure and thus the biomechanical properties of the surface. Future work aimed at analysing how the splice variants interact with the sparse and dense HA surfaces defined in chapter 5 would provide unique insights into how these different CSPG splice-variants may be incorporated into PNNs and affect the biomechanical properties of the surface. Also, future work aimed at analysing the density of HA surfaces present on the surface of PNN-producing cells is recommended. This could potentially be achieved by observing the relative distances between HAS molecules on the cell surfaces using histochemical and fluorescent imaging techniques.

In chapter 4 it was observed that it was possible to change the biomechanical properties of HA surfaces by changing the density of Hapln1 associating with HA films. A larger density of Hapln1 correlated with a decrease in surface compliance, suggesting that the surfaces become more rigid. Interestingly, in chapter 3 the relative abundance of Hapln1 in the cortical region was increased in comparison with other CNS regions. It currently remains unknown if this increase in relative abundance correlates with more rigid PNNs in the cortical region. Furthermore, the physiological density of Hapln1 within PNNs remains an important future research question, as this will have direct implications on the formation of PNNs, as well as the biomechanical properties of the surface. Taken together the results suggest a possible mechanism for changing the biomechanical properties of the surface, alongside results that suggest that Hapln1 abundance displays CNS regional variations.

Therefore, taken together this project has provided multiple potential mechanisms by which the biomechanical properties of PNNs may be regulated. The likelihood is that all of these mechanisms act together to

influence the biomechanical properties of PNNs and produce the PNN structure. This may partially explain why the distinct PNN morphologies observed in the different CNS regions could not be characterised through the biochemical analysis alone. The morphologically distinct PNN structures are likely to be a reflection of a combination of a number of the biomechanical parameters described above.

6.3.2 Potential mechanisms for biomechanical signalling

Having identified a number of potential mechanisms for regulating the biomechanical properties of PNNs, particularly in manipulating the compliance of the surface, it is important to consider how this may influence biological processes in the CNS. One of the most obvious ways that the change in compliance could regulate cell behaviour, is if these changes to the surface could be detected by neuronal cells, specifically the axonal growth cones and glial cells via a biomechanical signalling mechanism. Both cell bodies and growth cones are known to actively mechanosense via stress-sensitive ion channels and integrin mediated pathways to measure the stiffness of substrates (Bray, 1979; Harris *et al.*, 1980; Betz *et al.*, 2011; Koch *et al.*, 2012; Schwarz and Gardel, 2012). Therefore, it is possible that the changes to compliance observed through changing the biochemical properties of PNNs could be detected by cells in the CNS causing them to change their behaviour. Glial cells have been observed to increase in area in response to stiffer surfaces (Georges *et al.*, 2006; Cullen *et al.*, 2007; Jiang *et al.*, 2008; Moshayedi *et al.*, 2010; Moshayedi *et al.*, 2014). Also, neurons have been observed to change their behaviour in response to changing biomechanical properties (Flanagan *et al.*, 2002; Kostic *et al.*, 2007; Jiang *et al.*, 2008; Jiang *et al.*, 2010; Previtiera *et al.*, 2010; Stabenfeldt and Laplaca, 2011). Though this project has identified that it is possible for a biomechanical signalling mechanism to be present and offers various possible methods for altering the biomechanical properties of PNNs, this project has not measured the biomechanical properties of PNNs surrounding cells. Future research aimed at providing measurements of compliance and surface thickness, as well as detecting the surface topology of PNNs, potentially using AFM would be recommended as it would provide a unique insight into precisely how the PNNs change the surface properties of neurons they surround.

Another potential way that PNNs effect mechanosensing is by acting as a barrier that limits the ability for the cell bodies and dendrites of neurons they surround to detect the biomechanical properties of their surroundings.

Neurons have been observed to respond to dynamic mechanical stimuli (LaPlaca *et al.*, 2005; Cullen and LaPlaca, 2006; Jiang *et al.*, 2010; Franze *et al.*, 2013). Currently, what remains unknown is if the biomechanical properties of PNNs differs from the biomechanical properties of the loose ECM. Although direct measurements have not been taken in this project, the observation in chapter 4 that increasing the density of molecules caused changes to the compliance of surfaces indicates that the increased presence of PNN-associated molecules in PNNs in comparison with the loose ECM is likely to change the biomechanical properties of the PNN environment. It would be interesting to observe if the cells ensheathed by PNNs can detect their own PNN via mechanosensing and if that influences their behaviour. Furthermore, it would be interesting to observe if the PNN surface influences the cells ability to respond to dynamic mechanical stimuli.

PNNs may also provide insulation and neuroprotection to the cells they surround. The observation in chapter 4 that Acan appeared to be sterically hindered from interacting within the HA film when the HA molecules were densely packed indicated that it is possible for PNN-like surface to impede the movement of molecules. Considering that HapIn1 density caused the surface to become less compliant, and also affected the interaction of Acan further suggests that the composition of the surface can influence molecular movement into the film. What remains unknown is if this limits the diffusion of molecules through the surface, which may provide a mechanism for both neuroprotection as well as controlling biochemical signalling. It would be interesting for future research to observe if the changes to the biomechanical properties of the film can actively regulate the diffusion of molecules through the film.

6.4 The successful establishment of methodologies for analysing PNNs

An important aspect of this project was the establishment of a method for measuring the formation of PNN-like surfaces *in vitro*. This method will provide a useful tool for further identifying how the contributions of further PNN-associating molecules affect the overall formation of PNN structures. By establishing a method that can both investigate the formation of PNNs, while simultaneously measuring the biomechanical properties of PNNs it has the potential to interrogate questions that were previously difficult to analyse. For example, both Sema3a and Tn-R are hypothesised to cross-link PNNs,

however it is currently unknown if they cause a conformational change to PNN structure, therefore using this methodology will aid in understanding how they alter the assembly of PNNs.

Furthermore, in chapter 4 this project established a method for creating a PNN-like surface *in vitro*. Stable HA / Acan / HapIn1 films were produced that recreated the molecular interactions that underpin the supramolecular assembly of PNNs. Future experiments that tweak and alter the methodology using other PNN-associated components will be able to create even more biochemically accurate PNN-like surfaces in the future. Furthermore, the abundance of each molecule present within PNNs still remains poorly characterised and remains the main challenge in developing this methodology in the future. However, the methodology in its current form still provide a useful tool that could then be scaled commercially to investigate how molecular interactions of potential CNS drug candidates affect the properties of PNNs. As PNNs have been correlated with many neurological diseases, methods for analysing PNNs will provide useful insights into disease pathologies.

Secondly, this project has established two methodologies in chapter 5 for measuring the molecular weight of GAG chains. As there are limited methodologies available for measuring the molecular weight of GAGs the establishment of these methodologies will provide a useful tool for further analysing and understanding GAGs in future experiments. Combining PAGE with protein standards provides a quick, methodology that increases the standards size ranges that can be used for establishing GAG size. The second methodology, using the measurement technique QCM-D established a technique for analysing the size of GAGs that are tethered to surfaces. As well as measuring HA, it could also be used to size other GAGs, such as CS, that is also abundant within PNNs. Currently, the size of CS chains found within PNNs is not known, yet the size and density of these GAG chains offers a further potential mechanism for altering the biomechanical properties of PNN surfaces. The establishment of a methodology for measuring the size of GAG chains described in this project will help gain measurements of GAG chain lengths found in PNNs in the future experiments.

Chapter 7: Conclusions

To gain insights into how the biochemical properties of PNNs influence the biomechanical properties of PNNs the distribution of PNN associating molecules was first analysed. Through the analysis of 4 distinct CNS regions (cortex, hippocampus, cerebellum and spinal cord) the heterogenous distribution of PNN-associated molecules throughout the different regions was observed. Furthermore, the CSPG variants observed in the different CNS regions were characterised. Taken together the large degree of biochemical heterogeneity observed within the 4 regions identified that PNNs may be more biochemically heterogeneous than previously thought. Also, the identification that CNS Acan is smaller than cartilage Acan, presents a potentially notable difference that could have significant implications for PNN organisation and phase separation.

To investigate how the individual biochemical PNN components influence the formation and biomechanical properties of PNNs a new methodology was established that allowed for artificial PNNs to be produced in a cell-free *in vitro* system using QCM-D. This method provided unique insights into the formation of PNN structures, as Hapln1 was able to stabilise the interaction of HA and Acan irrespective of the order of incubation. This implicated Hapln1 as being the potential molecular trigger that is responsible for the formation of PNNs.

Through manipulating the density of surface-bound HA the ability of Hapln1 and Acan to interact with the surface and alter its biomechanical properties was affected. Furthermore, the biomechanical properties of HA films could also be affected by altering the density of Hapln1. By increasing Hapln1 abundance HA films became less compliant.

A new methodology for measuring the size of GAG chains was optimised and established. A consequence of the establishment of this technique was the observation that as GAG size increased, HA films became more compliant. Therefore, it highlighted the potential for the biomechanical properties of PNNs to be altered by varying the size of HA chains synthesised at the cell surface.

Taken together this thesis suggests numerous potential mechanisms through which altering the biochemical composition of the PNN surface could influence the biomechanical properties of PNNs.

Chapter 8: References

- Arnst, N., Kuznetsova, S., Lipachev, N., Shaikhutdinov, N., Melnikova, A., Mavlikeev, M., Uvarov, P., Baltina, T. V., Rauvala, H., Osin, Y.N., Kiyasov, A.P. and Paveliev, M. 2016. Spatial patterns and cell surface clusters in perineuronal nets. *Brain Research*. **1648**, pp.214–223.
- Asher, R. and Bignami, A. 1991. Localization of hyaluronate in primary glial cell cultures derived from newborn rat brain. *Experimental Cell Research*. **195**(2), pp.401–411.
- Asher, R.A., Scheibe, R.J., Keiser, H.D. and Bignami, A. 1995. On the existence of a cartilage-like proteoglycan and link proteins in the central nervous system. *Glia*. **13**(4), pp.294–308.
- Aspberg, A. 2012. The Different Roles of Aggrecan Interaction Domains. *Journal of Histochemistry and Cytochemistry*. **60**(12), pp.987–996.
- Aspberg, A. 1995. The versican C-type lectin domain recognizes the adhesion protein tenascin-R. *Proceedings of the National Academy of Sciences of the United States of America*. **92**(November), pp.10590–10594.
- Aspberg, A., Adam, S., Kostka, G., Timpl, R. and Heinegård, D. 1999. Fibulin-1 is a ligand for the C-type lectin domains of aggrecan and versican. *Journal of Biological Chemistry*. **274**(29), pp.20444–20449.
- Aspberg, A., Miura, R., Bourdoulous, S., Shimonaka, M., Heinegard, D., Schachner, M., Ruoslahti, E. and Yamaguchi, Y. 1997. The C-type lectin domains of lecticans, a family of aggregating chondroitin sulfate proteoglycans, bind tenascin-R by protein-protein interactions independent of carbohydrate moiety. *Proceedings of the National Academy of Sciences*. **94**(19), pp.10116–10121.
- Attili, S. and Richter, R.P. 2013. Self-assembly and elasticity of hierarchical proteoglycan-hyaluronan brushes. *Soft Matter*. **9**(44), p.10473.
- Avram, S., Shaposhnikov, S., Buiu, C. and Mernea, M. 2014. Chondroitin Sulfate Proteoglycans: Structure-Function Relationship with Implication in Neural Development and Brain Disorders.
- Balazs, E.A., Watson, D., Duff, I.F. and Roseman, S. 1967. Hyaluronic acid in synovial fluid. I. Molecular parameters of hyaluronic acid in normal and arthritic human fluids. *Arthritis & Rheumatism*.
- Balmer, T.S. 2016. Perineuronal nets enhance the excitability of fast-spiking neurons. *eNeuro*. **3**(4).
- Bandtlow, C.E. and Zimmermann, D.R. 2000. Proteoglycans in the developing brain: New conceptual insights for old proteins. *Physiological Reviews*. **80**(4), pp.1267–1290.
- Banerjee, S.B., Gutzeit, V.A., Baman, J., Aoued, H.S., Doshi, N.K., Liu, R.C., Ressler, K.J., Luo, Y.-X., Xu, L.-Z., Wu, P. and Lu, L. 2017. Perineuronal nets in the adult sensory cortex are necessary for fear learning. *Neuron*. **57**(0), pp.276–289.
- Bano, F., Banerji, S., Howarth, M., Jackson, D.G. and Richter, R.P. 2016. A single molecule assay to probe monovalent and multivalent bonds

between hyaluronan and its key leukocyte receptor CD44 under force. *Scientific Reports*. **6**(1), pp.1–14.

- Baranova, N.S., Foulcer, S.J., Briggs, D.C., Tilakaratna, V., Enghild, J.J., Milner, C.M., Day, A.J. and Richter, R.P. 2013. Inter- α -inhibitor impairs TSG-6-induced hyaluronan cross-linking. *Journal of Biological Chemistry*. **288**(41), pp.29642–29653.
- Baranova, N.S., Inforzato, A., Briggs, D.C., Tilakaratna, V., Enghild, J.J., Thakar, D., Milner, C.M., Day, A.J. and Richter, R.P. 2014. Incorporation of pentraxin 3 into hyaluronan matrices is tightly regulated and promotes matrix cross-linking. *Journal of Biological Chemistry*. **289**(44), pp.30481–30498.
- Baranova, N.S., Nilebäck, E., Haller, F.M., Briggs, D.C., Svedhem, S., Day, A.J. and Richter, R.P. 2011. The inflammation-associated protein TSG-6 cross-links hyaluronan via hyaluronan-induced TSG-6 oligomers. *Journal of Biological Chemistry*. **286**(29), pp.25675–25686.
- Bekku, Y., Saito, M., Moser, M., Fuchigami, M., Maehara, A., Nakayama, M., Kusachi, S., Ninomiya, Y. and Oohashi, T. 2012. Bra12 is indispensable for the proper localization of brevican and the structural integrity of the perineuronal net in the brainstem and cerebellum. *The Journal of Comparative Neurology*. **520**(8), pp.1721–1736.
- Bekku, Y., Su, W.D., Hirakawa, S., Fessler, R., Ohtsuka, A., Kang, J.S., Sanders, J., Murakami, T., Ninomiya, Y. and Oohashi, T. 2003. Molecular cloning of Bra12, a novel brain-specific link protein, and immunohistochemical colocalization with brevican in perineuronal nets. *Molecular and Cellular Neuroscience*. **24**(1), pp.148–159.
- Bertolotto, A., Manzardo, E. and Guglielmone, R. 1996. Immunohistochemical mapping of perineuronal nets containing chondroitin unsulfated proteoglycan in the rat central nervous system. *Cell and Tissue Research*. **283**(2), pp.283–295.
- Betz, T., Koch, D., Lu, Y.-B., Franze, K. and Käs, J.A. 2011. Growth cones as soft and weak force generators. *Proceedings of the National Academy of Sciences of the United States of America*. **108**(33), pp.13420–13425.
- Beurdeley, M., Spatazza, J., Lee, H.H.C., Sugiyama, S., Bernard, C., Di Nardo, a. a., Hensch, T.K. and Prochiantz, A. 2012. Otx2 binding to perineuronal nets persistently regulates plasticity in the mature visual cortex. *Journal of Neuroscience*. **32**(27), pp.9429–9437.
- Beutel, O., Nikolaus, J., Birkholz, O., You, C., Schmidt, T., Herrmann, A. and Piehler, J. 2014. High-Fidelity Protein Targeting into Membrane Lipid Microdomains in Living Cells. *Angewandte Chemie*. **126**(5), pp.1335–1339.
- Bhilocha, S., Ripal, A., Pandya, M., Yuan, H., Tank, M., LoBello, J., Shytuhina, A., Wang, W., Wisniewski, H.G., De La Motte, C. and Cowman, M.K. 2011. Agarose and polyacrylamide gel electrophoresis methods for molecular mass analysis of 5- to 500-kDa hyaluronan. *Analytical Biochemistry*.
- Binette, F., Cravens, J., Kahoussi, B., Haudenschield, D.R. and Goetinck, P.F.

1994. Link protein is ubiquitously expressed in non-cartilaginous tissues where it enhances and stabilizes the interaction of proteoglycans with hyaluronic acid. *Journal of Biological Chemistry*. **269**(29), pp.19116–19122.
- Bollmann, L., Koser, D.E., Shahapure, R., Gautier, H.O.B., Holzapfel, G.A., Scarcelli, G., Gather, M.C., Ulbricht, E. and Franze, K. 2015. Microglia mechanics: Immune activation alters traction forces and durotaxis. *Frontiers in Cellular Neuroscience*. **9**(September), pp.1–16.
- Bouzioukh, F., Daoudal, G., Falk, J., Debanne, D., Rougon, G. and Castellani, V. 2006. Semaphorin3A regulates synaptic function of differentiated hippocampal neurons. *European Journal of Neuroscience*. **23**(9), pp.2247–2254.
- Bray, D. 1979. Mechanical tension produced by nerve cells in tissue culture. *Journal of Cell Science*. **37**(1), pp.391–410.
- Brückner, G., Brauer, K., Härtig, W., Wolff, J.R., Rickmann, M.J., Derouiche, A., Delpech, B., Girard, N., Oertel, W.H. and Reichenbach, A. 1993. Perineuronal nets provide a polyanionic, glia-associated form of microenvironment around certain neurons in many parts of the rat brain. *Glia*. **8**(3), pp.183–200.
- Brückner, G., Bringmann, A., Köppe, G., Härtig, W. and Brauer, K. 1996. In vivo and in vitro labelling of perineuronal nets in rat brain. *Brain research*. **720**(1–2), pp.84–92.
- Brückner, G., Morawski, M. and Arendt, T. 2008. Aggrecan-based extracellular matrix is an integral part of the human basal ganglia circuit. *Neuroscience*. **151**(2), pp.489–504.
- Brückner, Gert, Pavlica, S., Morawski, M., Palacios, A.G. and Reichenbach, A. 2006. Organization of brain extracellular matrix in the Chilean fat-tailed mouse opossum *Thylamys elegans* (Waterhouse, 1839). *Journal of Chemical Neuroanatomy*. **32**(2–4), pp.143–158.
- Brückner, G., Szeöke, S., Pavlica, S., Grosche, J. and Kacza, J. 2006. Axon initial segment ensheathed by extracellular matrix in perineuronal nets. *Neuroscience*. **138**(2), pp.365–375.
- Bugiani, M., Postma, N., Polder, E., Dieleman, N., Scheffer, P.G., Sim, F.J., van der Knaap, M.S. and Boor, I. 2013. Hyaluronan accumulation and arrested oligodendrocyte progenitor maturation in vanishing white matter disease. *Brain : a journal of neurology*. **136**(Pt 1), pp.209–22.
- Cabungcal, J.-H., Steullet, P., Morishita, H., Kraftsik, R., Cuenod, M., Hensch, T.K. and Do, K.Q. 2013. Perineuronal nets protect fast-spiking interneurons against oxidative stress. *Proceedings of the National Academy of Sciences of the United States of America*. **110**(22), pp.9130–9135.
- Cargill, R., Kohama, S.G., Struve, J., Su, W., Banine, F., Witkowski, E., Back, S.A. and Sherman, L.S. 2012. Astrocytes in aged nonhuman primate brain gray matter synthesize excess hyaluronan. *Neurobiology of Aging*. **33**(4), 830.e13-830.e24.
- Carstens, K.E., Phillips, M.L., Pozzo-Miller, L., Weinberg, R.J. and Dudek,

- S.M. 2016. Perineuronal nets suppress plasticity of excitatory synapses on CA2 pyramidal neurons. *Journal of Neuroscience*. **36**(23), pp.6312–6320.
- Carulli, D., Broersen, R., de Winter, F., Muir, E.M., Meškovic, M., de Waal, M., de Vries, S., Boele, H.J., Canto, C.B., de Zeeuw, C.I. and Verhaagen, J. 2020. Cerebellar plasticity and associative memories are controlled by perineuronal nets. *Proceedings of the National Academy of Sciences of the United States of America*. **117**(12), pp.6855–6865.
- Carulli, D., Foscarin, S., Faralli, A., Pajaj, E. and Rossi, F. 2013. Modulation of semaphorin3A in perineuronal nets during structural plasticity in the adult cerebellum. *Molecular and Cellular Neuroscience*. **57**, pp.10–22.
- Carulli, D., Pizzorusso, T., Kwok, J.C.F., Putignano, E., Poli, A., Forostyak, S., Andrews, M.R., Deepa, S.S., Glant, T.T. and Fawcett, J.W. 2010. Animals lacking link protein have attenuated perineuronal nets and persistent plasticity. *Brain*. **133**, pp.2331–2347.
- Carulli, D., Rhodes, K.E., Brown, D.J., Bonnert, T.P., Pollack, S.J., Oliver, K., Strata, P. and Fawcett, J.W. 2006. Composition of perineuronal nets in the adult rat cerebellum and the cellular origin of their components. *The Journal of Comparative Neurology*. **494**(4), pp.559–577.
- Carulli, D., Rhodes, K.E. and Fawcett, J.W. 2007. Upregulation of aggrecan, link protein 1, and hyaluronan synthases during formation of perineuronal nets in the rat cerebellum. *The Journal of Comparative Neurology*. **501**(1), pp.83–94.
- Celio, M.R., Spreafico, R., De Biasi, S. and Vitellaro-Zuccarello, L. 1998. Perineuronal nets: past and present. *Trends in Neurosciences*. **21**(12), pp.510–515.
- Chalfie, M. 2009. Neurosensory mechanotransduction. *Nature Reviews Molecular Cell Biology*. **10**(1), pp.44–52.
- Chang, M.C., Park, J.M., Pelkey, K.A., Grabenstatter, H.L., Xu, D., Linden, D.J., Sutula, T.P., McBain, C.J. and Worley, P.F. 2010. Narp regulates homeostatic scaling of excitatory synapses on parvalbumin-expressing interneurons. *Nature Neuroscience*. **13**(9), pp.1090–1097.
- Cherr, G.N., Yudin, A.I. and Katz, D.F. 1990. Organization of the Hamster Cumulus Extracellular Matrix: A Hyaluronate-Glycoprotein Gel which Modulates Sperm Access to the Oocyte: Extracellular matrix/Hyaluronate/Oocyte-cumulus complex/Extracellular matrix glycoproteins/Sperm enzymes. *Development, Growth & Differentiation*.
- Chiquet-Ehrismann, R. and Tucker, R.P. 2011. Tenascins and the importance of adhesion modulation. *Cold Spring Harbor Perspectives in Biology*. **3**(5), pp.1–19.
- Citri, A. and Malenka, R.C. 2008. Synaptic Plasticity: Multiple Forms, Functions, and Mechanisms. *Neuropsychopharmacology volume*. **33**, pp.18–41.
- Clark, S.J., Keenan, T.D.L., Fielder, H.L., Collinson, L.J., Holley, R.J., Merry, C.L.R., van Kuppevelt, T.H., Day, A.J. and Bishop, P.N. 2011. Mapping the differential distribution of glycosaminoglycans in the adult human

- retina, choroid, and sclera. *Investigative Ophthalmology and Visual Science*. **52**(9), pp.6511–6521.
- Cowman, M.K., Chen, C.C., Pandya, M., Yuan, H., Ramkishun, D., LoBello, J., Bhilocha, S., Russell-Puleri, S., Skendaj, E., Mijovic, J. and Jing, W. 2011. Improved agarose gel electrophoresis method and molecular mass calculation for high molecular mass hyaluronan. *Analytical Biochemistry*.
- Cullen, D.K. and LaPlaca, M.C. 2006. Neuronal response to high rate shear deformation depends on heterogeneity of the local strain field. *Journal of Neurotrauma*. **23**(9), pp.1304–1319.
- Cullen, D.K., Simon, C.M. and LaPlaca, M.C. 2007. Strain rate-dependent induction of reactive astrogliosis and cell death in three-dimensional neuronal-astrocytic co-cultures. *Brain Research*. **1158**(1), pp.103–115.
- Cyphert, J.M., Trempus, C.S. and Garantziotis, S. 2015. Size Matters: Molecular Weight Specificity of Hyaluronan Effects in Cell Biology. *International journal of cell biology*. **2015**, p.563818.
- Day, A.J. and Prestwich, G.D. 2002. Hyaluronan-binding proteins: Tying up the giant. *Journal of Biological Chemistry*.
- Day, J.M., Olin, A.I., Murdoch, A.D., Canfield, A., Sasaki, T., Timpl, R., Hardingham, T.E. and Aspberg, A. 2004. Alternative Splicing in the Aggrecan G3 Domain Influences Binding Interactions with Tenascin-C and Other Extracellular Matrix Proteins. *Journal of Biological Chemistry*. **279**(13), pp.12511–12518.
- DeAngelis, P.L., Jing, W., Drake, R.R. and Achyuthan, A.M. 1998. Identification and molecular cloning of a unique hyaluronan synthase from *Pasteurella multocida*. *Journal of Biological Chemistry*. **273**(14), pp.8454–8458.
- Deepa, S.S., Carulli, D., Galtrey, C., Rhodes, K., Fukuda, J., Mikami, T., Sugahara, K. and Fawcett, J.W. 2006. Composition of perineuronal net extracellular matrix in rat brain: A different disaccharide composition for the net-associated proteoglycans. *Journal of Biological Chemistry*. **281**(26), pp.17789–17800.
- Dick, G., Liktan, C., Alves, J.N., Ehlert, E.M.E., Miller, G.M., Hsieh-Wilson, L.C., Sugahara, K., Oosterhof, A., Van Kuppevelt, T.H., Verhaagen, J., Fawcett, J.W. and Kwok, J.C.F. 2013. Semaphorin 3A binds to the perineuronal nets via chondroitin sulfate type E motifs in rodent brains. *Journal of Biological Chemistry*. **288**(38), pp.27384–27395.
- Dityatev, A., Brückner, G., Dityateva, G., Grosche, J., Kleene, R. and Schachner, M. 2007. Activity-dependent formation and functions of chondroitin sulfate-rich extracellular matrix of perineuronal nets. *Developmental Neurobiology*. **67**(5), pp.570–588.
- Djrbal, L., Vivès, R.R., Lopin-Bon, C., Richter, R.P., Kwok, J.C.F. and Lortat-Jacob, H. 2019. Semaphorin 3A binding to chondroitin sulfate E enhances the biological activity of the protein, and cross-links and rigidifies glycosaminoglycan matrices. *bioRxiv*, p.851121.
- Doerge, K., Sasaki, M., Horigan, E., Hassell, J. and Yamada, Y. 1987. Complete primary structure of the rat cartilage proteoglycan core protein

- deduced from cDNA clones. *J Biol Chem.* **262**(36), pp.17757–17767.
- Du, B. and Johannsmann, D. 2004. Operation of the quartz crystal microbalance in liquids: Derivation of the elastic compliance of a film from the ratio of bandwidth shift and frequency shift. *Langmuir.* **20**(7), pp.2809–2812.
- Dubacheva, G. V., Araya-Callis, C., Geert Volbeda, A., Fairhead, M., Codée, J., Howarth, M. and Richter, R.P. 2017. Controlling Multivalent Binding through Surface Chemistry: Model Study on Streptavidin. *Journal of the American Chemical Society.* **139**(11), pp.4157–4167.
- Dubacheva, G. V., Curk, T., Auzély-Velty, R., Frenkel, D. and Richter, R.P. 2015. Designing multivalent probes for tunable superselective targeting. *Proceedings of the National Academy of Sciences of the United States of America.* **112**(18), pp.5579–5584.
- Dyck, S.M. and Karimi-Abdolrezaee, S. 2015. Chondroitin sulfate proteoglycans: Key modulators in the developing and pathologic central nervous system. *Experimental Neurology.* **269**, pp.169–187.
- Dzyubenko, E., Manrique-Castano, D., Kleinschnitz, C., Faissner, A. and Hermann, D.M. 2018. Topological remodeling of cortical perineuronal nets in focal cerebral ischemia and mild hypoperfusion. *Matrix Biology.* **74**, pp.121–132.
- Edamatsu, M., Miyano, R., Fujikawa, A., Fujii, F., Hori, T., Sakaba, T. and Oohashi, T. 2018. Hapln4/Bral2 is a selective regulator for formation and transmission of GABAergic synapses between Purkinje and deep cerebellar nuclei neurons. *Journal of Neurochemistry.* **147**(6), pp.748–763.
- Eisele, N.B., Andersson, F.I., Frey, S. and Richter, R.P. 2012. Viscoelasticity of thin biomolecular films: A case study on nucleoporin phenylalanine-glycine repeats grafted to a histidine-tag capturing QCM-D sensor. *Biomacromolecules.* **13**(8), pp.2322–2332.
- English, N.M., Lesley, J.F. and Hyman, R. 1998. Site-specific De-N-glycosylation of CD44 Can Activate Hyaluronan Binding, and CD44 Activation States Show Distinct Threshold Densities for Hyaluronan Binding. *Cancer Research.* **58**(16), pp.3736–3742.
- Enwright, J.F., Sanapala, S., Foglio, A., Berry, R., Fish, K.N. and Lewis, D.A. 2016. Reduced labeling of parvalbumin neurons and perineuronal nets in the dorsolateral prefrontal cortex of subjects with schizophrenia. *Neuropsychopharmacology.* **41**(9), pp.2206–2214.
- Erickson, H.P. 2009. Size and shape of protein molecules at the nanometer level determined by sedimentation, gel filtration, and electron microscopy. *Biological Procedures Online.* **11**(1), pp.32–51.
- Faissner, A. 1997. The tenascin gene family in axon growth and guidance. *Cell and Tissue Research.* **290**(2), pp.331–341.
- Favuzzi, E., Marques-Smith, A., Deogracias, R., Winterflood, C.M., Sánchez-Aguilera, A., Mantoan, L., Maeso, P., Fernandes, C., Ewers, H. and Rico, B. 2017. Activity-Dependent Gating of Parvalbumin Interneuron Function by the Perineuronal Net Protein Brevican. *Neuron.* **95**(3), pp.639–

655.e10.

- Fisher, D., Xing, B., Dill, J., Li, H., Hoang, H.H., Zhao, Z., Yang, X.-L., Bachoo, R., Cannon, S., Longo, F.M., Sheng, M., Silver, J. and Li, S. 2011. Leukocyte common antigen-related phosphatase is a functional receptor for chondroitin sulfate proteoglycan axon growth inhibitors. *Journal of Neuroscience*. **31**(40), pp.14051–14066.
- Flanagan, L.A., Ju, Y.-E., Marg, B., Osterfield, M. and Janmey, P.A. 2002. Neurite branching on deformable substrates. *Neuroreport*. **13**(18), pp.2411–2415.
- Foscarin, S., Raha-Chowdhury, R., Fawcett, J.W. and Kwok, J.C.F. 2017. Brain ageing changes proteoglycan sulfation, rendering perineuronal nets more inhibitory. *Aging*. **9**(6), pp.1607–1622.
- Foulcer, S.J., Day, A.J. and Apte, S.S. 2015. Isolation and purification of versican and analysis of versican proteolysis. *Methods in Molecular Biology*. **1229**, pp.587–604.
- Franze, K., Gerdemann, J., Weick, M., Betz, T., Pawlizak, S., Lakadamyali, M., Bayer, J., Rillich, K., Gögler, M., Lu, Y.-B., Reichenbach, A., Janmey, P. and Käs, J. 2009. Neurite branch retraction is caused by a threshold-dependent mechanical impact. *Biophysical Journal*. **97**(7), pp.1883–1890.
- Franze, K., Janmey, P.A. and Guck, J. 2013. Mechanics in neuronal development and repair. *Annual Review of Biomedical Engineering*. **15**(1), pp.227–251.
- Frischknecht, R., Heine, M., Perrais, D., Seidenbecher, C.I., Choquet, D. and Gundelfinger, E.D. 2009. Brain extracellular matrix affects AMPA receptor lateral mobility and short-term synaptic plasticity. *Nature Neuroscience*. **12**(7), pp.897–904.
- Galtrey, C.M. and Fawcett, J.W. 2007. The role of chondroitin sulfate proteoglycans in regeneration and plasticity in the central nervous system. *Brain Research Reviews*. **54**(1), pp.1–18.
- Galtrey, C.M., Kwok, J.C.F., Carulli, D., Rhodes, K.E. and Fawcett, J.W. 2008. Distribution and synthesis of extracellular matrix proteoglycans, hyaluronan, link proteins and tenascin-R in the rat spinal cord. *The European Journal of Neuroscience*. **27**(6), pp.1373–1390.
- Genade, T. and Lang, D.M. 2013. Resveratrol extends lifespan and preserves glia but not neurons of the *Nothobranchius guentheri* optic tectum. *Experimental Gerontology*. **48**(2), pp.202–212.
- Georges, P.C., Miller, W.J., Meaney, D.F., Sawyer, E.S. and Janmey, P.A. 2006. Matrices with compliance comparable to that of brain tissue select neuronal over glial growth in mixed cortical cultures. *Biophysical Journal*. **90**(8), pp.3012–3018.
- Ghatak, S., Misra, S. and Toole, B.P. 2002. Hyaluronan oligosaccharides inhibit anchorage-independent growth of tumor cells by suppressing the phosphoinositide 3-kinase/Akt cell survival pathway. *Journal of Biological Chemistry*.

- Giamanco, K.A. and Matthews, R.T. 2012. Deconstructing the perineuronal net: Cellular contributions and molecular composition of the neuronal extracellular matrix. *Neuroscience*. **218**, pp.367–384.
- Giamanco, K.A., Morawski, M. and Matthews, R.T. 2010. Perineuronal net formation and structure in aggrecan knockout mice. *Neuroscience*. **170**(4), pp.1314–27.
- Goa, K.L. and Benfield, P. 1994. Hyaluronic Acid: A Review of its Pharmacology and Use as a Surgical Aid in Ophthalmology, and its Therapeutic Potential in Joint Disease and Wound Healing. *Drugs*.
- Golgi, C. 1898. Intorno alla struttura delle cellule nervose. *Bollettino della Società Medico Chirurgica di Pavia*. **13**, pp.3–16.
- Gomez, T.M. and Zheng, J.Q. 2006. The molecular basis for calcium-dependent axon pathfinding. *Nature Reviews Neuroscience*. **7**(2), pp.115–125.
- Goodenough, A.L. 2018. *Development of an in vivo probe for perineuronal nets*. University of Leeds.
- Grande-Allen, K., Calabro, A., Gupta, V., Wight, T., Hascall, V. and Vesely, I. 2004. Glycosaminoglycans and proteoglycans in normal mitral valve leaflets and chordae: association with regions of tensile and compressive loading. *Glycobiology*. **14**(7), pp.621–633.
- Grashoff, C., Hoffman, B.D., Brenner, M.D., Zhou, R., Parsons, M., Yang, M.T., McLean, M.A., Sligar, S.G., Chen, C.S., Ha, T. and Schwartz, M.A. 2010. Measuring mechanical tension across vinculin reveals regulation of focal adhesion dynamics. *Nature*. **466**(7303), pp.263–266.
- Grosberg, A.Y. and Khokhlov, A.R. 1994. *Statistical Physics of Macromolecules*. New York: AIP Press.
- Hagihara, K., Miura, R., Kosaki, R., Berglund, E., Ranscht, B. and Yamaguchi, Y. 1999. Immunohistochemical evidence for the brevican-tenascin-R interaction: colocalization in perineuronal nets suggests a physiological role for the interaction in the adult rat brain. *The Journal of Comparative Neurology*. **410**(2), pp.256–264.
- Halder, G., Dupont, S. and Piccolo, S. 2012. Transduction of mechanical and cytoskeletal cues by YAP and TAZ. *Nature Reviews Molecular Cell Biology*. **13**(9), pp.591–600.
- Hardie, R.C. and Franze, K. 2012. Photomechanical responses in Drosophila photoreceptors. *Science*. **338**, pp.260–263.
- Hardingham, T.E. 1979. The role of link-protein in the structure of cartilage proteoglycan aggregates. *The Biochemical Journal*. **177**(1), pp.237–247.
- Harris, A.K., Wild, P. and Stopak, D. 1980. Silicone rubber substrata: a new wrinkle in the study of cell locomotion. *Science*. **208**(4440), pp.177–179.
- Harris, N.G., Nogueira, M.S.M., Verley, D.R. and Sutton, R.L. 2013. Chondroitinase enhances cortical map plasticity and increases functionally active sprouting axons after brain injury. *Journal of Neurotrauma*. **30**(14), pp.1257–1269.
- Härtig, W., Brauer, K., Bigl, V. and Brückner, G. 1994. Chondroitin sulfate

- proteoglycan-immunoreactivity of lectin-labeled perineuronal nets around parvalbumin-containing neurons. *Brain Research*. **635**(1–2), pp.307–311.
- Härtig, W., Brauer, K. and Brückner, G. 1992. Wisteria floribunda agglutinin-labelled nets surround parvalbumin-containing neurons. *Neuroreport*. **3**(10), pp.869–872.
- Härtig, W., Derouiche, A., Welt, K., Brauer, K., Grosche, J., Mäder, M., Reichenbach, A. and Brückner, G. 1999. Cortical neurons immunoreactive for the potassium channel Kv3.1b subunit are predominantly surrounded by perineuronal nets presumed as a buffering system for cations. *Brain Research*. **842**(1), pp.15–29.
- Härtig, W., Singer, A., Grosche, J., Brauer, K., Ottersen, O.P. and Brückner, G. 2001. Perineuronal nets in the rat medial nucleus of the trapezoid body surround neurons immunoreactive for various amino acids, calcium-binding proteins and the potassium channel subunit Kv3.1b. *Brain research*. **899**(1–2), pp.123–33.
- Hascall, V.C. 1988. Proteoglycans: the chondroitin sulfate/keratan sulfate proteoglycans of cartilage. *ISI Atlas of Science: Biochemistry and Molecular Biology*. **1**, pp.189–198.
- Hascall, V.C. and Heinegård, D. 1974a. Aggregation of cartilage proteoglycans, I: the role of hyaluronic acid. *Journal of Biological Chemistry*. **249**, pp.4232–4241.
- Hascall, V.C. and Heinegård, D. 1974b. Aggregation of cartilage proteoglycans, II: oligosaccharide competitors of the proteoglycan-hyaluronic acid interaction. *Journal of Biological Chemistry*. **249**, pp.4242–4249.
- Hascall, V.C. and Sajdera, S.W. 1970. Physical properties and polydispersity of proteoglycan from bovine nasal cartilage. *The Journal of biological chemistry*. **245**(19), pp.4920–30.
- Heinegård, D. and Hascall, V.C. 1974. Aggregation of cartilage proteoglycans, 3: characteristics of the proteins isolated from trypsin digests of aggregates. *Journal of Biological Chemistry*. **249**, pp.4250–4256.
- Hirakawa, S., Oohashi, T., Su, W.-D., Yoshioka, H., Murakami, T., Arata, J. and Ninomiya, Y. 2000. The brain link protein-1 (BRAL1): cDNA cloning, genomic structure, and characterization as a novel link protein expressed in adult brain. *Biochemical and Biophysical Research Communications*. **276**(3), pp.982–989.
- Hokputsa, S., Jumel, K., Alexander, C. and Harding, S.E. 2003. A comparison of molecular mass determination of hyaluronic acid using SEC/MALLS and sedimentation equilibrium *In: European Biophysics Journal*.
- Honoré, E. 2007. The neuronal background K2P channels: Focus on TREK1. *Nature Reviews Neuroscience*. **8**(4), pp.251–261.
- Hrabětová, S., Masri, D., Tao, L., Xiao, F. and Nicholson, C. 2009. Calcium diffusion enhanced after cleavage of negatively charged components of brain extracellular matrix by chondroitinase ABC. *The Journal of Physiology*. **587**(16), pp.4029–4049.

- Hylin, M.J., Orsi, S.A., Moore, A.N. and Dash, P.K. 2013. Disruption of the perineuronal net in the hippocampus or medial prefrontal cortex impairs fear conditioning. *Learning & Memory*. **20**(5), pp.267–273.
- Ilya, R. and Brisson, A. 2001. Streptavidin 2D Crystals on Supported Phospholipid Bilayers: Toward Constructing Anchored Phospholipid Bilayers. *Langmuir*. **17**(26), pp.8293–8299.
- Irvine, S.F. and Kwok, J.C.F. 2018. Perineuronal nets in spinal motoneurons: Chondroitin sulphate proteoglycan around alpha motoneurons. *International Journal of Molecular Sciences*.
- Isogai, Z., Aspberg, A., Keene, D.R., Ono, R.N., Reinhardt, D.P. and Sakai, L.Y. 2002. Versican interacts with fibrillin-1 and links extracellular microfibrils to other connective tissue networks. *Journal of Biological Chemistry*. **277**(6), pp.4565–4572.
- Itano, N., Sawai, T., Yoshida, M., Lenas, P., Yamada, Y., Imagawa, M., Shinomura, T., Hamaguchi, M., Yoshida, Y., Ohnuki, Y., Miyauchi, S., Spicer, A.P., McDonald, J.A. and Kimata, K. 1999. Three isoforms of mammalian hyaluronan synthases have distinct enzymatic properties. *Journal of Biological Chemistry*.
- Ito, K., Shinomura, T., Zako, M., Ujita, M. and Kimata, K. 1995. Multiple forms of mouse PG-M, a large chondroitin sulfate proteoglycan generated by alternative splicing. *Journal of Biological Chemistry*. **270**(2), pp.958–965.
- Jiang, D., Liang, J. and Noble, P.W. 2007. Hyaluronan in Tissue Injury and Repair. *Annual Review of Cell and Developmental Biology*. **23**(1), pp.435–461.
- Jiang, F.X., Yurke, B., Firestein, B.L. and Langrana, N.A. 2008. Neurite outgrowth on a DNA crosslinked hydrogel with tunable stiffnesses. *Annals of Biomedical Engineering*. **36**(9), pp.1565–1579.
- Jiang, F.X., Yurke, B., Schloss, R.S., Firestein, B.L. and Langrana, N.A. 2010. Effect of dynamic stiffness of the substrates on neurite outgrowth by using a DNA-crosslinked hydrogel. *Tissue Engineering - Part A*. **16**(6), pp.1873–1889.
- Jing, W. and DeAngelis, P.L. 2004. Synchronized chemoenzymatic synthesis of monodisperse hyaluronan polymers. *Journal of Biological Chemistry*. **279**(40), pp.42345–42349.
- Jing, W., Michael Haller, F., Almond, A. and DeAngelis, P.L. 2006. Defined megadalton hyaluronan polymer standards. *Analytical Biochemistry*.
- Johannsmann, D., Reviakine, I. and Richter, R.P. 2009. Dissipation in films of adsorbed nanospheres studied by quartz crystal microbalance (QCM). *Analytical Chemistry*. **81**(19), pp.8167–8176.
- John, N., Krügel, H., Frischknecht, R., Smalla, K.H., Schultz, C., Kreutz, M.R., Gundelfinger, E.D. and Seidenbecher, C.I. 2006. Brevican-containing perineuronal nets of extracellular matrix in dissociated hippocampal primary cultures. *Molecular and Cellular Neuroscience*. **31**(4), pp.774–784.
- Kalb, R.G. and Hockfield, S. 1988. Molecular evidence for early activity-

- dependent development of hamster motor neurons. *The Journal of neuroscience: the official journal of the Society for Neuroscience*. **8**(7), pp.2350–2360.
- Kalita, K., Kuzniewska, B. and Kaczmarek, L. 2012. MKLs: Co-factors of serum response factor (SRF) in neuronal responses. *The International Journal of Biochemistry & Cell Biology*. **44**(9), pp.1444–1447.
- Kanchanawong, P., Shtengel, G., Pasapera, A.M., Ramko, E.B., Davidson, M.W., Hess, H.F. and Waterman, C.M. 2010. Nanoscale architecture of integrin-based cell adhesions. *Nature*. **468**(7323), pp.580–584.
- Keller, C.A. and Kasemo, B. 1998. Surface specific kinetics of lipid vesicle adsorption measured with a quartz crystal microbalance. *Biophysical Journal*. **75**(3), pp.1397–1402.
- Kiani, C., Chen, L., Wu, Y.J., Yee, A.J. and Yang, B.B. 2002. Structure and function of aggrecan. *Cell Research*. **12**(1), pp.19–32.
- Kitagawa, H., Tsutsumi, K., Tone, Y. and Sugahara, K. 1997. Developmental regulation of the sulfation profile of chondroitin sulfate chains in the chicken embryo brain. *Journal of Biological Chemistry*. **272**(50), pp.31377–31381.
- Koch, D., Rosoff, W.J., Jiang, J., Geller, H.M. and Urbach, J.S. 2012. Strength in the periphery: growth cone biomechanics and substrate rigidity response in peripheral and central nervous system neurons. *Biophysical Journal*. **102**(3), pp.452–460.
- Koser, D.E., Thompson, A.J., Foster, S.K., Dwivedy, A., Pillai, E.K., Sheridan, G.K., Svoboda, H., Viana, M., Costa, L.D.F., Guck, J., Holt, C.E. and Franze, K. 2016. Mechanosensing is critical for axon growth in the developing brain. *Nature Neuroscience*. **19**(12), pp.1592–1598.
- Kostic, A., Sap, J. and Sheetz, M.P. 2007. RPTP α is required for rigidity-dependent inhibition of extension and differentiation of hippocampal neurons. *Journal of Cell Science*. **120**(21), pp.3895–3904.
- Kurokawa, T., Tsuda, M. and Sugino, Y. 1976. Purification and characterization of a lectin from *Wistaria floribunda* seeds. *Journal of Biological Chemistry*. **251**(18), pp.5686–5693.
- Kwok, J.C., Carulli, D. and Fawcett, J.W. 2010. In vitro modeling of perineuronal nets: hyaluronan synthase and link protein are necessary for their formation and integrity. *Journal of neurochemistry*. **114**(5), pp.1447–1459.
- Kwok, J.C.F., Dick, G., Wang, D. and Fawcett, J.W. 2011. Extracellular matrix and perineuronal nets in CNS repair. *Developmental Neurobiology*. **71**(11), pp.1073–1089.
- Kwok, J.C.F., Foscarin, S. and Fawcett, J.W. 2014. Perineuronal nets: A special structure in the central nervous system extracellular matrix *In: Extracellular Matrix.*, pp.23–32.
- LaPlaca, M.C., Cullen, D.K., McLoughlin, J.J. and Cargill, R.S. 2005. High rate shear strain of three-dimensional neural cell cultures: A new in vitro traumatic brain injury model. *Journal of Biomechanics*. **38**(5), pp.1093–

1105.

- Larsson, C., Rodahl, M. and Höök, F. 2003. Characterization of DNA immobilization and subsequent hybridization on a 2D arrangement of streptavidin on a biotin-modified lipid bilayer supported on SiO₂. *Analytical Chemistry*. **75**(19), pp.5080–5087.
- Lee, H., McKeon, R.J. and Bellamkonda, R. V. 2010. Sustained delivery of thermostabilized chABC enhances axonal sprouting and functional recovery after spinal cord injury. *Proceedings of the National Academy of Sciences*. **107**(8), pp.3340–3345.
- Lee, H.G. and Cowman, M.K. 1994. An agarose gel electrophoretic method for analysis of hyaluronan molecular weight distribution. *Analytical Biochemistry*. **219**(2), pp.278–287.
- Lee, J., Ishihara, A., Oxford, G., Johnson, B. and Jacobson, K. 1999. Regulation of cell movement is mediated by stretch-activated calcium channels. *Nature*. **400**(6742), pp.382–386.
- Lesley, J., English, N., Charles, C. and Hyman, R. 2000. The role of the CD44 cytoplasmic and transmembrane domains in constitutive and inducible hyaluronan binding. *European Journal of Immunology*. **30**(1), pp.245–253.
- Levicky, R., Herne, T.M., Tarlov, M.J. and Satija, S.K. 1998. Using self-assembly to control the structure of DNA monolayers on gold: A neutron reflectivity study. *Journal of the American Chemical Society*. **120**(38), pp.9787–9792.
- Lin, W., Shuster, S., Maibach, H.I. and Stern, R. 1997. Patterns of hyaluronan staining are modified by fixation techniques. *Journal of Histochemistry and Cytochemistry*. **45**(8), pp.1157–1163.
- Long, K.R., Newland, B., Florio, M., Kalebic, N., Langen, B., Kolterer, A., Wimberger, P. and Huttner, W.B. 2018. Extracellular Matrix Components HAPLN1, Lumican, and Collagen I Cause Hyaluronic Acid-Dependent Folding of the Developing Human Neocortex. *Neuron*. **99**(4), pp.702–719.e7.
- Lu, Y., Weers, B. and Stellwagen, N.C. 2002. DNA persistence length revisited. *Biopolymers*. **61**(4), pp.261–275.
- Lundell, A., Olin, A.I., Mörgelin, M., Al-Karadaghi, S., Aspberg, A., Logan, D.T., Krug, M., Seidenbecher, C.I., Boeckers, T.M., Rauch, U. and Al., E. 2004. Structural basis for interactions between tenascins and lectican C-type lectin domains: evidence for a crosslinking role for tenascins. *Structure*. **12**(8), pp.1495–1506.
- M T Dours-Zimmermann and D R Zimmermann 1994. A novel glycosaminoglycan attachment domain identified in two alternative splice variants of human versican. *The Journal of Biological Chemistry*. **269**, pp.32992–32998.
- Mammoto, A., Mammoto, T. and Ingber, D.E. 2012. Mechanosensitive mechanisms in transcriptional regulation. *Journal of Cell Science*. **125**(13), pp.3061–3073.

- Maniotis, A.J., Chen, C.S. and Ingber, D.E. 1997. Demonstration of mechanical connections between integrins, cytoskeletal filaments, and nucleoplasm that stabilize nuclear structure. *Proceedings of the National Academy of Sciences of the United States of America*. **94**(3), pp.849–854.
- Manning 1986. Polymer persistence length characterized as a critical length for instability caused by a fluctuating twist. *Physical review. A, General physics*. **34**(1), pp.668–670.
- Marret, S., Delpech, B., Delpech, A., Asou, H., Girard, N., Courel, M.N., Chauzy, C., Maingonnat, C. and Fessard, C. 1994. Expression and effects of hyaluronan and of the hyaluronan-binding protein hyaluronectin in newborn rat brain glial cell cultures. *Journal of neurochemistry*. **62**(4), pp.1285–95.
- Massey, J.M., Hubscher, C.H., Wagoner, M.R., Decker, J. a, Amps, J., Silver, J. and Onifer, S.M. 2006. Chondroitinase ABC digestion of the perineuronal net promotes functional collateral sprouting in the cuneate nucleus after cervical spinal cord injury. *The Journal of Neuroscience*. **26**(16), pp.4406–4414.
- Matsumoto, K., Shionyu, M., Go, M., Shimizu, K., Shinomura, T., Kimata, K. and Watanabe, H. 2003. Distinct interaction of versican/PG-M with hyaluronan and link protein. *Journal of Biological Chemistry*. **278**(42), pp.41205–41212.
- Matthews, R.T., Gary, S.C., Zerillo, C., Pratta, M., Solomon, K., Arner, E.C. and Hockfield, S. 2000. Brain-enriched hyaluronan binding (BEHAB)/brevican cleavage in a glioma cell line is mediated by a disintegrin and metalloproteinase with thrombospondin motifs (ADAMTS) family member. *Journal of Biological Chemistry*. **275**(30), pp.22695–22703.
- Matthews, R.T., Kelly, G.M., Zerillo, C.A., Gray, G., Tiemeyer, M. and Hockfield, S. 2002. Aggrecan glycoforms contribute to the molecular heterogeneity of perineuronal nets. *The Journal of neuroscience: the official journal of the Society for Neuroscience*. **22**(17), pp.7536–7547.
- Maurel, P., Rauch, U., Flad, M., Margolis, R.K. and Margolis, R.U. 1994. Phosphacan, a chondroitin sulfate proteoglycan of brain that interacts with neurons and neural cell-adhesion molecules, is an extracellular variant of a receptor-type protein tyrosine phosphatase. *Proceedings of the National Academy of Sciences of the United States of America*. **91**(7), pp.2512–2516.
- Mazumder, A., Roopa, T., Basu, A., Mahadevan, L. and Shivashankar, G. V. 2008. Dynamics of chromatin decondensation reveals the structural integrity of a mechanically prestressed nucleus. *Biophysical Journal*. **95**(6), pp.3028–3035.
- Mazumder, A. and Shivashankar, G. V. 2010. Emergence of a prestressed eukaryotic nucleus during cellular differentiation and development. *Journal of The Royal Society Interface*. **7**(suppl_3).
- McCulloch, D.R., Nelson, C.M., Dixon, L.J., Silver, D.L., Wylie, J.D., Lindner, V., Sasaki, T., Cooley, M.A., Argraves, W.S. and Apte, S.S. 2009.

- ADAMTS Metalloproteases Generate Active Versican Fragments that Regulate Interdigital Web Regression. *Developmental Cell*. **17**(5), pp.687–698.
- McRae, P.A. and Porter, B.E. 2012. The perineuronal net component of the extracellular matrix in plasticity and epilepsy. *Neurochemistry International*. **61**(7), pp.963–972.
- McRae, P.A., Rocco, M.M., Kelly, G., Brumberg, J.C. and Matthews, R.T. 2007. Sensory deprivation alters aggrecan and perineuronal net expression in the mouse barrel cortex. *Journal of Neuroscience*. **27**(20), pp.5405–5413.
- Meyer, K. 1958. Chemical structure of hyaluronic acid. *Federation proceedings*. **17**(4), pp.1075–1077.
- Miralles, F., Posern, G., Zaromytidou, A.-I. and Treisman, R. 2003. Actin dynamics control SRF activity by regulation of its coactivator MAL. *Cell*. **113**(3), pp.329–342.
- Miyata, S. and Kitagawa, H. 2015. Mechanisms for modulation of neural plasticity and axon regeneration by chondroitin sulphate. *Journal of Biochemistry*. **157**(1), pp.13–22.
- Miyata, S., Komatsu, Y., Yoshimura, Y., Taya, C. and Kitagawa, H. 2012. Persistent cortical plasticity by upregulation of chondroitin 6-sulfation. *Nature Neuroscience*. **15**(3), pp.414–422.
- Miyata, S., Nadanaka, S., Igarashi, M. and Kitagawa, H. 2018. Structural Variation of Chondroitin Sulfate Chains Contributes to the Molecular Heterogeneity of Perineuronal Nets. *Frontiers in Integrative Neuroscience*. **12**.
- Miyata, S., Nishimura, Y., Hayashi, N. and Oohira, A. 2005. Construction of perineuronal net-like structure by cortical neurons in culture. *Neuroscience*. **136**(1), pp.95–104.
- Miyata, S., Nishimura, Y. and Nakashima, T. 2007. Perineuronal nets protect against amyloid β -protein neurotoxicity in cultured cortical neurons. *Brain Research*. **1150**, pp.200–206.
- Moeendarbary, E., Weber, I.P., Sheridan, G.K., Koser, D.E., Soleman, S., Haenzi, B., Bradbury, E.J., Fawcett, J. and Franze, K. 2017. The soft mechanical signature of glial scars in the central nervous system. *Nature Communications*. **8**(1), pp.1–11.
- Moore, S.W., Roca-Cusachs, P. and Sheetz, M.P. 2010. Stretchy proteins on stretchy substrates: The important elements of integrin-mediated rigidity sensing. *Developmental Cell*. **19**(2), pp.194–206.
- Morawski, M., Brückner, G., Arendt, T. and Matthews, R.T. 2012. Aggrecan: Beyond cartilage and into the brain. *The international journal of biochemistry & cell biology*. **44**(5), pp.690–693.
- Morawski, Markus, Brückner, G., Jäger, C., Seeger, G., Matthews, R.T. and Arendt, T. 2012. Involvement of perineuronal and perisynaptic extracellular matrix in Alzheimer's disease neuropathology. *Brain Pathology*. **22**(4), pp.547–561.

- Morawski, M., Brückner, M.K., Riederer, P., Brückner, G. and Arendt, T. 2004. Perineuronal nets potentially protect against oxidative stress. *Experimental Neurology*. **188**(2), pp.309–315.
- Morawski, M., Dityatev, A., Hartlage-Rübsamen, M., Blosa, M., Holzer, M., Flach, K., Pavlica, S., Dityateva, G., Grosche, J., Brückner, G. and Schachner, M. 2014. Tenascin-R promotes assembly of the extracellular matrix of perineuronal nets via clustering of aggrecan. *Philosophical transactions of the Royal Society of London. Series B, Biological sciences*. **369**(1654), p.20140046.
- Morgelin, M., Heinegard, D., Engel, J. and Paulsson, M. 1994. The cartilage proteoglycan aggregate: assembly through combined protein-carbohydrate and protein-protein interactions. *Biophysical Chemistry*. **50**(1–2), pp.113–128.
- Morris, N.P. and Henderson, Z. 2000. Perineuronal nets ensheath fast spiking, parvalbumin-immunoreactive neurons in the medial septum/diagonal band complex. *European Journal of Neuroscience*. **12**(3), pp.828–838.
- Mort, J.S., Geng, Y., Fisher, W.D. and Roughley, P.J. 2016. Aggrecan heterogeneity in articular cartilage from patients with osteoarthritis. *BMC Musculoskeletal Disorders*.
- Moshayedi, P., da F Costa, L., Christ, A., Lacour, S.P., Fawcett, J., Guck, J. and Franze, K. 2010. Mechanosensitivity of astrocytes on optimized polyacrylamide gels analyzed by quantitative morphometry. *Journal of Physics: Condensed Matter*. **22**(19), p.194114.
- Moshayedi, P., Ng, G., Kwok, J.C.F., Yeo, G.S.H., Bryant, C.E., Fawcett, J.W., Franze, K. and Guck, J. 2014. The relationship between glial cell mechanosensitivity and foreign body reactions in the central nervous system. *Biomaterials*. **35**(13), pp.3919–3925.
- Mueller, A.L., Davis, A., Sovich, S., Carlson, S.S. and Robinson, F.R. 2016. Distribution of N-acetylgalactosamine-positive perineuronal nets in the macaque brain: anatomy and implications. *Neural plasticity*. **2016**, p.6021428.
- Muto, J., Morioka, Y., Yamasaki, K., Kim, M., Garcia, A., Carlin, A.F., Varki, A. and Gallo, R.L. 2014. Hyaluronan digestion controls DC migration from the skin. *Journal of Clinical Investigation*. **124**(3), pp.1309–1319.
- Natowicz, M.R., Short, M.P., Wang, Y., Dickersin, G.R., Gebhardt, M.C., Rosenthal, D.I., Sims, K.B. and Rosenberg, A.E. 1996. Clinical and biochemical manifestations of hyaluronidase deficiency. *New England Journal of Medicine*. **335**(14), pp.1029–1033.
- Nelson, P. 2004. *Biological Physics*. New York: W. H. Freeman.
- Ng, L., Grodzinsky, A.J., Patwari, P., Sandy, J., Plaas, A. and Ortiz, C. 2003. Individual cartilage aggrecan macromolecules and their constituent glycosaminoglycans visualized via atomic force microscopy. *Journal of Structural Biology*. **143**(3), pp.242–257.
- Niederöst, B.P., Zimmermann, D.R., Schwab, M.E. and Bandtlow, C.E. 1999. Bovine CNS myelin contains neurite growth-inhibitory activity associated with chondroitin sulfate proteoglycans. *Journal of Neuroscience*. **19**(20),

pp.8979–8989.

- Nieduszynski, I.A., Sheehan, J.K., Phelps, C.F., Hardingham, T.E. and Muir, H. 1980. Equilibrium-binding studies of pig laryngeal cartilage proteoglycans with hyaluronate oligosaccharide fractions. *The Biochemical Journal*. **185**, pp.107–114.
- Noble, P.W. 2002. Hyaluronan and its catabolic products in tissue injury and repair. *Matrix Biology*.
- Oakes, P.W. and Gardel, M.L. 2014. Stressing the limits of focal adhesion mechanosensitivity. *Current Opinion in Cell Biology*. **30**(1), pp.68–73.
- Ogawa, H., Oohashi, T., Sata, M., Bekku, Y., Hirohata, S., Nakamura, K., Yonezawa, T., Kusachi, S., Shiratori, Y. and Ninomiya, Y. 2004. Lp3/Hapln3, a novel link protein that co-localizes with versican and is coordinately up-regulated by platelet-derived growth factor in arterial smooth muscle cells. *Matrix Biology*. **23**(5), pp.287–298.
- Ogston, A.G. 1966. Measurement by light scattering of the exclusion of protein by hyaluronic acid. *Federation Proceedings*. **25**(3), pp.1122–1123.
- Olin, A.I., Mörgelin, M., Sasaki, T., Timpl, R., Heinegård, D. and Aspberg, A. 2001. The proteoglycans aggrecan and versican form networks with fibulin-2 through their lectin domain binding. *Journal of Biological Chemistry*. **276**(2), pp.1253–1261.
- Oohira, A., Matsui, F. and Katoh-Semba, R. 1991. Inhibitory effects of brain chondroitin sulfate proteoglycans on neurite outgrowth from PC12D cells. *The Journal of Neuroscience*. **11**(3), pp.822–827.
- Oohira, A., Matsui, F., Watanabe, E., Kushima, Y. and Maeda, N. 1994. Developmentally regulated expression of a brain specific species of chondroitin sulfate proteoglycan, neurocan, identified with a monoclonal antibody 1G2 in the rat cerebrum. *Neuroscience*. **60**(1), pp.145–157.
- Orr, A.W., Helmke, B.P., Blackman, B.R. and Schwartz, M.A. 2006. Mechanisms of mechanotransduction. *Developmental Cell*. **10**(1), pp.11–20.
- Pantazopoulos, H., Markota, M., Jaquet, F., Ghosh, D., Wallin, A., Santos, A., Caterson, B. and Berretta, S. 2015. Aggrecan and chondroitin-6-sulfate abnormalities in schizophrenia and bipolar disorder: a postmortem study on the amygdala. *Translational Psychiatry*. **5**, p.e496.
- Pantazopoulos, H., Woo, T.-U.W., Lim, M.P., Lange, N. and Berretta, S. 2010. Extracellular matrix-glia abnormalities in the amygdala and entorhinal cortex of subjects diagnosed with schizophrenia. *Archives of General Psychiatry*. **67**(2), pp.155–166.
- Papadakis, G., Palladino, P., Chronaki, D., Tsortos, A. and Gizeli, E. 2017. Sample-to-answer acoustic detection of DNA in complex samples. *Chemical Communications*. **53**(57), pp.8058–8061.
- Papadakis, G., Tsortos, A., Mitsakakis, K. and Gizeli, E. 2010. Characterization of DNA-Hv1 histone interactions; discrimination of DNA size and shape. *FEBS Letters*. **584**(5), pp.935–940.
- Pasterkamp, R.J. and Kolodkin, A.L. 2003. Semaphorin junction: making

- tracks toward neural connectivity. *Current Opinion in Neurobiology*. **13**(1), pp.79–89.
- Patel, A.J. and Honore, E. 2002. 2P Domain K⁺ Channels: Novel Pharmacological Targets for Volatile General Anesthetics *In: Advances in Experimental Medicine and Biology*. Springer, Boston, MA, pp.9–23.
- Pizzorusso, T. 2002. Reactivation of ocular dominance plasticity in the adult visual cortex. *Science*. **298**(5596), pp.1248–1251.
- Pizzorusso, T., Medini, P., Landi, S., Baldini, S., Berardi, N. and Maffei, L. 2006. Structural and functional recovery from early monocular deprivation in adult rats. *Proceedings of the National Academy of Sciences of the United States of America*. **103**(22), pp.8517–8522.
- Prabhakar, V., Raman, R., Capila, I., Bosques, C.J., Pojasek, K. and Sasisekharan, R. 2005. Biochemical characterization of the chondroitinase ABC I active site. *Biochemical Journal*. **390**(2), pp.395–405.
- Prehm, P. 1984. Hyaluronate is synthesized at plasma membranes. *Biochemical Journal*. **220**(2), pp.597–600.
- Previtera, M.L., Langhammer, C.G., Langrana, N.A. and Firestein, B.L. 2010. Regulation of dendrite arborization by substrate stiffness is mediated by glutamate receptors. *Annals of Biomedical Engineering*. **38**(12), pp.3733–3743.
- Pyka, M., Wetzel, C., Aguado, A., Geissler, M., Hatt, H. and Faissner, A. 2011. Chondroitin sulfate proteoglycans regulate astrocyte-dependent synaptogenesis and modulate synaptic activity in primary embryonic hippocampal neurons. *European Journal of Neuroscience*. **33**(12), pp.2187–2202.
- Rankin-Gee, E.K., McRae, P.A., Baranov, E., Rogers, S., Wandrey, L. and Porter, B.E. 2015. Perineuronal net degradation in epilepsy. *Epilepsia*. **56**(7), pp.1124–1133.
- Rauch, U., Clement, A., Retzler, C., Fröhlich, L., Fässler, R., Göhring, W. and Faissner, A. 1997. Mapping of a defined neurocan binding site to distinct domains of tenascin-C. *Journal of Biological Chemistry*. **272**(43), pp.26905–26912.
- Rauch, U., Gao, P., Janetzko, A., Flaccus, A., Hilgenberg, L., Tekotte, H., Margolis, R.K.R.U. and Margolis, R.K.R.U. 1991. Isolation and characterization of developmentally regulated chondroitin sulfate and chondroitin/keratan sulfate proteoglycans of brain identified with monoclonal antibodies. *Journal of Biological Chemistry*. **266**(22), pp.14785–14801.
- Rauch, U., Hirakawa, S., Oohashi, T., Kappler, J. and Roos, G. 2004. Cartilage link protein interacts with neurocan, which shows hyaluronan binding characteristics different from CD44 and TSG-6. *Matrix Biology*. **22**(8), pp.629–639.
- Rauch, U., Karthikeyan, L., Maurel, P., Margolis, R.U. and Margolis, R.K. 1992. Cloning and primary structure of neurocan, a developmentally regulated, aggregating chondroitin sulfate proteoglycan of brain. *Journal*

of Biological Chemistry. **267**(27), pp.19536–19547.

- Reimers, S., Hartlage-Rübsamen, M., Brückner, G. and Roßner, S. 2007. Formation of perineuronal nets in organotypic mouse brain slice cultures is independent of neuronal glutamatergic activity. *European Journal of Neuroscience*. **25**(9), pp.2640–2648.
- Reviakine, I., Johannsmann, D. and Richter, R.P. 2011. Hearing what you cannot see and visualizing what you hear: Interpreting quartz crystal microbalance data from solvated interfaces. *Analytical Chemistry*. **83**(23), pp.8838–8848.
- Richter, R.P., Baranova, N.S., Day, A.J. and Kwok, J.C. 2018. Glycosaminoglycans in extracellular matrix organisation: are concepts from soft matter physics key to understanding the formation of perineuronal nets? *Current Opinion in Structural Biology*.
- Richter, R.P., Bérat, R. and Brisson, A.R. 2006. Formation of solid-supported lipid bilayers: An integrated view. *Langmuir*. **22**, pp.3497–3505.
- Richter, R.P. and Brisson, A. 2003. Characterization of lipid bilayers and protein assemblies supported on rough surfaces by atomic force microscopy. *Langmuir*. **19**(5), pp.1632–1640.
- Richter, R.P., Hock, K.K., Burkhartsmeier, J., Boehm, H., Bingen, P., Wang, G., Steinmetz, N.F., Evans, D.J. and Spatz, J.P. 2007. Membrane-grafted hyaluronan films: A well-defined model system of glycoconjugate cell coats. *Journal of the American Chemical Society*. **129**(17), pp.5306–5307.
- Del Rio, A., Perez-Jimenez, R., Liu, R., Roca-Cusachs, P., Fernandez, J.M. and Sheetz, M.P. 2009. Stretching single talin rod molecules activates vinculin binding. *Science*. **323**(5914), pp.638–641.
- Rivas, F., Zahid, O.K., Reesink, H.L., Peal, B.T., Nixon, A.J., DeAngelis, P.L., Skardal, A., Rahbar, E. and Hall, A.R. 2018. Label-free analysis of physiological hyaluronan size distribution with a solid-state nanopore sensor. *Nature Communications*.
- Roca-Cusachs, P., Iskratsch, T. and Sheetz, M.P. 2012. Finding the weakest link-exploring integrin-mediated mechanical molecular pathways. *Journal of Cell Science*. **125**(13), pp.3025–3038.
- Rodriguez-Martinez, H., Tienthai, P., Atikuzzaman, M., Vicente-Carrillo, A., Rubér, M. and Alvarez-Rodriguez, M. 2016. The ubiquitous hyaluronan: Functionally implicated in the oviduct? *Theriogenology*. **86**(1), pp.182–186.
- Romberg, C., Yang, S., Melani, R., Andrews, M.R., Horner, A.E., Spillantini, M.G., Bussey, T.J., Fawcett, J.W., Pizzorusso, T. and Saksida, L.M. 2013. Depletion of perineuronal nets enhances recognition memory and long-term depression in the perirhinal cortex. *The Journal of Neuroscience*. **33**(16), pp.7057–7065.
- Roughley, P.J. and Mort, J.S. 2014. The role of aggrecan in normal and osteoarthritic cartilage. *Journal of Experimental Orthopaedics*. **1**(1), pp.1–11.

- Rowlands, D., Lensjø, K.K., Dinh, T., Yang, S., Andrews, M.R., Hafting, T., Fyhn, M., Fawcett, J.W. and Dick, G. 2018. Aggrecan directs extracellular matrix-mediated neuronal plasticity. *Journal of Neuroscience*. **38**(47), pp.10102–10113.
- Ruoslahti, E. 1996. Brain extracellular matrix. *Glycobiology*. **6**(5), pp.489–92.
- Salustri, A., Garlanda, C., Hirsch, E., De Acetis, M., Maccagno, A., Bottazi, B., Doni, A., Bastone, A., Mantovani, G., Peccoz, P.B., Salvatori, G., Mahoney, D.J., Day, A.J., Siracusa, G., Romani, L. and Mantovani, A. 2004. PTX3 plays a key role in the organization of the cumulus oophorus extracellular matrix and in in vivo fertilization. *Development*.
- Sandy, J.D., Flannery, C.R., Boynton, R.E. and Neame, P.J. 1990. Isolation and characterization of disulfide-bonded peptides from the three globular domains of aggregating cartilage proteoglycan. *Journal of Biological Chemistry*. **265**(34), pp.21108–21113.
- Sandy, J.D., Westling, J., Kenagy, R.D., Iruela-Arispe, M.L., Verscharen, C., Rodriguez-Mazaneque, J.C., Zimmermann, D.R., Lemire, J.M., Fischer, J.W., Wight, T.N. and Clowes, A.W. 2001. Versican V1 Proteolysis in Human Aorta in Vivo Occurs at the Glu 441-Ala442 Bond, a Site That Is Cleaved by Recombinant ADAMTS-1 and ADAMTS-4. *Journal of Biological Chemistry*. **276**(16), pp.13372–13378.
- Sauerbrey, G. 1959. The use of quartz oscillators for weighing thin layers and for microweighing. *Z Phys*. **155**, pp.206–222.
- Scarchilli, L., Camaioni, A., Bottazzi, B., Negri, V., Doni, A., Deban, L., Bastone, A., Salvatori, G., Mantovani, A., Siracusa, G. and Salustri, A. 2007. PTX3 interacts with inter- α -trypsin inhibitor: Implications for hyaluronan organization and cumulus oophorus expansion. *Journal of Biological Chemistry*.
- Schachner, M., Taylor, J., Bartsch, U. and Pesheva, P. 1994. The perplexing multifunctionality of janusin, a tenascin-related molecule. *Perspectives Developmental Neurobiology*. **2**, pp.33–41.
- Schwarz, U.S. and Gardel, M.L. 2012. United we stand - Integrating the actin cytoskeleton and cell-matrix adhesions in cellular mechanotransduction. *Journal of Cell Science*. **125**(13), pp.3051–3060.
- Seeger, G., Brauer, K., Härtig, W. and Brückner, G. 1994. Mapping of perineuronal nets in the rat brain stained by colloidal iron hydroxide histochemistry and lectin cytochemistry. *Neuroscience*. **58**(2), pp.371–388.
- Seidenbecher, C.I., Richter, K., Rauch, U., Fassler, R., Garner, C.C. and Gundelfinger, E.D. 1995. Brevican, a chondroitin sulfate proteoglycan of rat brain, occurs as secreted and cell surface glycosylphosphatidylinositol-anchored isoforms. *Journal of Biological Chemistry*. **270**(45), pp.27206–27212.
- Seyfried, N.T., McVey, G.F., Almond, A., Mahoney, D.J., Dudhia, J. and Day, A.J. 2005. Expression and purification of functionally active hyaluronan-binding domains from human cartilage link protein, aggrecan and versican: Formation of ternary complexes with defined hyaluronan

- oligosaccharides. *Journal of Biological Chemistry*. **280**(7), pp.5435–5448.
- Shi, S., Grothe, S., Zhang, Y., O'Connor-McCourt, M.D., Poole, A.R., Roughley, P.J. and Mort, J.S. 2004. Link protein has greater affinity for versican than aggrecan. *The Journal of Biological Chemistry*. **279**(13), pp.12060–12066.
- Siechen, S., Yang, S., Chiba, A. and Saif, T. 2009. Mechanical tension contributes to clustering of neurotransmitter vesicles at presynaptic terminals. *Proceedings of the National Academy of Sciences of the United States of America*. **106**(31), pp.12611–12616.
- Sigal, Y.M., Bae, H., Bogart, L.J., Hensch, T.K. and Zhuang, X. 2019. Structural maturation of cortical perineuronal nets and their perforating synapses revealed by superresolution imaging. *Proceedings of the National Academy of Sciences of the United States of America*. **116**(14), pp.7071–7076.
- Slaker, M., Blacktop, J.M. and Sorg, B.A. 2016. Caught in the net: perineuronal nets and addiction. *Neural Plasticity*. **2016**, pp.1–8.
- Snow, D.M., Brown, E.M. and Letourneau, P.C. 1996. Growth cone behavior in the presence of soluble chondroitin sulfate proteoglycan (CSPG), compared to behavior on CSPG bound to laminin or fibronectin. *International Journal of Developmental Neuroscience*. **14**(3), pp.331–349.
- Šoltés, L., Mendichi, R., Kogan, G., Schiller, J., Stankovská, M. and Arnhold, J. 2006. Degradative action of reactive oxygen species on hyaluronan. *Biomacromolecules*. **7**(3), pp.659–668.
- Sorg, B.A., Berretta, S., Blacktop, J.M., Fawcett, J.W., Kitagawa, H., Kwok, J.C.F. and Miquel, M. 2016. Casting a Wide Net: Role of Perineuronal Nets in Neural Plasticity. *The Journal of neuroscience : the official journal of the Society for Neuroscience*. **36**(45), pp.11459–11468.
- Souter, L. and Kwok, J.C.F. 2020. *Visualization of Perineuronal Nets in Central Nervous System Tissue Sections*.
- Spicer, A.P., Joo, A. and Bowling, R.A. 2003. A hyaluronan binding link protein gene family whose members are physically linked adjacent to chondroitin sulfate proteoglycan core protein genes: the missing links. *The Journal of Biological Chemistry*. **278**(23), pp.21083–21091.
- Spicer, A.P. and McDonald, J.A. 1998. Characterization and molecular evolution of a vertebrate hyaluronan synthase gene family. *Journal of Biological Chemistry*.
- Stabenfeldt, S.E. and Laplaca, M.C. 2011. Variations in rigidity and ligand density influence neuronal response in methylcellulose-laminin hydrogels. *Acta Biomaterialia*. **7**(12), pp.4102–4108.
- Stern, R. 2003. Devising a pathway for hyaluronan catabolism: Are we there yet? *Glycobiology*.
- Stern, R. 2004. Hyaluronan catabolism: A new metabolic pathway. *European Journal of Cell Biology*. **83**(7), pp.317–325.
- Stern, R. and Jedrzejewski, M.J. 2006. Hyaluronidases: Their genomics,

- structures, and mechanisms of action. *Chemical Reviews*. **106**(3), pp.818–839.
- Sucha, P., Chmelova, M., Kamenicka, M., Bochin, M., Oohashi, T. and Vargova, L. 2020. The Effect of Hapln4 Link Protein Deficiency on Extracellular Space Diffusion Parameters and Perineuronal Nets in the Auditory System During Aging. *Neurochemical Research*. **45**(1), pp.68–82.
- Sugiyama, S., Di Nardo, A.A., Aizawa, S., Matsuo, I., Volovitch, M., Prochiantz, A. and Hensch, T.K. 2008. Experience-dependent transfer of Otx2 homeoprotein into the visual cortex activates postnatal plasticity. *Cell*. **134**(3), pp.508–520.
- Sukharev, S. and Sachs, F. 2012. Molecular force transduction by ion channels – diversity and unifying principles. *Journal of Cell Science*. **125**(13), pp.3075–3083.
- Suttkus, A., Holzer, M., Morawski, M. and Arendt, T. 2016. The neuronal extracellular matrix restricts distribution and internalization of aggregated Tau-protein. *Neuroscience*. **313**, pp.225–235.
- Suttkus, A., Rohn, S., Jäger, C., Arendt, T. and Morawski, M. 2012. Neuroprotection against iron-induced cell death by perineuronal nets - an in vivo analysis of oxidative stress. *American Journal of Neurodegenerative Disease*. **1**(2), pp.122–129.
- Suttkus, A., Rohn, S., Weigel, S., Glöckner, P., Arendt, T. and Morawski, M. 2014. AggreCAN, link protein and tenascin-R are essential components of the perineuronal net to protect neurons against iron-induced oxidative stress. *Cell Death & Disease*. **5**(3), p.e1119.
- Takahashi-Iwanaga, H., Murakami, T. and Abe, K. 1998. Three-dimensional microanatomy of perineuronal proteoglycan nets enveloping motor neurons in the rat spinal cord. *Journal of neurocytology*. **27**(11), pp.817–27.
- Takahashi, R., Al-Assaf, S., Williams, P.A., Kubota, K., Okamoto, A. and Nishinari, K. 2003. Asymmetrical-Flow Field-Flow Fractionation with On-Line Multiangle Light Scattering Detection. 1. Application to Wormlike Chain Analysis of Weakly Stiff Polymer Chains. *Biomacromolecules*. **4**, pp.404–409.
- Tavianatou, A.G., Caon, I., Franchi, M., Piperigkou, Z., Galesso, D. and Karamanos, N.K. 2019. Hyaluronan: molecular size-dependent signaling and biological functions in inflammation and cancer. *The FEBS Journal*. **286**(15), pp.2883–2908.
- Tellechea, E., Johannsmann, D., Steinmetz, N.F., Richter, R.P. and Reviakine, I. 2009. Model-independent analysis of QCM data on colloidal particle adsorption. *Langmuir*. **25**(9), pp.5177–5184.
- Temple-Wong, M.M., Ren, S., Quach, P., Hansen, B.C., Chen, A.C., Hasegawa, A., D’Lima, D.D., Koziol, J., Masuda, K., Lotz, M.K. and Sah, R.L. 2016. Hyaluronan concentration and size distribution in human knee synovial fluid: Variations with age and cartilage degeneration. *Arthritis Research and Therapy*.

- Thakar, D., Migliorini, E., Coche-Guerente, L., Sadir, R., Lortat-Jacob, H., Boturyn, D., Renaudet, O., Labbe, P. and Richter, R.P. 2014. A quartz crystal microbalance method to study the terminal functionalization of glycosaminoglycans. *Chemical communications*. **50**(96), pp.15148–51.
- Tien, J.Y.L. and Spicer, A.P. 2005. Three vertebrate hyaluronan synthases are expressed during mouse development in distinct spatial and temporal patterns. *Developmental Dynamics*.
- Törrönen, K., Nikunen, K., Kärnä, R., Tammi, M., Tammi, R. and Rilla, K. 2014. Tissue distribution and subcellular localization of hyaluronan synthase isoenzymes. *Histochemistry and Cell Biology*.
- Triggs-Raine, B., Salo, T.J., Zhang, H., Wicklow, B.A. and Natowicz, M.R. 1999. Mutations in HYAL1, a member of a tandemly distributed multigene family encoding disparate hyaluronidase activities, cause a newly described lysosomal disorder, mucopolysaccharidosis IX. *Proceedings of the National Academy of Sciences of the United States of America*. **96**(11), pp.6296–6300.
- Tsien, R.Y. 2013. Very long-term memories may be stored in the pattern of holes in the perineuronal net. *Proceedings of the National Academy of Sciences of the United States of America*. **110**(30), pp.12456–12461.
- Tsortos, A., Papadakis, G. and Gizeli, E. 2008. Shear acoustic wave biosensor for detecting DNA intrinsic viscosity and conformation: A study with QCM-D. *Biosensors and Bioelectronics*. **24**(4), pp.836–841.
- Tsortos, A., Papadakis, G., Mitsakakis, K., Melzak, K.A. and Gizeli, E. 2008. Quantitative determination of size and shape of surface-bound DNA using an acoustic wave sensor. *Biophysical Journal*. **94**(7), pp.2706–2715.
- Ueno, H., Suemitsu, S., Okamoto, M., Matsumoto, Y. and Ishihara, T. 2017a. Parvalbumin neurons and perineuronal nets in the mouse prefrontal cortex. *Neuroscience*. **343**, pp.115–127.
- Ueno, H., Suemitsu, S., Okamoto, M., Matsumoto, Y. and Ishihara, T. 2017b. Sensory experience-dependent formation of perineuronal nets and expression of Cat-315 immunoreactive components in the mouse somatosensory cortex. *Neuroscience*. **355**, pp.161–174.
- Ueno, H., Takao, K., Suemitsu, S., Murakami, S., Kitamura, N., Wani, K., Okamoto, M., Aoki, S. and Ishihara, T. 2018. Age-dependent and region-specific alteration of parvalbumin neurons and perineuronal nets in the mouse cerebral cortex. *Neurochemistry International*. **112**, pp.59–70.
- Vo, T., Carulli, D., Ehlert, E.M.E., Kwok, J.C.F., Dick, G., Mecollari, V., Moloney, E.B., Neufeld, G., de Winter, F., Fawcett, J.W. and Verhaagen, J. 2013. The chemorepulsive axon guidance protein semaphorin3A is a constituent of perineuronal nets in the adult rodent brain. *Molecular and Cellular Neuroscience*. **56**, pp.186–200.
- Volpi, N., Maccari, F., Suwan, J. and Linhardt, R.J. 2012. Electrophoresis for the analysis of heparin purity and quality. *Electrophoresis*. **33**(11), pp.1531–1537.
- Wang, D. and Fawcett, J. 2012. The perineuronal net and the control of CNS

- plasticity. *Cell and Tissue Research*. **349**(1), pp.147–160.
- Wang, N., Tytell, J.D. and Ingber, D.E. 2009. Mechanotransduction at a distance: mechanically coupling the extracellular matrix with the nucleus. *Nature Reviews Molecular Cell Biology*. **10**(1), pp.75–82.
- Watanabe, H., Cheung, S.C., Itano, N., Kimata, K. and Yamada, Y. 1997. Identification of hyaluronan-binding domains of aggrecan. *Journal of Biological Chemistry*. **272**(44), pp.28057–28065.
- Wedlich-Söldner, R. and Betz, T. 2018. Self-organization: the fundament of cell biology. *Philosophical Transactions of the Royal Society B: Biological Sciences*. **373**(1747), p.20170103.
- Wegner, F., Härtig, W., Bringmann, A., Grosche, J., Wohlfarth, K., Zuschratter, W. and Brückner, G. 2003. Diffuse perineuronal nets and modified pyramidal cells immunoreactive for glutamate and the GABA_A receptor α 1 subunit form a unique entity in rat cerebral cortex. *Experimental Neurology*. **184**(2), pp.705–714.
- Weigel, P.H. 2015. Hyaluronan Synthase: The Mechanism of Initiation at the Reducing End and a Pendulum Model for Polysaccharide Translocation to the Cell Exterior. *International Journal of Cell Biology*., pp.1–15.
- West, D.C. and Kumar, S. 1989. The effect of hyaluronate and its oligosaccharides on endothelial cell proliferation and monolayer integrity. *Experimental Cell Research*.
- Winston, V. 1989. Use of a polynomial exponential function to describe migration of proteins on sodium dodecyl sulfate-polyacrylamide gels. *Electrophoresis*. **10**(3), pp.220–222.
- de Winter, F., Kwok, J.C.F., Fawcett, J.W., Vo, T.T., Carulli, D., Verhaagen, J., de Winter, F., Kwok, J.C.F., Fawcett, J.W., Vo, T.T., Carulli, D. and Verhaagen, J. 2016. The chemorepulsive protein semaphorin 3A and perineuronal net-mediated plasticity. *Neural Plasticity*. **2016**, pp.1–14.
- Wolny, P.M., Banerji, S., Gounou, C., Brisson, A.R., Day, A.J., Jackson, D.G. and Richter, R.P. 2010. Analysis of CD44-hyaluronan interactions in an artificial membrane system: Insights into the distinct binding properties of high and low molecular weight hyaluronan. *Journal of Biological Chemistry*. **285**(39), pp.30170–30180.
- Woodworth, A., Fiete, D. and Baenziger, J.U. 2002. Spatial and temporal regulation of tenascin-R glycosylation in the cerebellum. *Journal of Biological Chemistry*. **277**(52), pp.50941–50947.
- Xiao, Z.C., Bartsch, U., Margolis, R.K., Rougon, G., Montag, D. and Schachner, M. 1997. Isolation of a tenascin-R binding protein from mouse brain membranes: A phosphacan-related chondroitin sulfate proteoglycan. *Journal of Biological Chemistry*. **272**(51), pp.32092–32101.
- Xue, Y.-X., Xue, L.-F., Liu, J.-F., He, J., Deng, J.-H., Sun, S.-C., Han, H.-B., Luo, Y.-X., Xu, L.-Z., Wu, P. and Lu, L. 2014. Depletion of perineuronal nets in the amygdala to enhance the erasure of drug memories. *Journal of Neuroscience*. **34**(19), pp.6647–6658.
- Yamada, H., Watanabe, K., Shimonaka, M. and Yamaguchi, Y. 1994.

- Molecular cloning of brevican, a novel brain proteoglycan of the aggrecan/versican family. *Journal of Biological Chemistry*. **269**(13), pp.10119–10126.
- Yamada, J. and Jinno, S. 2017. Molecular heterogeneity of aggrecan-based perineuronal nets around five subclasses of parvalbumin-expressing neurons in the mouse hippocampus. *Journal of Comparative Neurology*. **525**(5), pp.1234–1249.
- Yamaguchi, Y. 1996. Brevican: a major proteoglycan in adult brain. *Perspectives on developmental neurobiology*. **3**(4), pp.307–317.
- Yamaguchi, Y. 2000. Lecticans: organizers of the brain extracellular matrix. *Cellular and Molecular Life Sciences*. **57**(2), pp.276–289.
- Yang, S., Cacquevel, M., Saksida, L.M., Bussey, T.J., Schneider, B.L., Aebischer, P., Melani, R., Pizzorusso, T., Fawcett, J.W. and Spillantini, M.G. 2015. Perineuronal net digestion with chondroitinase restores memory in mice with tau pathology. *Experimental neurology*. **265**, pp.48–58.
- Yuan, H., Amin, R., Ye, X., De La Motte, C.A. and Cowman, M.K. 2015. Determination of hyaluronan molecular mass distribution in human breast milk. *Analytical Biochemistry*. **474**, pp.78–88.
- Zaidel-Bar, R., Itzkovitz, S., Ma'ayan, A., Iyengar, R. and Geiger, B. 2007. Functional atlas of the integrin adhesome. *Nature Cell Biology*. **9**(8), pp.858–867.
- Zako, M., Shinomura, T., Ujita, M., Ito, K. and Kimata, K. 1995. Expression of PG-M(V3), an alternatively spliced form of PG-M without a chondroitin sulfate attachment region in mouse and human tissues. *Journal of Biological Chemistry*. **270**(8), pp.3914–3918.
- Zhuo, L., Yoneda, M., Zhao, M., Yingsung, W., Yoshida, N., Kitagawa, Y., Kawamura, K., Suzuki, T. and Kimata, K. 2001. Defect in SHAP-hyaluronan complex causes severe female infertility. A study by inactivation of the bikunin gene in mice. *Journal of Biological Chemistry*.
- Zimmermann, D.R. and Dours-Zimmermann, M.T. 2008. Extracellular matrix of the central nervous system: From neglect to challenge. *Histochemistry and Cell Biology*. **130**(4), pp.635–653.
- Zimmermann, D.R. and Ruoslahti, E. 1989. Multiple domains of the large fibroblast proteoglycan, versican. *The EMBO journal*. **8**(10), pp.2975–2981.

Chapter 9: Appendices

Appendix 1: Quantitative analysis of film rigidity

$$\Delta D_n / (-\Delta f_n / n) \ll 4 \times 10^{-7} \text{Hz}^{-1}$$

For dense HA50 films:

$$\Delta f_n = -35 \text{ Hz}$$

$$\Delta D_n = 14 \times 10^{-6}$$

$$n = 5$$

Therefore:

$$14 \times 10^{-6} / (- -35/5) \ll 4 \times 10^{-7} \text{Hz}^{-1}$$

$$2 \times 10^{-6} \ll 4 \times 10^{-7} \text{Hz}^{-1}$$

This statement is not true, therefore the film is classified as soft.

For sparse HA50 films:

$$\Delta f_n = -5 \text{ Hz}$$

$$\Delta D_n = 2 \times 10^{-6}$$

$$n = 5$$

Therefore:

$$2 \times 10^{-6} / (- -5/5) \ll 4 \times 10^{-7} \text{Hz}^{-1}$$

$$2 \times 10^{-6} \ll 4 \times 10^{-7} \text{Hz}^{-1}$$

This statement is not true, therefore the film is classified as soft.

Appendix 2: Lipid datasheets for DOPC : DOPE-cap-biotin liposomes [95 : 5] and DOPC : DODA-tris-NTA [99.5 : 0.5]

DOPC : DOPE-cap-biotin

-	stock spec	C (g/L)	Mw (g/mol)
lipid	DOPC	26.2	786.15
lipid	DOPE-cap-biotin	26.2	1105.47
<i>solvent</i>	<i>CHCl3</i>		

Desired conc.		Sample mix (mol ratio)		Amount sample (μmol)	
(mg/mL)	μmol	DOPC	DOPE-cap-biotin	DOPC	DOPE-cap-biotin
2.00	2.40	95.0	5.0	2.28	0.12

Mass sample (mg)			Volume stock (μL)		Volume buffer (mL)
DOPC	DOPE-cap-biotin	sum	DOPC	DOPE-cap-biotin	
1.79	0.13	1.93	68.41	5.06	0.96

DOPC : DODA-tris-NTA

.	stock spec	C (g/l)	Mw (g/mol)
lipid	DODA-Tris-NTA	2.29	786.15
lipid	DOPC	26.2	1540.00
<i>solvent</i>	<i>CHCl3</i>		

Desired conc.		Sample mix (mol ratio)		Amount sample (μmol)	
(mg/mL)	μmol	DOPC	DODA-tris-NTA	DOPC	DODA-tris-NTA
2.00	2.40	99.5	0.5	2.39	0.01

Mass sample (mg)			Volume stock (μL)		Volume buffer (mL)
DOPC	DODA-tris-NTA	sum	DOPC	DODA-tris-NTA	
1.88	0.01	1.89	71.65	5.79	0.95

Appendix 3: Analysis process and tables of results for HA and CS used in the PAGE analysis

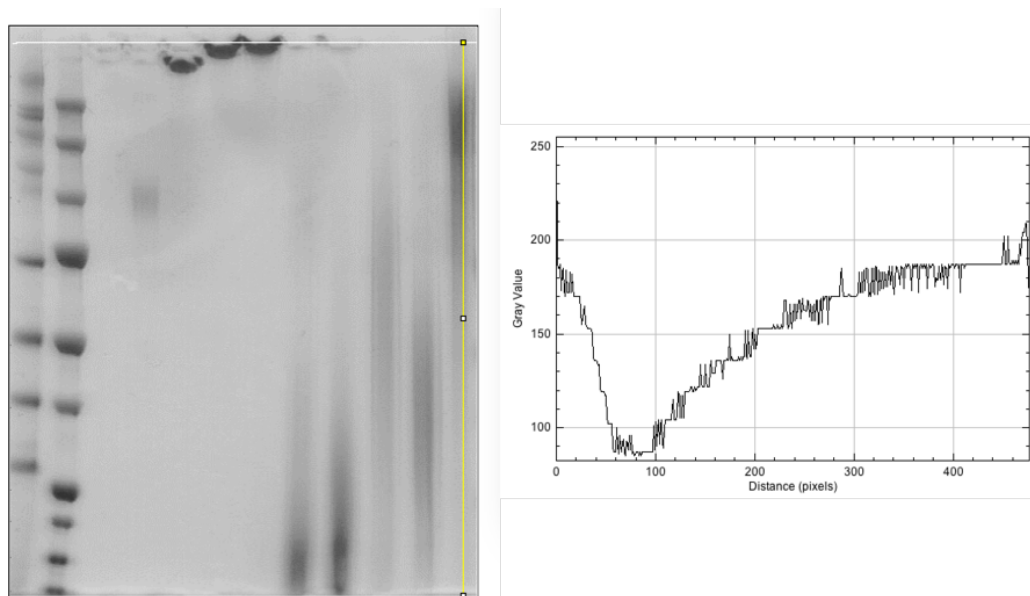


Figure 47. An example of how d_{mig} , d_{min} and d_{max} were measured is represented in the image below.

The white line across the top indicates the top of the gel. The yellow line running down the image is an example of the line used to measure the value of pixel intensity. The Graph to the right of the image reflects the relationship between distance travelled and pixel intensity. The discrete steps in intensity reflect the quality of the image taken, as the image was not as high in resolution as was intended.

Table 8. HA and CS migration distance values (normalised).

	d_{mig}	d_{max}	d_{min}
HA	0.29	0.25	0.32
CS-A	0.93	0.85	1.00
CS-B	0.92	0.79	1.00
CS-C	0.47	0.31	0.79
CS-D	0.67	0.49	0.85
CS-E	0.16	0.08	0.37

Table 9. $M_{w,protein}$ values for HA50 and CS samples.

	For d_{mig}	For d_{max}	For d_{min}
HA	93	110	86
CS-A	11	22	10
CS-B	12	28	10
CS-C	63	89	18
CS-D	38	59	22
CS-E	180	390	79

Table 10. $M_{w,GAG}$ values for CS samples.

	mean	mean - half max	mean + half max
CS-A	6	13	6
CS-B	7	16	6
CS-C	37	52	11
CS-D	22	35	13
CS-E	106	229	46

Appendix 4: Tables of migration distances for the protein standards, HA and CS used in the PAGE analysis

d_{total} = 477 pixels (measure of the maximum gel distance).

Table 11. Protein standard results.

kDa	d_{mig}
Precision plus™	
10	0.02
15	0.03
20	0.04
25	0.05
37	0.08
50	0.10
75	0.16
100	0.21
150	0.31
250	0.52
HiMark™	
31	0.06
41	0.09
55	0.12
71	0.15
117	0.25
171	0.36
238	0.50
268	0.56
460	0.96

Appendix 5: Values for measuring HA $\Delta D / - \Delta f$ using different methods

Table 12. Values for measuring HA $\Delta D / - \Delta f$ using different methods.

Sample	-4 to -5 Hz	Maximal coverage	Average
HA_dp15	0.19 ± 0.01	0.13 ± 0.01	0.14 ± 0.01
HA50	0.37 ± 0.03	0.36 ± 0.01	0.37 ± 0.01
HA250	0.72 ± 0.03	0.88 ± 0.01	0.85 ± 0.02
HA500	1.33 ± 0.18	1.34 ± 0.20	1.15 ± 0.34
HA1000	1.07 ± 0.02	1.10 ± 0.22	1.17 ± 0.24